



**HAL**  
open science

# Auto-assemblage de bicouches de copolymères à blocs amphiphiles induit par une surface

Flávia Mesquita Cabrini

► **To cite this version:**

Flávia Mesquita Cabrini. Auto-assemblage de bicouches de copolymères à blocs amphiphiles induit par une surface. Polymères. Université de Bordeaux, 2022. Français. NNT : 2022BORD0037 . tel-03633871

**HAL Id: tel-03633871**

**<https://theses.hal.science/tel-03633871>**

Submitted on 7 Apr 2022

**HAL** is a multi-disciplinary open access archive for the deposit and dissemination of scientific research documents, whether they are published or not. The documents may come from teaching and research institutions in France or abroad, or from public or private research centers.

L'archive ouverte pluridisciplinaire **HAL**, est destinée au dépôt et à la diffusion de documents scientifiques de niveau recherche, publiés ou non, émanant des établissements d'enseignement et de recherche français ou étrangers, des laboratoires publics ou privés.

THÈSE PRÉSENTÉE  
POUR OBTENIR LE GRADE DE

**DOCTEUR DE**  
**L'UNIVERSITÉ DE BORDEAUX**  
ÉCOLE DOCTORALE DES SCIENCES CHIMIQUES  
Spécialité: Polymères

Par Flávia MESQUITA CABRINI

**SURFACE-INDUCED SELF-ASSEMBLY OF  
AMPHIPHILIC BLOCK COPOLYMER BILAYERS**

Sous la direction de: Jean-Paul CHAPEL & Christophe SCHATZ

Soutenance prévue le 17 février 2022

Membres du jury:

Erica WANLESS	Professeure, University of Newcastle	Rapporteure
Thierry CHARITAT	Professeur, Université de Strasbourg	Rapporteur
Cécile ZAKRI	Professeure, Université de Bordeaux	Présidente
Guilherme FERREIRA	Professeur, Universidade Federal da Bahia	Examineur
Fabrice Cousin	Ingénieur-chercheur, CEA	Invité
Guillaume FLEURY	Professeur, Université de Bordeaux	Invité
Christophe SCHATZ	Maître de conférences, Bordeaux INP	Co-directeur de thèse
Jean-Paul CHAPEL	Directeur de Recherche, CNRS	Directeur de thèse



# **Title: Surface-Induced Self-Assembly of Amphiphilic Block Copolymer Bilayers**

**Abstract:** Block copolymers (BCs) are widely used in materials science due to their capacity to self-assemble in bulk, thin film or solution into a variety of nanoscale ordered structures with different morphologies. In particular, BCs have attracted much interest over the past years for the generation of bilayer membranes in solution and, more recently, solid-supported bilayers. Mainly used for biomimetic purposes at the lab scale, solid-supported BC bilayers have the potential for becoming a new class of functional organic thin films that is currently not investigated due to the difficulty to generate them under good conditions at a large scale and/or on non-planar substrates with current methods (*e.g.* Langmuir-Blodgett depositions, Vesicle Fusion, etc). This thesis is part of the **ANR SISAL** project (2018 – 2022), which proposes a scalable fabrication method of solid-supported BC bilayer membranes that can be applied on substrates of any type, shape and size, for the generation of symmetric and asymmetric bilayers. The proposed fabrication method involves, first, the adsorption of a BC monolayer in a non-selective solvent through specific interactions between the hydrophilic blocks and the substrate; and second, the self-assembly of BCs in solution with those forming the adsorbed monolayer, taking place after the introduction of a selective solvent which will change the polarity of the medium and trigger interactions between the BC hydrophobic blocks. The aim of this thesis work was the full examination of the proposed fabrication method using mostly polystyrene-*block*-poly(acrylic acid) (PS-*b*-PAA) diblock copolymers in flat substrates (silicon wafers), as they allow the use of a wide range of complementary state-of-the-art techniques to precisely characterize the different steps of the assembly. Both steps of the fabrication method were systematically studied using Atomic Force microscopy (AFM), ellipsometry, water contact angle measurements, Polarization Modulation Infrared Reflection Absorption Spectroscopy (PM-IRRAS), Quartz Crystal Microbalance with Dissipation (QCM-D) and Neutron Reflectivity (NR). An intermediate step, between the mono- and bilayer formation, called “monolayer densification”, has been evidenced for PS-*b*-PAA BCs and characterized by the above-mentioned techniques. In a last but not least effort, the process has been generalized and extended to the fabrication of asymmetric bilayers, to the encapsulation of active ingredients as gold particles in the hydrophobic reservoir of the bilayers and extended to

colloidal substrates with promising results. These organic films with well-controlled thickness and functionality have also been proposed as model systems to study the particular properties of polymeric thin films

**Key words:** Amphiphilic block copolymers, self-assembly, organic thin film, solid-supported bilayer

# **Titre: Auto-assemblage de bicouches de copolymères à blocs amphiphiles induit par une surface**

**Résumé:** Les copolymères à blocs (CBs) sont largement utilisés en science des matériaux en raison de leur capacité à s'auto-assembler en une variété de structures ordonnées à l'échelle nanométrique en volume, en film mince ou en solution. En particulier, les CBs ont suscité un grand intérêt au cours des dernières années pour la génération de membranes bicouches en solution et, plus récemment, de bicouches sur supports solides. Principalement utilisées à des fins biomimétiques à l'échelle du laboratoire, les bicouches de CBs sur supports solides ont le potentiel pour devenir une nouvelle classe de films minces organiques fonctionnels, actuellement peu étudiés en raison des difficultés de mise en œuvre à grande échelle et/ou sur des substrats non planaires avec les méthodes actuelles (par exemple les dépôts Langmuir-Blodgett, la fusion de vésicules, etc). Cette thèse s'inscrit dans le cadre du projet ANR SISAL (2018 - 2022), qui propose une méthode de fabrication évolutive de membranes bicouches symétriques et asymétriques de CB sur des supports solides variés en forme et en taille. La méthode de fabrication est constituée de deux étapes : dans un premier temps, l'adsorption d'une monocouche de CB dans un solvant non sélectif par des interactions spécifiques entre le bloc hydrophile et le substrat ; puis dans un deuxième temps, l'auto-assemblage des CBs libres en solution avec ceux formant la monocouche adsorbée sous l'effet d'un changement de polarité du milieu grâce à l'ajout d'un solvant sélectif (eau) qui va déclencher des interactions hydrophobes entre les blocs hydrophobes des CBs. L'objectif de ce travail de thèse est d'apporter la preuve de concept de cette méthode de fabrication en utilisant des copolymères diblocs de type polystyrène-*bloc*-poly(acide acrylique) (PS-*b*-PAA) sur des substrats plans (wafers de silicium) qui permettent d'utiliser un large éventail de techniques complémentaires de pointe pour caractériser précisément les différentes étapes de l'assemblage. Ces deux étapes ont été systématiquement étudiées à l'aide de la microscopie à force atomique (AFM), de l'ellipsométrie, des mesures d'angles de contact avec l'eau, de la spectroscopie d'absorption par réflexion infrarouge à modulation de polarisation (PM-IRRAS), de la microbalance à quartz avec dissipation (QCM-D) et de la réflectivité des neutrons (NR). Une étape intermédiaire, entre la formation de la monocouche et de la bicouche, appelée "densification de la monocouche", a été mise en évidence dans le cas des copolymères PS-*b*-

PAA et caractérisée à l'aide des mêmes techniques. Dans un dernier effort, le processus a été généralisé et étendu à la fabrication de bicouches asymétriques, à l'encapsulation d'ingrédients actifs comme des particules d'or dans le réservoir hydrophobe des bicouches et étendu à des substrats colloïdaux avec des résultats prometteurs. Ces films organiques dont l'épaisseur et les fonctionnalités sont bien contrôlées ont également été proposés comme systèmes modèles pour étudier les propriétés particulières des films minces polymères.

**Mots clés:** Copolymères à blocs amphiphiles, auto-assemblage, films minces organiques, bicouches supportées

---

## **Unité de recherche**

**Centre de Recherche Paul Pascal (CRPP), CNRS, UMR 5031**

115 Avenue du Dr. Albert Schweitzer, 33600 Pessac – France.

# Acknowledgments

This thesis work was carried out at the Centre de Recherche Paul Pascal (CRPP), between November 2018 and February 2022, funded by the Centre National de la Recherche Scientifique (CNRS) through the SISAL project (ANR-18-CE06-0016, 2018 – 2022), for which I am grateful.

I would like to express my deepest gratitude for my thesis supervisor Jean-Paul Chapel and co-supervisor Christophe Schatz for accepting me to this PhD position. I specially thank Jean-Paul for his genuine kindness of taking care of us, international students, from the very first moment we get in France, making our lives in a foreign place much easier. In a very professional way, Jean-Paul and Christophe were able to guide my research work by constantly bring up innovative ideas during very long (but surprisingly very exciting!) group meetings with a lot of positivity, always showing recognition for the work done and support for those to come. Although quite different, Jean-Paul and Christophe definitely define a “dynamic duo”, working in a very harmonic, respectful and complementary way, which was undoubtedly the reason why I was able to learn a lot from both of their own domains and succeed during my PhD. It was really a pleasure to work with both of you, I will be forever grateful for this opportunity and I will surely miss you in the future.

I would like to thank the jury members for accepting to evaluate my work, either attending the thesis defense online (Erica Wanless from Australia, Guilherme Ferreira from Brazil, at very unusual schedules) or in person (Thierry Charitat, Fabrice Cousin, Guillaume Fleury and Cecile Zakri). Your dedicated time for remarks and comments from different domains resulted in a very rich discussion which I deeply appreciated.

I would like to thank all of the group members working in this project, including the former master student Julien Romain; the post-docs Alliny Naves and Martin Fauquignon; the master students Antoine, Ludovic and Franck: and, last but not least, the research engineer of the group, Joanna Giermanska, for all of the trainings, discussions, teaching and specially for always being prompt to help with anything I could need.

I deeply thank the whole CRPP, from reception, guardian, human resources, management, informatics and mechanical atelier, permanent and non-permanent staff. Notably, I thank the president Cecile Zakri for accepting me in the laboratory. I extend my

gratitude to Hassan Saadaoui and Gilles Pecastaings for AFM training and analysis, Serge Ravaine for the synthesis of gold nanoparticles and Ahmed Bentaleb for the SAXS training and measurements, and to the CIA team for all of the discussions during our regular meetings.

I specially thank all of the collaborators in this project, including: from the Laboratoire de Chimie des Polymères Organiques (LCPO), Benjamin Cabannes-Boue and Guillaume Fleury for the PS-b-P2VP copolymers; and Simon Harris for the support of PBA-b-PAA synthesis, together with Franck Gilbert; from the Université Bretagne Sud, Guillaume Vignaud for the  $T_g$  determination; from Sorbonne Université, Francois Stoffelbach for the synthesis of deuterated PS-b-PAA.

I deeply thank Fabrice Cousin for the NR and SANS experiments performed in LLB, which were essential for a deep understanding of my thesis work. I specially thank for his time spent to teach me during the measurements and for the training in LLB. The measurements optimization and data analysis done together with Jean-Paul definitely helped me a lot, for which I am deeply grateful.

I would like to thank Thierry Buffeteau for the all of the PM-IRRAS measurements performed at ISM, especially for spending his time to teach me with about the technique and discuss the results. I was very lucky to be able to extract many conclusions from these measurements thanks to your expertise, and it will be a pleasure to collaborate again with you in the future for new projects if that happens.

I particularly thank my CST committee, Luc Veluttini and Guillaume Fleury, for the valuable discussion we had at the middle of the PhD which brought me new ideas for the project.

I would like to thank all of the friends I have made in CRPP and in Bordeaux, who turned my journey much more light and fun, and my loyal Brazilian ones that have never left my side, although not physically present. Special thanks to my closest ones: Yuliana, Nathan, Arantza, Lachlan, Alejandra, Sharvina, Rawan, Henri, Hongwei, Nahyun, Nathassia, Rafael, Manu, Rajam, Simone, Romain and Andrew.

Last but not least, I would like to express my deepest gratitude to my parents, Antonio and Heloísa, and my brother, Eduardo, for always being my source of inspiration and support and the greatest examples in life. I extend my gratitude to all of my family that, although not physically present, always supports me, and to Thibault 🐾, my beloved and loyal company in Bordeaux since 2019.

# Table of contents

<b>List of Abbreviations</b>	<b>xiii</b>
<b>General introduction</b>	<b>xv</b>
<b>References</b>	<b>xvii</b>
<b>Chapter 0. State-of-the-art</b>	<b>19</b>
<b>1. Functional organic thin films</b> .....	<b>22</b>
1.1. Molecular layers – Langmuir films and Self-Assembled Monolayers (SAMs) .....	22
1.1.1. Langmuir monolayers films .....	23
1.1.2. Self-assembled monolayers (SAMs) .....	24
1.2. Macromolecular layers – Polymer deposition, grafting and Layer-by-Layer techniques...	30
1.2.1. Polymer deposition techniques.....	30
1.2.2. Grafting techniques – Polymer brushes .....	32
1.2.3. Layer-by-Layer (LbL) technique .....	34
<b>2. Block copolymers (BCs)</b> .....	<b>39</b>
2.1. BC self-assembly in bulk .....	39
2.2. BC self-assembly in solution .....	40
<b>3. Solid-supported BC membranes</b> .....	<b>43</b>
3.1. Grafting methodologies.....	44
3.2. Langmuir-Blodgett (LB) method .....	47
3.3. Vesicle Fusion (VF) method .....	49
3.4. Solvent-assisted Lipid Bilayer (SALB) method .....	50
3.4.1. Solvent-assisted method using BC .....	53
<b>Motivation of this thesis work</b> .....	<b>55</b>
<b>References</b> .....	<b>57</b>
<b>Chapter 1. Monolayer formation</b>	<b>63</b>
<b>Experimental</b> .....	<b>66</b>
<b>Materials</b> .....	<b>66</b>
<b>Methodology</b> .....	<b>66</b>
1.1. Pre-functionalization of silicon wafers and characterization .....	66

Aminosilylation with APTES.....	66
Determination of the absolute surface density of amino groups of APTES films .....	67
Physiosorption on PAH .....	67
1.2. Characterization of the APTES or PAH-modified substrates .....	67
Surface topography .....	67
Thickness .....	68
Contact angle titration .....	68
1.3. BC monolayer formation .....	68
BCs solutions in different solvents .....	68
Dynamic Light Scattering (DLS).....	68
Small-Angle Neutron Scattering (SANS) .....	69
Adsorption of the BC monolayer.....	69
1.4. Characterization of the BC monolayer .....	69
Surface topography & thickness.....	69
Contact angle measurements .....	69
Adsorption of the BC monolayer.....	70
Polarization Modulation Infrared Reflection Absorption Spectroscopy (PM-IRRAS).....	70
Neutron Reflectivity (NR) .....	72
<b>Results and discussion .....</b>	<b>73</b>
<b>1.1. Pre-functionalization of the silicon wafer surface .....</b>	<b>73</b>
<b>1.2. Monolayer formation.....</b>	<b>78</b>
1.2.1 Choice of the non-selective solvent .....	78
1.2.2. Evidence of the interaction of PS- <i>b</i> -PAA copolymers with the aminated surface.....	80
1.2.3. Characterization of the adsorbed PS- <i>b</i> -PAA monolayer .....	82
1.2.4. Conformation of the BC chains in the adsorbed BC monolayer.....	85
<b>Conclusions.....</b>	<b>92</b>
<b>References.....</b>	<b>93</b>

## **Chapter 2. Bilayer formation** 95

<b>Experimental .....</b>	<b>98</b>
<b>Materials .....</b>	<b>98</b>
<b>Methodology .....</b>	<b>98</b>
1.1. Characterization of the BC behaviour in solution .....	98
Dynamic Light Scattering (DLS).....	98

Transmission Electronic Microscopy (TEM) .....	98
1.2. Self-assembly of the BC bilayer at the silicon wafer surface.....	99
1.3. Characterization of the BC bilayer at the silicon wafer surface .....	100
Thickness .....	100
Surface topography .....	100
Contact angle measurements .....	101
Latex nanoparticles adsorption .....	101
Polarization Modulation Infrared Reflection Absorption Spectroscopy (PM-IRRAS).....	101
Neutron Reflectivity (NR) .....	101
<b>Results and discussion .....</b>	<b>103</b>
<b>1. General process of bilayer formation .....</b>	<b>103</b>
1.1. Setting-up the surface self-assembly conditions.....	103
1.2. Bilayer characterization.....	110
1.3. Advanced bilayer characterization with NR .....	114
1.3.1. Bilayer thickness.....	114
1.3.2. Variation of the monomer volume fraction .....	118
<b>2. Optimization of the BC self-assembly process.....</b>	<b>122</b>
<b>Conclusions.....</b>	<b>125</b>
<b>References.....</b>	<b>126</b>

## **Chapter 3. Densification of the monolayer** 129

<b>Experimental .....</b>	<b>133</b>
<b>Materials .....</b>	<b>133</b>
<b>Methodology .....</b>	<b>133</b>
1.1. PS- <i>b</i> -PAA bilayer rinsing process in a non-selective solvent .....	133
Thickness .....	133
Surface topography .....	133
Adsorption of PAA <sub>69</sub> on substrates functionalized with a PS <sub>394</sub> - <i>b</i> -PAA <sub>58</sub> monolayer .....	134
Contact angle measurements .....	134
Polarization Modulation Infrared Reflection Absorption Spectroscopy (PM-IRRAS).....	135
<b>Results and discussion .....</b>	<b>136</b>
<b>1.1. Evidences of the densification of the monolayer .....</b>	<b>136</b>
<b>1.2. Quantifying the BC mass on the densified monolayer .....</b>	<b>143</b>
<b>1.3. Investigating the possible interactions generating the densification.....</b>	<b>145</b>

<b>1.3. Densification of the monolayer in other BC bilayer systems.....</b>	<b>148</b>
<b>Conclusions.....</b>	<b>150</b>
<b>References.....</b>	<b>150</b>
<b>Chapter 4. Generalizations, openings and perspectives</b>	<b>151</b>
<b>1. Generation of asymmetric BC bilayers .....</b>	<b>155</b>
<b>2. Encapsulation of AuNP in the hydrophobic reservoir.....</b>	<b>159</b>
<b>3. Generation of PS-<i>b</i>-PAA bilayers onto colloids.....</b>	<b>166</b>
<b>4. Solid-supported BC bilayers containing a rubbery hydrophobic block.....</b>	<b>170</b>
<b>5. Solid-supported BC bilayers as models for the study of thin film properties .....</b>	<b>171</b>
<b>6. Methodologies .....</b>	<b>174</b>
<b>6.1. Generation of asymmetric BC bilayers .....</b>	<b>174</b>
<b>6.2. Encapsulation of AuNPs .....</b>	<b>175</b>
6.2.1. Synthesis and characterization of PS-capped AuNP.....	175
Materials.....	175
Experimental .....	175
Characterization .....	175
6.2.2. Self-assembly of PS- <i>b</i> -PAA bilayers in the presence of PS-capped AuNPs.....	176
<b>6.3. Generation of PS-<i>b</i>-PAA bilayer onto colloids.....</b>	<b>177</b>
6.3.1. PS- <i>b</i> -PAA monolayer formation .....	177
6.3.2. PS- <i>b</i> -PAA bilayer formation.....	177
<b>6.4. Solid-supported BC bilayers containing a rubbery hydrophobic block .....</b>	<b>178</b>
6.4.1. Synthesis of PBA- <i>b</i> -PAA .....	178
Materials.....	178
RAFT polymerization of PtBA .....	178
RAFT polymerization of PBA- <i>b</i> -PtBA .....	178
Acidolysis of PBA- <i>b</i> -PtBA .....	179
<b>Conclusions.....</b>	<b>179</b>
<b>References.....</b>	<b>180</b>
<b>General conclusions</b>	<b>183</b>
<b>Appendix</b>	<b>187</b>

# List of Abbreviations

AFM	Atomic force microscopy
APTES	(3-aminopropyl)triethoxysilane
BC(s)	Block copolymer(s)
BL	Bilayer
Cwc	Critical water content
DLS	Dynamic light scattering
DMF	N, N-dimethylformamide
DP	Degree of polymerization
LB	Langmuir-Blodgett (transfer)
LbL	Layer-by-Layer
LS	Langmuir-Schaeffer (transfer)
MJ	Marques-Joanny
ML	Monolayer
Mw	Weight average molecular weight
NR	Neutron reflectivity
PAA	Poly(acrylic acid)
PAH	Poly(allylamine hydrochloride)
PM-IRRAS	Polarization modulation infrared reflection absorption spectroscopy
PS	Polystyrene
QCM-d	Quartz crystal microbalance with dissipation
$R_g$	Radius of gyration
$R_h$	Hydrodynamic radius
RMS	Root mean square
SALB	Solvent-assisted lipid bilayer
SAM	Self-assembled monolayer
SANS	Small-angle neutron scattering
TEM	Transmission electron microscopy
$T_g$	Glass transition
THF	Tetrahydrofuran
VF	Vesicle fusion



# General introduction

Block copolymers (BCs) are widely used in materials science due to their capacity to self-assemble, in bulk, thin film or solution into a variety of nanoscale ordered structures with different morphologies.<sup>1-4</sup> In particular the ease of amphiphilic BCs to form bilayer membranes in solution has attracted much interest over the past 20 years as shown by the vast literature on polymer vesicles (polymersomes).<sup>5,6</sup> More recently, solid-supported BC bilayers have also been put forward.<sup>7-9</sup> Although they share similar morphologies with the popular lipid-supported membranes used commonly as models for biomimetic interfaces, it is well-established from liposomes and polymersomes studies that BCs form much more stable membranes than conventional lipids owing to a partial interpenetration of individual membrane layers that minimize any delamination.<sup>10,11</sup> Furthermore, the larger hydrophobic reservoir offered by BC bilayers is a key advantage for encapsulating actives (molecules, or nanoparticles) over the generally smaller reservoirs of lipid membranes.

Applications of solid-supported BC bilayers are currently poorly investigated owing to the difficulty to generate them in good conditions at a large scale and/or on non-planar substrates with current methods. Notably, the Langmuir-Blodgett (LB) and the Langmuir-Schaefer (LS) deposition techniques are powerful lab scale methods to build high resolution BC bilayers with negligible defects.<sup>12,13</sup> Unfortunately, the LB/LS approaches cannot be satisfactorily implemented at large scale or on colloidal and hollow structures. In addition, the vesicle fusion (VF) which is the standard method for liposomes to produce continuous lipid bilayers suffers from certain limitations when applied to polymersomes. Notably, the mechanical robustness of polymer vesicles prevents their rupture and fusion in the absence of strong attractive interaction with the surface.<sup>14-16</sup> The more recently solvent-assisted lipid bilayer (SALB) pathway is an alternative to the VF method in which a lipid solution prepared in a water-miscible organic solvent is deposited on a solid substrate, followed by gradual exchange with water to generate lamellar-phase structures, leading to the formation of supported lipid bilayers.<sup>17-20</sup> However, in the absence of specific interaction with the substrate, this method can hardly be applied to BCs to form homogeneous bilayers anchored to the surface. Additionally, VF and SALB methods are limited to block copolymers with

geometric properties that are consistent with the formation of vesicles ( $\frac{1}{2} < \rho < 1$ ) or lamellar structures ( $\rho \sim 1$ ) with  $\rho$  the packing parameter.<sup>21</sup>

Towards a universal fabrication of solid-supported BC bilayers, in this thesis we report a simple and robust bottom-up approach able to generate symmetrical and asymmetrical bilayers on solid substrates of any size and shape without any particular limitation on  $\rho$ . For this purpose, amphiphilic diblock copolymers with a hydrophilic adsorbing block and a hydrophobic non-adsorbing block are used. The proposed two-step method, reminiscent of the layer-by-layer approach used with polyelectrolytes<sup>22</sup> is based on **i)** the formation of a first BC layer through non-covalent interactions between the substrate and the hydrophilic blocks in a non-selective solvent like DMF or THF and **ii)** the triggered assembly of the second layer through hydrophobic interactions between free and grafted hydrophobic blocks by adding a critical water fraction to the medium (**Figure 1**).

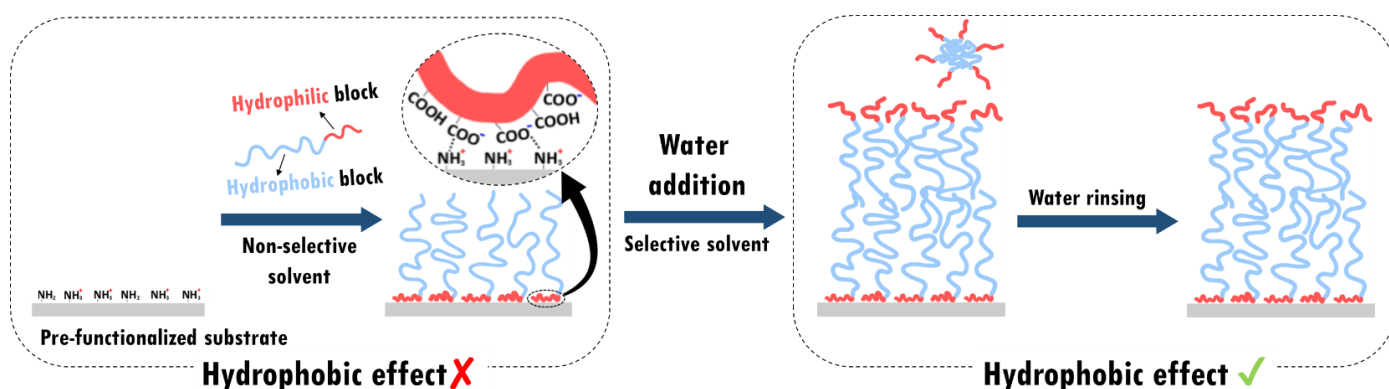


**Figure 1.** General scheme of the surface self-assembly of amphiphilic BCs into solid-supported bilayers.

A final rinsing step then to remove the excess BC micelles, vesicles and any aggregates generated in the aqueous solutions during the second step. Basically, the overall process mimics at the solid-liquid interface the hydrophobically-driven self-assembly mechanism of amphiphilic BCs in solution.

Although the proof-of-concept has been previously reported with BC forming bilayer around polyelectrolyte complex particles,<sup>23</sup> we aim here to deepen our understanding of each step self-assembly and standardize the overall process by performing an extensive study on model planar substrates. BCs containing glassy and hydrophobic polystyrene blocks (polystyrene-*block*-poly(acrylic acid), PS-*b*-PAA) have been selected as model system because of their reputation for being difficult to assemble by conventional approaches like vesicle

spreading. Both steps of the fabrication method were deeply studied and symmetric BC bilayers were successfully obtained and characterized. In an effort to generalize and take advantage of this new process, the generation of asymmetric BC bilayers, the extension to colloidal substrates as well as the encapsulation of gold nanoparticles within the hydrophobic reservoir of the bilayers were proposed in the end.

Solid-supported lipid bilayers have been mainly used to study membrane-related processes *in vitro*. BC bilayers can offer additional features as robust organic thin films with on-demand surface functionality, attractive active encapsulating capability and compatibility with different physicochemical environments as well as model systems to study the peculiar properties of polymer thin films. In this regard, the ‘surface-induced’ self-assembly of BCs as described in this thesis enriches the panel of directed self-assembly approaches used to design organized and functional ultrathin films.

In this thesis work, a detailed study on the different steps of the proposed fabrication method, namely the BC mono- and bilayer formation, was carried out, described in **Chapters 1 and 2**, respectively. An expected stage in the fabrication process was also identified, referred to as the densification of the monolayer, described in **Chapter 3**. Finally, a summary of generalizations, openings and perspectives of the proposed fabrication method are discussed in **Chapter 4**.

## References

- (1) Feng, H.; Lu, X.; Wang, W.; Kang, N. G.; Mays, J. W. Block Copolymers: Synthesis, Self-Assembly, and Applications. *Polymers (Basel)*. **2017**, *9* (10). <https://doi.org/10.3390/polym9100494>.
- (2) Bates, C. M.; Bates, F. S. 50th Anniversary Perspective: Block Polymers-Pure Potential. *Macromolecules* **2017**, *50* (1), 3–22. <https://doi.org/10.1021/acs.macromol.6b02355>.
- (3) Hu, H.; Gopinadhan, M.; Osuji, C. O. Directed Self-Assembly of Block Copolymers: A Tutorial Review of Strategies for Enabling Nanotechnology with Soft Matter. *Soft Matter* **2014**, *10* (22), 3867–3889. <https://doi.org/10.1039/c3sm52607k>.
- (4) Deng, Z.; Liu, S. Emerging Trends in Solution Self-Assembly of Block Copolymers. *Polymer (Guildf)*. **2020**, *207* (August), 122914. <https://doi.org/10.1016/j.polymer.2020.122914>.
- (5) Discher, B. M.; Won, Y. Y.; Ege, D. S.; Lee, J. C. M.; Bates, F. S.; Discher, D. E.; Hammer, D. A. Polymersomes: Tough Vesicles Made from Diblock Copolymers. *Science (80-. )*. **1999**, *284* (5417), 1143–1146. <https://doi.org/10.1126/science.284.5417.1143>.
- (6) Rikken, R. S. M.; Engelkamp, H.; Nolte, R. J. M.; Maan, J. C.; Van Hest, J. C. M.; Wilson, D. A.; Christianen, P. C. M. Shaping Polymersomes into Predictable Morphologies via Out-of-Equilibrium Self-Assembly. *Nat. Commun.* **2016**, *7*, 1–7. <https://doi.org/10.1038/ncomms12606>.
- (7) Goertz, M. P.; Marks, L. E.; Montañó, G. A. Biomimetic Monolayer and Bilayer Membranes Made from Amphiphilic Block Copolymer Micelles. *ACS Nano* **2012**, *6* (2), 1532–1540. <https://doi.org/10.1021/nn204491q>.

- (8) Kowal, J.; Zhang, X.; Dinu, I. A.; Palivan, C. G.; Meier, W. Planar Biomimetic Membranes Based on Amphiphilic Block Copolymers. *ACS Macro Lett.* **2014**, *3* (1), 59–63. <https://doi.org/10.1021/mz400590c>.
- (9) Chimisso, V.; Maffei, V.; Hürlimann, D.; Palivan, C. G.; Meier, W. Self-Assembled Polymeric Membranes and Nanoassemblies on Surfaces : Preparation , Characterization , and Current Applications. *Macromol. Biosci.* **2019**, *1900257*. <https://doi.org/10.1002/mabi.201900257>.
- (10) Bermudez, H.; Brannan, A. K.; Hammer, D. A.; Bates, F. S.; Discher, D. E. Molecular Weight Dependence of Polymersome Membrane Structure, Elasticity, and Stability. *Macromolecules* **2002**, *35* (21), 8203–8208. <https://doi.org/10.1021/ma020669l>.
- (11) Le Meins, J. F.; Sandre, O.; Lecommandoux, S. Recent Trends in the Tuning of Polymersomes' Membrane Properties. *Eur. Phys. J. E* **2011**, *34* (2). <https://doi.org/10.1140/epje/i2011-11014-y>.
- (12) Belegriou, S.; Dorn, J.; Kreiter, M.; Kita-Tokarczyk, K.; Sinner, E. K.; Meier, W. Biomimetic Supported Membranes from Amphiphilic Block Copolymers. *Soft Matter* **2009**, *6* (1), 179–186. <https://doi.org/10.1039/b917318h>.
- (13) Zhang, X.; Fu, W.; Palivan, C. G.; Meier, W. Natural Channel Protein Inserts and Functions in a Completely Artificial, Solid-Supported Bilayer Membrane. *Sci. Rep.* **2013**, *3*, 1–7. <https://doi.org/10.1038/srep02196>.
- (14) Rakhmatullina, E.; Manton, A.; Bürgi, T.; Malinova, V.; Meier, W. Solid-Supported Amphiphilic Triblock Copolymer Membranes Grafted from Gold Surface. *J. Polym. Sci. Part A Polym. Chem.* **2009**, *47* (1), 1–13. <https://doi.org/10.1002/pola.23116>.
- (15) Dorn, J.; Belegriou, S.; Kreiter, M.; Sinner, E. K.; Meier, W. Planar Block Copolymer Membranes by Vesicle Spreading. *Macromol. Biosci.* **2011**, *11* (4), 514–525. <https://doi.org/10.1002/mabi.201000396>.
- (16) Yang, Y. L.; Tsao, H. K.; Sheng, Y. J. Solid-Supported Polymer Bilayers Formed by Coil-Coil Block Copolymers. *Soft Matter* **2016**, *12* (30), 6442–6450. <https://doi.org/10.1039/c6sm00741d>.
- (17) Hohner, A. O.; David, M. P. C.; Rädler, J. O. Controlled Solvent-Exchange Deposition of Phospholipid Membranes onto Solid Surfaces. *Biointerphases* **2010**, *5* (1), 1–8. <https://doi.org/10.1116/1.3319326>.
- (18) Tabaei, S. R.; Jackman, J. A.; Kim, M.; Yorulmaz, S.; Vafaei, S.; Cho, N. J. Biomembrane Fabrication by the Solvent-Assisted Lipid Bilayer (SALB) Method. *J. Vis. Exp.* **2015**, *2015* (106), 1–12. <https://doi.org/10.3791/53073>.
- (19) Ferhan, A. R.; Yoon, B. K.; Park, S.; Sut, T. N.; Chin, H.; Park, J. H.; Jackman, J. A.; Cho, N. J. Solvent-Assisted Preparation of Supported Lipid Bilayers. *Nat. Protoc.* **2019**, *14* (7), 2091–2118. <https://doi.org/10.1038/s41596-019-0174-2>.
- (20) Jackman, J. A.; Cho, N. J. Supported Lipid Bilayer Formation: Beyond Vesicle Fusion. *Langmuir* **2020**, *36* (6), 1387–1400. <https://doi.org/10.1021/acs.langmuir.9b03706>.
- (21) Mai, Y.; Eisenberg, A. Self-Assembly of Block Copolymers. *Chem. Soc. Rev.* **2012**, *41* (18), 5969–5985. <https://doi.org/10.1039/c2cs35115c>.
- (22) Decher, G. Fuzzy Nanoassemblies: Toward Layered Polymeric Multicomposites. *Science (80-. )*. **1997**, *277* (5330), 1232–1237. <https://doi.org/10.1126/science.277.5330.1232>.
- (23) Bui, L.; Abbou, S.; Ibarboure, E.; Guidolin, N.; Staedel, C.; Toulmé, J. J.; Lecommandoux, S.; Schatz, C. Encapsulation of RNA-Polyelectrolyte Complexes with Amphiphilic Block Copolymers: Toward a New Self-Assembly Route. *J. Am. Chem. Soc.* **2012**, *134* (49), 20189–20196. <https://doi.org/10.1021/ja310397j>.

# 0

## **State-of-the-art**



As introduced by Pierre-Gilles de Gennes, “Soft Matter” describes a vast research field of materials including colloids, polymers and surfactants.<sup>1</sup> In a very illustrative way, Gompper describes a “Soft matter triangle”, which illustrates the continuum of molecular structures existing between these three main chemical entities (**Figure 2**).<sup>2</sup>

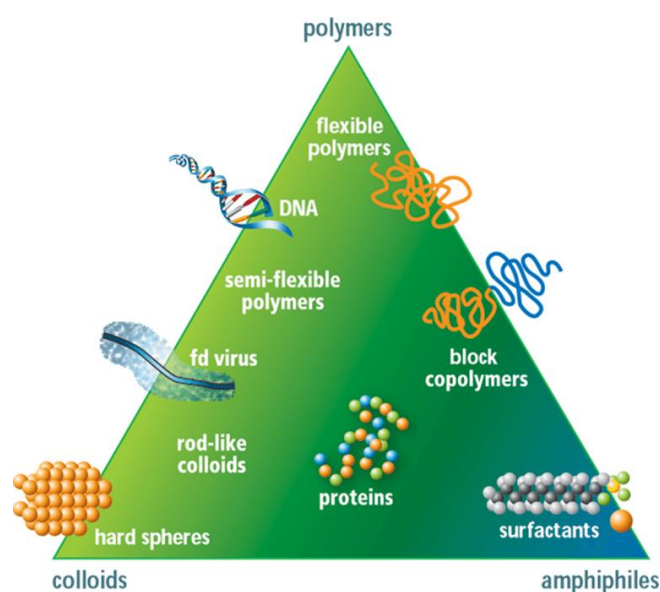


**Figure 2.** Soft matter triangle. The image is reproduced from ref. 2.

In contrast to hard solids, in soft matter the size of the structural units is significantly larger (on mesoscopic length scale) and the interaction/binding energy, in turn, considerably weaker (typically  $k_B T$ , where  $k_B$  is the Boltzmann constant and  $T$  represents temperature). As a result, soft matter can be easily perturbed by moderate external stimuli (electrical, mechanical...) as well as thermal fluctuations.<sup>3</sup> Indeed, the well-known self-assembly process in soft matter, responsible for the generation of numerous structures in Nature, is defined as the spontaneous organization of individual blocks into ordered structures through intermolecular interactions of energy close to  $k_B T$ .<sup>4,5</sup> Another definition, more philosophical, introduces the self-assembly concept as the action of independent entities leading to the formation of organized structures in the absence of any apparent control. Two types of self-assembly have been identified: i) the static self-assembly involving systems at equilibrium that do not dissipate energy (in this work we are mostly concerned by this type of systems); and ii) the dynamic self-assembly where the formation of organized structures occurs when the system dissipates energy, like the famous patterns found in oscillating chemical reactions.<sup>6</sup>

The phenomenon of self-organization is present in many different fields and is driven by the minimization of the free energy of a molecular system by its arrangement into energetically favourable configurations.<sup>7</sup> In chemistry, the classical example is the spontaneous formation of well-defined structures such as micelles and liquid crystals by the self-assembly through non-covalent forces; and in biology, complex structures are known to be formed under specific environmental conditions exclusively based on the molecular properties of their building blocks, such as the formation of lipid membranes and folded proteins.<sup>8</sup>

## 1. Functional organic thin films

Organic thin films have a ubiquitous presence in numerous processes on our everyday life, including on our own bodies. From cell membranes to surface coatings and drug carriers, this class of materials have attracted much attention on the basis of their softness, flexibility, processability and ease of functionalization.<sup>9</sup> On the right edge of the soft matter triangle shown in **Figure 2** one can find a continuum of building blocks that are used for the fabrication of such thin films, ranging from small amphiphilic molecules (surfactants) to macromolecular structures including polymers, neutral or charged ones, as the case of polyelectrolytes, and block copolymers. In this chapter, an overview on the most common methods for the generation of organic thin films will be made, concerning the use of molecules or macromolecules as building blocks.

### 1.1. Molecular layers – Langmuir films and Self-Assembled Monolayers (SAMs)

In this subsection, organic thin films made up of a single layer of molecules will be presented, specifically the formation of Langmuir films at liquid-liquid or gas-liquid interfaces and the fabrication of SAMs, by the covalently attachment of thiol or silane-based molecules, onto solid substrates.

### 1.1.1. Langmuir monolayers films

Langmuir monolayers, named after Irvin Langmuir for his major theoretical and experimental contributions in surface science, are insoluble films generated at a gas-liquid or liquid-liquid interface by the spreading of a diluted solution of amphiphilic molecules (surfactants) (**Figure 3**).<sup>10</sup>

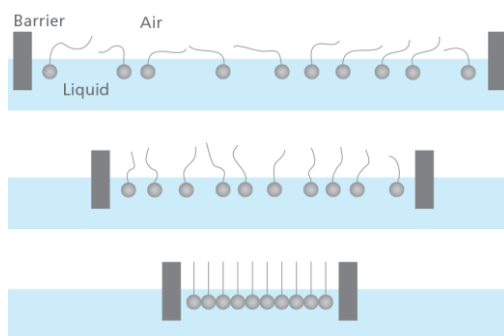


**Figure 3.** Schematic illustration of a Langmuir monolayer in different compression states. The image is reproduced from ref. 11.

Interestingly to note, the first attempts to scientifically describe the behaviour of oil films in water date back to the 18<sup>th</sup> century. Indeed, the first pressure isotherm was published by Pockels in the 19<sup>th</sup> century, whom was able to measure the surface tension of water with a simple apparatus, devised by herself, which later became the famous and widely known Langmuir-Blodgett trough (**Figure 4**).<sup>10,12</sup>

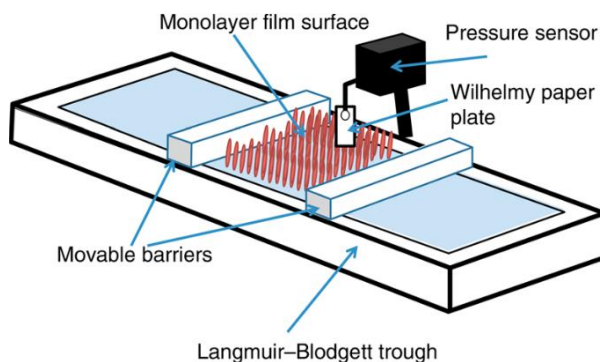


**Figure 4.** Schematic illustration of a Langmuir-Blodgett trough. The image is reproduced from ref. 13.

Typically, pressure-area isotherms which describes the monolayer properties of a material can be obtained using a Langmuir-Blodgett trough. The variation of surface pressure

per area is measured as movable Teflon barriers compress the monolayers while a surface balance (*e.g.* Wilhelmy paper plate) detects the surface pressure variation. The resulting surface pressure *versus* area occupied per molecule plot provides information about the phase and phase transitions of the monolayer, as exemplified in (**Figure 5**).

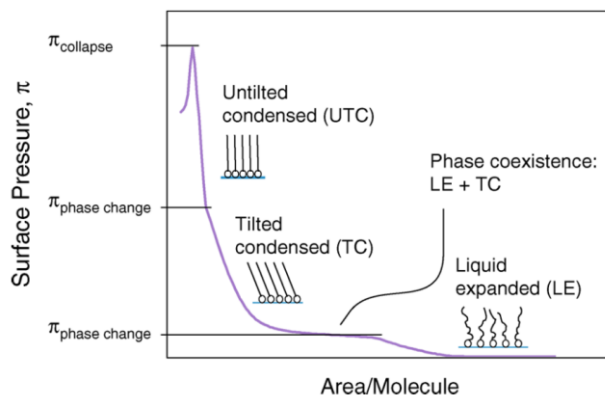


**Figure 5.** An example of a pressure-area isotherm. The image is reproduced from ref. 13.

Several other techniques are used to characterize the monolayers at liquid/air interfaces such as Brewster-Angle Microscopy (BAM), Fourier Transform Infrared (FTIR) Spectroscopy, X-ray Reflectometry and Grazing-Incidence X-ray Diffractometry, for example.<sup>9</sup> Overall, Langmuir monolayers are unique physical models for the study of the molecular arrangement at interfaces, and, very importantly, they can also be transferred to solid-supports by the so-called Langmuir-Blodgett (LB) deposition technique, which will be discussed later for the generation of highly ordered monolayers of amphiphilic molecules on solid-supports.

### 1.1.2. Self-assembled monolayers (SAMs)

The self-assembled monolayers (SAMs) describe a class of solid-supported organic thin films (1-3 nm) in which amphiphilic molecules containing a chemical functionality are covalently bound to the substrate.<sup>14</sup> As the name says, a self-assembled monolayer is formed as the adsorbed molecules, either from gas phase or solution, organize themselves spontaneously for the generation of crystalline (or semi-crystalline) structures.<sup>15,16</sup> A confusion might arise from the fact that the Langmuir monolayers, previously described are, in a way, self-assembled monolayers at a liquid interface. Additionally, the Langmuir-Blodgett

technique, described further on, involves the transfer of Langmuir monolayers at a liquid interface to a solid surface, which also results in a self-assembled monolayer structure. The main difference, however, is that SAMs concern specifically the self-assembled monolayers interacting covalently with the substrate. That is not the case for the Langmuir films, which sit at a liquid interface, nor the LB films onto solid supports, as they are bound together via weak interactions.

In general, the amphiphilic molecules forming the SAMs consist of three parts: a "head group" with a chemical function that allows strong interaction with a given substrate (e.g., thiol-functional molecules for gold or noble metal substrates, or silane-functional molecules for oxide surfaces), a backbone (the alkyl chain, which participates in the inter-chain van der Waals interactions that primarily control self-assembly), and a terminal, non-surface-bound group that imparts functionality to the SAMs (**Figure 6**).<sup>15–18</sup> In order to increase the stability and the mechanical properties of the SAMs, functional groups can also be added to the alkyl chain to allow an alternative way to control the molecular self-assembly of the chains, such as aromatic or amides, for instance, which can interact laterally by  $\pi$ -stacking or hydrogen bonding, respectively.<sup>19</sup>

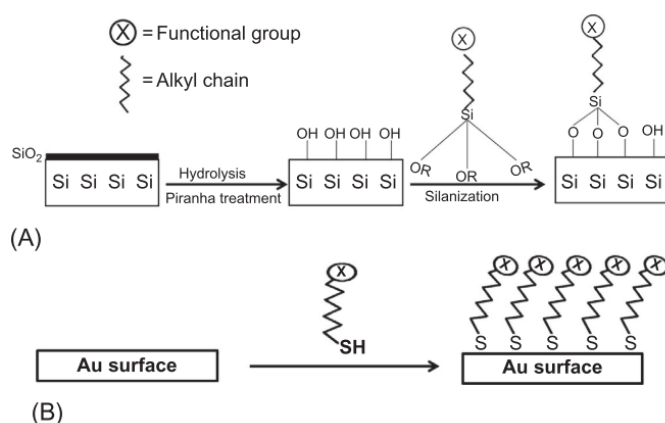


**Figure 6.** Schematic illustration on the SAMs formation onto (A) silicon oxide and (B) gold surfaces. The image is reproduced from ref. 18.

The preparation of SAMs is based on the molecule adsorption either from liquid or vapour phase. In the case of gold substrates, in solution, the process consists of cleaning the substrates and then dipping into a solution containing organo-sulphur compounds, commonly thiol-based ones (HS-R-X), but also disulfides and dialkylsulfides. The resulting thiol-based SAMs can be used for different purposes including as (bio)sensors, in order to monitor pH,

inorganic and/or organic compounds using both chemical and biological recognition elements.<sup>20</sup> As shown in **Figure 7**, thiols can be used in electroanalytical devices by different approaches, including the use of functionalized thiols (**a**), the functionalization of thiols prior to its adsorption (**b**); and the attachment of thiols followed by functionalization (**c**).

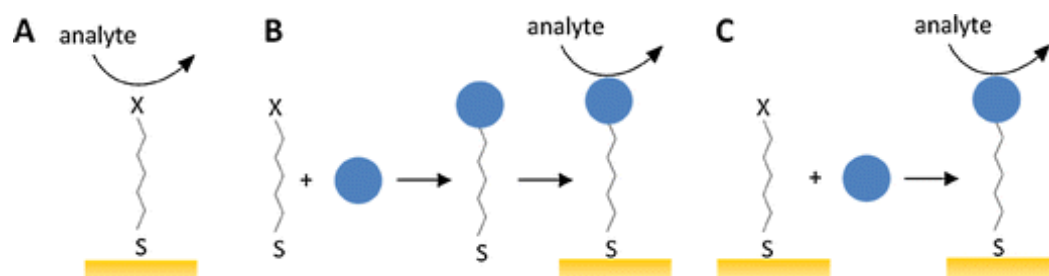


**Figure 7.** Schematic illustration of the different approaches for assembling thiol-based SAMs. The image is adapted and reproduced from ref. 20.

For silicon oxide surfaces, the overall process for SAMs preparation involves the use of silane-based compounds (which, in turn, require the use of hydroxylated surfaces) and can be a bit more challenging. First, a pre-treatment of the substrate needs to be done either with oxygen plasma or piranha solution to generate hydroxyl groups at the surface; then, by dipping the substrate in a solution containing the organo-silane compound, the formation of a SAM is achieved by the formation of siloxane (Si-O-Si) bonds between the hydroxylated surface and the silane-based molecules (**Figure 6**).<sup>18</sup>

Several parameters affect the formation of SAMs such the nature of the solvent, the concentration of the dipping solution, the immersion time and temperature. For organo-silanes, water is an important additional factor making challenging the preparation of SAMs since its absence or excess can influence the final monolayer, either by causing incomplete monolayer or by promoting polymerization of compounds in the bulk.<sup>21</sup> A classic example is the grafting of 3-aminopropyltriethoxysilane (APTES) onto silicon surfaces extensively reported in the literature.<sup>22–24</sup> Aminoalkoxysilanes are often used for the generation of SAMs because the terminal amine groups provide an active site for further attachment of actives. APTES has three ethoxy groups that can be hydrolysed, in the presence of catalytic amounts of water; the resulting structure then interacts with the hydroxylated substrate for the generation of a siloxane bond (**Figure 8**).

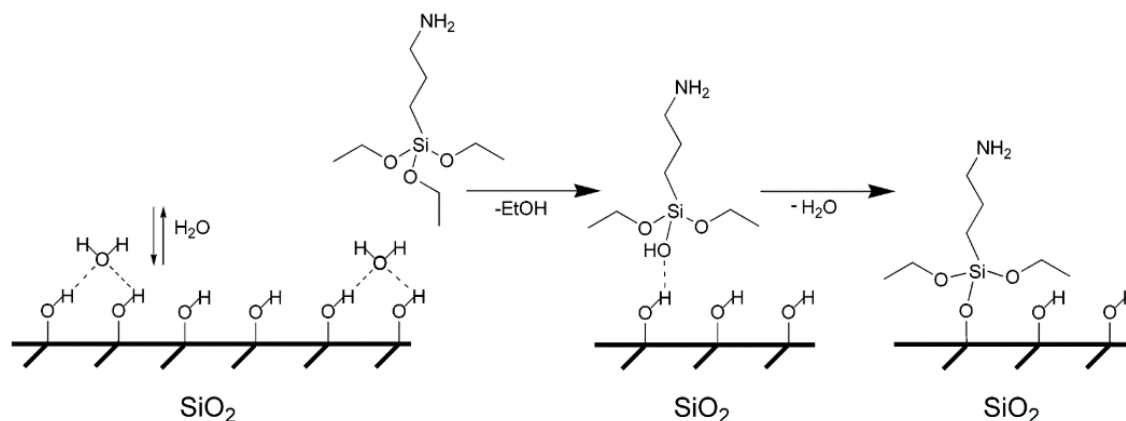


**Figure 8.** Scheme of the attachment of an APTES molecule to a hydroxylated silicon surface. The image is reproduced from ref. 22.

Ideally, the same process for the siloxane bond should occur for the two other ethoxy groups in the APTES molecule to have a total of three bonds per molecule, resulting in a configuration where the terminal amino group is pointing upwards perpendicular to the surface, available for further functionalization. However, there is a range of possible configurations of the APTES at the silicon substrate (**Figure 9**), with a single, double or triple siloxane bond formation with the substrate (a, b and c), the cross-linking of APTES molecules (d) or attachment of the molecule through the  $\text{NH}_2$  group to the surface (e).<sup>25</sup>

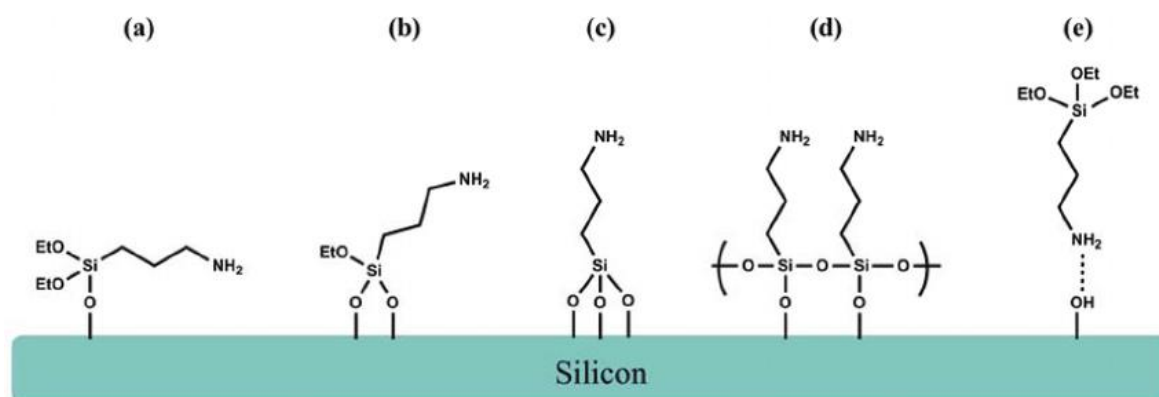


**Figure 9.** Different possible configurations for APTES attachment onto hydroxylated silicon surfaces. The image is reproduced from ref. 25.

Additionally, if water is present in large amounts, the polymerization of the APTES molecules can take place (due to its tri-valent silane) and lead to a thick (3D) and disordered APTES layer. As shown in **Figure 10**, one APTES molecule can be attached to the substrate via

a siloxane bond, whereas the two other silane moieties can react with adjacent APTES molecules. In addition, APTES can react with other APTES molecules for the formation of siloxane bonds (polymerization) and this long and non-controlled chains, in turn, can react with an attached APTES molecule with non-grafted silane moieties, generating a very thick multilayer.

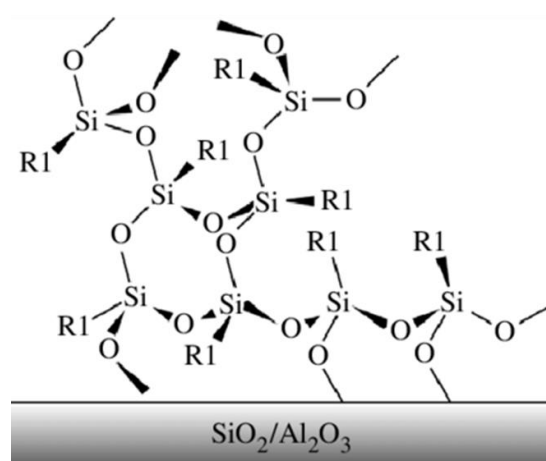


**Figure 10.** Schematic illustration of the multi-layered APTES. The image is reproduced from ref. 26.

Experimental conditions have been optimized to favour a monolayer formation without aggregates, such as the use of high temperatures, low concentration of APTES and short reaction times, even though multilayers can still be formed under the same conditions due to the complexity of the reaction mechanism.<sup>25,27,28</sup> Thus, although widely used for SAMs fabrication, the full mechanism concerning APTES remains unclear and other compounds have been used as alternatives. For instance,  $\gamma$ -aminopropylsilatrane (APS) is used to obtain a surface amino layer as an alternative to APTES, due to its intrinsic lower reactivity and better resistance to polymerization and hydrolysis.<sup>29,30</sup> Produced by the reaction of APTES with triethanolamine (TEA) (**Figure 11**), APS can be used to functionalize hydroxylated substrates through the strong covalent interaction of silicon residues of APS to exposed hydroxyl groups at the surface process of preparing SAMs using APS is also much easier than APTES and results in higher reproducibility, notably due to its insensitivity to water.<sup>31</sup>

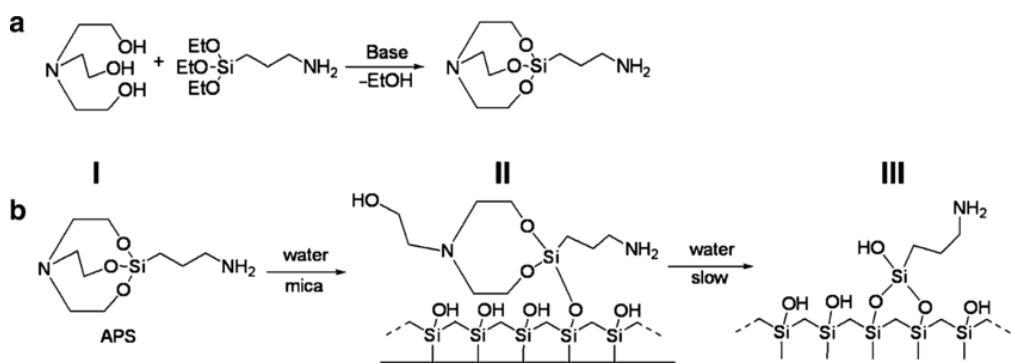


**Figure 11.** Scheme for the synthesis of APS (a) and for surface reaction of APS (I) with an hydroxylated surface for the generation of SAMs (b). The image is reproduced from ref. 29.

However, APS, like APTES, possess terminal amino groups which prevents long term-storage at room conditions. To overcome this issue, a recent publication suggests the N-protection of APS molecules using the well-known Boc protection group (tert-Butoxycarbonyl), which can be deprotected under acidic medium (**Figure 12**).<sup>30</sup>

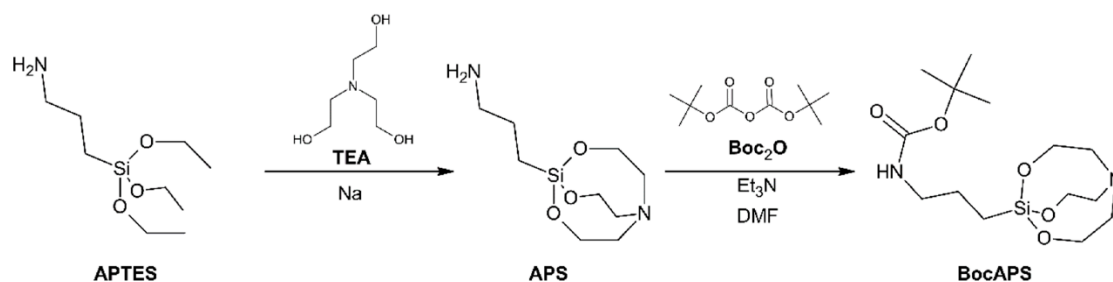


**Figure 12.** Synthesis of N-tert-butoxycarbonylaminopropylsilatrane (BocAPS). The image is reproduced from ref. 30.

The first step of the synthesis involves the generation of APS, which is reacted with Boc<sub>2</sub>O for the introduction of amine protective groups (Boc). Differently from APTES and even APS, BocAPS can be stored without special conditions (*i.e.* RT, without inert gas).<sup>30</sup>

Overall, SAMs represent not only an excellent approach for a wide range of applications in protective coatings, sensor and biosensors, but it is also a powerful tool for further surface modification.

## 1.2. Macromolecular layers – Polymer deposition, grafting and Layer-by-Layer techniques

In this subsection, thin films prepared onto solid substrates using macromolecular structures such as polymers, block copolymers and polyelectrolytes will be described. A specific focus will be given to the structures formed using amphiphilic BC because they are the focus of this thesis work. The aim of this section is to provide knowledge of the currently available fabrication techniques for the generation of organic thin films, either in the form of a mono-, bi- or multilayer.

### 1.2.1. Polymer deposition techniques

The formation of polymeric thin films onto substrates can be easily accessed by a range of simple and cost-effectiveness techniques such as dipping, spinning, spraying, doctor blade and bar coater, for instance. Such techniques allow the formation of films whose thickness vary from few nanometers up to a few microns.

As an example, the process of spin coating, illustrated in **Figure 13**, is comprised on four steps, named: (a) the deposition, where a polymeric solution prepared in a volatile solvent is placed at the centre of a flat substrate attached to a spinning stage (spin coater); (b) the spin-up, that is the even spread of the polymeric solution over the substrate due to centrifugal forces under rotation, which is followed by the (c) spin-off, in which the further rotation removes the excess of the polymer solution resulting in a partial thinning and homogenization of the film, followed by the final step (d) in which further rotation at a constant speed coupled with evaporation of the solvent allows the thinning and homogenization of the film thickness (indeed, the evaporation of the solvent happens in all of the steps).<sup>32</sup>

Many parameters, related to the properties of the solution or to the deposition process, directly affect the obtained polymer film, the most critical being the concentration and viscosity of the polymer solution as well as the angular speed of the centrifuge.

Additionally, different competing process such as phase separation or crystallization may also occur under strong shear forces and high evaporation rates.<sup>32</sup> Apart from its simplicity, low cost and effectiveness, the spin coating process is limited to small, rigid flat

surfaces and requires high material consumption, and therefore completely unsuitable for large-scale use.

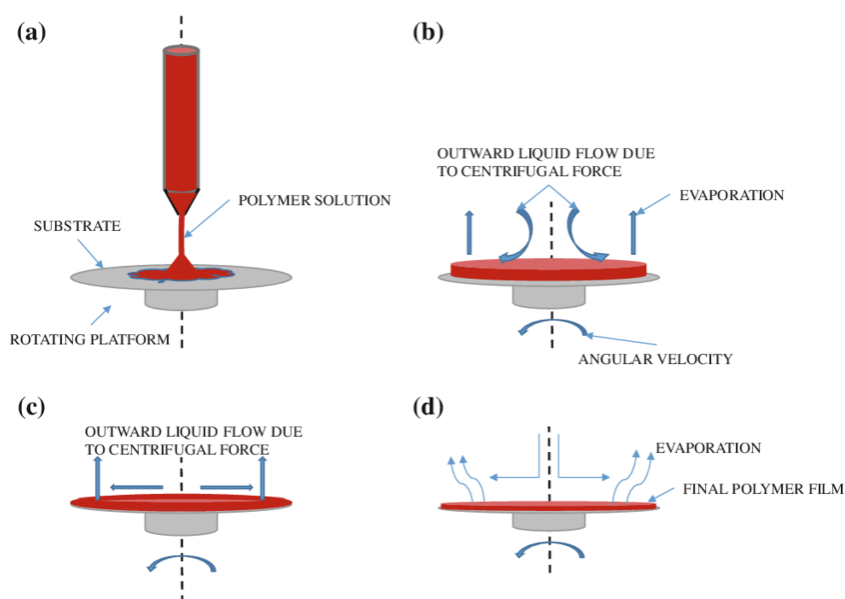


**Figure 13.** Schematic illustration on the spin-coating process. The image is reproduced from ref. 32.

An alternative method is spray-coating, applied at lab or industrial scale, that allows the formation of a thin film by the controlled spraying of a polymeric solution onto a surface. Providing a more uniform layer thickness than spin-coating, the technique is applied not only to planar surfaces but also on three-dimensional substrates or containing topographical features.<sup>33</sup> Meng and co-workers have recently prepared mixed hydrophilic/hydrophobic polymer layers by the deposition of polyvinyl alcohol (PVA) onto a polytetrafluoroethylene (PTFE) porous membrane using spray coating for desalination purposes (**Figure 14**).<sup>34</sup>

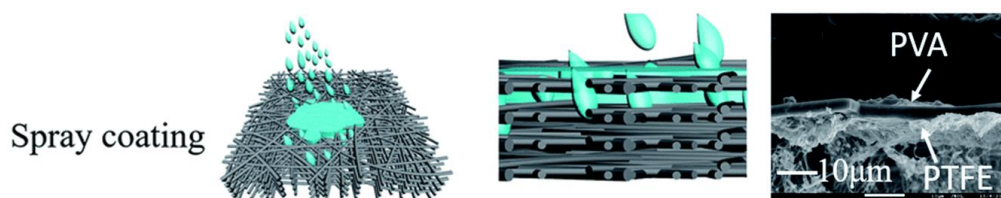


**Figure 14.** Schematic illustration of the spray coating method to produce the thin film polymer composites (left) and a SEM micrograph of the PVA/PTFE composite (right). The image is adapted and reproduced from ref. 34.

Usually, the technology of polymer membranes for desalination purposes comprises thin and dense layers (with hydrophobic polymers deposited in between) on porous supports.

Because the polymers used are hydrophobic, the membranes are prone to bio- and organic fouling and require frequent cleaning cycles for recovering their initial separation performances. Since the fouling can be reduced by the presence of hydrophilic polymers, one strategy would be to combine hydrophobic and hydrophilic polymers on such membranes. However, since there is a natural incompatibility between the hydrophobic and hydrophilic polymers, the preparation of such materials often result in delamination.

By spraying a PVA solution on the PTFE membranes using an air brush and a mini air compressor, Meng and co-workers were able to produce the composites from incompatible hydrophobic and hydrophilic polymers by forming a strong mechanical interlocking structure at the interface between the PTFE fibers and the PVA coating layer. Additionally, they were able to tune the thickness of the PVA layer by varying the number of sprays, from 1 to 5.2 mm. The resulting PVA/PTFE membranes apart from showing excellent separation performances (competitive to the best commercial membranes available) were more resistant to organic and inorganic fouling during long-term desalination due to the presence of the hydrophilic PAA.<sup>34</sup>

### 1.2.2. Grafting techniques – Polymer brushes

For nanometer-thick polymer coatings, grafting methodologies allow the generation of polymer brushes onto solid substrates. Polymer brushes present a wide range of applications particularly due to the ability to alter surface properties depending on the characteristics of the polymer, from tuning the wettability and surface activity to the development of antifouling medical devices or implant materials, for instance.<sup>17</sup>

These structures result from the tethering, either via covalent attachment or physical adsorption, of a polymeric assembly at one end to a solid substrate, while the free end is exposed to the surrounding medium.<sup>35,36</sup> Depending on the nature of the attachment, grafting methodologies can be divided into “grafting from” (“bottom-up”) and “grafting to” (“top down”) approaches, as illustrated in **Figure 15**.

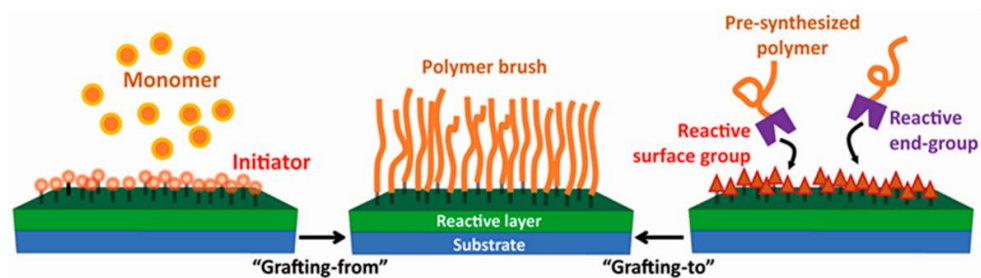


**Figure 15.** Schematic representation of the two grafting techniques. The image is reproduced from ref. 17.

The “grafting from” technique consists on the *in situ* growth a polymer brush by polymerization reactions to an initiator previously anchored to the substrate, namely “surface-initiated polymerization”. Even though various polymerization methods can be applied, controlled and living polymerizations such as reversible addition–fragmentation chain transfer (RAFT) and atom transfer radical polymerization (ATRP) are chosen over free radical or polycondensations ones for the generation of homogeneous chain lengths.<sup>17,37,38</sup> The main advantages of this method are the high grafting density (*i.e.* number of polymer chains per area), possible due to the easy diffusion of monomers through the growing chains, and the versatility to design polymer brushes with functional groups for further functionalization or molecule anchoring.<sup>37</sup> However, since the growth of the chains occurs directly on the substrate, the overall control over the polymerization reaction is challenging. Moreover, it remains difficult to directly characterize the polymer layer, in terms of grafting density and brush length.<sup>37,38</sup> The “grafting to” technique, on the other hand, consists on the attachment, either by non-covalent interactions or chemical interactions, of end-functionalized macromolecules in various architectures, from linear to hyper-branched and 3D network polymers.<sup>39,40</sup> Usually, a chemical modification of the surface is performed to introduce functional groups that will allow the attachment of the polymer of interest.

Conversely to the “grafting from” approach, a high control over the brush thickness is achieved with the “grafting to” method since the thickness of the brush can be controlled by the chain length of the polymer chains produced in advance. However, since the attachment of the new polymers at the substrate involves polymer diffusion, the “grafting to” technique usually leads to low grafting densities due to the high steric hindrance of the brushes that were already attached to the substrate.<sup>37</sup> Beside the numerous advantages of grafting methodologies for fabrication of polymer brushes, specific limitations have been recently reviewed.<sup>39</sup> As an example, the surface-initiated ATRP, widely used on the “grafting from”

method, requires the use of a metal catalyst and, thus, inert atmosphere conditions to prevent its oxidation, which represents a high cost when applied to large scale; additionally, the resulting polymer brushes always present residual catalyst, which limits the applicability.

Moreover, the biggest challenge remains to generate a universal grafting method that is easy to perform and with reduced waste of unreacted monomers.

### 1.2.3. Layer-by-Layer (LbL) technique

The Layer-by-Layer (LbL) approach, is another technique used for the generation of polymeric films from charged macromolecules (polyelectrolytes) or particles. Introduced by Decher and co-workers in the nineties, the LbL technique allows the fabrication of nano-structured films by sequential adsorption of oppositely charged organic or inorganic materials onto a solid substrate (**Figure 16**).<sup>41</sup>

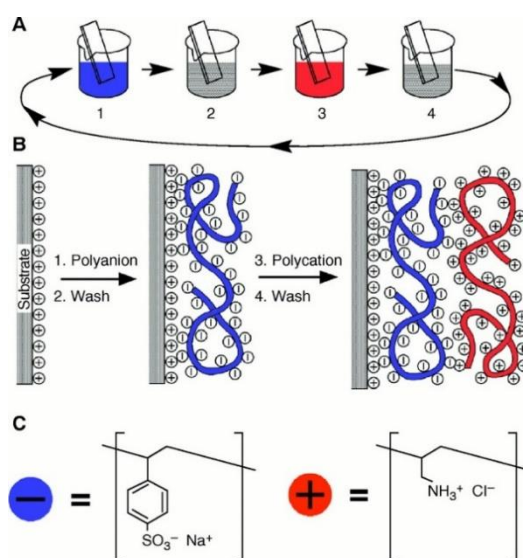


**Figure 16.** Schematic illustration on the Layer-by-Layer (LbL) fabrication method using planar substrates. The image is reproduced from ref. 42.

The LbL process for the generation of polyelectrolyte multilayers comprises the use of a charged substrate (in this case, planar) and solutions of oppositely charged polyelectrolytes, *i.e.* a polyanion and a polycation. If the substrate is positively charged, the immersion will first be performed in a polyanion solution; a monolayer of the polyelectrolyte is then formed by electrostatic attraction of the polyanion with the positively charged surface. The substrate

containing the first layer of polyelectrolyte, now negatively charged due to an excess of uncomplexed charges, is rinsed to remove weakly attached polyanion and dried. Following, a subsequent immersion of the substrate into a solution of polycation leads to the formation of a new layer by complexation of the polycations in solution with the polyanions previously anchored to the solid substrate. Because the surface charged is reversed at each step, the process can be performed as many times as desired after each immersion and rinsing steps. The resulting layers present a robust stability and are very unlikely to suffer re-dissolution, apart from specific conditions of high temperatures or salt concentrations. In contrast to the ideal representation of the multilayer shown in **Figure 16**, the organization of the film involves an interdiffusion of adjacent neighbouring chains, which can be evidenced using Neutron Reflectivity (NR) for example.

NR is a widely non-destructive technique used for the study of thin films on surfaces or interfaces, capable providing information perpendicular to the substrate (z-direction) on thickness, roughness, interdiffusion and chemical composition ranging from 5 to 5000 Å. The principle of NR is to measure the reflection coefficient (R) of a neutron beam sent in a grazing angle on a surface. The specular reflection provides the chemical composition profile perpendicular to the surface. Because of the specific characteristic of neutrons to interact with the nuclei of atoms, it is possible to differentiate the interactions with different isotopes, for example hydrogen and deuterium. This allows the design of contrast variation experiments, in which some molecules are labelled to create a neutron contrast.<sup>43</sup> A clear illustration is shown in **Figure 17**, where multilayers films composed of poly(styrene sulfonate) and poly(allylamine hydrochloride) (PSS/PAH) were studied.<sup>43,44</sup>

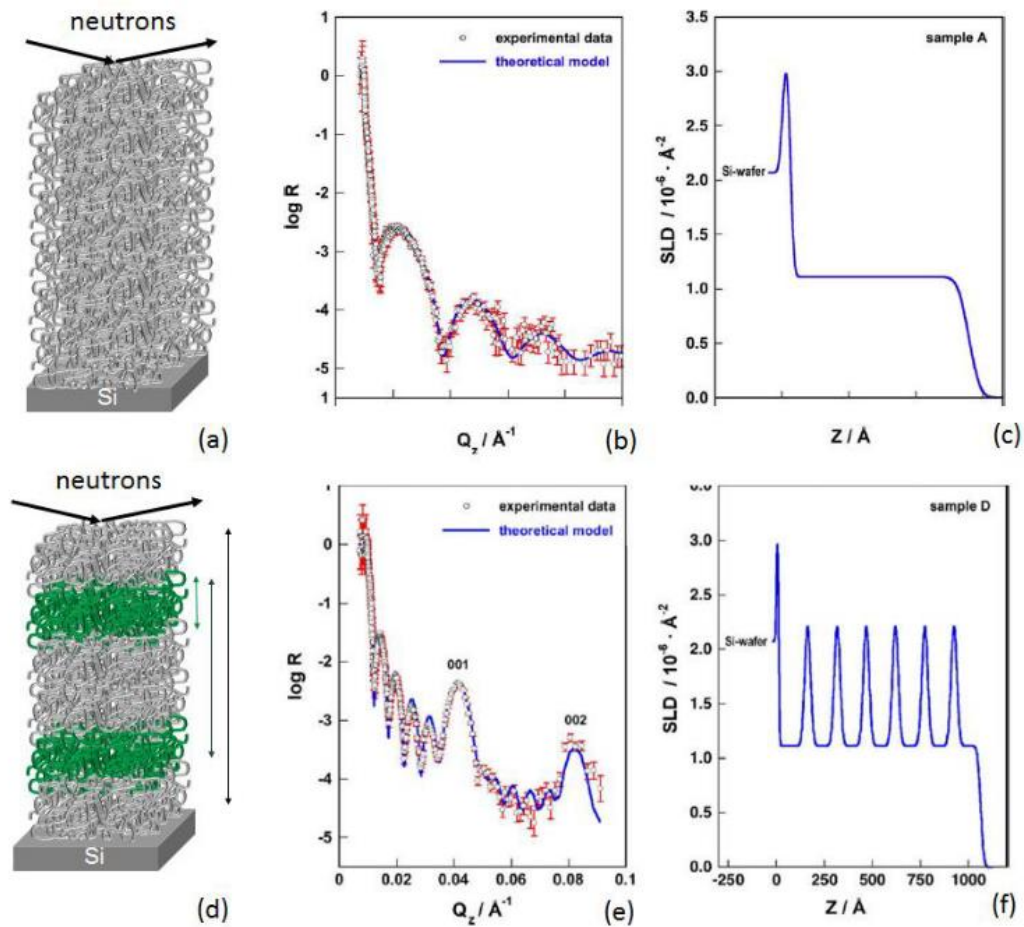


**Figure 17.** NR curves for multilayers films composed of PSS/PAH layers, where both polyelectrolytes have been hydrogenated (top) or when the PSS is deuterated while the PAH is hydrogenated (bottom). The image is reproduced from ref. 43.

When both PSS and PAH are hydrogenated (top panel), the NR reflectivity curve exhibits the so-called Kiessig fringes, which arise from the interference reflected neutron beams at the substrate-film and film-air interfaces, which are associated with the overall thickness.<sup>45</sup> As the multilayer is prepared with PSS being deuterated while PAH is hydrogenated (bottom panel) the appearance of Bragg peaks reveal the true nanostructure of the system.<sup>44</sup> Extracted from the NR curves, the curves showed on the right represent the variation of the Scattering Length Density (SLD) with distance perpendicular to the surface. The SLD quantities, calculated for PSS and PAH, are related to the coherent length scattering (which describes the amplitude of the interaction between neutrons and the nuclei of the atom), which are different for  $^1\text{H}$  (-0.374) and D (0.667). Therefore, it is possible to observe the distance occupied for each deuterated layer.

Similar to the formation of multilayers onto planar substrates, colloidal objects can also be used for LbL assembly with only a slightly different fabrication path, since it now requires, first, dispersion of the colloids in a polymeric solution, followed by pelletization and then spin washing, *i.e.*, separation of adsorbed and non-adsorbed polymer at each layer deposition step, as illustrated in **Figure 18**.<sup>46,47</sup>

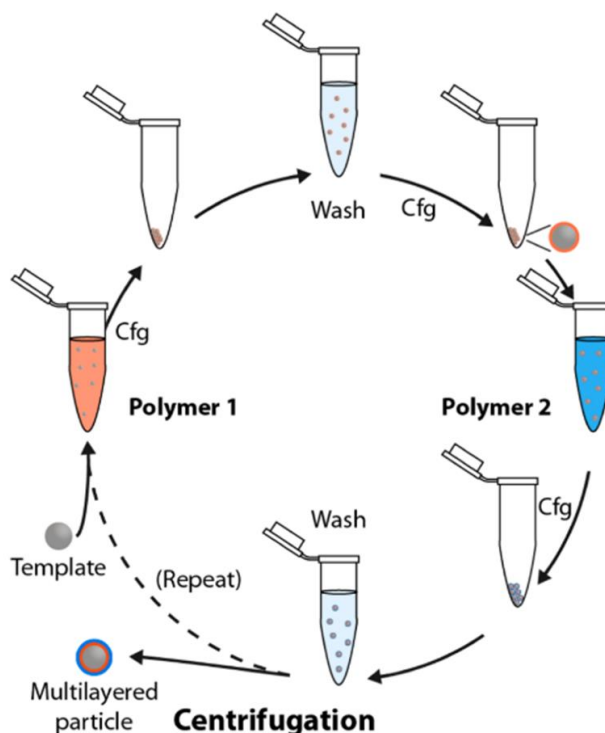


**Figure 18.** Schematic illustration on the Layer-by-Layer (LbL) fabrication method using colloidal substrates. The image is adapted and reproduced from ref. 47.

Schonhöff and co-workers have used silica nanoparticles to prepare a multilayer system with alternating layers of poly(allylamine hydrochloride) (PAH) and poly(sodium 4-styrenesulfate) (PSS).<sup>48</sup> As shown in **Figure 19a**, the monitoring of the  $\zeta$ -potential (by electrophoresis) shows the variation of the potential of the particles with the depositing layers, starting from a negative potential of the bare particles (latex stabilization charges), to positive potentials (after deposition of polycationic PAH) and negative potentials (after the deposition of polyanionic PSS). The total layer thickness (determined by single-particle light scattering), shown in **Figure 19b** for the same system, shows a linear increasing with the number of layers, demonstrating a regular growth of the multilayer and reproducibility of each single deposition step.<sup>48,49</sup>

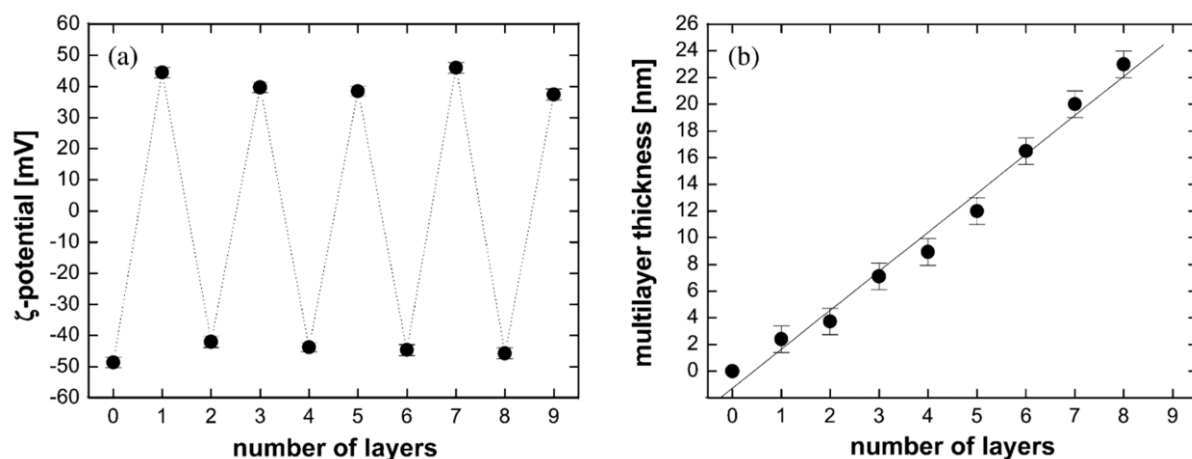


**Figure 19.** (a)  $\zeta$ -potential and (b) total thickness characterization of polyelectrolyte-coated latex particles after alternate deposition of PAH and PSS. The image is reproduced from ref. 49.

The versatility of LbL coatings, which can combine colloids and polymers to generate monolayers or multilayers, is undeniable. Several applications as protective coatings are listed in the literature, from the simple multilayer deposition of oppositely charged polyelectrolytes to protect against corrosion to the coating of implantable materials with anti-bacterial behaviours, for instance, or even drug-delivery systems, as illustrated in **Figure 20**.<sup>50</sup>

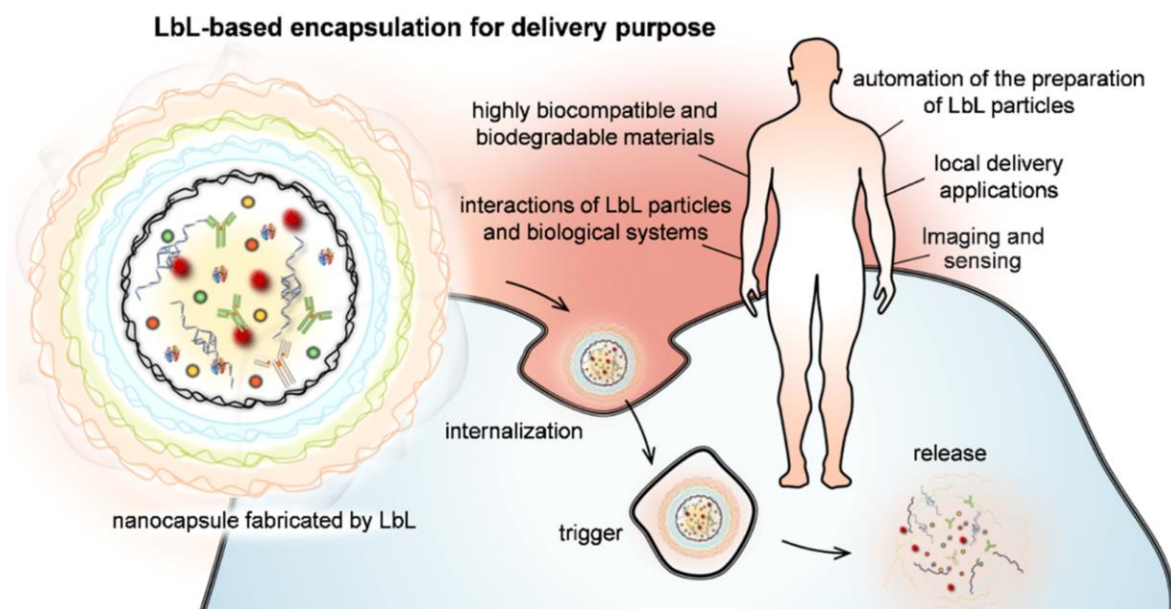


**Figure 20.** Schematic illustration on the use of LbL assemblies for the fabrication of encapsulation platforms for drug delivery. The image is reproduced from ref. 50.

More sophisticated structures, named capsosomes (formed through the LbL assembly of polymers and liposomes) were introduced for applications in drug delivery. Not only the structures can encapsulate actives for local delivery applications, but also the capsule shell can be labelled with different types of nanoparticles for contrast for imaging for instance.<sup>50</sup>

## 2. Block copolymers (BCs)

Among the different building blocks of soft matter, block copolymers (BC) constitute a class of functional polymers capable of self-assembly in bulk or in solution, giving rise to a wide variety of self-organized structures.<sup>51</sup> By definition, BC are macromolecules containing two or more different homopolymers covalently linked together and can be configured into different architectures, as shown in **Figure 21**.

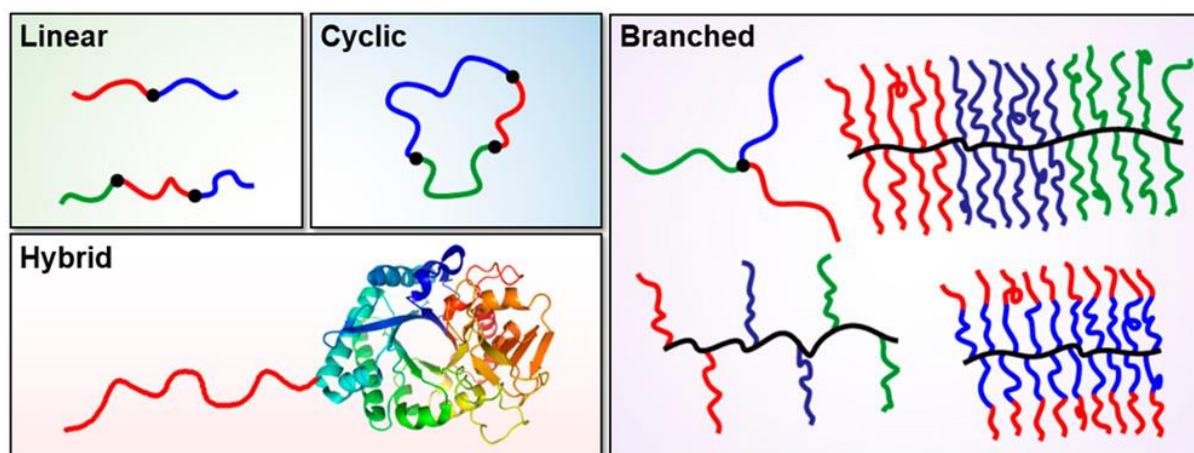


**Figure 21.** Illustration of the different BC currently accessible, including linear diblock or triblock copolymers, as well as cyclic, branched or even hybrid architectures. The image is reproduced from ref. 52.

### 2.1. BC self-assembly in bulk

In the bulk, the self-assembly of BC occurs through the formation of micro-domains of different morphologies with characteristic lengths of the order of  $R_g$  as a result of demixing due to chemical incompatibility between the blocks. Unfavourable enthalpy of mixing, combined with low entropy of mixing, leads to phase separation on a micro scale, since there is a covalent bond between the blocks that prevents a macroscopic phase separation.<sup>53,54</sup> Usually, external stimuli such as thermal annealing, solvent vapour annealing or external fields

are used to promote the self-assembly of BC by tending towards thermodynamic equilibrium. The morphology of the resulting nanostructures is dependent on three main parameters, namely the Flory-Huggins parameter, which expresses the chemical incompatibility between the blocks, the total degree of polymerization and the volume fraction of the blocks.<sup>55</sup> As illustrated in **Figure 22**, the volume fraction dictates the equilibrium morphology adopted by the BC, while the molecular weight determines the periodicity of the structure.

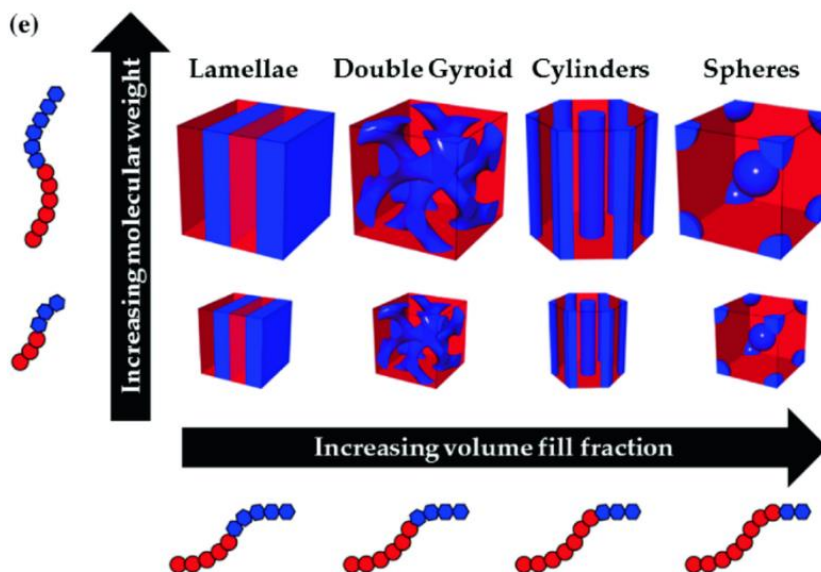


**Figure 22.** Equilibrium morphology and periodicity for a diblock copolymer. The image is reproduced from ref. 7.

## 2.2. BC self-assembly in solution

In solution, the self-assembly of amphiphilic BC (that is, block copolymers consisting on at least one hydrophobic and one hydrophilic block), will take place once a solvent selective for one of the blocks (typically water) is added. This is essentially the result of the so-called “hydrophobic effect”, that is the entropically driven attractive interaction between hydrophobic surfaces in aqueous media due to the release of water molecules forming a cage structure. When the hydrophobic blocks of the BC interact with each other for the formation of the aggregates, a decrease in the interfacial energy of the hydrophobic-hydrophilic interface is observed as a result of the reduction of the contact area of the hydrophobic block with the selective solvent. Even though the formation of such organized structures may appear to be a loss of entropy of the system, the large number of water molecules released

from the cage structure once around the hydrophobic parts greatly increases the overall entropy of the system, resulting, thus, on the minimization of the free energy of the system.<sup>56</sup>

In contrast to the self-assembly in the bulk, the introduction of a solvent increases the level of complexity for BC in solution.<sup>57</sup> The volume ratio of hydrophobic to hydrophilic blocks determines the interfacial curvature and thus dictate their overall shape, as illustrated in **Figure 23**, where different self-assembled nanostructures can be formed depending on the packing parameter,  $\rho$ .<sup>58,59</sup> As a reminder,  $\rho$  is the ratio of the hydrophobic volume of the amphiphile ( $v$ ) to the product of the interfacial area ( $a$ ) and the length of the hydrophobic block ( $\ell$ ) ( $\rho = v/a.\ell$ ).

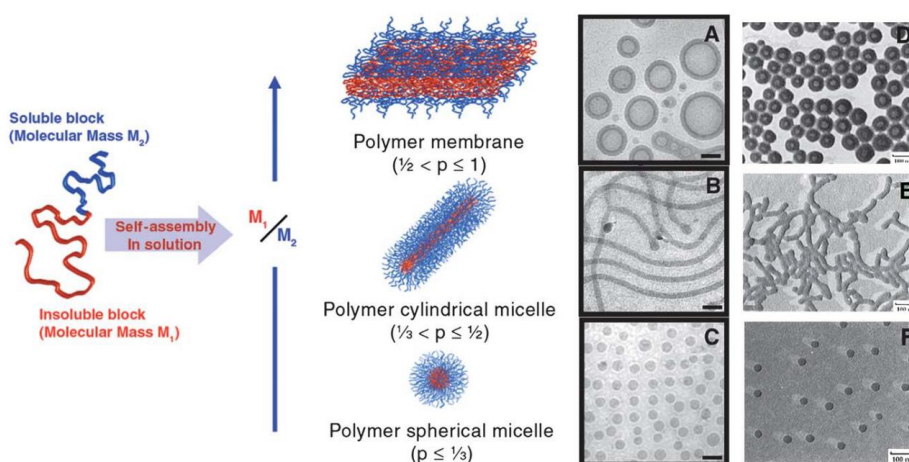


**Figure 23.** Schematic illustration on the BC organization according to the packing parameter ( $p$ ) (left), and respective TEM micrographies (right). The image is reproduced from ref. 59.

Polystyrene-*block*-poly(acrylic acid) (PS-*b*-PAA) is a well-known and well-understood system whose self-assembly has been extensively studied. It consists of a highly hydrophobic and glassy block, PS ( $T_g \sim 100$  °C in bulk), and a hydrophilic and weakly acid block, PAA, which allows fine tuning of the charge density by varying the pH of the medium. As an example, **Figure 24** shows various thermodynamically controlled morphologies observed by the group of Eisenberg, a pioneer in the study of BC self-assembly, specifically with PS-*b*-PAA.<sup>57</sup> It has been suggested that the thermodynamic formation of PS-*b*-PAA aggregates involves three main factors, namely: the stretching of the PS blocks in the core, the interfacial tension between the core and the solvent outside the core and the interaction among the PAA chains at the corona. Thus, the morphology of the aggregates can be controlled by using different BC

compositions and concentrations, the water content or the nature of the non-selective solvent initially used to dissolve the BC.<sup>57</sup>

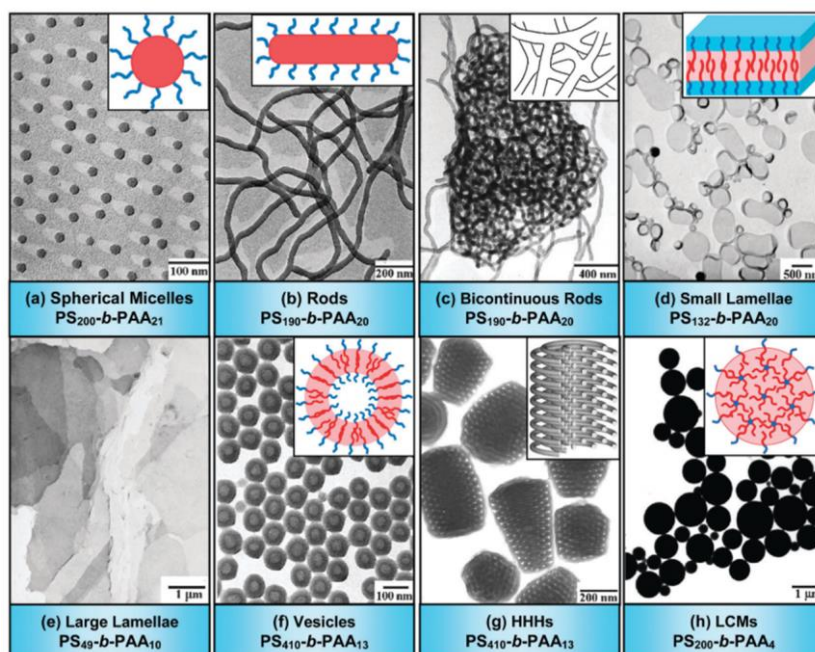


**Figure 24.** Different aggregate morphologies from PS-*b*-PAA diblock copolymers. The image is reproduced from ref. 57.

However, the self-assembly process of amphiphilic BC can be thought not only under thermodynamic but also kinetic aspects. Under thermodynamic control, the morphology of the aggregates can be controlled by the composition of the BC or temperature, and, if the chains remain sufficiently mobile, the morphological transitions can be reversed through altering these parameters. Very importantly, the morphology of such equilibrium structures is independent of the preparation method. On the other hand, under kinetic control, hydrodynamic interactions between aggregates and/or polymer chains, as well as the chain dynamic in the hydrophobic core are important factors that can affect aggregate morphology. In this case, it is highly dependent on the aggregation pathway.<sup>57</sup>

In fact, the main differences between self-assembly processes of surfactants (small molecules) and amphiphilic BC are the low critical micelle concentration (CMC), which nearly eliminates the presence of free BC chains in solution, and the long chains of BC that result in low diffusion coefficients. As a result, the exchange kinetics of individual chains between aggregates, which is much slower in the case of BC systems, leading to kinetically frozen systems.<sup>60,61</sup> However, it is also suggested that kinetically frozen systems result when BC

containing a glassy hydrophobic core (such as PS-*b*-PAA) are used: in these systems, the slow dynamics most likely originates from the glassy nature of the core-forming block.<sup>62</sup> On the other hand, vesicular morphologies, for instance, which can be formed with low  $T_g$  hydrophobic blocks, are not dictated by the kinetically frozen glassy nature of the hydrophobic block.<sup>63</sup>

For BC containing flexible and weakly hydrophobic blocks like PEO-*b*-PPO-*b*-PEO copolymers (Pluronics, BASF) where PPO is polypropylene oxide, self-assembly typically occurs under thermodynamic control. In contrast, for BC containing vitreous and highly hydrophobic blocks like PS-*b*-PEO or PS-*b*-PAA, self-assembly is under kinetic control and therefore highly dependent on initial conditions. For these systems, BC cannot directly self-assemble by dispersing the polymer powder in water. Therefore, the usual way to proceed consists in dissolving the copolymer in a non-selective solvent that is miscible in water (THF, DMSO, DMF, dioxane) and then adding water to gradually increase the intensity of the hydrophobic effect. One can identify by simple transmittance measurements, the critical water content corresponding to the onset of the BC self-assembly.<sup>64</sup>

In summary, considering an amphiphilic BC dissolved in a non-selective solvent, while water is gradually added to the system and aggregates are formed, we move from a state with highly mobile chains, at low water contents, where polymer chains can exchange between the bulk solution and aggregates (self-assembly is under thermodynamic control), to a frozen, high water content situation, in which the polymer chain exchange slows down considerably as the overall kinetic process becomes slower than the rate of water addition, generating kinetically-trapped structures (here, a sum of factors account for this phenomena: the low CMC of BC, the low diffusion of BC and very importantly the glassiness of the hydrophobic forming core, PS). At this point, thermodynamic equilibrium is, thus, unreachable, and the morphology of the so-called kinetically-frozen aggregates will reflect the thermodynamics at the water content where the structures become frozen.<sup>65</sup>

### 3. Solid-supported BC membranes

Solid-supported BC membranes can be divided in two main classes, the first being membranes constituted by the grafting of ABA or ABC block copolymers (in which B is the

hydrophobic block and A and C are the hydrophilic ones), and the second, specifically designed bilayer membranes, in which a planar array of two BC monolayers is derived from the self-assembly of amphiphilic molecules, similarly to a lipid bilayer structure. The preparation of these membranes onto solid supports gives them mechanical stability and allows to use many surface characterization techniques. In addition, the formation of such structures onto solid substrates can be considered as a new class of functional coatings, provided that industrial processes are available, which is not currently the case.

### 3.1. Grafting methodologies

The grafting methodologies described above for the preparation of homopolymer brushes can also be extended for obtaining BC membranes composed of ABA triblock copolymers. Mandal and colleagues have recently reported a flow system for the synthesis of a triblock copolymer brush composed of poly(*N*-isopropylacrylamide)-*block*-poly(*N,N*-dimethylacrylamide)-*block*-*N*-hydroxyethyl acrylamide, p(NIPAM)-*b*-p(DMAM)-*b*-p(HEAM), by surface-initiated atom-transfer radical polymerization.<sup>66</sup> As illustrated in **Figure 25**, the substrate is first functionalized with a SI-ATRP initiator, which allows the growth of an initial p(NIPAM) brush; subsequent switching to reaction mixtures containing DMAM and then HEAM yields the triblock copolymer brush.

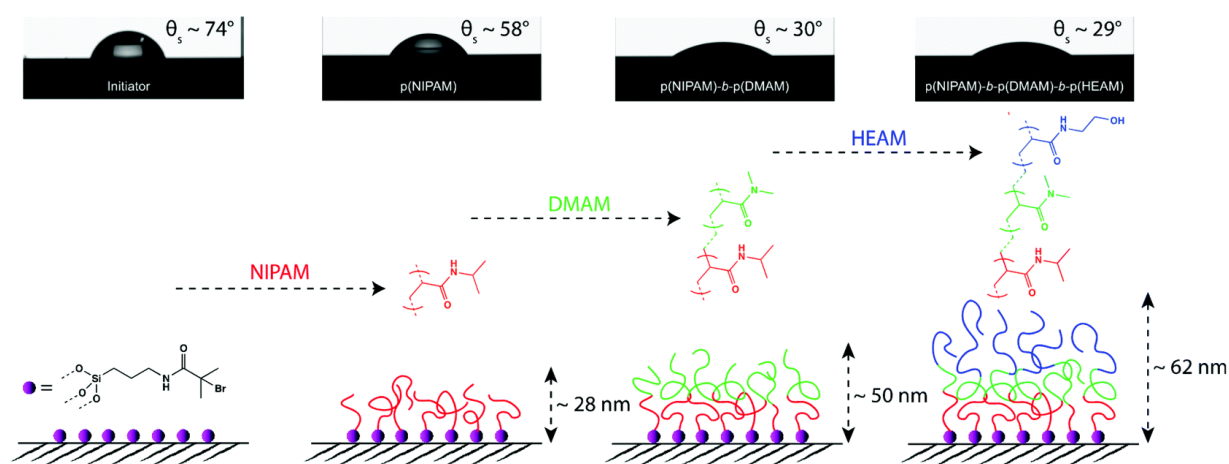


**Figure 25.** Schematic illustration of a “grafting from” approach for the preparation of triblock-copolymer brushes. The image is reproduced from ref. 66.

Alternatively, Shen and colleagues reported the use of a “grafting to” method to generate self-cleaning anti-fouling surfaces.<sup>67</sup> Using a drop coating process, polymer brushes

of (PtBA-co-PPEGMEMA-co-PDOMA)-g-PPFA (Figure 26) were successfully prepared by the efficient attachment of the catechol moieties in the DOMA block to the ITO (Indium tin oxide) substrate (Figure 27).

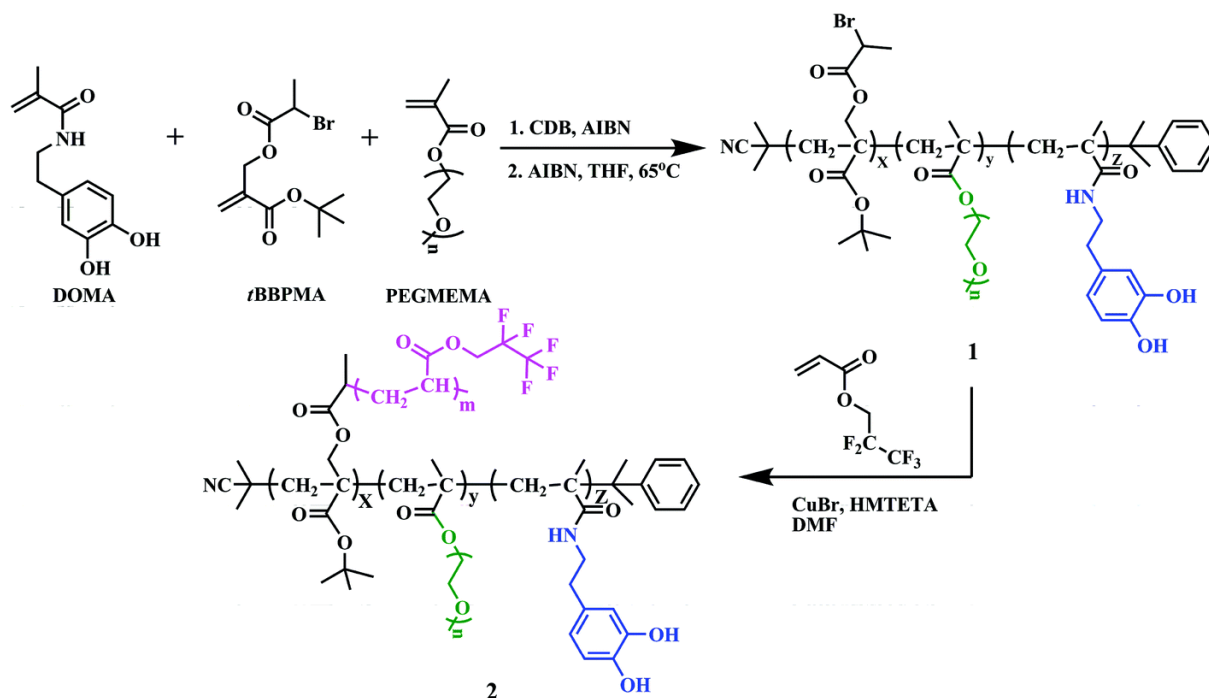


**Figure 26** Synthesis of (PtBA-co-PPEGMEMA-co-PDOMA)-g-PPFA amphiphilic polymer brush. The image is reproduced from ref. 67.

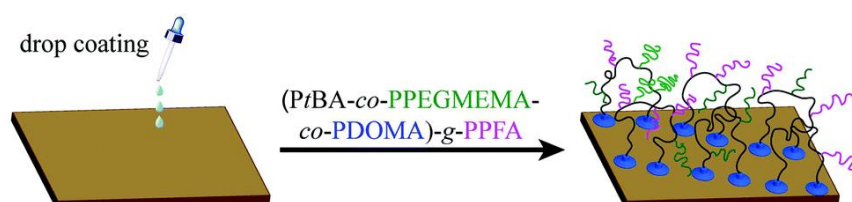


**Figure 27.** Schematic illustration of a "grafting to" approach for the generation of triblock-copolymer brushes. The image is reproduced from ref. 67.

In addition to the grafting methodologies, BC membranes can be prepared using vesicle fusion (VF) or Langmuir-Blodgett/Langmuir-Schaefer techniques (LB/LS). In these cases, the BC membrane has the structure of a bilayer, in which the hydrophobic core of the bilayer membrane results from the interaction of hydrophobic blocks of two layers facing each other, similar to a lipid bilayer structure.

Solid-supported BC bilayers have been widely studied as biomimetic model

membranes.<sup>68–71</sup> To this end, the use of the solid supports helps to increase stability of the bilayer and also allows the use of a wide range of analytical and surface-sensitive techniques for bilayer characterization.<sup>37</sup> Compared to lipid, BC bilayers outperform in terms of mechanical stability, tuneable thickness and functionality. BC bilayers are much more chemical and mechanical stable bilayer membranes than lipids, due to partial interpenetration of the individual polymeric layers, which in turn minimizes any delamination.<sup>72</sup> In addition, the bilayer thickness, particularly the hydrophobic reservoir, is considerably larger for BC bilayers. For polymersomes, it can exceed 20 nm with copolymers having hydrophobic blocks of a molar mass above 20 kDa, which can be a key advantage for the encapsulation of any actives (molecules, nanoparticles...) compared to the generally smaller reservoirs (3-5 nm) of lipid membranes.<sup>72–74</sup> Finally, many parameters of the BC macromolecular synthesis such as chemical composition, hydrophilic-hydrophobic balance, block length and molecular weight can be easily tuned, overcoming the lack of functionality of lipid bilayers.<sup>51,75,76</sup>

In order to mimic natural membranes, solid-supported BC membranes can be used as scaffolds for the insertion of functional biomolecules, as described by the group of Palivan and Meier.<sup>77</sup> Indeed, their work shows the first preliminary model of a channel membrane protein that is functionally incorporated in a completely artificial solid-supported BC bilayer membrane (**Figure 28**).

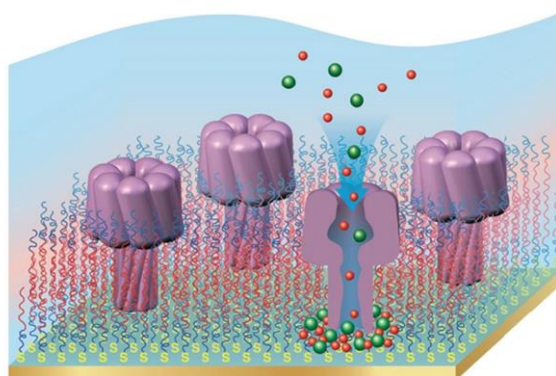


**Figure 28.** Schematic illustration of solid-supported BC bilayer membranes consisting on PB-b-PEO block copolymers with inserted natural channel proteins. The image is reproduced from ref. 77.

Some recent fabrication strategies consist in using a mixture of lipids and BC to generate hybrid membranes.<sup>78–80</sup> In this case, the final structures combine the advantages of both lipid and BC bilayers, notably the biorelevance and fluidity of the lipid building blocks with the mechanical robustness and chemical tunability of the BC.<sup>79</sup>

### 3.2. Langmuir-Blodgett (LB) method

The Langmuir-Blodgett (LB) technique, developed by Katharine Blodgett and Irwin Langmuir in the early 20<sup>th</sup> century,<sup>81</sup> is a widely used method for the fabrication of lipid and BC thin films onto solid substrates. Supported thin films obtained by the LB technique, monolayer or multilayers, are highly ordered due to the control of the architecture at the molecular level, which also results on negligible defects and high reproducibility.<sup>82</sup> With the LB method, a BC solution (prepared in an organic solvent) is first spread on the surface of ultrapure water (subphase) in a Langmuir trough. Then, moving barriers compress the BC molecules until a Langmuir monolayer is formed. The latter is then transferred to a solid substrate either by lifting or by immersion of the solid support. The transfer mode onto the solid support can also be performed by horizontal lifting method, described as the Langmuir-Schaefer (LS) technique. An illustration of LB technique is shown in **Figure 29**.

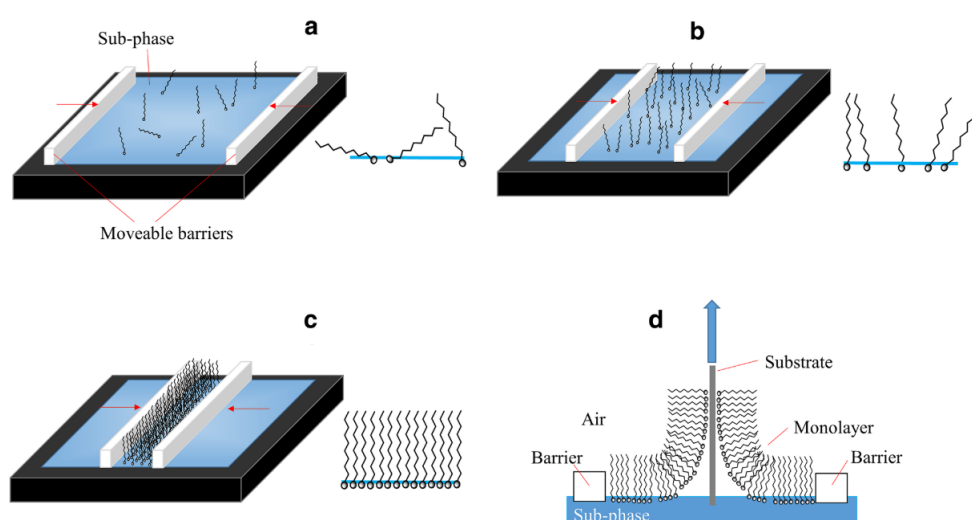


**Figure 29.** Schematic illustration of the steps involved in the formation of solid-supported Langmuir-Blodgett films. The image is reproduced from ref. 83.

The LB method can be applied not only for the generation of a monolayer but also for the generation of multilayers simply by subsequent repetitions of the dipping and removal processes, whose final thickness can be fine-tuned by the number of cycles and sizes of the polymer chains.<sup>68</sup> A clear example of the versatility of the LB method was recently published by the group of Palivan and Meier.<sup>71</sup> In their work, various supported films of poly-(ethylene glycol)-*block*-poly( $\gamma$ -methyl- $\epsilon$ -caprolactone)-*block*-poly[2-(dimethylamino)ethyl methacrylate

(PEG-*b*-PMCL-*b*-PDMEAMA) were prepared with different directions and transfer sequences, from air to water subphase or vice versa, as described in **Figure 30**.

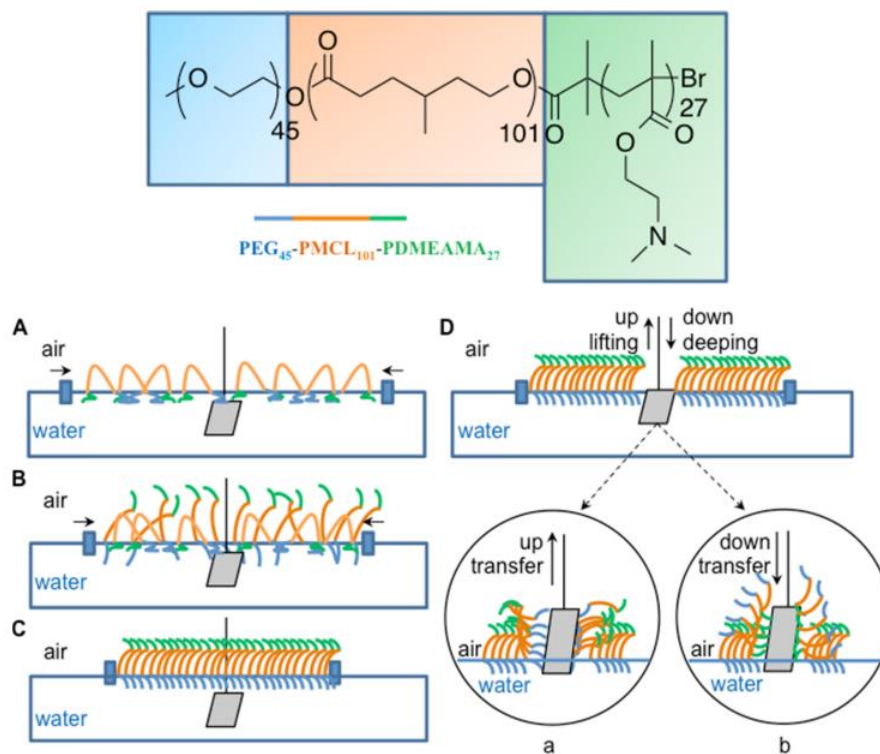


**Figure 30.** Schematic illustration of the LB transfer process for the generation of solid-supported BC monolayers. The image is reproduced from ref. 71.

The LB technique allows not only the formation of a BC monolayer but also a bilayer after two consecutive transfers, as illustrated in **Figure 30d** and **Figure 31**.

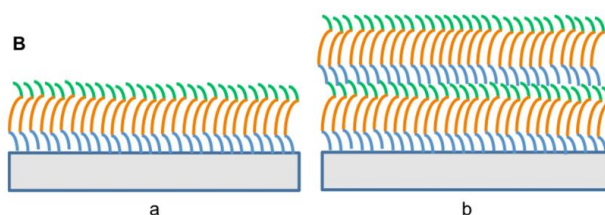


**Figure 31.** Schematic illustration of the PEG-*b*-PMCL-*b*-PDMEAMA mono- and bilayers. Adapted and reproduced from ref. 71.

An important feature of the LB technique is the possibility of preparing asymmetric BC bilayer membranes, in which the term “asymmetric” here signifies a bilayer structure in which the hydrophobic reservoir contains the same hydrophobic block from two different BC, but

the hydrophilic block anchoring to the surface and the hydrophilic block at the top of the bilayer structure are different, as illustrated in **Figure 32**.

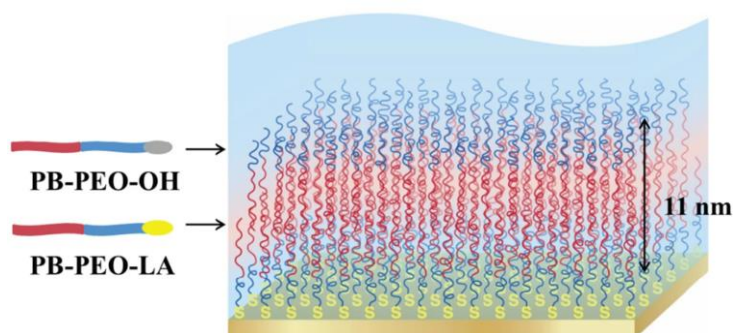


**Figure 32.** Schematic illustration of solid supported BC bilayer structure comprised on hydroxyl-functionalized PS-*b*-PEO diblock copolymer (PS-PEO-OH) and lipoic acid (LA) functionalized PS-*b*-PEO diblock copolymer (PB-PEO-LA). The image is reproduced from ref. 77.

This example of an asymmetric bilayer membrane was obtained by combined surface chemistry and self-assembly of amphiphilic BC.<sup>77</sup> They first transferred the bottom polymer layer by LB to a patterned gold electrode (the layer is attached to the substrate via gold/sulphur chemistry), and then the second layer was transferred by LS and attached to the bottom layer by hydrophobic interaction. The first and second layer are respectively PS-*b*-PEO-LA and PS-*b*-PEO-OH, so that the hydrophilic blocks, even though present the same PEO block, have different terminations.

Beside the possibility of generating a variety of mono- and multilayers of amphiphilic molecules with high resolution and negligible defects at laboratory scale, the LB/LS approaches cannot be implemented satisfactorily at large scale (mainly due to the extremely high cleanliness of the Langmuir trough) or on colloidal and hollow structures.<sup>37</sup>

### 3.3. Vesicle Fusion (VF) method

The vesicle fusion (VF) method, first introduced with lipids and later extended to polymers, is based on the deposition of lipid or polymer vesicles on a substrate that will trigger the vesicle fusion and the subsequent generation of a solid-supported bilayer membrane, as schematically represented in **Figure 33**.

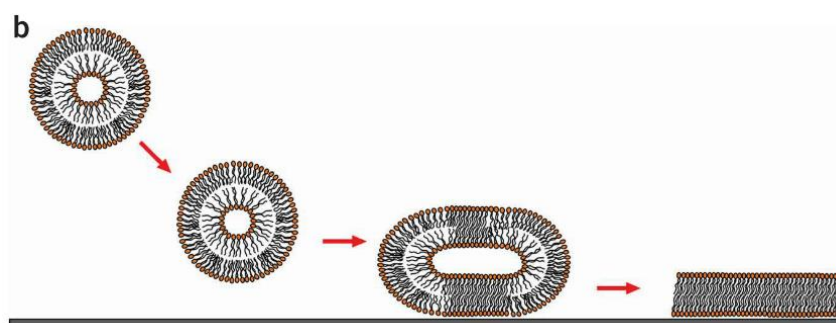


**Figure 33.** Schematic illustration of the vesicle fusion method. The image is adapted and reproduced from ref. 84.

The VF method allows the generation of defect-free lipid bilayers with high reproducibility.<sup>85</sup> However, when extended to polymersomes, the bilayer formation suffers from some limitations. Notably, the mechanical robustness of polymer vesicles prevents their rupture and fusion in the absence of strong attractive interaction with the surface.<sup>86,87</sup> Furthermore, inhomogeneity and poor reproducibility of these membranes as well as the restriction of the BC compositions to fit the packing parameter for the formation of vesicles ( $(\frac{1}{2} < \rho < 1)$ ) or lamellar structures ( $\rho \sim 1$ ), greatly reduces the applicability of the VF method.<sup>88</sup>

Additionally, even if the VF method can present some versatility when coupled with LB technique, for instance (**Figure 34**), it cannot generate itself asymmetric BC bilayers, as previously demonstrated with LB technique.

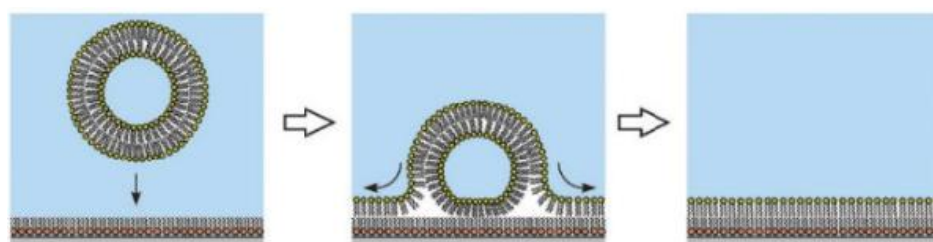


**Figure 34.** Schematic illustration of a vesicle fusion onto a LB-deposited monolayer. The image is reproduced from ref. 89.

### 3.4. Solvent-assisted Lipid Bilayer (SALB) method

Recently, Cho and co-workers have introduced the so-called Solvent-Assisted Lipid Bilayer formation (SALB) pathway as an alternative to the LB and VF methods described above.<sup>90–92</sup> The method, illustrated in **Figure 35**, involves the deposition of a lipid solution prepared in a water-miscible organic solvent onto a solid substrate, followed by a gradual

exchange of the organic phase with water to generate lamellar-phase structures, leading to the formation of supported lipid bilayers.

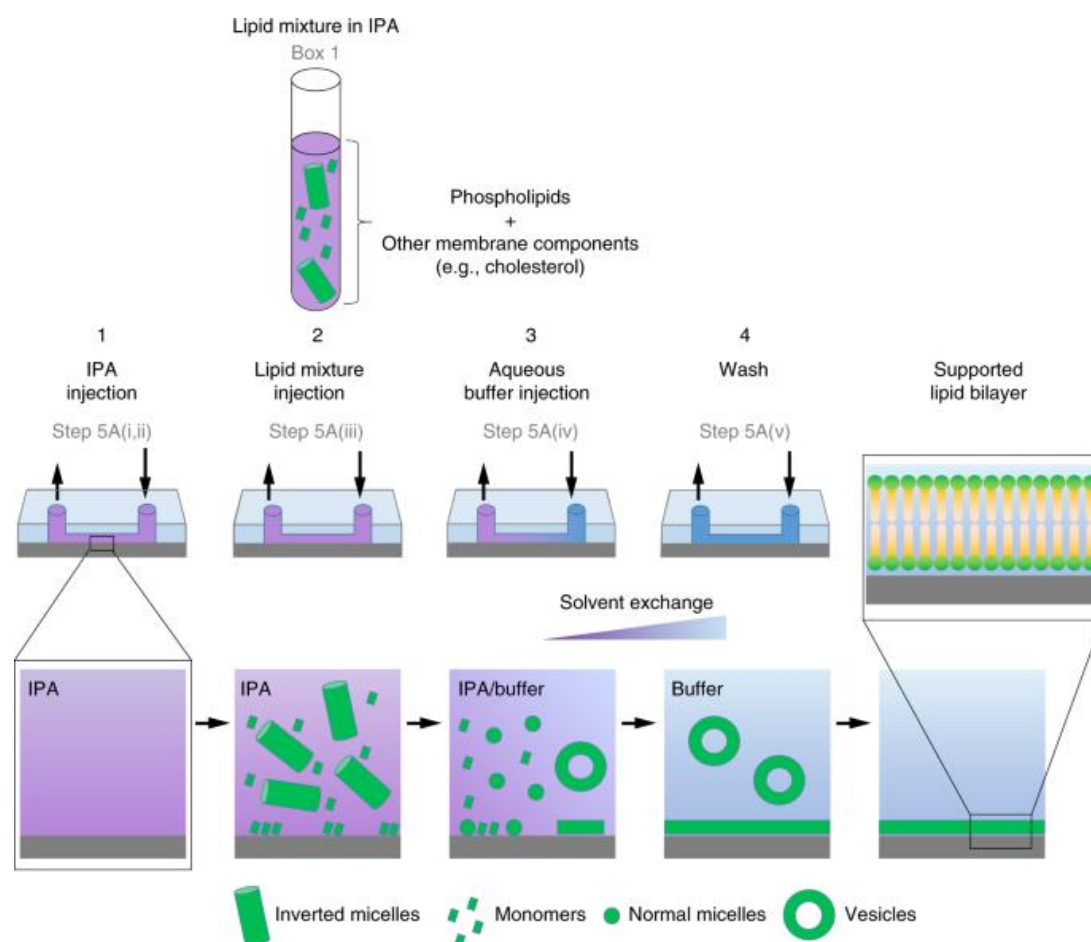


**Figure 35.** Schematic illustration of the SALB method. IPA refers to isopropanol. The image is reproduced from ref. 90.

Fairly fast and versatile, the SALB approach allows real-time monitoring of the lipid membrane formation and the use of a wide range of substrates and lipids.<sup>93</sup> A well-known technique that allows the real-time monitoring of adsorption onto a substrate is the Quartz Crystal Microbalance with Dissipation monitoring (QCM-d). QCM-d is an extremely sensitive balance capable of measuring mass changes of films deposited on a substrate with nanogram sensitivity. **Figure 36** illustrates the QCM-d crystal sensor and its sensing principle.

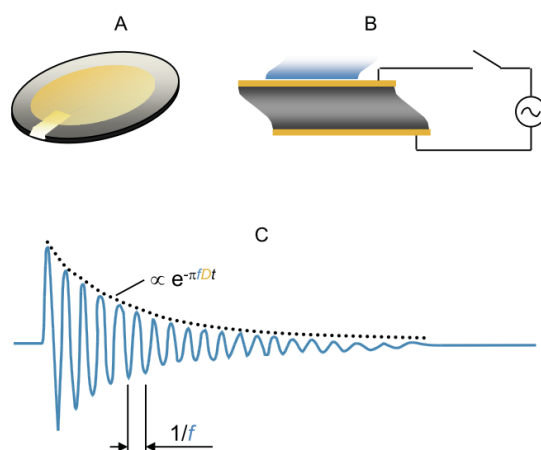


**Figure 36.** Schematic illustration of a QCM-d crystal sensor and sensing principle, showing (a) the typically used QCM-d sensors; (b) The cyclical shear deformation of the sensor resulted from the application of oscillatory voltage; and (c) the decay curve, which provides the information of the resonance frequency and energy dissipation. The image is reproduced from ref. 94.

QCM-d sensors are based on quartz crystals typically coated with gold electrodes about 14 mm of diameter possessing a fundamental resonance of  $\sim 5$  MHz. The application of an oscillatory voltage results in cyclic shear deformation of the sensor (**Figure 36b**) and, as the driving voltage is intermittently turned off, the decay time of the oscillation is monitored and the resonance frequency and dissipation can be extracted (**Figure 36c**). In a very simplified manner, decreasing frequency (*i.e.* negative  $\Delta f$ ) indicates mass adsorption, while low dissipation values indicate the formation a rigid film onto the sensor.<sup>94</sup> A linear relationship between changes in the in the resonator mass and resonant frequency was derived by Sauerbrey<sup>95</sup> and applied exclusively to relatively rigid films (**Eq. 1**):

$$\frac{\Delta F_n}{n} = - \frac{2F_0^2}{\sqrt{\rho_q \mu_q}} \cdot \Delta m \quad \text{Eq.1}$$

where  $F_0$  is the resonant frequency of the crystal (5 MHz),  $\rho_q$  ( $2.648 \text{ g.cm}^{-3}$ ) the quartz density and  $\mu_q$  ( $2.947 \times 10^{11} \text{ g.cm}^{-1} \text{ s}^{-2}$ ) the shear modulus.

Using QCM-d experiments, Cho and workers demonstrated the formation of a 1,2-dioleoyl-sn-glycero-3-phosphocholine (DOPC) bilayer onto gold and silicon dioxide substrates by their proposed SALB method.<sup>91</sup> As it can be observed in **Figure 37c**, the QCM graph is divided into 4 parts which correspond to successive injections of aqueous buffer (1), isopropanol (2), lipid solution in isopropanol (3) and aqueous buffer (4). A large frequency shift

(accompanied by a large dissipation shift) is seen when isopropanol is added to the cell containing the aqueous buffer (arrow 2), which does not represent any mass adsorption. Indeed, the frequency shift may also be due to changes in density and viscosity of the liquid medium. This is the reason why, measurements are started and finished with the same liquid environment (aqueous buffer solution), in order to extract the frequency shift ( $-25.6$  Hz) purely due to mass adsorption. QCM-d demonstrated the versatility of the SALB method, which allowed the bilayer formation onto silicon dioxide (**Figure 37c**) or gold substrates (**Figure 37d**) (additional publications also showed the formation onto  $\text{Al}_2\text{O}_3$  and  $\text{TiO}_2$  substrates<sup>90</sup>), in contrast to the VF, which is known to be limited to the use of silicon dioxide surfaces bearing silanol groups or other hydrophilic substrates. As it can be observed, in **Figure 37 a** and **b**, the formation of a lipid bilayer via VF method is only successful onto silicon oxide substrates.

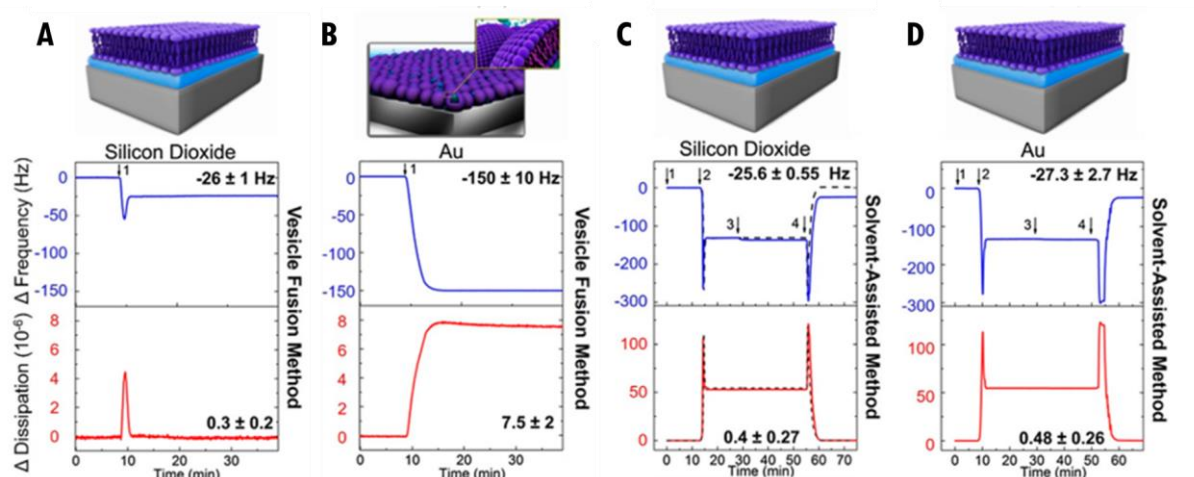


**Figure 37.** Real-time QCM-d monitoring experiments comparing the VF (a, b) and SALB methods (c, d) onto silicon dioxide and gold substrates. The image is adapted and reproduced from ref. 91.

### 3.4.1. Solvent-assisted method using BC

Based on the SALB method, the Palivan and Meier's group introduced very recently a similar approach for the development of solid-supported polymer membranes for further biomolecules incorporation.<sup>96</sup> In their work, solid-supported membranes of amphiphilic diblock copolymer poly(dimethylsiloxane)-*block*-poly(2-methyl-2-oxazoline) (PDMS-*b*-PMOXA) containing some BC modified with biotin were generated as illustrated in **Figure 38**.

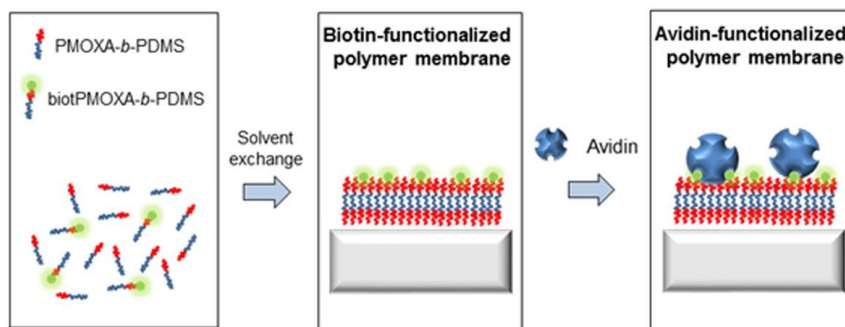


**Figure 38.** Schematic illustration on the block copolymer bilayer formation using BC and biotin-BC to create biotinylated-supported membranes onto QCM silica sensors. The image is reproduced from ref. 96.

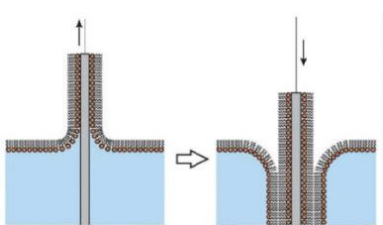
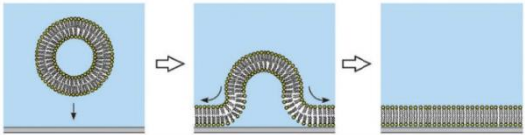
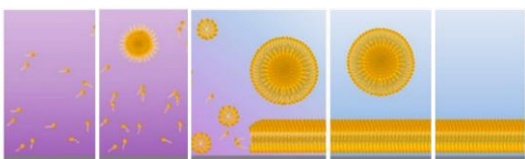
The process used by Palivan and Meier differs from the SALB method only in that they use a polymer solution instead of a lipid solution, so the steps in the fabrication process include successive injections of aqueous buffer, ethanol, polymer solution (prepared in ethanol) and finally aqueous buffer which triggers the copolymer self-assembly. A planar membrane is formed once the system reaches equilibrium.<sup>96</sup>

Although the SALB approach has been successful when applied to BC, the lack of specific interactions with the substrate can be a difficulty in generating homogeneous bilayers attached to the surface. Furthermore, just like VF, SALB method is limited to block copolymers having specific geometric properties ( $\rho \sim 1$ ) in order to generate the formation of lamellar structures.

## Motivation of this thesis work

The thesis work aims at developing a scalable process of BC self-assembly into solid-supported bilayered membranes. The advantages and disadvantages of the main techniques currently used to generate solid-supported BC bilayer membranes are summarized in **Table 1**.

**Table 1.** Advantages and disadvantages of the LB, VF and SA fabrication methods. Images shown were reproduced from refs. 89 and 91.

Method	Advantages	Disadvantages
<p><b>Langmuir-Blodgett (LB)</b></p> 	<ul style="list-style-type: none"> <li>▪ High resolution</li> <li>▪ High reproducibility</li> <li>▪ Negligible defects</li> <li>▪ Molecular level control of the layer</li> <li>▪ Asymmetric and symmetric bilayers</li> </ul>	<ul style="list-style-type: none"> <li>▪ Special equipment</li> <li>▪ High degree of cleanliness</li> <li>▪ Flat substrates</li> <li>▪ Small-scale substrates</li> </ul>
<p><b>Vesicle Fusion (VF)</b></p> 	<ul style="list-style-type: none"> <li>▪ Ease of preparation</li> <li>▪ No need of special equipment</li> </ul>	<ul style="list-style-type: none"> <li>▪ Requires polymersome preparation</li> <li>▪ Low reproducibility and membrane defects</li> <li>▪ Limited BC compositions</li> <li>▪ Hydrophilic and flat substrates</li> <li>▪ Symmetric membranes only</li> <li>▪ Small-scale substrates</li> </ul>
<p><b>Solvent-Assisted (SA)</b></p> 	<ul style="list-style-type: none"> <li>▪ Ease of preparation</li> <li>▪ Variety of substrates</li> <li>▪ Scalable</li> </ul>	<ul style="list-style-type: none"> <li>▪ Limited BC composition</li> <li>▪ Absence of interactions with the substrate may generate heterogeneous bilayers and limited anchoring</li> <li>▪ Symmetric bilayers only</li> </ul>

Among all these techniques, the lack of versatility and the inability to scale up are the obstacles to their use at the industrial level. In an effort to develop a more universal approach to the fabrication of BC bilayers on solid substrates, we present in this thesis work a simple and robust bottom-up approach capable of generating symmetric and asymmetric bilayers onto silicon dioxide wafers. The substrates were selected as they allow the use of a wide range of complementary state-of-the-art techniques to precisely characterize the different steps of the assembly process. However, it is important to note that this work is part of an ANR project (SISAL 2018 – 2022) in which the fabrication strategy is also being explored onto colloids. Ideally, the fabrication method could be applied to substrates of any time, shape and size.

For this purpose, amphiphilic diblock copolymers with one adsorbing hydrophilic block and one non-adsorbing hydrophobic block are used. The proposed fabrication method consists of two steps. First, there is the formation of a BC monolayer by establishing non-covalent interactions between the substrate and the hydrophilic blocks in a non-selective solvent (**Figure 39**).

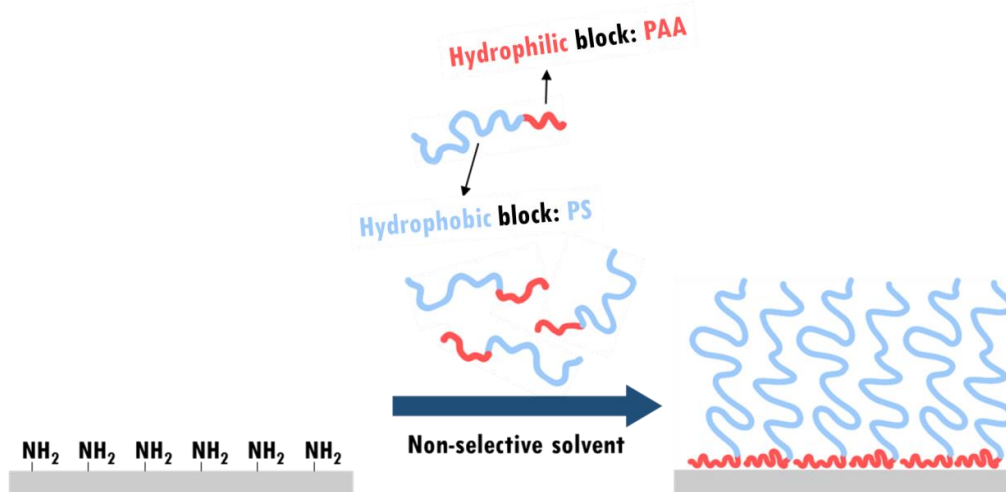


**Figure 39.** Schematic illustration of the first step of the surface-induced self-assembly process, *i.e.*, the BC formation of the BC monolayer formation.

Then, the controlled water addition (*i.e.* the injection of a non-selective solvent) triggers the assembly of the second layer through hydrophobic interactions between free and grafted hydrophobic blocks, resulting in the formation of an additional monolayer on top of the first layer by self-assembly, ultimately leading to a BC bilayer on a solid support BC (**Figure 40**).

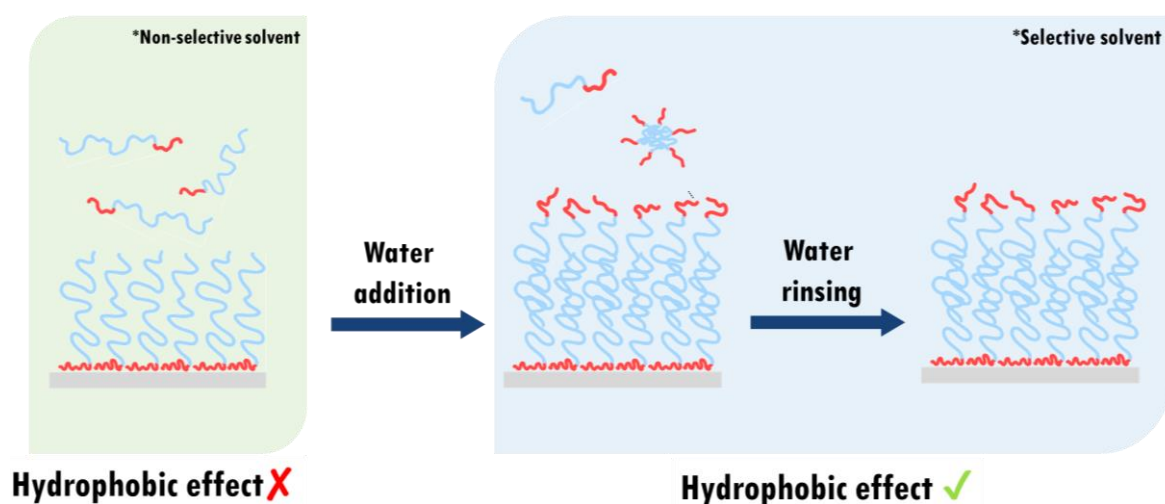


**Figure 40.** Schematic illustration of the second step of the surface-induced self-assembly process, i.e., the BC bilayer formation.

A final rinsing step then removes the excess BC aggregates generated in the aqueous solutions during the second step. In essence, the overall pathway replicates at a solid-liquid interface the hydrophobic self-assembly mechanism of amphiphilic BC in solution BC.

BC bilayer thin films can offer additional features as robust organic thin films with on-demand surface functionality, appealing active encapsulation capability and compatibility with different physicochemical environments. In this regard, the ‘surface-induced’ self-assembly of BC as described herein enriches the panel of directed self-assembly approaches used to design functional organized ultrathin films.

## References

- (1) Gennes, P. De. Soft Matter (Nobel Lecture) \*\*. *Angew. Chem., Int. Ed. Engl.* **1992**, *31*, 842–845.
- (2) Gompper, G.; Dhont, J. K. G.; Richter, D. A Unified View of Soft Matter Systems? *Eur. Phys. J. E* **2008**, *26* (1–2), 1–2. <https://doi.org/10.1140/epje/i2008-10328-1>.
- (3) Jangizehi, A.; Schmid, F.; Besenius, P.; Kremer, K.; Seiffert, S. Defects and Defect Engineering in Soft Matter. *Soft Matter* **2020**, *16* (48), 10809–10859. <https://doi.org/10.1039/d0sm01371d>.
- (4) Cummins, C.; Lundy, R.; Walsh, J. J.; Ponsinet, V.; Fleury, G.; Morris, M. A. Enabling Future Nanomanufacturing through Block Copolymer Self-Assembly: A Review. *Nano Today* **2020**, *35*, 100936. <https://doi.org/10.1016/j.nantod.2020.100936>.
- (5) van der Gucht, J. Grand Challenges in Soft Matter Physics. *Front. Phys.* **2018**, *6*, 6–8. <https://doi.org/10.3389/fphy.2018.00087>.
- (6) Hamley, I. W. *Introduction to Soft Matter: Polymers, Colloids, Amphiphiles and Liquid Crystals*; John Wiley & Sons, Inc., 2007. <https://doi.org/10.1002/9780470517338>.
- (7) Dolan, J. A. *Gyroid Optical Metamaterials*; Springer, Cham, 2018. [https://doi.org/https://doi.org/10.1007/978-3-030-03011-7\\_2](https://doi.org/https://doi.org/10.1007/978-3-030-03011-7_2).

- (8) Forster, S.; Plantenberg, T. From Self-organizing Polymers to Nanohybrid and Biomaterials.Pdf. *Angew. Chem. Int. Ed.* **2002**, *41*, 688–714. [https://doi.org/10.1002/1521-3773\(20020301\)41:5<688::AID-ANIE688>3.0.CO;2-3](https://doi.org/10.1002/1521-3773(20020301)41:5<688::AID-ANIE688>3.0.CO;2-3).
- (9) Ariga, K. *Organized Organic Ultrathin Films: Fundamentals and Applications*; Wiley-VCH Verlag GmbH & Co. KGaA, 2012. <https://doi.org/10.1002/9783527654666>.
- (10) Kaganer, V. M. Kaganer, Möhwald, Dutta - 1999 - Structure and Phase Transitions in Langmuir Monolayers.Pdf. *Rev. Mod. Phys.* **1999**, *71* (3), 779–819.
- (11) Scientific, B. Langmuir and Langmuir-Blodgett <https://www.biolinscientific.com/measurements/langmuir-and-langmuir-blodgett> (accessed Sep 23, 2021).
- (12) Gareth Roberts. *Langmuir-Blodgett Films*, 1st ed.; Gareth Roberts, Ed.; Springer US, 1990; Vol. 148. <https://doi.org/10.1007/978-1-4899-3716-2>.
- (13) Larsen, M. C. Binary Phase Diagrams at the Air-Water Interface: An Experiment for Undergraduate Physical Chemistry Students. *J. Chem. Educ.* **2014**, *91* (4), 597–601. <https://doi.org/10.1021/ed4004854>.
- (14) Schreiber, F. Structure and Growth of Self-Assembling Monolayers. *Prog. Surf. Sci.* **2000**, *65* (5–8), 151–257. [https://doi.org/10.1016/S0079-6816\(00\)00024-1](https://doi.org/10.1016/S0079-6816(00)00024-1).
- (15) Love, J. C.; Estroff, L. A.; Kriebel, J. K.; Nuzzo, R. G.; Whitesides, G. M. *Self-Assembled Monolayers of Thiolates on Metals as a Form of Nanotechnology*; 2005; Vol. 105. <https://doi.org/10.1021/cr0300789>.
- (16) Park, J. W.; Kim, H.; Han, M. Polymeric Self-Assembled Monolayers Derived from Surface-Active Copolymers: A Modular Approach to Functionalized Surfaces. *Chem. Soc. Rev.* **2010**, *39* (8), 2935–2947. <https://doi.org/10.1039/b918135k>.
- (17) Kim, M.; Schmitt, S. K.; Choi, J. W.; Krutty, J. D.; Gopalan, P. From Self-Assembled Monolayers to Coatings: Advances in the Synthesis and Nanobio Applications of Polymer Brushes. *Polymers (Basel)*. **2015**, *7* (7), 1346–1378. <https://doi.org/10.3390/polym7071346>.
- (18) Hasan, A.; Pandey, L. M. *Self-Assembled Monolayers in Biomaterials*; Elsevier Ltd., 2018. <https://doi.org/10.1016/B978-0-08-100716-7.00007-6>.
- (19) Ramin, M. A.; Le Bourdon, G.; Daugey, N.; Bennetau, B.; Vellutini, L.; Buffeteau, T. PM-IRRAS Investigation of Self-Assembled Monolayers Grafted onto SiO<sub>2</sub>/Au Substrates. *Langmuir* **2011**, *27* (10), 6076–6084. <https://doi.org/10.1021/la2006293>.
- (20) Mandler, D.; Kraus-Ophir, S. Self-Assembled Monolayers (SAMs) for Electrochemical Sensing. *J. Solid State Electrochem.* **2011**, *15* (7–8), 1535–1558. <https://doi.org/10.1007/s10008-011-1493-6>.
- (21) Singh, M.; Kaur, N.; Comini, E. The Role of Self-Assembled Monolayers in Electronic Devices. *J. Mater. Chem. C* **2020**, *8* (12), 3938–3955. <https://doi.org/10.1039/d0tc00388c>.
- (22) Howarter, J. A.; Youngblood, J. P. Optimization of Silica Silanization by 3-Aminopropyltriethoxysilane. *Langmuir* **2006**, *22* (26), 11142–11147. <https://doi.org/10.1021/la061240g>.
- (23) Kim, J.; Seidler, P.; Wan, L. S.; Fill, C. Formation, Structure, and Reactivity of Amino-Terminated Organic Films on Silicon Substrates. *J. Colloid Interface Sci.* **2009**, *329* (1), 114–119. <https://doi.org/10.1016/j.jcis.2008.09.031>.
- (24) Liang, Y.; Huang, J.; Zang, P.; Kim, J.; Hu, W. Molecular Layer Deposition of APTES on Silicon Nanowire Biosensors: Surface Characterization, Stability and PH Response. *Appl. Surf. Sci.* **2014**, *322*, 202–208. <https://doi.org/10.1016/j.apsusc.2014.10.097>.
- (25) Acres, R. G.; Ellis, A. V.; Alvino, J.; Lenahan, C. E.; Khodakov, D. A.; Metha, G. F.; Andersson, G. G. Molecular Structure of 3-Aminopropyltriethoxysilane Layers Formed on Silanol-Terminated Silicon Surfaces. *J. Phys. Chem. C* **2012**, *116* (10), 6289–6297. <https://doi.org/10.1021/jp212056s>.
- (26) Bhushan, B.; Kwang, J. K.; Gupta, S.; Lee, S. C. Nanoscale Adhesion, Friction and Wear Studies of Biomolecules on Silane Polymer-Coated Silica and Alumina-Based Surfaces. *J. R. Soc. Interface*

- 2009**, 6 (37), 719–733. <https://doi.org/10.1098/rsif.2008.0398>.
- (27) Aissaoui, N.; Bergaoui, L.; Landoulsi, J.; Lambert, J. F.; Boujday, S. Silane Layers on Silicon Surfaces: Mechanism of Interaction, Stability, and Influence on Protein Adsorption. *Langmuir* **2012**, 28 (1), 656–665. <https://doi.org/10.1021/la2036778>.
- (28) Kim, J.; Seidler, P.; Fill, C.; Wan, L. S. Investigations of the Effect of Curing Conditions on the Structure and Stability of Amino-Functionalized Organic Films on Silicon Substrates by Fourier Transform Infrared Spectroscopy, Ellipsometry, and Fluorescence Microscopy. *Surf. Sci.* **2008**, 602 (21), 3323–3330. <https://doi.org/10.1016/j.susc.2008.09.001>.
- (29) Lyubchenko, Y. L.; Shlyakhtenko, L. S.; Gall, A. A. Atomic Force Microscopy Imaging and Probing of DNA, Proteins, and Protein–DNA Complexes: Silatrane Surface Chemistry. In *DNA-Protein Interactions. Methods in Molecular Biology™ (Methods and Protocols)*; Humana Press, 2009; Vol. 543, pp 337–351. [https://doi.org/10.1007/978-1-60327-015-1\\_21](https://doi.org/10.1007/978-1-60327-015-1_21).
- (30) Puchnin, K.; Grudtsov, V.; Andrianova, M.; Bezzubov, S.; Kuznetsov, A. A Surface Modifier for the Production of Selectively Activated Amino Surface Groups. *Coatings* **2019**, 9 (11), 3–11. <https://doi.org/10.3390/coatings9110726>.
- (31) Puri, J. K.; Singh, R.; Chahala, V. K. Silatranes: A Review on Their Synthesis, Structure, Reactivity and Applications. *Chem. Soc. Rev.* **2011**, 40 (3), 1791–1840. <https://doi.org/10.1039/b925899j>.
- (32) Fakirov, S. *Nano-Size Polymers: Preparation, Properties, Applications*; Springer Nature, 2016. <https://doi.org/10.1007/978-3-319-39715-3>.
- (33) Augello, C.; Liu, H. *Surface Modification of Magnesium by Functional Polymer Coatings for Neural Applications*; Elsevier Ltd, 2015; Vol. 2. <https://doi.org/10.1016/B978-1-78242-078-1.00012-8>.
- (34) Meng, J.; Lau, C. H.; Xue, Y.; Zhang, R.; Cao, B.; Li, P. Compatibilizing Hydrophilic and Hydrophobic Polymers via Spray Coating for Desalination. *J. Mater. Chem. A* **2020**, 8 (17), 8462–8468. <https://doi.org/10.1039/d0ta00871k>.
- (35) Azzaroni, O. Polymer Brushes Here, There, and Everywhere: Recent Advances in Their Practical Applications and Emerging Opportunities in Multiple Research Fields. *J. Polym. Sci. Part A Polym. Chem.* **2012**, 50 (16), 3225–3258. <https://doi.org/10.1002/pola.26119>.
- (36) Borozenko, O.; Ou, C.; Skene, W. G.; Giasson, S. Polystyrene-Block-Poly(Acrylic Acid) Brushes Grafted from Silica Surfaces: PH- and Salt-Dependent Switching Studies. *Polym. Chem.* **2014**, 5 (7), 2242–2252. <https://doi.org/10.1039/c3py01339a>.
- (37) Chimisso, V.; Maffei, V.; Hürlimann, D.; Palivan, C. G.; Meier, W. Self-Assembled Polymeric Membranes and Nanoassemblies on Surfaces : Preparation , Characterization , and Current Applications. *Macromol. Biosci.* **2019**, 1900257. <https://doi.org/10.1002/mabi.201900257>.
- (38) Gungor, E.; Armani, A. M. Photocleavage of Covalently Immobilized Amphiphilic Block Copolymer: From Bilayer to Monolayer. *Macromolecules* **2016**, 49 (16), 5773–5781. <https://doi.org/10.1021/acs.macromol.6b01609>.
- (39) Ma, S.; Zhang, X.; Yu, B.; Zhou, F. Brushing up Functional Materials. *NPG Asia Mater.* **2019**, 11 (1). <https://doi.org/10.1038/s41427-019-0121-2>.
- (40) Gao, H.; Matyjaszewski, K. Synthesis of Molecular Brushes by “Grafting onto” Method: Combination of ATRP and Click Reactions. *J. Am. Chem. Soc.* **2007**, 129 (20), 6633–6639. <https://doi.org/10.1021/ja0711617>.
- (41) Decher, G.; Hong, J.; Gutenberg-universitt, J. Gero Decher\* and Jong-Dal Hong Institut Fur Physikalische Chemie; Johannes Gutenberg-Universitt Welder Weg 11; D-6500 Maim; Fed. Rep. of Germany AbstraG. **1991**, 327, 321–327.
- (42) Decher, G. Fuzzy Nanoassemblies: Toward Layered Polymeric Multicomposites. *Science (80-. )*. **1997**, 277 (5330), 1232–1237. <https://doi.org/10.1126/science.277.5330.1232>.
- (43) Cousin, F.; Chennevière, A. Neutron Reflectivity for Soft Matter. *EPJ Web Conf.* **2018**, 188. <https://doi.org/10.1051/epjconf/201818804001>.
- (44) Félix, O.; Zheng, Z.; Cousin, F.; Decher, G. Are Sprayed LbL-Films Stratified? A First Assessment of

- the Nanostructure of Spray-Assembled Multilayers by Neutron Reflectometry. *Comptes Rendus Chim.* **2009**, *12* (1–2), 225–234. <https://doi.org/10.1016/j.crci.2008.09.009>.
- (45) Devaux, C.; Cousin, F.; Beyou, E.; Chapel, J. P. Low Swelling Capacity of Highly Stretched Polystyrene Brushes. *Macromolecules* **2005**, *38* (10), 4296–4300. <https://doi.org/10.1021/ma047478y>.
- (46) Richardson, J. J.; Cui, J.; Björnmalm, M.; Braunger, J. A.; Ejima, H.; Caruso, F. Innovation in Layer-by-Layer Assembly. *Chem. Rev.* **2016**, *116* (23), 14828–14867. <https://doi.org/10.1021/acs.chemrev.6b00627>.
- (47) Yan, Y.; Björnmalm, M.; Caruso, F. Assembly of Layer-by-Layer Particles and Their Interactions with Biological Systems. *Chem. Mater.* **2014**, *26* (1), 452–460. <https://doi.org/10.1021/cm402126n>.
- (48) Schwarz, B.; Schönhoff, M. Surface Potential Driven Swelling of Polyelectrolyte Multilayers. *Langmuir* **2002**, *18* (8), 2964–2966. <https://doi.org/10.1021/la015636y>.
- (49) Schönhoff, M. Self-Assembled Polyelectrolyte Multilayers. *Curr. Opin. Colloid Interface Sci.* **2003**, *8* (1), 86–95. [https://doi.org/10.1016/S1359-0294\(03\)00003-7](https://doi.org/10.1016/S1359-0294(03)00003-7).
- (50) Zhao, S.; Caruso, F.; Dahne, L.; Decher, G.; De Geest, B. G.; Fan, J.; Feliu, N.; Gogotsi, Y.; Hammond, P. T.; Hersam, M. C.; Khademhosseini, A.; Kotov, N.; Loporatti, S.; Li, Y.; Lisdat, F.; Liz-Marzan, L. M.; Moya, S.; Mulvaney, P.; Rogach, A. L.; Roy, S.; Shchukin, D. G.; Skirtach, A. G.; Stevens, M. M.; Sukhorukov, G. B.; Weiss, P. S.; Yue, Z.; Zhu, D.; Parak, W. J. The Future of Layer-by-Layer Assembly: A Tribute to ACS Nano Associate Editor Helmuth Mohwald. *ACS Nano* **2019**, *13* (6), 6151–6169. <https://doi.org/10.1021/acsnano.9b03326>.
- (51) Feng, H.; Lu, X.; Wang, W.; Kang, N.-G.; Mays, J. Block Copolymers: Synthesis, Self-Assembly, and Applications. *Polymers (Basel)*. **2017**, *9* (10), 494. <https://doi.org/10.3390/polym9100494>.
- (52) Bates, C. M.; Bates, F. S. 50th Anniversary Perspective: Block Polymers-Pure Potential. *Macromolecules* **2017**, *50* (1), 3–22. <https://doi.org/10.1021/acs.macromol.6b02355>.
- (53) Hu, H.; Gopinadhan, M.; Osuji, C. O. Directed Self-Assembly of Block Copolymers: A Tutorial Review of Strategies for Enabling Nanotechnology with Soft Matter. *Soft Matter* **2014**, *10* (22), 3867–3889. <https://doi.org/10.1039/c3sm52607k>.
- (54) Deng, Z.; Liu, S. Emerging Trends in Solution Self-Assembly of Block Copolymers. *Polymer (Guildf)*. **2020**, *207* (August), 122914. <https://doi.org/10.1016/j.polymer.2020.122914>.
- (55) Li, C.; Li, Q.; Kaneti, Y. V.; Hou, D.; Yamauchi, Y.; Mai, Y. Self-Assembly of Block Copolymers towards Mesoporous Materials for Energy Storage and Conversion Systems. *Chem. Soc. Rev.* **2020**, *49* (14), 4681–4736. <https://doi.org/10.1039/d0cs00021c>.
- (56) Tanford, C. The Hydrophobic Effect and the Organization of Living Matter. *Science (80-. )*. **1978**, *200* (4345), 1012–1018. <https://doi.org/10.1126/science.653353>.
- (57) Mai, Y.; Eisenberg, A. Self-Assembly of Block Copolymers. *Chem. Soc. Rev.* **2012**, *41* (18), 5969–5985. <https://doi.org/10.1039/c2cs35115c>.
- (58) Antonietti, M.; Förster, S. Vesicles and Liposomes: A Self-Assembly Principle Beyond Lipids. *Adv. Mater.* **2003**, *15* (16), 1323–1333. <https://doi.org/10.1002/adma.200300010>.
- (59) Holder, S. J.; Sommerdijk, N. A. J. M. New Micellar Morphologies from Amphiphilic Block Copolymers: Disks, Toroids and Bicontinuous Micelles. *Polym. Chem.* **2011**, *2* (5), 1018–1028. <https://doi.org/10.1039/c0py00379d>.
- (60) Blanazs, A.; Madsen, J.; Battaglia, G.; Ryan, A. J.; Armes, S. P. Mechanistic Insights for Block Copolymer Morphologies: How Do Worms Form Vesicles? *J. Am. Chem. Soc.* **2011**, *133* (41), 16581–16587. <https://doi.org/10.1021/ja206301a>.
- (61) Riess, G. Micellization of Block Copolymers. *Prog. Polym. Sci.* **2003**, *28* (7), 1107–1170. [https://doi.org/10.1016/S0079-6700\(03\)00015-7](https://doi.org/10.1016/S0079-6700(03)00015-7).
- (62) Jain, S.; Bates, F. S. Consequences of Nonergodicity in Aqueous Binary PEO-PB Micellar Dispersions. *Macromolecules* **2004**, *37* (4), 1511–1523. <https://doi.org/10.1021/ma035467j>.
- (63) Blanazs, A.; Armes, S. P.; Ryan, A. J. Self-Assembled Block Copolymer Aggregates: From Micelles to

- Vesicles and Their Biological Applications. *Macromol. Rapid Commun.* **2009**, *30* (4–5), 267–277. <https://doi.org/10.1002/marc.200800713>.
- (64) Zhang, L.; Shen, H.; Eisenberg, A. Phase Separation Behavior and Crew-Cut Micelle Formation of Polystyrene-6-Poly(Acrylic Acid) Copolymers in Solutions. *Macromolecules* **1997**, *30* (4), 1001–1011. <https://doi.org/10.1021/ma961413g>.
- (65) Yu, Y.; Zhang, L.; Eisenberg, A. Morphogenic Effect of Solvent on Crew-Cut Aggregates of Amphiphilic Diblock Copolymers. *Macromolecules* **1998**, *31* (4), 1144–1154. <https://doi.org/10.1021/ma971254g>.
- (66) Mandal, J.; Arcifa, A.; Spencer, N. D. Synthesis of Acrylamide-Based Block-Copolymer Brushes under Flow: Monitoring Real-Time Growth and Surface Restructuring upon Drying. *Polym. Chem.* **2020**, *11* (18), 3209–3216. <https://doi.org/10.1039/d0py00219d>.
- (67) Shen, D.; Xu, B.; Huang, X.; Zhuang, Q.; Lin, S. (P: T BA- Co -PPEGMEMA- Co -PDOMA)- g -PPFA Polymer Brushes Synthesized by Sequential RAFT Polymerization and ATRP. *Polym. Chem.* **2018**, *9* (20), 2821–2829. <https://doi.org/10.1039/c8py00470f>.
- (68) Belegriou, S.; Dorn, J.; Kreiter, M.; Kita-Tokarczyk, K.; Sinner, E. K.; Meier, W. Biomimetic Supported Membranes from Amphiphilic Block Copolymers. *Soft Matter* **2010**, *6* (1), 179–186. <https://doi.org/10.1039/b917318h>.
- (69) Kowal, J.; Zhang, X.; Dinu, I. A.; Palivan, C. G.; Meier, W. Planar Biomimetic Membranes Based on Amphiphilic Block Copolymers. *ACS Macro Lett.* **2014**, *3* (1), 59–63. <https://doi.org/10.1021/mz400590c>.
- (70) Belegriou, S.; Menon, S.; Dobrunz, D.; Meier, W. Solid-Supported Polymeric Membranes. *Soft Matter* **2011**, *7* (6), 2202–2210. <https://doi.org/10.1039/c0sm01163k>.
- (71) Draghici, C.; Mikhalevich, V.; Gunkel-Grabole, G.; Kowal, J.; Meier, W.; Palivan, C. G. Biomimetic Planar Polymer Membranes Decorated with Enzymes as Functional Surfaces. *Langmuir* **2018**, *34* (30), 9015–9024. <https://doi.org/10.1021/acs.langmuir.8b00541>.
- (72) Le Meins, J. F.; Sandre, O.; Lecommandoux, S. Recent Trends in the Tuning of Polymersomes' Membrane Properties. *Eur. Phys. J. E* **2011**, *34* (2). <https://doi.org/10.1140/epje/i2011-11014-y>.
- (73) Bermudez, H.; Brannan, A. K.; Hammer, D. A.; Bates, F. S.; Discher, D. E. Molecular Weight Dependence of Polymersome Membrane Structure, Elasticity, and Stability. *Macromolecules* **2002**, *35* (21), 8203–8208. <https://doi.org/10.1021/ma020669l>.
- (74) Aranda-Espinoza, H.; Bermudez, H.; Bates, F. S.; Discher, D. E. Electromechanical Limits of Polymersomes. *Phys. Rev. Lett.* **2001**, *87* (20), 208301-1-208301–208304. <https://doi.org/10.1103/PhysRevLett.87.208301>.
- (75) Belegriou, S.; Dorn, J.; Kreiter, M.; Kita-Tokarczyk, K.; Sinner, E. K.; Meier, W. Biomimetic Supported Membranes from Amphiphilic Block Copolymers. *Soft Matter* **2009**, *6* (1), 179–186. <https://doi.org/10.1039/b917318h>.
- (76) Egli, S.; Schlaad, H.; Bruns, N.; Meier, W. Functionalization of Block Copolymer Vesicle Surfaces. *Polymers (Basel)*. **2011**, *3* (1), 252–280. <https://doi.org/10.3390/polym3010252>.
- (77) Zhang, X.; Fu, W.; Palivan, C. G.; Meier, W. Natural Channel Protein Inserts and Functions in a Completely Artificial, Solid-Supported Bilayer Membrane. *Sci. Rep.* **2013**, *3*, 1–7. <https://doi.org/10.1038/srep02196>.
- (78) Mumtaz Virk, M.; Hofmann, B.; Reimhult, E. Formation and Characteristics of Lipid-Blended Block Copolymer Bilayers on a Solid Support Investigated by Quartz Crystal Microbalance and Atomic Force Microscopy. *Langmuir* **2019**, *35* (3), 739–749. <https://doi.org/10.1021/acs.langmuir.8b03597>.
- (79) Balestri, A.; Chiappisi, L.; Montis, C.; Micciulla, S.; Lonetti, B.; Berti, D. Organized Hybrid Molecular Films from Natural Phospholipids and Synthetic Block Copolymers: A Physicochemical Investigation. *Langmuir* **2020**, *36* (37), 10941–10951. <https://doi.org/10.1021/acs.langmuir.0c01544>.

- (80) Kowal, J.; Wu, D.; Mikhalevich, V.; Palivan, C. G.; Meier, W. Hybrid Polymer-Lipid Films as Platforms for Directed Membrane Protein Insertion. *Langmuir* **2015**, *31* (17), 4868–4877. <https://doi.org/10.1021/acs.langmuir.5b00388>.
- (81) Blodgett, K. B.; Langmuir, I. Built-up Films of Barium Stearate and Their Optical Properties. *Phys. Rev.* **1937**, *51* (11), 964–982. <https://doi.org/10.1103/PhysRev.51.964>.
- (82) Ariga, K.; Yamauchi, Y.; Mori, T.; Hill, J. P. 25th Anniversary Article: What Can Be Done with the Langmuir-Blodgett Method? Recent Developments and Its Critical Role in Materials Science. *Adv. Mater.* **2013**, *25* (45), 6477–6512. <https://doi.org/10.1002/adma.201302283>.
- (83) Wales, D. J.; Kitchen, J. A. Surface-Based Molecular Self-Assembly: Langmuir-Blodgett Films of Amphiphilic Ln(III) Complexes. *Chem. Cent. J.* **2016**, *10* (1), 1–8. <https://doi.org/10.1186/s13065-016-0224-6>.
- (84) Mingeot-Leclercq, M. P.; Deleu, M.; Brasseur, R.; Dufrêne, Y. F. Atomic Force Microscopy of Supported Lipid Bilayers. *Nat. Protoc.* **2008**, *3* (10), 1654–1659. <https://doi.org/10.1038/nprot.2008.149>.
- (85) Reimhult, E.; Kasemo, B.; Höök, F. Rupture Pathway of Phosphatidylcholine Liposomes on Silicon Dioxide. *Int. J. Mol. Sci.* **2009**, *10* (4), 1683–1696. <https://doi.org/10.3390/ijms10041683>.
- (86) Rakhmatullina, E.; Meier, W. Solid-Supported Block Copolymer Membranes through Interfacial Adsorption of Charged Block Copolymer Vesicles. *Langmuir* **2008**, *24* (12), 6254–6261. <https://doi.org/10.1021/la8003068>.
- (87) Dorn, J.; Belegriou, S.; Kreiter, M.; Sinner, E. K.; Meier, W. Planar Block Copolymer Membranes by Vesicle Spreading. *Macromol. Biosci.* **2011**, *11* (4), 514–525. <https://doi.org/10.1002/mabi.201000396>.
- (88) Palivan, C. G.; Goers, R.; Najer, A.; Zhang, X.; Car, A.; Meier, W. Bioinspired Polymer Vesicles and Membranes for Biological and Medical Applications. *Chem. Soc. Rev.* **2016**, *45* (2), 377–411. <https://doi.org/10.1039/c5cs00569h>.
- (89) Sondhi, P.; Lingden, D.; Stine, K. J. Structure, Formation, and Biological Interactions of Supported Lipid Bilayers (SLB) Incorporating Lipopolysaccharide. *Coatings* **2020**, *10* (10), 1–32. <https://doi.org/10.3390/coatings10100981>.
- (90) Ferhan, A. R.; Yoon, B. K.; Park, S.; Sut, T. N.; Chin, H.; Park, J. H.; Jackman, J. A.; Cho, N. J. Solvent-Assisted Preparation of Supported Lipid Bilayers. *Nat. Protoc.* **2019**, *14* (7), 2091–2118. <https://doi.org/10.1038/s41596-019-0174-2>.
- (91) Jackman, J. A.; Cho, N. J. Supported Lipid Bilayer Formation: Beyond Vesicle Fusion. *Langmuir* **2020**, *36* (6), 1387–1400. <https://doi.org/10.1021/acs.langmuir.9b03706>.
- (92) Tabaei, S. R.; Jackman, J. A.; Kim, M.; Yorulmaz, S.; Vafaei, S.; Cho, N. J. Biomembrane Fabrication by the Solvent-Assisted Lipid Bilayer (SALB) Method. *J. Vis. Exp.* **2015**, *2015* (106), 1–12. <https://doi.org/10.3791/53073>.
- (93) Tabaei, S. R.; Choi, J. H.; Haw Zan, G.; Zhdanov, V. P.; Cho, N. J. Solvent-Assisted Lipid Bilayer Formation on Silicon Dioxide and Gold. *Langmuir* **2014**, *30* (34), 10363–10373. <https://doi.org/10.1021/la501534f>.
- (94) Hinrichs, K.; Eichhorn, K. J.; Ertl, G.; Mills, D. L.; Lüth, H. *Ellipsometry of Functional Organic Surfaces and Films*; 2014; Vol. 52. <https://doi.org/10.1007/978-3-642-40128-2>.
- (95) Sauerbrey, G. Use of Quartz Vibration for Weighing Films on a Microbalance. *Zeitschrift für Phys.* **1959**, *155* (2), 206–222. <https://doi.org/10.1007/BF01337937>.
- (96) Di Leone, S.; Vallapurackal, J.; Yorulmaz Avsar, S.; Kyropolou, M.; Ward, T. R.; Palivan, C. G.; Meier, W. Expanding the Potential of the Solvent-Assisted Method to Create Bio-Interfaces from Amphiphilic Block Copolymers. *Biomacromolecules* **2021**, *22* (7), 3005–3016. <https://doi.org/10.1021/acs.biomac.1c00424>.

# 1 **Monolayer formation**



This chapter comprises the study of the first step of the process: the formation of a BC monolayer. In the case of the model BC used in this thesis, polystyrene-*block*-poly (acrylic acid) (PS-*b*-PAA), a pre-functionalization of the surface must be performed in order to provide amine groups at the surface of the silicon wafer to allow the anchoring of the PAA groups through formation of ion pairs ( $-\text{COO}^- \cdots \cdots ^+\text{NH}_3-$ ). To do so, either covalent grafting (chemisorption) of an aminosilane (3-(aminopropyl)triethoxysilane, APTES) or a non-covalent grafting (physisorption) of a weak polyamine (poly(allylamine hydrochloride, PAH) were explored. Following that, the monolayer is formed by BC adsorption in a non-selective solvent, where the BC chains are well solvated and not prone to self-assembly. As the choice of a suitable solvent is a key step, Dynamic Light Scattering (DLS) measurements of BC solutions were performed in different organic solvents. Finally, as the BC solutions were prepared and the substrate pre-functionalized, the anchoring of the PAA blocks with the oxidized silicon substrate was evidenced by Polarization Modulation Infrared Reflection Absorption Spectroscopy (PM-IRRAS), and various complementary surface characterization techniques such as Atomic Force Microscopy (AFM), water contact angle measurements and Quartz Crystal Microbalance with Dissipation (QCM-D) were used to fully characterize the resulting monolayers. A brief discussion of the scaling laws of BCs adsorption in a non-selective solvent is presented along with Neutron Reflectivity (NR) experiments.

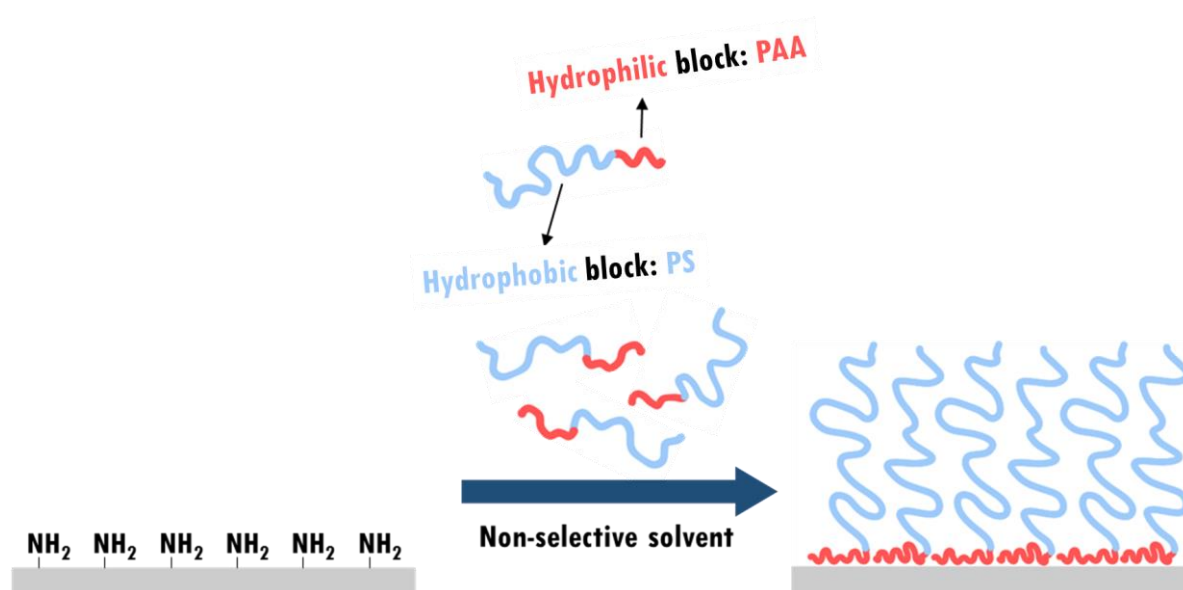


**Figure 1.1.** Illustrative scheme of the monolayer formation by the adsorption of amphiphilic PS-*b*-PAA BCs onto the functionalized surface of a silicon wafer substrate.

# Experimental

## Materials

Single-side polished silicon wafers ( $1 \times 2 \text{ cm}^2$ ) covered with a native silicon oxide ( $\text{SiO}_2$ ) layer were purchased from Silicon Inc. (US). Double-side polished silicon wafers ( $1 \times 2 \text{ cm}^2$ ) covered with a native silicon oxide ( $\text{SiO}_2$ ) layer were purchased from Silicon Inc. (US). Quartz crystal sensors covered with 50 nm  $\text{SiO}_2$  layer were obtained from Biolin Scientific (Sweden). Both substrates were cleaned in absolute ethanol in an ultrasonic bath ( $25^\circ\text{C}$ , 20 min), dried under a flow of  $\text{N}_2$  and exposed to oxygen plasma (50 W, 0.06 mbar, 60 sec) for organic impurities removal and surface hydroxylation. (3-aminopropyl)triethoxysilane (APTES) and poly(allylamine hydrochloride (PAH)  $M_w$  56,000  $\text{g}\cdot\text{mol}^{-1}$ ) were purchased from Sigma-Aldrich. BCs with different compositions and molecular weights ( $\text{PS}_{182}\text{-}b\text{-PAA}_{19}$ ,  $\text{PS}_{394}\text{-}b\text{-PAA}_{58}$  and  $\text{PS}_{677}\text{-}b\text{-PAA}_{180}$ ) were purchased from Polymer Source (Canada) and used as received – it should be noted that the subscript numbers indicate the degree polymerization (DP) of each polymer. N,N-dimethylformamide (DMF, 99.8%) was purchased from Acros Organics and tetrahydrofuran (THF, 99%) was purchased from Sigma-Aldrich and used in a solvent purification system (PureSolv MD) (that is, anhydrous THF with no stabilizers).

## Methodology

### 1.1. Pre-functionalization of silicon wafers and characterization

Aminosilylation with APTES: Cleaned silicon wafers were reacted with a freshly prepared APTES solution at 2 wt.% in anhydrous toluene for 20 min at  $60^\circ\text{C}$ .<sup>1</sup> The substrates were immersed into the aminosilane solution with the help of a Teflon support as shown in **Figure 1.2**. The wafers were rinsed three times with anhydrous toluene to remove excess or physisorbed molecules and dried under nitrogen. The modified substrates were stored in anhydrous toluene to avoid any contamination.

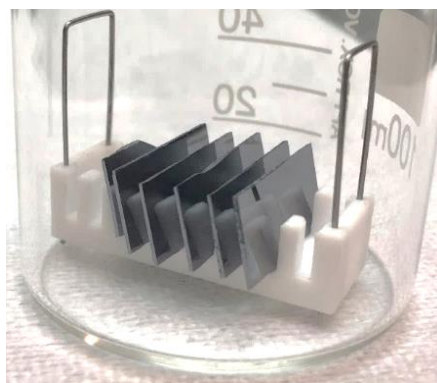


**Figure 1.2.** Illustration of the silicon wafers on the Teflon support used for aminosilylation.

Determination of the absolute surface density of amino groups of APTES films: The method reported elsewhere<sup>2</sup> based on the successive formation and hydrolysis of imine groups was used to quantify the surface bound amino groups of APTES. The only difference is that double-side silicon substrates were used instead of glass slides in order to increase the sensitivity of the titration. Briefly, the double-polished wafers coated with APTES are immersed in a 4-nitrobenzaldehyde alcoholic solution (0.05 wt.%, 0.08 vol.% of acetic acid) for 3 h at 50 °C for imine formation. After the reaction, the substrates were washed with absolute ethanol, sonicated for 2 min and dried under nitrogen. Following that, the imine-formed substrates were immersed in a specific volume of aqueous solution of acetic acid (0.2 vol.%) at 30 °C for 1 h. The absorbance of the produced 4-nitrobenzaldehyde in the hydrolyzed solution was measured by UV-Vis in a 200-500 nm wavelength range. A calibration curve of 4-nitrobenzaldehyde was prepared and used for quantification.

Physiosorption on PAH: The silicon wafers were immersed in an aqueous solution of PAH (0.1%, pH adjusted to 7) at RT for 20 min or 2 h. After that, the substrates were immersed in water at the same pH for 5 min to remove excess of PAH, dried under nitrogen and used immediately afterwards.

## **1.2. Characterization of the APTES or PAH-modified substrates**

Surface topography: AFM images of dry substrates modified with APTES or PAH were acquired in air using a Dimension ICON (Veeco, Bruker) in Tapping Mode at a resolution of 512 x 512 pixels at a scan rate of 1 Hz and analysed with the Nanoscope Analysis software.

Thickness: Ellipsometry was used to determine the thickness of the APTES and PAH layers. The measurements were done using a UVISEL spectroscopic ellipsometer (Horiba Jobin Yvon, France). The data were acquired at three angles of incidence: 65°, 70° and 75° at wavelengths ranging from 260 to 860 nm. Data were fitted to a multi-layer model using the DeltaPsi Horiba built-in program. The thickness of the layers was determined by subtracting of the native oxide layer previously measured on a bare and clean substrate.

Contact angle titration: Advancing contact angles at various pH values were measured for the substrates coated with APTES or PAH with a Tracker tensiometer from Teclis (France) at room temperature. Citrate-phosphate buffer solutions were used. The substrates were placed in a glass chamber previously filled with dodecane and the static contact angle was recorded using the sessile drop method. With the help of a dosing syringe, a droplet of 3  $\mu\text{L}$  of a given solution was deposited on the substrate and the value of advancing contact angle was recorded 30 s after droplet deposition (importantly to note, no significant change was observed on the contact angle during this period). The average value was obtained by measuring two samples in two different positions.

### 1.3. BC monolayer formation

BCs solutions in different solvents: PS<sub>394</sub>-*b*-PAA<sub>58</sub> solutions at various concentrations were prepared by dissolution of the BC in THF, DMF or DMF:THF (80:20, in volume) under stirring for 2 h at room temperature and filtered on a 0.1  $\mu\text{m}$  PTFE membrane before use.

Dynamic Light Scattering (DLS): The hydrodynamic radius ( $R_h$ ) of PS<sub>394</sub>-*b*-PAA<sub>58</sub> solutions prepared in THF, DMF or DMF:THF (80:20, in volume) at concentrations of 7  $\text{g}\cdot\text{L}^{-1}$  were measured by DLS using an ALV goniometer, with a 22 mW linearly polarized laser (632.8 nm HeNe) and an ALV- 5000/EPP multiple tau digital correlator. The DLS autocorrelation functions were obtained at a scattering angle of 90° and a temperature of 25 °C. Each result corresponds to the average of 6 acquisitions of 10 seconds each. The intensity-weighted relaxation time ( $\tau$ ) distributions were extracted from the autocorrelation data using the multi-exponential CONTIN method. The apparent diffusion coefficients ( $D_{\text{app}}$ ) were obtained by considering  $D_{\text{app}} = (1/\tau q^2)$  where  $\tau$  is the mean relaxation time and  $q$  the scattering vector. The hydrodynamic

radii ( $R_H$ ) were determined using the Stokes-Einstein relation,  $R_H = (k_B T) / 6\pi\eta D$  where  $k_B$  is the Boltzmann constant,  $T$  the temperature,  $\eta$  the viscosity of the solvent and  $D$  the diffusion coefficient.

Small-Angle Neutron Scattering (SANS): The  $R_g$  of PS<sub>394</sub>-*b*-PAA<sub>58</sub> solutions prepared in deuterated solvents (THF, DMF or DMF:THF (80:20, in volume)) at concentrations of 20 g.L<sup>-1</sup> were measured on the PAXY spectrometer at the Laboratoire Léon Brillouin (Saclay, France).

Adsorption of the BC monolayer: The pre-functionalized wafers were immersed in a rectangular Teflon trough filled with 8 mL of BC solution in DMF:THF (80:20, v/v) prepared at various concentrations and filtered on 0.1  $\mu$ m PTFE membrane. After 2h, the wafers were rinsed in 10-15 mL DMF:THF (80:20, v/v) to remove excess of BC and gently dried under a nitrogen flow. The samples were characterized immediately after preparation and stored in air on closed vials at room temperature.

## 1.4. Characterization of the BC monolayer

Surface topography & thickness: AFM images of dry monolayers were acquired in similar conditions as previously described. AFM images of swollen monolayers were performed with the dry monolayer previously incubated with toluene droplets inside a closed Petri dish for 5 min and analysed immediately after.

Contact angle measurements: Advancing and receding water contact angles ( $\theta_{adv}$ ,  $\theta_{rec}$ ) were measured with a Tracker tensiometer from Teclis (France) at room temperature. The static contact angle was recorded using the sessile drop method at room temperature. With the help of a dosing syringe, a droplet of 3  $\mu$ L of water (pH 7) was deposited on the substrate and the value of advancing contact angle was recorded at 30 s after the droplet was set. The average value was obtained by measuring the two samples in two different positions. The natural receding contact angles were determined by monitoring the evaporation of the sessile drop with time: a contact angle initially set in the advancing mode ( $\theta_A$ ) decreases linearly with time when the liquid starts to evaporate. When the water droplet is not pinned anymore, it then recedes at a constant angle ( $\theta_R$ ) marked by the presence of a visible plateau.<sup>3,4</sup>

Adsorption of the BC monolayer: A QCM-D set-up (Q-Sense E4 instrument, Biolin Scientific, Sweden) with home-made amino-modified quartz crystal sensors (either with APTES or PAH) was used to monitor the adsorption isotherm of the PS-*b*-PAA copolymers in good solvent conditions. The QCM sensors are quartz crystals in which metal electrodes (typically gold) are directly patterned onto the top and bottom faces, as showed in **Figure 1.3**.

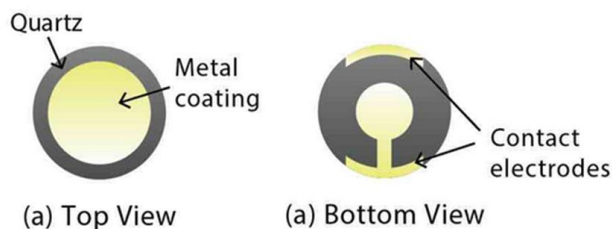


**Figure 1.3.** Schematic illustration of top and bottom views of a quartz crystal (gray) with gold electrodes (yellow). The image is reprinted from ref. 5.

The adsorption of polymer chains on a sensor can be precisely monitored by measuring the decrease in the resonance frequency  $F_n$  for each odd overtone. If the adsorbed mass is forming a rigid homogeneous lossless film, the relation between frequency change  $\Delta F_n$  and the areal mass increment  $\Delta m$  is linear, as found by Sauerbrey<sup>6</sup> (**Eq. 1**):

$$\frac{\Delta F_n}{n} = - \frac{2F_0^2}{\sqrt{\rho_q \mu_q}} \cdot \Delta m \quad \text{Eq.1}$$

where  $F_0$  is the resonant frequency of the crystal (5 MHz),  $\rho_q$  ( $2.648 \text{ g.cm}^{-3}$ ) the quartz density and  $\mu_q$  ( $2.947 \times 10^{11} \text{ g.cm}^{-1} \text{ s}^{-2}$ ) the shear modulus. The original silicon tubing of the QCM setup was replaced by Teflon-based because they offered a better resistance in THF and DMF solvents (no swelling). The solutions were injected using a push/pull style syringe pump. A flow rate of  $150 \mu\text{L.min}^{-1}$  was used for each BC injection and solvent rinsing. After the injection of the BC at a given concentration, the real time monitoring was conducted until no significant differences in frequency were observed. As a result, the waiting time between consecutive injections of BCs solutions with different concentrations is not fixed and depends on the time required to reach this plateau.

Polarization Modulation Infrared Reflection Absorption Spectroscopy (PM-IRRAS): The PM-IRRAS measurements were performed by Thierry Buffeteau at the Institute of Molecular

Sciences (L'Institut des Sciences Moléculaires – ISM). PS<sub>394</sub>-*b*-PAA<sub>57</sub> monolayers were prepared onto SiO<sub>2</sub>/Au substrates (2.5 x 2.5 cm<sup>2</sup>) similarly to the protocol described for the monolayer formation onto silicon wafers. Solutions of PS<sub>394</sub>-*b*-PAA<sub>57</sub> (2 wt.% in THF), PAA<sub>28</sub> (2 wt.% in EtOH:THF (90:10)) and PAA-Na<sub>28</sub> (2 wt.% in water) were spin-coated by depositing 200 μL of solution onto the SiO<sub>2</sub>/Au substrates at 3000 rpm for a total spinning time of 60 s. The spin-coated samples were then dried at 95 °C under vacuum overnight.

The PM-IRRAS spectra were recorded on a ThermoNicolet Nexus 670 FTIR spectrometer at a resolution of 4 cm<sup>-1</sup>, by co-adding several blocks of 1500 scans (30 min acquisition time). Generally, eight blocks (4 h acquisition time) were necessary to obtain PM-IRRAS spectra of ultrathin films or SAMs with good signal-to-noise ratios. Experiments were performed at an incidence angle of 75° using an external homemade goniometer reflection attachment.<sup>7</sup> As shown in **Figure 1.4**, the infrared parallel beam (modulated in intensity at frequency  $f_i$  lower than 5 KHz) was directed out of the spectrometer with an optional flipper mirror and made slightly convergent with a first BaF<sub>2</sub> lens (191 mm focal length). The IR beam passed through a BaF<sub>2</sub> wire grid polarizer (Specac) to select the p-polarized radiation and a ZnSe photoelastic modulator (PEM, Hinds Instruments, type III). The PEM modulated the polarization of the beam at a high fixed frequency,  $2f_m=100$  KHz, between the parallel and perpendicular linear states. After reflection on the sample, the double modulated (in intensity and in polarization) infrared beam was focused with a second ZnSe lens (38.1 mm focal length) onto a photovoltaic MCT detector (Kolmar Technologies, Model KV104) cooled at 77 K. The polarization modulated signal  $I_{AC}$  was separated from the low frequency signal  $I_{DC}$  ( $f_i$  between 500 and 5000 Hz) with a 40 KHz high pass filter and then demodulated with a lock-in amplifier (Stanford Model SR 830). The output time constant was set to 1 ms. The two interferograms were high-pass and low-pass filtered (Stanford Model SR 650) and simultaneously sampled in the dual channel electronics of the spectrometer. In all experiments, the PEM was adjusted for a maximum efficiency at 2500 cm<sup>-1</sup> to cover the mid-IR range in only one spectrum. For calibration measurements, a second linear polarizer (oriented parallel or perpendicular to the first preceding the PEM) was inserted between the sample and the second ZnSe lens. This procedure was used to calibrate and convert the PM-IRRAS signal in terms of the IRRAS signal (*i.e.*  $1 - (R_p(d)/R_p(0))$ , where  $R_p(d)$  and  $R_p(0)$  stand for the p-polarized reflectance of the film/substrate and bare substrate systems, respectively).<sup>8,9</sup>

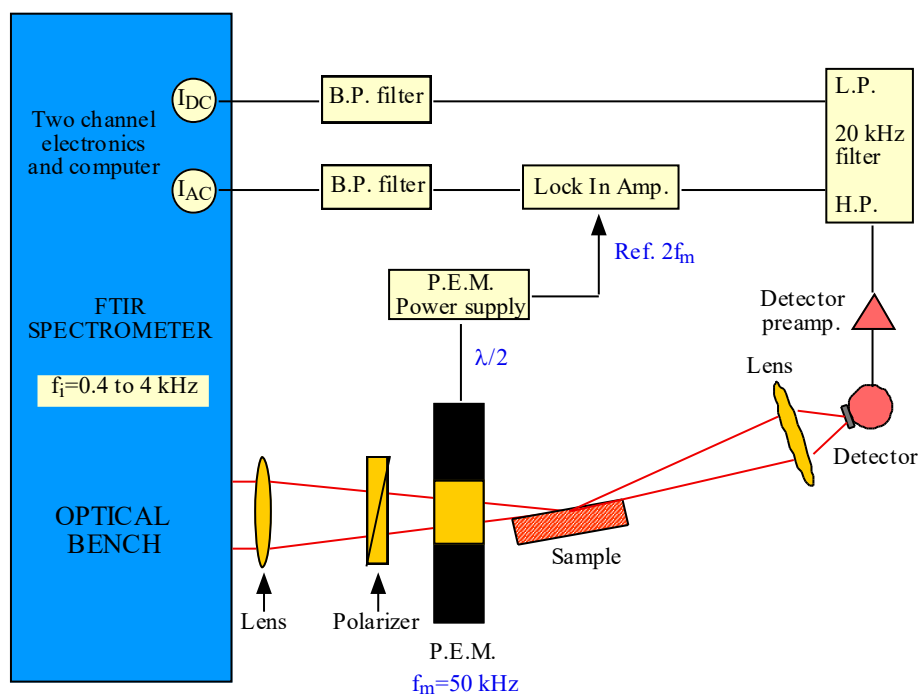


**Figure 1.4.** Schematic diagram of PM-IRRAS optical setup.

**Neutron Reflectivity (NR):** NR measurements were performed on the HERMES time-of-flight reflectometer at the Laboratoire Léon Brillouin (LLB) in CEA-Saclay. Two geometries were used. In the first one the silicon/air interface was probed with a  $q$ -range varying from 0.008 to 0.07  $\text{\AA}^{-1}$ . In the second one, the silicon/deuterated toluene interface was probed (the neutron getting through the sample) with a  $q$ -range varying from 0.01 to 0.08  $\text{\AA}^{-1}$ . A specific home-made cell was used to perform the experiments in d-THF. During the experiment, we use all the wavelengths provided by the neutron source from 3  $\text{\AA}$  to 25  $\text{\AA}$  with a constant DI of 0.3  $\text{\AA}$ . We use for the silicon/air interface  $q = 0.93^\circ$  and for the silicon/deuterated THF  $q = 1.23^\circ$  with a  $\Delta q$  of 0.05 $^\circ$ . The experimental resolution is taken into account in the fitting procedure using the MotoFit software package. We have considered a multilayer model consisting of silicon, silicon oxide and a polystyrene brush, which each layer (slab) is characterized by the scattering length density (SLD), thickness and roughness. When solvent was present, it was equally taken into account.

## Results and discussion

### 1.1. Pre-functionalization of the silicon wafer surface

Polymer solutions close to interfaces may behave in two opposite ways, by either increasing the concentration close to the interfacial region (adsorption) or decreasing it (depletion). If the free energy difference between the polymer-surface and solvent-surface contacts is negative enough, adsorption will take place.<sup>10</sup> Currently, there are many different procedures for the modification of surfaces to generate or improve immobilization/adsorption. In this work, the model chosen was poly(styrene)-*block*-poly(acrylic acid) copolymers containing relatively short PAA blocks and large PS blocks (PS<sub>394</sub>-*b*-PAA<sub>58</sub>). The choice of this asymmetry between the blocks, which will be detailed further on, allows the formation of a BC monolayer in which the adsorption is limited by the saturation of the surface with the anchoring blocks, *i.e.*, PAA. In order to provide specific interactions and trigger the adsorption/anchoring of the PAA blocks onto the substrate, a pre-functionalizing step was performed onto the silicon wafers to modify them with primary amino groups, either through covalent grafting of 3-(aminopropyl)triethoxysilane (APTES) or non-covalent grafting of polyallylamine hydrochloride (PAH) weak polyamine (**Figure 1.5**).

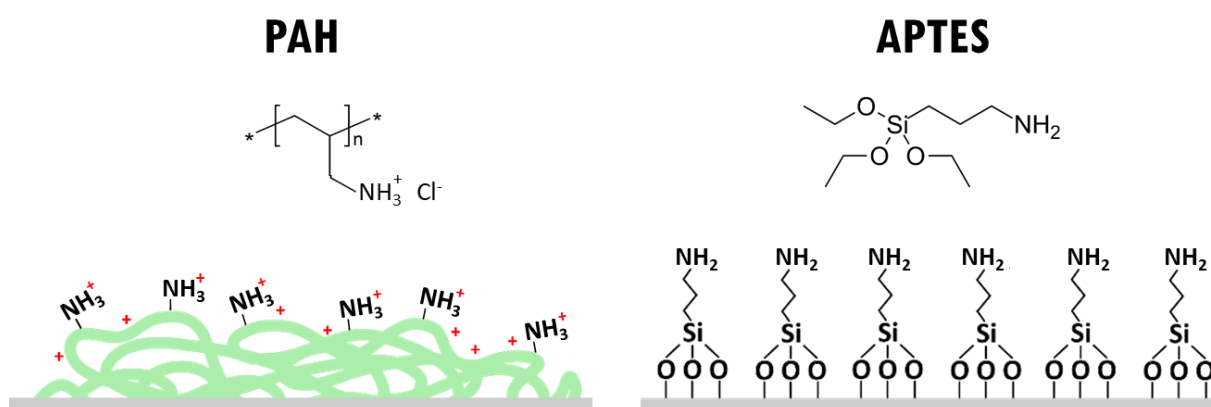


**Figure 1.5.** Schematic illustration of the two methods used to impart the substrate with amino groups: PAH, a weak polycation physisorbed onto the substrate (left) or APTES, an aminosilane covalently attached to the substrate (right).

Popularly used as coupling agents for modifying hydroxylated glass or silicon wafers, organosilanes, particularly APTES, have been widely used to generate self-assembled monolayers (SAMs) onto surfaces for years due to its simplistic structure and low cost<sup>11</sup>. However, the silane grafting mechanism is far from being simple, and, indeed, the overall control and reproducibility of the grafting reaction remains a big challenge mainly because the processes strongly depend on the hydration state, as explained in details in the subsection SAMs at State-of-the-art chapter.<sup>12,13</sup> On the other hand, PAH is a water-soluble weak polybase, widely used for the development of multilayer thin films by the well-known layer-by-layer method (LbL) that only involves adsorption from aqueous solutions.<sup>14,15</sup>

As it can be observed from the AFM measured roughness values shown in **Figure 1.6** the substrate prepared with APTES are much smoother surfaces than those prepared by PAH adsorption. Indeed, while the APTES coating reflects (ideally) the formation of a single monolayer of small molecules, the adsorption of PAH which involves the deposition of long polyelectrolyte chains does not imply the complete adsorption of the all chain segments with the substrate. Even though polymer chains will completely adsorb, the steric interaction between adsorbed chains hinder a full coverage of the surface.

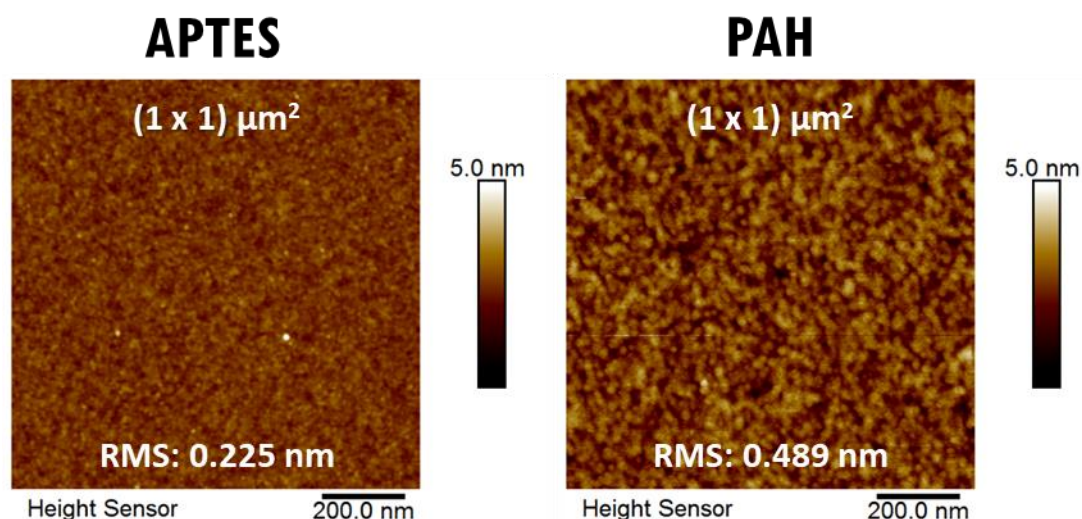


**Figure 1.6.** AFM images of APTES and PAH modified silicon substrates. The values indicated on the figures represent the scan area (top) and the surface roughness (Root Mean Square, RMS), which is defined as the square root of the distribution of surface height.

In fact, when analysing both samples by ellipsometry, while an average thickness of  $(1.0 \pm 0.1)$  nm was found for APTES, thickness values for the PAH layer fluctuated significantly,

from 0.3 to 1 nm. Since ellipsometry is a model-dependent technique, when the roughness of the substrate is important it has to be taken in consideration when drawing a convenient model for the data treatment. As in the case of APTES, the low roughness of the samples allows the modelling using a dense thin layer and the results are in line with the expected theoretical thickness of a single APTES layer (0.7-0.8 nm).<sup>16</sup> On the other hand, since PAH layers are rougher, the model of a thin, dense layer is not the ideal, and an appropriate model containing voids should be used to correctly estimate the thickness of the layer.

In addition to the differences observed by AFM and ellipsometry, the contact angle titration using different pH values resulted in different variations for APTES or PAH covered substrates, as shown in **Figure 1.7**.

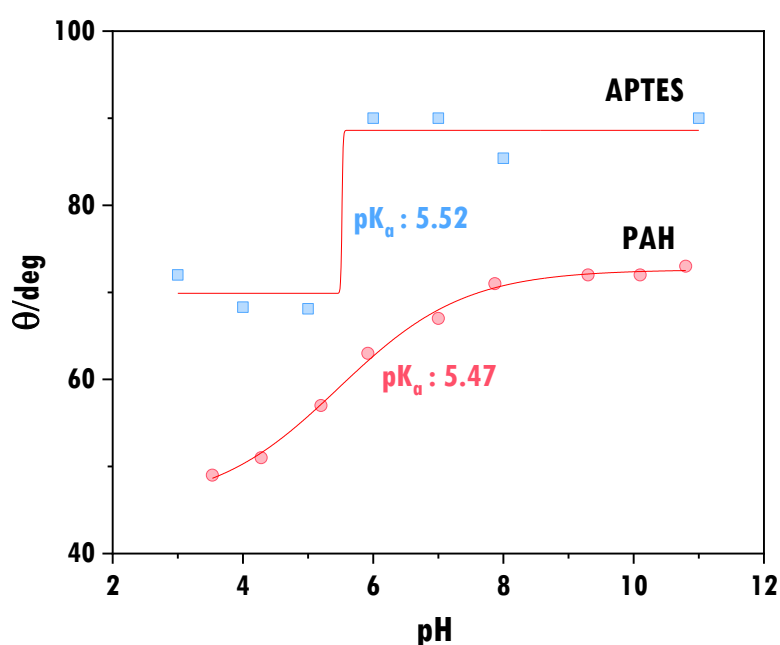


**Figure 1.7.** Surface titration of APTES and PAH covered substrates. The  $pK_a$  values shown were calculated using a sigmoidal fit.

The titration curve reflects the change of the amino-functionalized surface from a charged ( $-NH_3^+$ ) to a neutral ( $-NH_2$ ) situation (below and after the  $pK_a$  value, respectively). For both APTES and PAH, the calculated  $pK_a$  values are quite similar and much lower than the one observed for amino groups in solution ( $pK_a \approx 10$ ), which is explained by the rather hydrophobic environment of the amino groups at the surface.<sup>17</sup> However, the titration curve observed with APTES is shifted to higher water contact values than that observed for PAH, which could be an indication of a surface with lower amino density, even though AFM imaged showed the

formation of a more homogeneous coating with APTES than with PAH (**Figure 1.6**). We can also note that the variation of contact angles with pH is much more gradual for the PAH surface. This difference is linked to the monobasic behaviour of APTES in contrast to the polybasic behaviour of PAH (the  $pK_a$  of polyamine is not constant, rather it depends on its degree of ionization).

Using the method described by J. W. Park and co-workers, the quantification of surface bound amino groups bound to the APTES surface was achieved by successive formation and hydrolysis of imine groups using 4-nitrobenzaldehyde.<sup>2</sup> The absorbance of the produced 4-nitrobenzaldehyde in the hydrolyzed solution is shown in **Figure 1.8**, along with a calibration curve which allowed its quantification.<sup>2</sup>

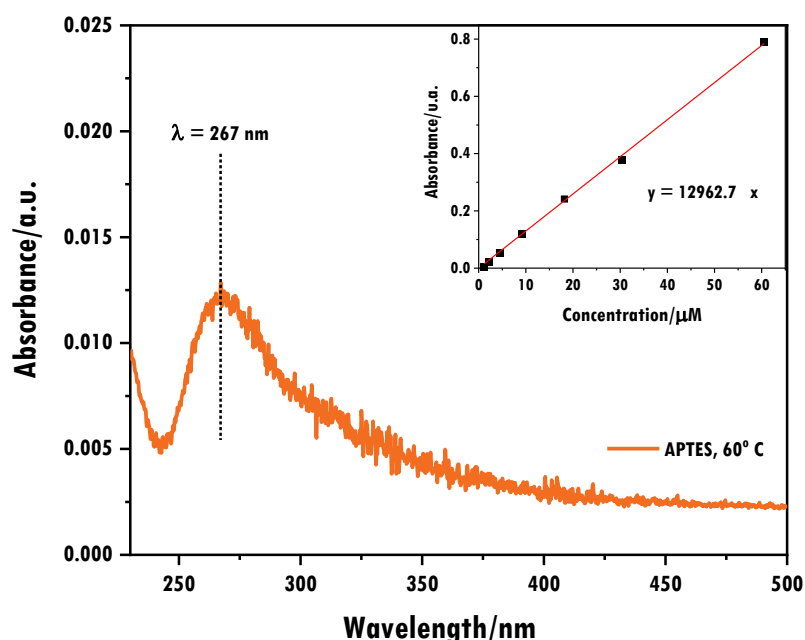


**Figure 1.8.** UV-Vis absorbance spectrum of the hydrolysed solution prepared from APTES covered substrates. Inset plot: Calibration curve of 4-nitrobenzaldehyde obtained by fitting a linear equation to the observed data.

By using this titration approach, an amine surface density of 4 APTES molecules per  $100 \text{ \AA}^2$  (*i.e.*, one APTES molecule occupying  $25 \text{ \AA}^2$ ) was found which is in line with the occupation of a single imine molecule, *c.a.*  $20 \text{ \AA}^2$ .<sup>2</sup> A higher value would reflect a rougher surface with not one but several layers of APTES. The amine surface density for PAH is not available for comparison as the use of the polyamine for the pre-functionalization of the surface was only introduced in the later stages of the thesis work after numerous problems faced with the APTES functionalization, notably the lack of humidity control during the

synthesis (the weather, much or less dry, highly influenced the APTES polymerization in the bulk giving rise to non-controlled grafted multilayers). In any case, taking into account the rougher surface seen by AFM and the lower contact values at the titration curve, PAH-coated substrate should have a higher density of amino groups. This assumption does not necessarily imply that the number of BC molecules, which will subsequently be adsorbed, will be higher for PAH-coated substrates compared to APTES, as the amino groups accessible using the titration might not be accessible to the macromolecules. Indeed, by performing adsorption isotherms using the model BC  $PS_{394}\text{-}b\text{-}PAA_{58}$ , similar adsorbed amounts were retrieved onto sensors prepared with APTES and/or PAH coatings. The adsorption isotherms, shown in **Figure 1.9**, will be studied in details further on. At this time, it can be observed that the maximum BC adsorbed amount (obtained after curve fitting) from APTES or PAH (11.6 and 13.7 mg per  $m^2$ , respectively) results in nearly similar BC grafting densities (0.15 and 0.18 chain per  $nm^2$  for APTES and PAH modified substrates, respectively). A slightly higher grafting density for PAH could come from an assumed higher density of amino groups at the surface. The small observed difference between the two treatments suggests however that both approaches can be used to pre-functionalize the substrates, resulting in no difference in BC adsorption.

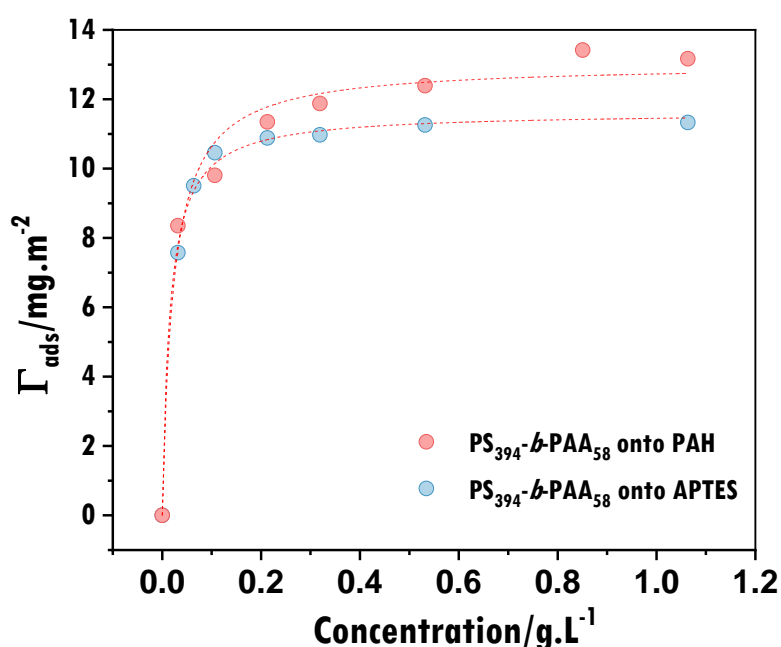


**Figure 1.9.** Adsorption isotherms of  $PS_{394}\text{-}b\text{-}PAA_{58}$  onto APTES and PAH modified QCM quartz sensors. The data were fitted with a Langmuir adsorption model, which will be described in detail later.

In conclusion, rather simple and as effective as APTES for our surface modification purpose, PAH was chosen as the best candidate. Beyond a much simpler and cleaner functionalization process with PAH, this layer is only physisorbed unlike chemisorbed APTES (siloxane bonds). Knowing that these bonds can be easily hydrolysed in the presence of water, it is anticipated that films prepared with PAH will have better stability in aqueous media.<sup>12</sup> In any case, mostly of the data of this thesis was obtained from APTES coatings, as previously explained.

## 1.2. Monolayer formation

### 1.2.1 Choice of the non-selective solvent

The choice of a suitable solvent for dissolving a BC is an essential and yet difficult task that might influence not only the conformation of the BC in the bulk solution but also the aggregate core dimension once the selective solvent is added, for instance, as demonstrated by Eisenberg and co-workers.<sup>18</sup> They observed that the amount of solvent in the core of a BC aggregate during micellization is related to the thermodynamics of the interaction between the solvent and the core-forming block, that is, the stronger the interaction, the more solvent is in the core.

The interactions between polymer and solvent are reflected by the Flory-Huggins parameter,  $\chi$ , which is related to the solubility parameter ( $\delta$ ):

$$\chi = \frac{V_1}{RT} (\delta_1 - \delta_2)^2 \quad \text{Eq. 2}$$

where  $V_1$  is the liquid molar volume of the solvent and  $\delta_1$  and  $\delta_2$  are the solubility parameters of the solvent and polymer, respectively.<sup>19</sup> Specifically, the Hansen solubility parameters (HSP,  $\delta$ ), introduced by Charles M. Hansen in his PhD thesis, can be used to study and predict the dissolution of materials.<sup>20</sup> The solubility/miscibility of two substances is based on the “like-dissolves-like” rule, that is, if the HSP of the substance 1 is close to the one of substance 2, they are likely to dissolve. The HSP of a compound ( $\delta_0$ ), however, results from the contribution of three partial solubility parameters,  $\delta_D$ ,  $\delta_P$ , and  $\delta_H$ , related to dispersion, polar and hydrogen-bonding, respectively ( $\delta_0^2 = \delta_D^2 + \delta_P^2 + \delta_H^2$ ).<sup>21</sup> Typically, DMF and THF have been used to

prepare PS-*b*-PAA solutions. **Table 1.1** illustrates some of the parameters for polystyrene and polyacrylic acid and selected solvents.

**Table 1.1.** Total Hansen Solubility Parameter (HSP) and partial solubility parameters ( $\delta_D$ ,  $\delta_P$ , and  $\delta_H$ ) for polystyrene, acrylic acid, THF and DMF.

	$\delta_d$	$\delta_p$	$\delta_h$	$\delta_0$ (MPa <sup>1/2</sup> )
<b>Polystyrene</b>	18.5	4.5	2.9	19.3
<b>Polyacrylic acid<sup>a</sup></b>	17.7	6.4	14.9	24.0
<b>THF</b>	16.8	5.7	8.0	19.5
<b>DMF</b>	17.4	13.7	11.3	24.9

<sup>a</sup> values for the acrylic acid monomer (for PAA,  $\delta_0 = 23.4$  MPa<sup>1/2</sup> but  $\delta_D$ ,  $\delta_P$ , and  $\delta_H$  values were not found in literature)

For non-polar PS chains, THF is the best candidate with the closest HSP values. On the other hand, since PAA is polar, the strength of the PAA-solvent interaction (*i.e.*, the best solvent for PAA) should be related to the polarity of the solvent. Most importantly, the possibility of making hydrogen bonds in the PAA is a key factor for choosing a suitable solvent. As it can be observed by the  $\delta_h$  values, DMF is the one that with closest values. However, since the compound is a BC, it is necessary to find a suitable solvent or mixtures to be a good (non-selective) solvent for both blocks. Dynamic Light Scattering (DLS) and Small-Angle Neutron Scattering (SANS) (**Appendix, Figure A1, Figure A2**) were used to access the solubility of the BC in different solvent conditions, *i.e.*, pure DMF, pure THF and a mixture of DMF and THF with the results shown in **Table 1.2**.

**Table 1.2.**  $R_g$  and  $R_h$  values of PS<sub>394</sub>-*b*-PAA<sub>58</sub> in different solvents with respective  $R_g/R_h$  ratio.

	$R_g$ /nm <sup>a</sup>	$R_h$ /nm <sup>b</sup>	$R_g/R_h$
<b>DMF</b>	3.6	3.84	0.93
<b>DMF:THF (80:20)</b>	5.1	4.18	1.22
<b>THF</b>	9.1	5.38	1.69

<sup>a</sup> determined by SANS. <sup>b</sup> determined by DLS.

BC contains 87% PS monomers and 13% PAA monomers. Not surprisingly, BC is well soluble in THF with a value of  $R_g/R_h$  ratio higher than 1.5 which is expected for a random coil

in good solvent conditions.<sup>22</sup> Conversely, in DMF, the BC adopts a collapsed structure with a globular conformation ( $R_g/R_h \approx 0.80$ ), which is not a surprising since DMF is good solvent for PAA only (for 13% of the BC composition). In the DMF:THF mixture (80:20, by volume), an intermediate solubility is found, between a collapsed structure and a random coil in theta conditions ( $R_g/R_h = 1.50$ ).<sup>22</sup> In choosing a suitable solvent, not only BC solubility, but also other key characteristics of the assembly process must be considered. THF is indeed a very volatile solvent. On an industrial scale, this could be a big problem with the evaporation of the solvent during the self-assembly process (to be presented later). On the other hand, THF is also relatively hygroscopic which may impact the assembly of the bilayer triggered by a controlled addition of water (to be presented in the next chapter). In summary, the choice of the DMF:THF mixture (80:20, by volume) is based on a compromise between thermodynamic characteristics (relative solubility) and processing constraints (non-volatile and non-hygroscopic solvent).

### 1.2.2. Evidence of the interaction of PS-*b*-PAA copolymers with the aminated surface

The carboxylic groups (-COOH) groups present on the PAA blocks can strongly interact with the amino groups now present at the surface through acid-base interactions generating ion pairs ( $-\text{COO}^- \cdots \text{}^+\text{NH}_3-$ ). In an organic solution, this interaction was easily evidenced by Honggang Cui and co-workers with PAA and a diamine in THF using FTIR (**Figure 1.10**).<sup>23</sup> As noted in **Figure 1.10** (left), the peaks at 1701 and 1560  $\text{cm}^{-1}$  are associated with the C=O stretching of the uncharged form of the carboxylic acid groups and the asymmetric stretching of deprotonated carboxylate groups, respectively. PAA alone remains in its uncharged form until the addition of diamine, which promotes the deprotonation of the carboxylic groups as seen by the large increase in the absorption peak related to the carboxylate groups (**Figure 1.10**, right). When sufficient diamine is present, PAA becomes fully deprotonated as a result of the acid-base reaction between carboxylic acid and amine groups leading to the formation of ion pairs.

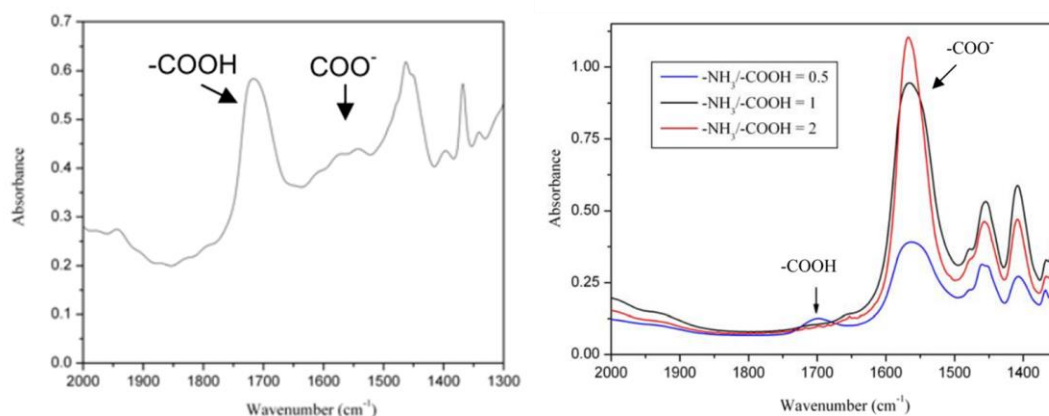


**Figure 1.10.** FTIR absorbance spectra of PAA in a mixture of THF:H<sub>2</sub>O (60:40) (left) and PAA + diamine mixtures in THF:H<sub>2</sub>O (60:40) with amine-to-acid ratios of 0.5, 1 and 2 (right). The images are reprinted from ref. 23.

In the case of solid-supported BC monolayers, this interaction was evidenced using PM-IRRAS spectroscopy (**Figure 1.11**). Similar to the results described above, the presence of a strong band at 1560 cm<sup>-1</sup> corresponds to the asymmetric stretching of COO<sup>-</sup> groups, which evidences the formation of the acid-base reaction. Comparing the relative intensities of this peak with that at 1720 cm<sup>-1</sup> relating to the uncharged form of the carboxylic acid groups, it can be seen that 57.5% of the acrylic acids deprotonate upon interaction with the amines, i.e. more than half of the available acid groups.

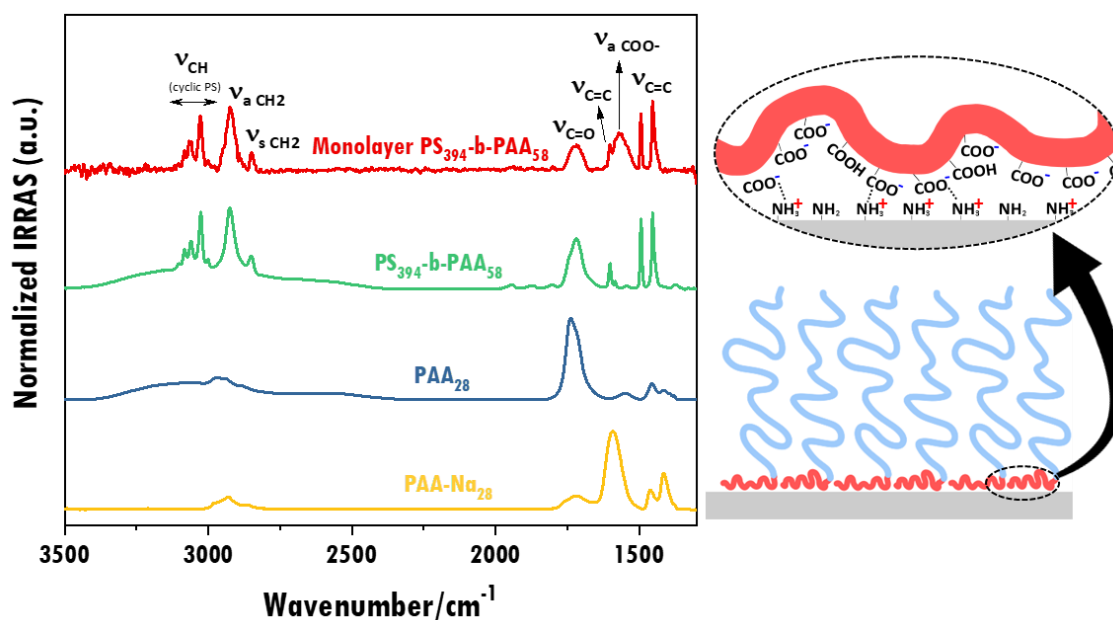


**Figure 1.11.** IRRAS spectra of the PS<sub>394</sub>-b-PAA<sub>58</sub> adsorbed monolayer together with spin-coated PS<sub>394</sub>-b-PAA<sub>58</sub>, PAA<sub>28</sub> (acid form) and (PAA-Na)<sub>28</sub> (left). A schematic representation of acid-base interaction between the COOH groups of the PAA chains and the surface NH<sub>2</sub> is proposed (right).

As controls, spin-coated films on bare silicon wafers (i.e. without amine groups) of PS<sub>394</sub>-*b*-PAA<sub>58</sub>, poly(acrylic acid) and sodium polyacrylate were also analysed. The peaks at 1739 and 1592 cm<sup>-1</sup> observed on poly(acrylic acid) and sodium polyacrylate, respectively, are associated with the C=O stretching of the uncharged form of the carboxylic acid groups and the asymmetric stretching of COO<sup>-</sup> groups, as expected. In the case of the spin-coated PS<sub>394</sub>-*b*-PAA<sub>58</sub> film, it can be observed that only the peak at 1721 cm<sup>-1</sup> related to the uncharged form of PAA is present, well in line with the results of bulk PAA.<sup>23</sup>

### 1.2.3. Characterization of the adsorbed PS-*b*-PAA monolayer

In an adsorbed BC monolayer, the blocks are oriented in a so-called “anchor-and-buoy” conformation, that is, one of the blocks (anchor) is preferentially adsorbed, while the other one (buoy), with lower adsorption affinity, is excluded from the surface and then forms a brush-like structure (**Figure 1.12**). When using PS-*b*-PAA block copolymers and amino-modified substrates, as demonstrated by PM-IRRAS, the formation of the strong ionic pairs (-COO<sup>-</sup>.....<sup>+</sup>NH<sub>3</sub>) is responsible for the adsorption of the PAA block, while the PS acts as the non-adsorbing block. Indeed, PS is known not to adsorb onto silica under similar solvent conditions<sup>24</sup>.

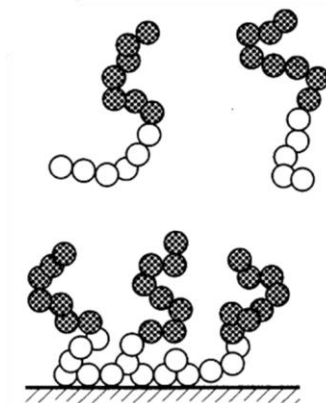


**Figure 1.12.** Schematic representation of the conformation of a BC in a non-selective solvent on a surface. The white dots represent the adsorbing block (anchor) while the dark dots represent the non-adsorbing block (buoy). The image is reproduced from ref. 10.

For the study of BC monolayer formation, three BC different compositions were used: PS<sub>182</sub>-*b*-PAA<sub>19</sub>, PS<sub>394</sub>-*b*-PAA<sub>58</sub> and PS<sub>677</sub>-*b*-PAA<sub>180</sub>. As explained previously, the indices refer to the DP of each block. In order to access the wettability of the monolayers, water contact angles were measured in air and the results are shown in **Table 1.3**. The advancing contact

angle values close to 70° for all the monolayers indicate a relative weak hydrophobic character compared to that expected for bulk polystyrene ( $\theta_A \approx 88^\circ$ ).<sup>25</sup> In addition, the high contact angle hysteresis ( $\Delta\theta \sim 30^\circ$ ) measured points to physical and/or chemical heterogeneity of the monolayer.

**Table 1.3.** Water contact angle values for the dried monolayers.

	$\theta_A/\text{degree}$	$\theta_R/\text{degree}$	$\Delta\theta/\text{degree}$
<b>PS<sub>182</sub>-<i>b</i>-PAA<sub>19</sub></b>	67 ± 1	43 ± 3	25 ± 2
<b>PS<sub>394</sub>-<i>b</i>-PAA<sub>58</sub></b>	66.05 ± 0.07	33 ± 1	33 ± 1
<b>PS<sub>677</sub>-<i>b</i>-PAA<sub>180</sub></b>	68 ± 3	39 ± 1	29 ± 4

The BC adsorption as a monolayer is nothing but a “grafting to” approach resulting on the formation of a polymer brush. This grafting method is known to lead to low grafting densities due to the high steric hindrance of the polymer chains that were already attached to the substrate. This explains the relative weak hydrophobic character of the monolayers: when measuring contact angles, water does not only access the PS but also the uncoated substrate, containing amino groups (hydrophilic). The high hysteresis value is also consistent with this statement, since the low-density coverage is directly related to the surface heterogeneity. The low grafting density of the BC monolayer is clearly visible at the dry state by AFM, as shown in **Figure 1.13** (top).

The presence of a two-dimensional periodic pattern of islet structures, previously evidenced for the adsorption of PS-*b*-P2VP on mica,<sup>26</sup> is a result of the dewetting of the PS blocks on the adsorbed PAA layer during the crossing of the substrate at the liquid-air interface as a consequence of the chemical incompatibility between PS and PAA blocks. This phenomenon can only take place if there is room for it, *i.e.*, if the surface is not very dense. However, when the BC monolayer is exposed to toluene vapor, which is a good solvent for PS, the clusters are no longer discernible as the chains swell and a smooth surface appears (**Figure 1.13**, bottom). The same behavior is observed for the other BC molecular weights (**Figure 1.14**).

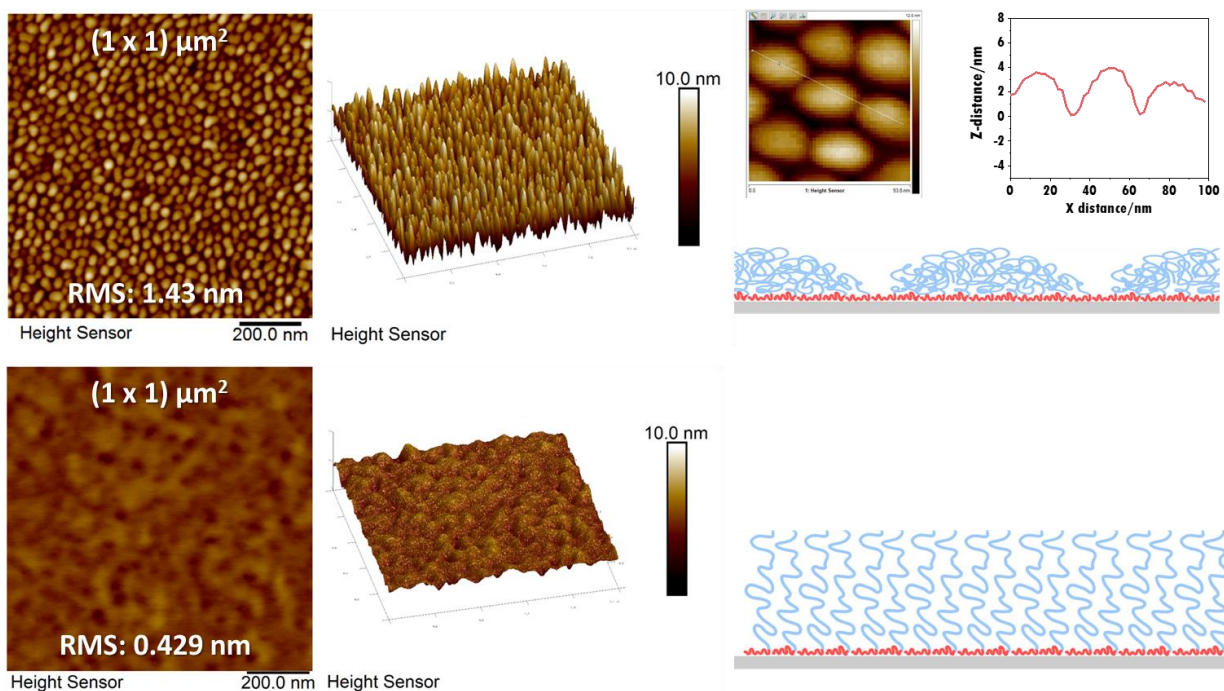


**Figure 1.13.** AFM images and schematic representation of the monolayer of PS<sub>394</sub>-b-PAA<sub>58</sub> in the dry state (top) and in a saturated atmosphere of toluene (bottom).

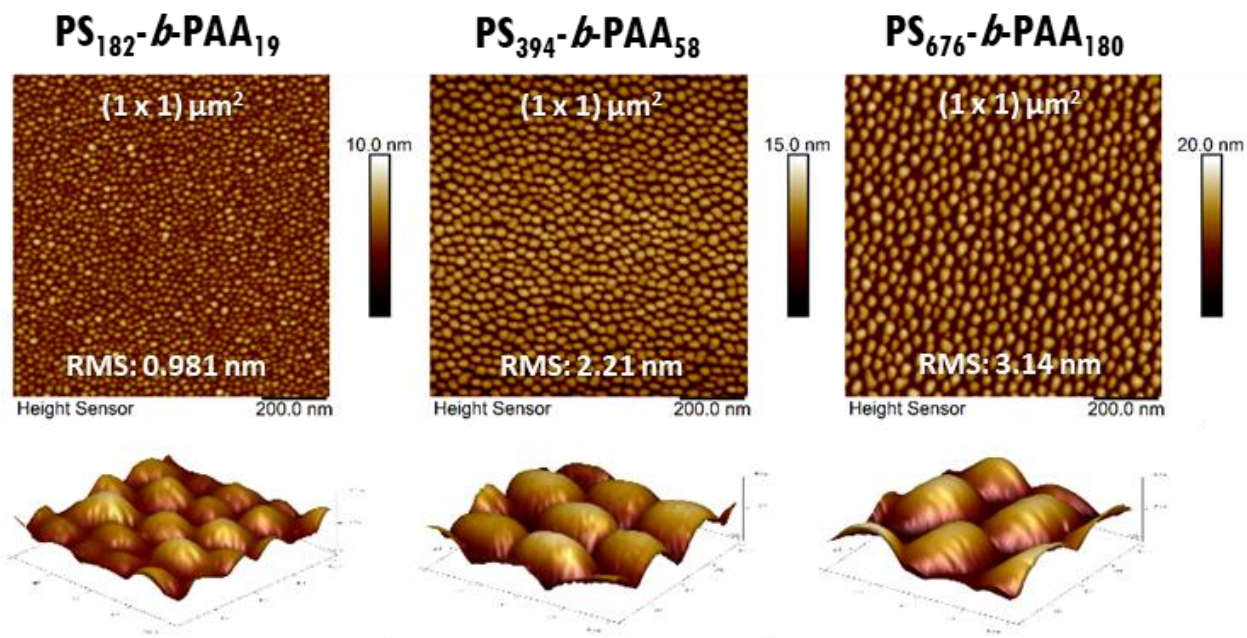


**Figure 1.14.** AFM images in air of the different PS-b-PAA BC compositions.

The average height of the PS clusters increases with PS block size due to a greater chemical incompatibility with PAA, as observed in **Table 1.4**.

**Table 1.4.** Monolayer parameters extracted from AFM images.

	Average islet height/nm <sup>a</sup>	Islet-to-islet distance/nm <sup>b</sup>
<b>PS<sub>182</sub>-<i>b</i>-PAA<sub>19</sub></b>	4 ± 1	25.0
<b>PS<sub>394</sub>-<i>b</i>-PAA<sub>58</sub></b>	8 ± 1	33.3
<b>PS<sub>677</sub>-<i>b</i>-PAA<sub>180</sub></b>	10.5 ± 0.3	43.5

<sup>a</sup>average of 5 islets height determined using the 'section' tool in Nanoscope Analysis software. <sup>b</sup>calculated by the Power Spectral Density (PSD) in Nanoscope Analysis software.

Additionally, the distance between each cluster increased with PAA block, which is consistent with an increase in the islet size. An effect certainly due to an increase in the number of PS chains in each islet discussed in more detail later on using a quantitative technique (QDM-d).

### 1.2.4. Conformation of the BC chains in the adsorbed BC monolayer

In the early nineties, Marques and Joanny described the scaling model of BC adsorption in non-selective solvents.<sup>27</sup> In their proposed theory, the relative size of the blocks is a key parameter for determining the layer structure of the adsorbed BC. Typically, two regimes are considered in their model: the buoy-dominated regime and the anchor-dominated regime. The asymmetry ratio,  $\beta$ , defined with respect to the Flory ( $R_F$ ) radius of the adsorbed (A) and free (B) blocks (Eq. 3) will dictate the transition between these two regimes (Eq. 4):

$$\beta = \frac{R_{F,B}}{R_{F,A}} = \left(\frac{N_B}{N_A}\right)^{3/5} \quad \text{Eq. 3}$$

$$\text{Anchor-dominated regime } \sqrt{N_A} > \beta > \sqrt{N_A} \quad \text{Buoy-dominated regime} \quad \text{Eq. 4}$$

In the buoy-dominated regime ( $\beta > \sqrt{N_A}$ ), by increasing the size of the anchoring block ( $N_A$ ), the adsorption of BC will increase as a result of the greater adsorption energy per chain. The maximum adsorption is moderated by the lateral repulsion between the buoys.<sup>28</sup>

Additional parameters such as the grafting density ( $\sigma$ , number of adsorbed chains per area) and the layer thickness ( $\ell$ ) can be extracted, and should scale as:

$$\sigma \sim N_A^{6/5} N_B^{-6/5} (\sim \beta^2) \quad \text{Eq. 5}$$

$$\ell \sim N_A^{2/5} N_B^{3/5} \quad \text{Eq. 6}$$

Conversely, in the anchor-dominated regime ( $\beta < \sqrt{N_A}$ ) the lateral repulsion between the buoy blocks is much less important. In this case, the adsorption is limited only by the saturation of the surface with the anchor blocks, and the grafting density and layer thickness scale as:

$$\sigma \sim N_A^{-1} \quad \text{Eq. 7}$$

$$\ell \sim N_A^{1/3} N_B \quad \text{Eq. 8}$$

By comparing the anchor and buoy DP values with the asymmetry factor, it is possible to obtain the theoretical regime for each BC compositions, as shown in **Table 1.5**.

**Table 1.5.** DP values and calculated BC asymmetry factors for different BC compositions.

	$N_B$	$N_A$	$\beta$	$\sqrt{N_A}$	Regime
<b>PS<sub>182</sub>-<i>b</i>-PAA<sub>19</sub></b>	182	19	3.83	4.41	$\beta < \sqrt{N_A}$ , anchor-dominated
<b>PS<sub>394</sub>-<i>b</i>-PAA<sub>58</sub></b>	394	58	3.15	7.63	$\beta < \sqrt{N_A}$ , anchor-dominated
<b>PS<sub>677</sub>-<i>b</i>-PAA<sub>180</sub></b>	677	180	2.21	13.13	$\beta < \sqrt{N_A}$ , anchor-dominated

The anchor-dominated regime is observed for all BC compositions studied in this work, meaning that the adsorption of each BC is limited by the saturation of the surface with PAA blocks. As theory predicts (Eq. 7), in this regime the grafting density of each BC is inversely proportional to the size of the anchoring block ( $N_A$ ), which means that PS<sub>677</sub>-*b*-PAA<sub>180</sub> is expected to have the lowest grafting density while PS<sub>182</sub>-*b*-PAA<sub>19</sub> is expected to have the highest one.

With the QCM-d technique, one can access the experimental grafting density of each BC on a substrate (QCM sensor). Special QCM sensors containing a thin silicon oxide layer

deposited onto the metal coating were used for the construction of the different adsorption isotherms of the three BC compositions. Like silicon wafers, the QCM sensors were firstly coated with APTES, and then the frequency change observed for subsequent injections of BC solutions of a given composition at different concentrations was recorded. The frequency change observed after each injection of different BC concentrations were converted to adsorbed mass using **Eq. 1**. The QCM data was then fitted using a Langmuir model (**Eq. 9**):

$$\Gamma(c) = \frac{k\Gamma_{sat}c}{1+kc} \quad \text{Eq. 9}$$

where  $\Gamma$  is the adsorbed amount of BC per area (calculated from the  $\Delta f$  of each BC injection of different concentration),  $k$  is the adsorption constant ( $k = k_{adsorption}/k_{desorption}$ ),  $\Gamma_{sat}$  is the maximum adsorbed mass per unit area and  $c$  is the BC mass concentration. From the adsorption constant, the adsorption free energy ( $\Delta G^{ads}$ ) can be estimated by **Eq. 10**:

$$\Delta G^{ads} = -k_B T \cdot \ln\left(\frac{k}{V_{solvent}^m}\right) \quad \text{Eq. 10}$$

where  $k_B$  is the Boltzmann constant,  $T$  is the temperature and  $V_{solvent}^m$  is the molar volume of the solvent (for DMF:THF (80:20), the molar volume was approximated from the molar volumes of DMF and THF and their respective volume fraction,  $V_{solvent}^m \approx 0.07824$  L/mol). Very importantly, from the maximum adsorbed amount,  $\Gamma_{sat}$ , one can extract the experimental BC grafting density (number of chains per unit area),  $\sigma$  (**Eq. 11**):

$$\sigma = \frac{\Gamma_{sat}}{M_w} \cdot N_{av} \cdot 10^{-21} \quad \text{Eq. 11}$$

where  $\sigma$  is the grafting density (expressed in chain per  $\text{nm}^2$ ),  $\Gamma_{sat}$  is the maximum adsorbed mass per unit area (expressed in  $\text{mg per m}^2$ ),  $M_w$  is the molecular weight of a given BC composition (expressed in  $\text{g per mol}$ ) and  $N_{av}$  is the Avogadro's constant. The adsorption isotherms are shown in **Figure 1.15**, and the calculated values of  $k$ ,  $\Delta G^{ads}$ ,  $\Gamma_{sat}$  and  $\sigma$  are shown in **Table 1.6**.

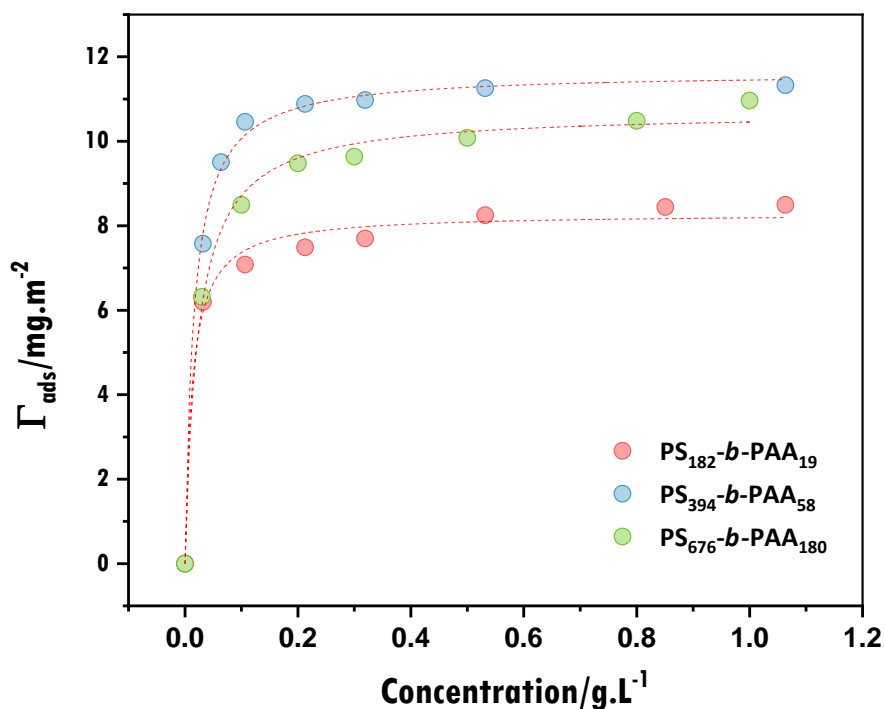


**Figure 1.15.** Adsorption isotherms of PS-*b*-PAA BCs varying in composition and  $M_w$  in a non-selective solvent. The dotted red lines represent a Langmuir fit of the data.

**Table 1.6.** BC parameters extracted from the QCM-d data from a Langmuir fit.

	$k/L.mol^{-1}$	$\Delta G^{ads}/kJ.mol^{-1}$	$\Gamma_{sat}/mg.m^{-2}$	$\sigma/chain.nm^{-2}$
<b>PS<sub>182</sub>-<i>b</i>-PAA<sub>19</sub></b>	$1.6 \cdot 10^6$	-41.7	8.3	0.244
<b>PS<sub>394</sub>-<i>b</i>-PAA<sub>58</sub></b>	$2.9 \cdot 10^6$	-43.1	11.6	0.154
<b>PS<sub>677</sub>-<i>b</i>-PAA<sub>180</sub></b>	$3.5 \cdot 10^6$	-43.6	10.7	0.077

In all BC adsorption isotherms, we find the characteristics of a high-affinity type isotherm: a very steep initial rise followed by a plateau (indeed, the large  $k$  values correspond to small  $k_{desorption}$ ). The calculated  $\Delta G^{ads}$  values are in the range of non-covalent electrostatic interactions, in agreement with the results obtained by PM-IRRAS. Finally, the observed increase in grafting density with decreasing  $N_A$  is in agreement with the anchor-dominated regime proposed by MJ. Additionally, the grafting density is in agreement with the water contact angle values (**Table 1.3**), as the monolayer with the highest grafting density, PS<sub>182</sub>-*b*-PAA<sub>19</sub>, shows the lowest hysteresis values, as a result of a more homogeneous BC layer.

As observed earlier, the size of the islets (and the height) of the monolayer exposed at air increases with the size of the PS blocks (**Figure 1.14, Table 1.4**). To address this, the number of PS chains per islet was determined for each BC composition from the average area of islets as calculated by the AFM software and the grafting density ( $\sigma$ ) obtained by QCM (**Table 1.7**).

**Table 1.7.** Parameters extracted from AFM images (area of a single islet) and QCM-d experiments (grafting density) and calculated number of PS chains per islet.

	Area of an islet/nm <sup>2</sup>	$\sigma$ /chain.nm <sup>-2</sup>	Number of PS chains per islet
<b>PS<sub>182</sub>-<i>b</i>-PAA<sub>19</sub></b>	426	0.244	104
<b>PS<sub>394</sub>-<i>b</i>-PAA<sub>58</sub></b>	675	0.154	103
<b>PS<sub>677</sub>-<i>b</i>-PAA<sub>180</sub></b>	1335	0.077	103

The density of the three monolayers obtained by a “grafting to” approach remains relatively low compared to PS brushes made by “grafting from” densely surface-grafted initiator.<sup>29,30</sup> The passage from a good to a bad solvent (air) will force the PS chains to dewet; a phenomenon which is not observed for denser brushes. The parameters that characterize the dewetting patterns must then be related somehow to the grafting density. The system seems to minimize the enthalpic incompatibility between the PS and PAA chains by reducing the contact surface as a function of the grafting density, as suggested in **Table 1.7**, where these two parameters vary in opposite ways. On the other hand, we also note that the number of chains per island seems to be kept constant (within the error bar). The dewetting is then the more pronounced as the grafting density is important with a constant number of chains per island. A statistical study on a larger number of BCs should allow to verify definitively this last hypothesis.

Along with QCM, Neutron Reflectivity (NR) proved to be very useful in testing the MJ theory. Hydrogenated PS<sub>182</sub>-*b*-PAA<sub>19</sub> and PS<sub>394</sub>-*b*-PAA<sub>58</sub> monolayers were analyzed in deuterated THF. The thicknesses of the swollen BC monolayers obtained from the fit of the NR data (**Figure 1.16**) were compared to the theoretical ones proposed by the MJ theory (for the anchor-dominated regime, **Eq. 8**).

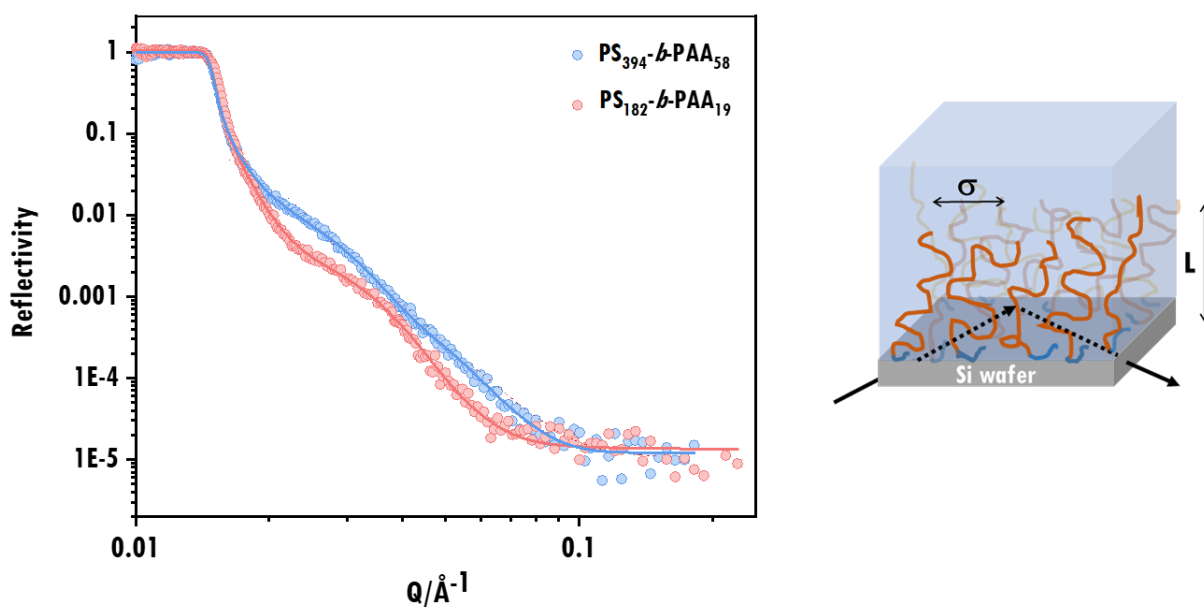


**Figure 1.16.** NR curves for PS<sub>182</sub>-b-PAA<sub>19</sub> (red) and PS<sub>394</sub>-b-PAA<sub>58</sub> (blue) monolayers in d-THF with swollen thickness  $L_1$  and  $L_2$  respectively - the continuous lines represent a fit to the data. (left) and schematic representation of the NR measurement where the supported monolayers were swollen in THF (right).

Additionally, the solvent volume fraction was extracted for each monolayer system (Figure 1.17). The results are summarized in Table 1.8.

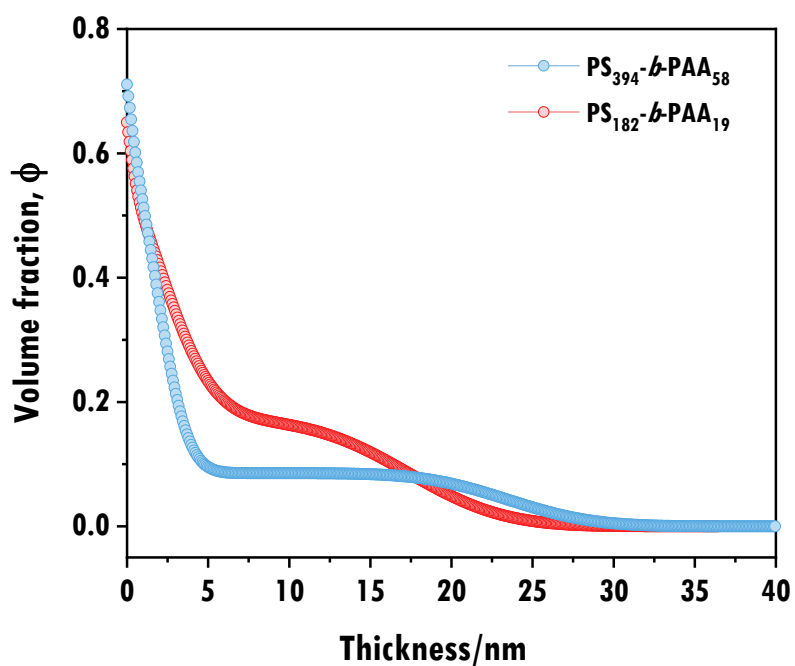


**Figure 1.17.** Polymer volume fraction of PS<sub>182</sub>-b-PAA<sub>19</sub> and PS<sub>394</sub>-b-PAA<sub>58</sub> monolayer systems immersed in THF.

**Table 1.8.** Thickness values of PS<sub>182</sub>-*b*-PAA<sub>19</sub> (named L<sub>1</sub>) and PS<sub>394</sub>-*b*-PAA<sub>58</sub> (named L<sub>2</sub>) and the respective solvent volume fraction (NR). The two last columns show the ratios between the monolayers (L<sub>2</sub>/L<sub>1</sub>) determined by NR or using MJ scaling laws.

	L/nm	THF Volume fraction/%	L <sub>2</sub> /L <sub>1</sub> (NR)	L <sub>2</sub> /L <sub>1</sub> (MJ scaling laws)
L <sub>1</sub> , PS <sub>182</sub> - <i>b</i> -PAA <sub>19</sub>	16.1	0.41	1.37	1.49
L <sub>2</sub> , PS <sub>394</sub> - <i>b</i> -PAA <sub>58</sub>	22.1	0.90		

One can observe that the L<sub>2</sub>/L<sub>1</sub> ratio of 1.37 observed with NR is in fair agreement with the MJ scaling laws (L<sub>2</sub>/L<sub>1</sub> ~ 1.49). Additionally, the THF volume fractions measured for both monolayers are also in line with their grafting density, with the PS<sub>182</sub>-*b*-PAA<sub>19</sub> monolayer having the highest density (seen by QCM, **Table 1.6**) and, consequently, containing the lowest volume of solvent (seen by NR, **Table 1.8**).

A final consideration on the BC monolayers is related to their conformation near the surface. The structure of the adsorbed BC chains can be evaluated by considering the radius of gyration (R<sub>g</sub>) of the buoy block and the distance between grafting points. As pointed by De Gennes, the spacing  $D = \sigma^{-1/2}$  between the grafting points determines the conformation of the buoy chains.<sup>10</sup> If the spacing is larger than the R<sub>g</sub> of the buoy block (PS), the grafted chains take on the form of isolated mushrooms, as illustrated in **Figure 1.18**. As the distance D decreases, the grafted chains overlap and the structure shifts to a brush regime.<sup>31</sup>

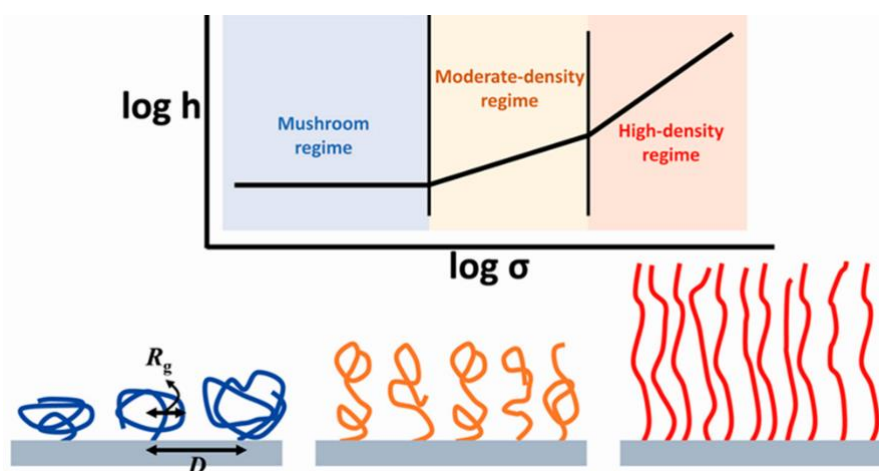


**Figure 1.18.** Schematic representation of the scaling law for brush thickness and grafting density. The image is reprinted from ref. 32.

By comparing the D spacing, calculated from the grafting density obtained by QCM, with the theoretical values of R<sub>g</sub> of PS in good solvent calculated from ref. 33, one can

determine the regime of the buoy chains, as shown in **Table 1.9** (theoretical values were used since experimental data (SANS) was available only for PS<sub>394</sub>-*b*-PAA<sub>58</sub>).

**Table 1.9.** Calculated  $R_g$ ,  $D$  and the respective regime of the buoy chains close to the surface.

	$R_g/\text{nm}^a$	$D/\text{nm}$	Regime
<b>PS<sub>182</sub>-<i>b</i>-PAA<sub>19</sub></b>	4.1	2.0	Brush
<b>PS<sub>394</sub>-<i>b</i>-PAA<sub>58</sub></b>	6.5	2.5	Brush
<b>PS<sub>677</sub>-<i>b</i>-PAA<sub>180</sub></b>	9.0	3.6	Brush

<sup>a</sup> theoretical radius of gyration of PS having similar DP in THF, according to ref. 33.

One can observe that the  $D$  spacing between the grafted points is much smaller than the  $R_g$  of PS for all of the BC compositions, in agreement with a brush conformation of the PS chains in good solvent conditions. However, as already seen at the AFM images in the dry state (**Figure 1.14**), the brushes are not in a high density regime, which is expected for the type of grafting used to prepare the BC monolayers.

## Conclusions

PS-*b*-PAA monolayers were successfully prepared with different  $M_w$  BCs by adsorption from a non-selective solvent. Different solvents were studied for the solubilisation of the BC, a mixture of DMF:THF (80:20) being the most suitable for the present fabrication process. The anchoring of the PAA groups at the surface of the silicon wafers was possible after the modification of the substrates with amino groups (APTES or PAH) through formation of ion pairs ( $-\text{COO}^- \cdots \text{NH}_3^+$ ), accessed by PM-IRRAS. Importantly to note, the covalent or non-covalent grafting of amine groups (APTES and PAH, respectively) did not alter the BC grafting density of the monolayer, and thus, for future applications, the physisorption using PAH should be preferentially used to avoid the intrinsic issues of APTES. The resulting monolayers presented an islet patterning when dried, as a result of the PS dewetting linked to the low BC grafting of the layers. The monolayers studied with three BC compositions are in agreement with the scaling laws presented by Marques and Joanny in the so-called “anchor-dominated” regime. In good solvent conditions, the ML can be pictured as a PS brush layer with a moderate

grafting density whose exact value depends on the block copolymer compositions. The PS brush will be now used as a 'substrate' to induce the bilayer self-assembly with free BC chains in solution once the physicochemical conditions to trigger the hydrophobic effect are met.

## References

- (1) Siqueira Petri, D. F.; Wenz, G.; Schunk, P.; Schimmel, T. An Improved Method for the Assembly of Amino-Terminated Monolayers on SiO<sub>2</sub> and the Vapor Deposition of Gold Layers. *Langmuir* **1999**, *15* (13), 4520–4523. <https://doi.org/10.1021/la981379u>.
- (2) Moon, J. H.; Kim, J. H.; Kim, K. J.; Kang, T. H.; Kim, B.; Kim, C. H.; Hahn, J. H.; Park, J. W. Absolute Surface Density of the Amine Group of the Aminosilylated Thin Layers: Ultraviolet-Visible Spectroscopy, Second Harmonic Generation, and Synchrotron-Radiation Photoelectron Spectroscopy Study. *Langmuir* **1997**, *13* (16), 4305–4310.
- (3) Bourgès, C.; Shanahan, M. E. R. Influence of Evaporation on Contact Angle. *Langmuir* **1995**, *11*, 2820–2829. <https://doi.org/10.1021/j100218a018>.
- (4) Shanahan, M. E. R.; Bourgès, C. Effects of Evaporation on Contact Angles on Polymer Surfaces. *Int. J. Adhes. Adhes.* **1994**, *14* (3), 201–205. [https://doi.org/10.1016/0143-7496\(94\)90031-0](https://doi.org/10.1016/0143-7496(94)90031-0).
- (5) Liu, Y.; Jaiswa, A.; Poggi, M. A.; Wilson, W. D. Surface Plasmon Resonance and Quartz Crystal Microbalance Methods for Detection of Molecular Interactions. In *Chemosensors: Principles, Strategies, and Applications* (Principles, Strategies, and Applications); John Wiley & Sons, Inc., 2011; pp 329–344. <https://doi.org/10.1002/9781118019580.ch16>.
- (6) Sauerbrey, G. Use of Quartz Vibration for Weighing Films on a Microbalance. *Zeitschrift für Phys.* **1959**, *155* (2), 206–222. <https://doi.org/10.1007/BF01337937>.
- (7) Buffeteau, T.; Desbat, B.; Turlet, J. M. Polarization Modulation FT-IR Spectroscopy of Surfaces and Ultra-Thin Films: Experimental Procedure and Quantitative Analysis. *Appl. Spectrosc.* **1991**, *45* (3), 380–389. <https://doi.org/10.1366/0003702914337308>.
- (8) Buffeteau, T.; Desbat, B.; Blaudez, D.; Turlet, J. M. Calibration Procedure to Derive IRRAS Spectra from PM-IRRAS Spectra. *Appl. Spectrosc.* **2000**, *54* (11), 1646–1650. <https://doi.org/10.1366/0003702001948673>.
- (9) Ramin, M. A.; Le Bourdon, G.; Daugey, N.; Bennetau, B.; Vellutini, L.; Buffeteau, T. PM-IRRAS Investigation of Self-Assembled Monolayers Grafted onto SiO<sub>2</sub>/Au Substrates. *Langmuir* **2011**, *27* (10), 6076–6084. <https://doi.org/10.1021/la2006293>.
- (10) Fleer, G.; Stuart, M. A. C.; Scheutjens, J. M. H. M.; Cosgrove, T.; Vincent, B. *Polymers at Interfaces*, 1st ed.; Springer Netherlands, 1998. <https://doi.org/10.1007/978-94-011-2130-9>.
- (11) Liang, Y.; Huang, J.; Zang, P.; Kim, J.; Hu, W. Molecular Layer Deposition of APTES on Silicon Nanowire Biosensors: Surface Characterization, Stability and PH Response. *Appl. Surf. Sci.* **2014**, *322*, 202–208. <https://doi.org/10.1016/j.apsusc.2014.10.097>.
- (12) Aissaoui, N.; Bergaoui, L.; Landoulsi, J.; Lambert, J. F.; Boujday, S. Silane Layers on Silicon Surfaces: Mechanism of Interaction, Stability, and Influence on Protein Adsorption. *Langmuir* **2012**, *28* (1), 656–665. <https://doi.org/10.1021/la2036778>.
- (13) Acres, R. G.; Ellis, A. V.; Alvino, J.; Lenahan, C. E.; Khodakov, D. A.; Metha, G. F.; Andersson, G. G. Molecular Structure of 3-Aminopropyltriethoxysilane Layers Formed on Silanol-Terminated Silicon Surfaces. *J. Phys. Chem. C* **2012**, *116* (10), 6289–6297. <https://doi.org/10.1021/jp212056s>.
- (14) Decher, G. Fuzzy Nanoassemblies: Toward Layered Polymeric Multicomposites. *Science (80-. )*. **1997**, *277* (5330), 1232–1237. <https://doi.org/10.1126/science.277.5330.1232>.
- (15) Yoo, D.; Shiratori, S. S.; Rubner, M. F. Controlling Bilayer Composition and Surface Wettability of Sequentially Adsorbed Multilayers of Weak Polyelectrolytes. *Macromolecules* **1998**, *31* (13), 4309–

4318. <https://doi.org/10.1021/ma9800360>.
- (16) Kim, M.; Basarir, F.; Park, J.; Yoon, T.; Jang, Y. H. Computational Calculation of Thickness of Self-Assembled Monolayer of 3- Aminopropyltriethoxysilane on Quartz ( 100 ). *Mol. Simul.* **2014**, No. 100, 3–5.
- (17) Vezenov, D. V.; Noy, A.; Rozsnyai, L. F.; Lieber, C. M. Force Titrations and Ionization State Sensitive Imaging of Functional Groups in Aqueous Solutions by Chemical Force Microscopy. *J. Am. Chem. Soc.* **1997**, *119* (8), 2006–2015. <https://doi.org/10.1021/ja963375m>.
- (18) Yu, Y.; Zhang, L.; Eisenberg, A. Morphogenic Effect of Solvent on Crew-Cut Aggregates of Amphiphilic Diblock Copolymers. *Macromolecules* **1998**, *31* (4), 1144–1154. <https://doi.org/10.1021/ma971254g>.
- (19) Danner, R. P.; High, M. S. *Handbook of Polymer Solution Thermodynamics*; 1993. <https://doi.org/10.1002/9780470938232>.
- (20) Hansen, C. M. The Three Dimensional Solubility Parameter and Solvent Diffusion Coefficient, Their Importance in Surface Coating Formulation, Danish Technical Press, 1967.
- (21) Hansen, C. M. *Hansen Solubility Parameters (HSP)*, 2nd ed.; Taylor & Francis, 2011; Vol. 118.
- (22) Burchard, W. *Static and Dynamic Light Scattering from Branched Polymers and Biopolymers*; The Royal Society of Chemistry, Cambridge, 1992. <https://doi.org/10.1002/pi.1994.210330318>.
- (23) Cui, H.; Chen, Z.; Zhong, S.; Wooley, K. L.; Pochan, D. J. Block Copolymer Assembly via Kinetic Control. *Science* (80-. ). **2007**, *317* (5838), 647–650. <https://doi.org/10.1126/science.1141768>.
- (24) El'Tekov, A. Y.; El'Tekova, N. A.; El'Tekov, Y. A. Thin-Layer Chromatography in the Investigation of Polystyrene Macromolecule Interaction with Nanoporous Silica. *Prot. Met. Phys. Chem. Surfaces* **2014**, *50* (1), 45–48. <https://doi.org/10.1134/S2070205114010031>.
- (25) Li, Y.; Pham, J. Q.; Johnston, K. P.; Green, P. F. Contact Angle of Water on Polystyrene Thin Films: Effects of CO<sub>2</sub> Environment and Film Thickness. *Langmuir* **2007**, *23* (19), 9785–9793. <https://doi.org/10.1021/la0636311>.
- (26) Spatz, J. P.; Möller, M.; Noeske, M.; Behm, R. J.; Pietralla, M. Nanomosaic Surfaces by Lateral Phase Separation of a Diblock Copolymer. *Macromolecules* **1997**, *30* (13), 3874–3880. <https://doi.org/10.1021/ma9607372>.
- (27) Marques, C. M.; Joanny, J. F. Block Copolymer Adsorption in a Nonselective Solvent. *Macromolecules* **1989**, *22*, 1454–1458. <https://doi.org/10.1021/ma00193a075>.
- (28) King, S. M.; Cosgrove, T.; Eaglesham, A. The Adsorption of Polystyrene Saturated-Polydiene Block Copolymers on Silica Substrates. *Colloids Surfaces A Physicochem. Eng. Asp.* **1996**, *108*, 159–171. [https://doi.org/10.1016/0927-7757\(95\)03397-1](https://doi.org/10.1016/0927-7757(95)03397-1).
- (29) Devaux, C.; Chapel, J. P.; Beyou, E.; Chaumont, P. Controlled Structure and Density of “Living” Polystyrene Brushes on Flat Silica Surfaces. *Eur. Phys. J. E* **2002**, *7* (4), 345–352. <https://doi.org/10.1140/epje/i2001-10098-2>.
- (30) Jain, S.; Bates, F. S. Consequences of Nonergodicity in Aqueous Binary PEO-PB Micellar Dispersions. *Macromolecules* **2004**, *37* (4), 1511–1523. <https://doi.org/10.1021/ma035467j>.
- (31) Brittain, W. J.; Minko, S. A Structural Definition of Polymer Brushes. *J. Polym. Sci. Part A Polym. Chem.* **2007**, *45* (16), 3505–3512. <https://doi.org/10.1002/pola.22180>.
- (32) Kim, M.; Schmitt, S. K.; Choi, J. W.; Krutty, J. D.; Gopalan, P. From Self-Assembled Monolayers to Coatings: Advances in the Synthesis and Nanobio Applications of Polymer Brushes. *Polymers (Basel)*. **2015**, *7* (7), 1346–1378. <https://doi.org/10.3390/polym7071346>.
- (33) Fetters, L. J.; Hadjichristidis, N.; Lindner, J. S.; Mays, J. W. Molecular Weight Dependence of Hydrodynamic and Thermodynamic Properties for Well-Defined Linear Polymers in Solution. *J. Phys. Chem. Ref. Data* **1994**, *23* (4), 619–640. <https://doi.org/10.1063/1.555949>.

# 2

## **Bilayer formation**



This chapter comprises the study of the second step of the process: the formation of a BC bilayer. By adding water into the system containing the grafted BC monolayer in equilibrium with excess of free BC chains in DMF:THF solution, the formation of a second BC layer is triggered through hydrophobic interactions between free and “grafted” hydrophobic PS blocks (**Figure 2.1**). A final rinsing step allows then to remove any BC micelles and other aggregates generated in the aqueous solutions. As the self-assembly process is highly sensitive and dependent on many processing parameters (out-of-equilibrium conditions), the amount of water that will eventually trigger the bilayer formation is certainly the most critical parameter of the process and was determined precisely by dynamic light scattering (DLS) in solution. The resulting solid-supported BC bilayers of around 20 nm were characterized in air by various characterization techniques. Bilayers with BC containing PS blocks whose molar mass is below its critical mass ( $M_c = 31.2 \cdot 10^3 \text{ g}\cdot\text{mol}^{-1}$ ) were also generated, suggesting that hydrophobic interactions participate greatly to the bilayer integrity through a good cohesion between the layers. We have used the sensitivity of Neutron Reflectivity (NR) experiments to look at the polymer/polymer interfaces by using the *contrast matching* technique in order to investigate the organization of the bilayer perpendicular to the substrate and, in particular, the “entanglement” interphase between the two hydrophobic blocks. The results pointed out the presence of an intermediate step between the mono- and bilayer formation, named hereafter “densification of the BC monolayer”, particular of PS-*b*-PAA BCs, that was deeply investigated in **Chapter 3**.

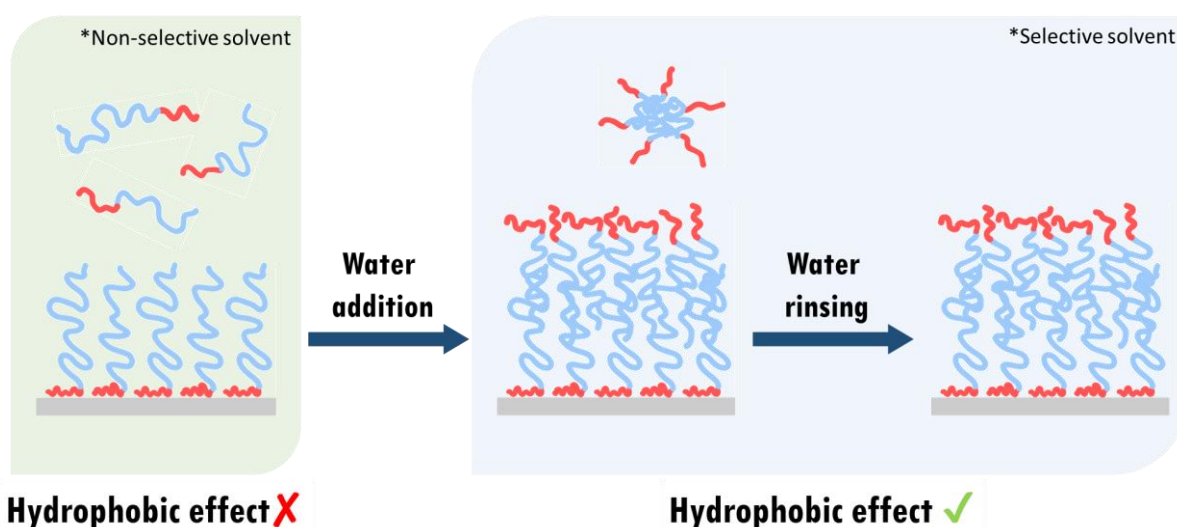


**Figure 2.1.** Illustrative scheme of the triggering of the hydrophobic effect by the addition of a selective solvent to generate the PS-*b*-PAA bilayers on solid support.

---

# Experimental

---

## Materials

PS<sub>182</sub>-*b*-PAA<sub>19</sub> and PS<sub>394</sub>-*b*-PAA<sub>58</sub> were purchased from Polymer Source (Canada) and used as received – it should be noted that the subscript numbers indicate the degree of polymerization (DP) of each polymer. Deuterated BC PS<sub>394</sub>-*b*-PAA<sub>58</sub> (PS<sub>d</sub>-*b*-PAA) was synthesized and characterized with Dr. F. Stoffelbach at IPCM (Sorbonne Université). *N,N*-dimethylformamide (DMF, 99.8%) was purchased from Acros Organics and tetrahydrofuran (THF, 99%) was purchased from Sigma-Aldrich and used in a solvent purification system (PureSolv MD) (that is, anhydrous THF with no stabilizers). Deionised water with a resistivity of 18.2 MΩ.cm at 25°C was obtained from a Milli-Q system (Millipore).

## Methodology

### 1.1. Characterization of the BC behaviour in solution

Dynamic Light Scattering (DLS): The critical water contents (cwc) of PS<sub>394</sub>-*b*-PAA<sub>58</sub> and PS<sub>182</sub>-*b*-PAA<sub>19</sub> solutions prepared in THF or DMF:THF (80:20, v:v) at a concentration of 1 g.L<sup>-1</sup> were measured by DLS using an ALV goniometer, with a 22 mW linearly polarized laser (632.8 nm HeNe) and an ALV- 5000/EPP multiple tau digital correlator. The DLS autocorrelation functions were obtained at a scattering angle of 90° and a temperature of 25 °C. Each result corresponds to the average of 6 acquisitions of 10 seconds each. The intensity-weighted relaxation time ( $\tau$ ) distributions were extracted from the autocorrelation data using the multi-exponential CONTIN method. The polymer solutions were prepared by dissolving polymers into THF or DMF:THF mixtures. The solutions were filtered through a membrane filter with nominal pore size of 0.1  $\mu$ m. Deionized water (Milli-Q) was added to the BC solutions with a micropipette. The experiments were performed at room temperature. The scattered light intensity was recorded 5 min after the addition of water and mixing of the solution.

Transmission Electronic Microscopy (TEM): The images were recorded at Bordeaux Imaging Center (BIC) on a Hitachi H7650 microscope operating at 80 kV. The copolymers were

solubilized at 2 g.L<sup>-1</sup> in DMF:THF (80:20, v:v). A given volume of water was added to be slightly above the critical water content (CWC). After 2 hours of incubation, extra water was added to reach 50 vol.%. Samples were prepared by depositing 5 µl of the suspension onto a copper grid (200 mesh coated with carbon) using a homemade spray tool and allowed to air dry for 20 min.

## 1.2. Self-assembly of the BC bilayer at the silicon wafer surface

The pre-functionalized wafers were first immersed in the trough containing the BC solution under conditions similar to those used for the BC monolayer (BC 1 g.L<sup>-1</sup> filtration with 0.1 µm PTFE filter, 2h incubation). Water was then slowly added with an infusion syringe pump (New Era, NE-300) at a rate of 50 µL.min<sup>-1</sup> until a water content of 6 vol.% was reached. The system was allowed to equilibrate for 18h (overnight). Afterward, a rinsing step including simultaneous injection of DI water at one end and removal of the solution at the other were performed with two infusion syringe pumps at increasing flow rates (300 µL.min<sup>-1</sup> during 2 h followed by 5 mL.min<sup>-1</sup> during 5 min). Finally, manual injection and removal of water was performed using a wash bottle and a peristaltic pump up to 400 mL to fully exchange the BC solution with water. The BC bilayers self-assembled on wafer substrates were then taken out carefully and dried under a nitrogen flow. Specifically, to minimize capillary forces at the air/water interface, the wafers were slowly removed vertically from the solution. An aqueous NaOH solution (pH 11) was also tested to trigger bilayer formation. The protocol of rinsing slightly changes when water or an aqueous NaOH solution is used, as shown in **Figure 2.2**. When using aqueous NaOH solution, an initial rinsing step is performed with the same solution, followed by two further rinsing steps with pure water to remove any NaOH left in solution.

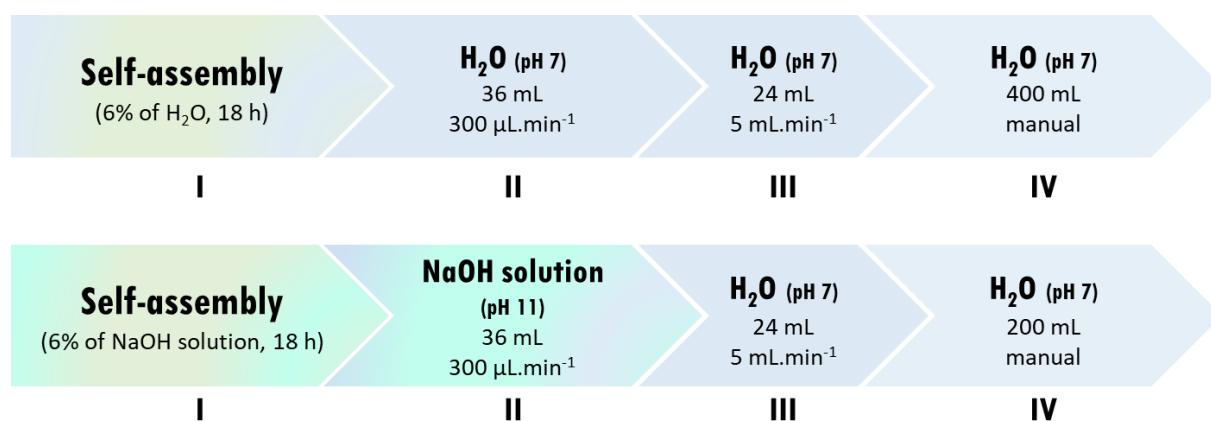


**Figure 2.2.** Rinsing process of PS<sub>394</sub>-b-PAA<sub>58</sub> bilayers as a function of the triggering solution. When water is used to trigger the self-assembly (up), after 18h (I) a 3-step rinsing sequence takes place, II and III, involving injection and removal of water at 300  $\mu\text{L}\cdot\text{min}^{-1}$  and 5  $\text{mL}\cdot\text{min}^{-1}$  using injection pumps, and a final step (IV), termed “manual”, using a wash bottle and a peristaltic pump to inject and remove, respectively. When a NaOH solution at pH 11 is used to trigger the self-assembly (down), a similar rinsing process takes place, only differing that a first rinsing (II) is made using pH 11 NaOH solution.

### 1.3. Characterization of the BC bilayer at the silicon wafer surface

**Thickness:** The bilayer thickness deposited silicon wafers was measured using an UVISEL spectroscopic ellipsometer (Horiba Jobin Yvon, France). The data were acquired at three angles of incidence: 65°, 70° and 75° and wavelengths ranging from 260 to 860 nm. Data were fitted to a multi-layer model using the DeltaPsi Horiba built-in program. The thicknesses obtained through spectroscopic ellipsometry were systematically confirmed by AFM measurements. Several scratches were made on the polymer layer deposited on silicon wafers by pulling (and not cutting) sideways a sharp surgical scalpel blade and then imaging the generated scratches to estimate the film thickness (step height).

**Surface topography:** AFM images of the bilayers were recorded either in the dry state by using Tapping Mode in air at a resolution of 512 x 512 pixels with a scan rate of 1 Hz with a Dimension ICON (Veeco, Bruker) or the wet state (water) using a Peak Force Mode at similar resolution and scan rates with a Bioscope Resolve (Bruker). For the wet state analyses, a droplet of water was placed on both the AFM tip and the bilayer surface prior to the engagement to allow a capillary bridge to form. Unless otherwise noted, the AFM images shown were obtained using Tapping Mode in air. All the data were analysed with Nanoscope Analysis software.

Contact angle measurements: Advancing and receding water contact angles ( $\theta_{adv}$ ,  $\theta_{rec}$ ) were measured with a Tracker tensiometer from Teclis (France) at room temperature. The static contact angle was recorded using the sessile drop method. With the help of a dosing syringe, a droplet of 3  $\mu$ L of water (pH 7) was deposited on the substrate and the value of advancing contact angle was recorded 30 s after droplet deposition (importantly to note, no significant change was observed on the contact angle during this period). The average value was obtained by measuring two samples in two different position. The natural receding contact angles were determined by monitoring the evaporation of the sessile drop with time: the contact angle initially set in the advancing mode ( $\theta_A$ ) decreases linearly with time when the liquid starts to evaporate. When the water droplet is not pinned anymore, it then recedes at a constant angle ( $\theta_R$ ) marked by the presence of a visible plateau.<sup>1,2</sup>

Latex nanoparticles adsorption: PS-*b*-PAA mono- and bilayer were incubated with an aqueous dispersion of amine-functionalized-PS particles (average diameter 68 nm, Bangs Laboratories, Inc. Fishers, IN) at pH 8 for 2 h at room temperature. Then, the substrates were immersed in an aqueous solution at the same pH to remove non-adsorbed particles and dried under nitrogen.

Polarization Modulation Infrared Reflection Absorption Spectroscopy (PM-IRRAS): The PM-IRRAS measurements were performed by Thierry Buffeteau at the Institute of Molecular Sciences (L'Institut des Sciences Moléculaires – ISM). PS<sub>394</sub>-*b*-PAA<sub>57</sub> bilayers were prepared onto SiO<sub>2</sub>/Au substrates (2.5 x 2.5 cm<sup>2</sup>) similarly to the protocol described for the bilayer formation onto silicon wafers.

Neutron Reflectivity (NR): Contrast matching experiments – Substitutions between hydrogen and deuterium were used to manipulate the scattering length density (SLD) of the copolymers chains and match the different phases, to obtain contrast only at the buried interface between the two PS blocks. PS<sub>394</sub>-*b*-PAA<sub>58</sub> bilayers prepared with deuterated and/or hydrogenated PS blocks were then studied using NR. Note that in the case of deuterated BC, only the PS chains are deuterated, the PAA blocks are always hydrogenated. Fully hydrogenated or fully deuterated bilayers were prepared as described in the methodology,

using hydrogenated or deuterated BC. Mixed hydrogenated/deuterated bilayers were also prepared, in which one of the layers consists on a hydrogenated (or deuterated) BC and the other of a deuterated (or hydrogenated) BC. To do so, the monolayer formation was first performed by immersing the APTES (or PAH) modified substrates in a solution of *e.g.* hydrogenated BC. Then, the substrates containing the BC were rinsed in DMF:THF to remove BC excess. The substrates containing the hydrogenated BC monolayer were placed back into the trough, this time filled with the deuterated BC solution (importantly to note, no hydrogenated BC is left as the substrate was rinsed before re-immersion). Then, the bilayer formation protocol was the same, with triggering using an aqueous solution of NaOH, followed by overnight equilibration and rinsing. In doing so, the top layer, formed by the self-assembly of the BC in solution with those at the substrate, is deuterated. A similar process was done to obtain a bottom layer of deuterated BC and a top layer of hydrogenated BC.

NR measurements were performed on the time-of-flight reflectometer HERMES at the Laboratoire Léon Brillouin (LLB) in CEA-Saclay. Two geometries were used. In the first one the silicon/air interface was probed with a  $q$ -range varying from 0.008 to 0.07  $\text{\AA}^{-1}$ . In the second one, the silicon/deuterated THF interface was probed with a  $q$ -range varying from 0.01 to 0.08  $\text{\AA}^{-1}$ . A specific home-made cell was used to perform the experiments in d-THF. For the experiments, we used all the wavelengths provided by the neutron source from 3  $\text{\AA}$  to 25  $\text{\AA}$  with a constant DI of 0.3  $\text{\AA}$ . We used for the silicon/air interface  $q = 0.93^\circ$  and for the silicon/deuterated THF  $q = 1.23^\circ$  with a  $\Delta q$  of  $0.05^\circ$ . The experimental resolution is taken into account in the fitting procedure using the MotoFit software package. We have considered a multilayer model consisting of silicon, silicon oxide and a polystyrene brush, which each layer (slab) is characterized by the scattering length density (SLD), thickness and roughness. When solvent was present, it was equally taken into account.

# Results and discussion

## 1. General process of bilayer formation

### 1.1. Setting-up the surface self-assembly conditions

As illustrated in **Figure 2.1**, after the monolayer formation an excess of non-adsorbed BC unimers remains in solution. The subsequent controlled addition of water will increase gradually the polarity of the solvent turning on the hydrophobic effect and triggering the interaction between free and adsorbed PS blocks. From a thermodynamic point of view, the addition of water translates into an increase in the Flory-Huggins PS-solvent interaction parameter ( $\chi$ ), namely a loss of solubility of the PS blocks. As discussed in the state-of-the-art chapter, amphiphilic BCs form non-equilibrium structures when the solvent polarity of the medium changes. It follows that BC self-assembly in bulk solution and by extension at solid-liquid interfaces is overly sensitive and dependent on processing parameters. Among them, the water content is most critical: it must be sufficient to confer amphiphilic properties to the BCs while avoiding their aggregation on the surface, in particular with copolymers containing long PS blocks. The minimum water content to induce self-assembly of BC, also called critical water content (cwc), was determined by light scattering in solution, as illustrated in **Figure 2.3**.

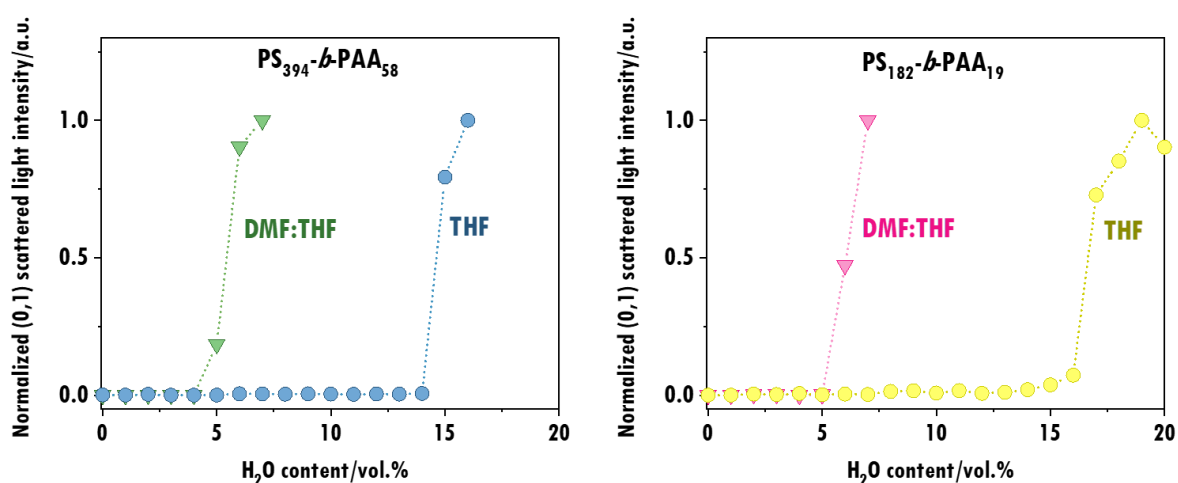


**Figure 2.3.** Critical water content of PS<sub>394</sub>-b-PAA<sub>58</sub> and PS<sub>182</sub>-b-PAA<sub>19</sub> solutions prepared at 1 g/L in DMF:THF (80:20) and THF, as determined from the increase in light scattered intensity upon addition of water.

The scattered light intensity is almost constant at low water contents up to a critical value, when it increases rapidly at the onset of the BC micellization. The cwc values are consistent with previous studies of Eisenberg and co-workers, as the quality of the solvent highly affects the solubility of the chains once a non-selective is added. In THF, which is a good solvent for PS, the chains remain soluble to a much higher water content ( $\approx 15\%$ ) than in the DMF:THF mixture ( $\approx 5\%$ ). At values close to the cwc, the system is expected to be equilibrated, *i.e.*, a dynamic equilibrium exists between the copolymer unimers and self-assembled structures; this is an important aspect to consider to perform the bilayer formation under equilibrium conditions. At higher water contents, the chain mobility is drastically reduced due to a lower concentration of DMF:THF in the hydrophobic domains. Then, the system becomes frozen and the subsequent addition of water does not alter anymore its structural integrity. Additionally, one can notice that there is a slight decrease of the cwc value when the size of the block increases, as already described by Eisenberg.<sup>6</sup>

By replacing pure water with a NaOH solution (pH 11), there is no significant change of the cwc value (**Figure 2.4**), which means that the much larger PS blocks fully determine the hydrophobic-hydrophilic balance of the BCs, the short PAA blocks (charged or not) having little influence on the BC overall solubility. Based on these data, a water (or NaOH solution pH 11) fraction of 6 % vol. will be used in next experiments to trigger the bilayer self-assembly of PS-PAA BCs in DMF:THF mixture.

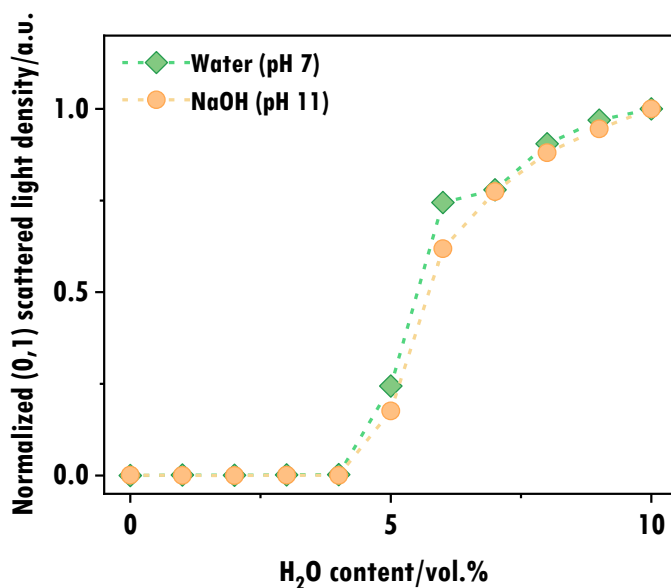


**Figure 2.4.** Critical water content of PS<sub>394</sub>-b-PAA<sub>58</sub> at 1 g/L in DMF:THF (80:20) using water or diluted NaOH solution (pH 11).

The morphology of BC self-assembled structures in solution was examined by TEM. Same experimental conditions as those used for the BC self-assembly into bilayer were applied, that is, a slow addition of water ( $50 \mu\text{L}\cdot\text{min}^{-1}$ , see below) to reach the cwc (6% vol.) and then a more rapid addition to reach  $\sim 50\%$  vol. of water. As it can be observed by the TEM image shown in **Figure 2.5**, the BC self-assembled into crew-cut micelles (*i.e.*, micelles containing a relatively large core and a relatively small corona) of approximately 25 nm in diameter. It means that such block copolymer compositions are not favourable to form a bilayer structure through direct self-assembly in solution. Otherwise, we should have obtained vesicles (polymersomes). However, as it will be further described, according to our approach one can direct its surface self-assembly into a solid-supported bilayer.

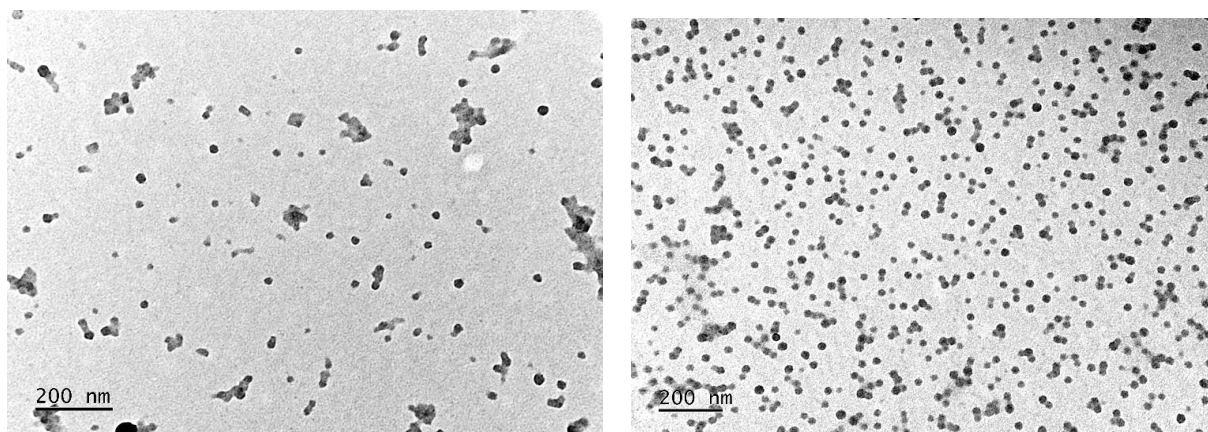


**Figure 2.5.** TEM image of BC micelles obtained from  $\text{PS}_{394}\text{-b-PAA}_{58}$  (left) and  $\text{PS}_{182}\text{-b-PAA}_{19}$  (right) solutions at 1 g/L in DMF:THF (80:20) mixture containing 6% of water.

The two-step surface self-assembly process was performed by placing the substrates in a Teflon trough filled with the BC solution in non-selective solvent, using two syringe pumps for injection and withdrawal of the selective solvent, as shown in **Figure 2.6**. First, the previously described monolayer formation was performed in a similarly manner by immersing an APTES (or PAH)-modified substrates in the trough containing the BC solution at 1 g/L in DMF:THF for 2 h.

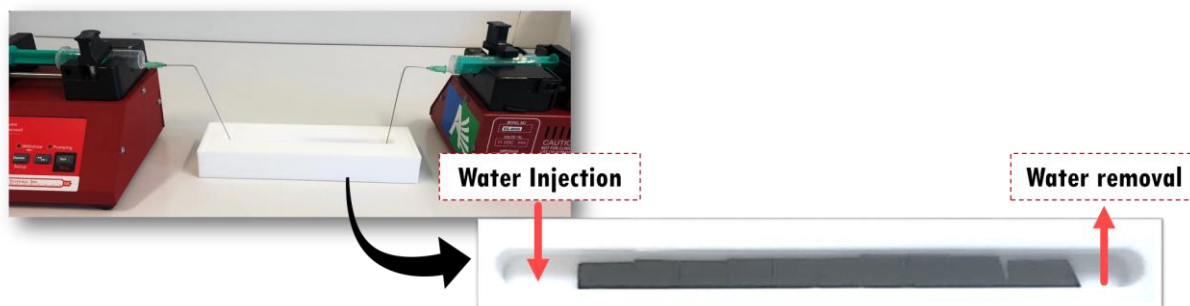


**Figure 2.6.** Illustration of the experimental set-up for the preparation of the solid-supported bilayers. Injection and withdraw pumps are placed on the left and right sides of the Teflon trough, respectively.

The second step is then performed when water added from the left, diffuses throughout the trough, triggering self-assembly, as illustrated in **Figure 2.7** (II). The system is allowed to equilibrate overnight (III) followed by extensive water rinsing, to remove bulk aggregates that were formed simultaneously during continuous injection and to fully replace the non-selective solvent, resulting in the final solid-supported bilayer (IV).

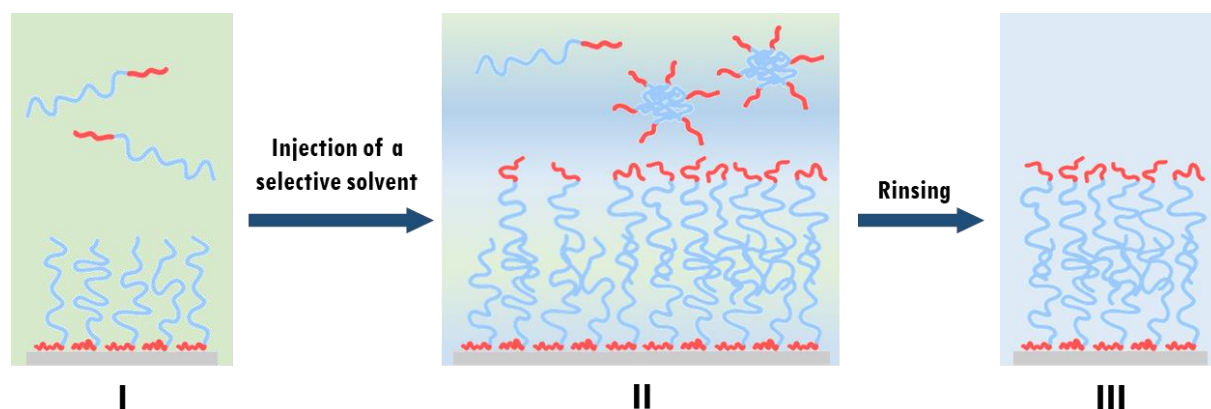


**Figure 2.7.** Illustration of the self-assembly process. After ML formation (I), when the selective solvent is added, the self-assembly takes place both at the wafer surface and in solution (II); after an overnight equilibrium, the bilayer is not yet formed and requires extensive rinsing to completely exchange the selective solvent with water while removing any BC aggregates generated in the bulk (III).

As mentioned previously, BC self-assembly often takes place under non-equilibrium conditions, giving frozen structures whose size is then related to the mixing time of water and non-selective solvent.<sup>7</sup> Therefore, in order to ensure self-assembly conditions as close as possible to equilibrium, the solvent exchange must ideally proceed through diffusion rather than advection in order to have homogeneous solvent conditions. Control experiments were performed by adding a dye solution at various flow rates which clearly distinguished the injection and diffusion zones in the trough (**Figure 2.8**).

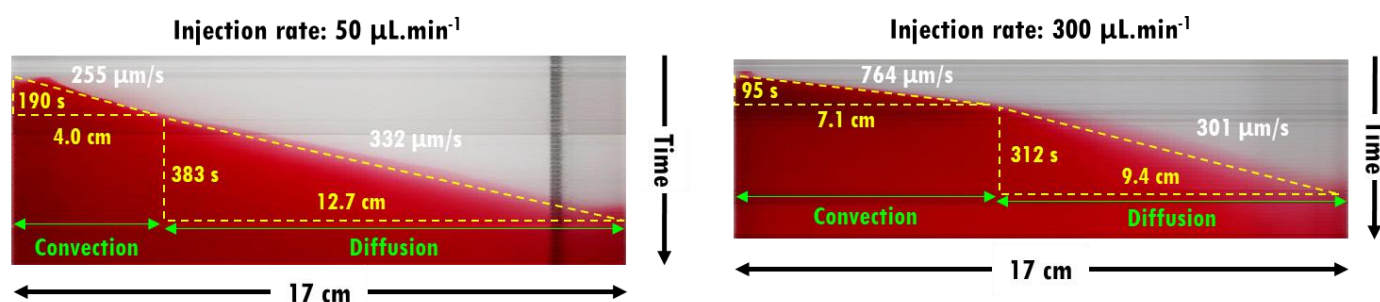


**Figure 2.8.** Diffusion of an aqueous solution of a red dye into the trough containing 8 mL of DMF:THF. A video of the experiment was recorded until the red colour (due to water diffusion) was homogeneous along the 17 cm trough. The videos were converted into frames, whose were stacked (each 70 frames) into orthogonal views using the software Image J. In the image, y axis represents the time while the x axis represents the distance (length of the trough). From the images, one can distinguish between the areas of related to convection (solid lines, due to injection) and diffusion (blurry lines, due to Brownian motion).

The optimal water injection rate was determined as the one generating the largest diffusion zone. One can observe that the injection of 6% of water using 50 or 300 µL.min<sup>-1</sup> generated quite similar diffusion rates, however a smaller injection zone was observed when the injection rate was lower. In order to maximize the sample placement area, this rate was selected for all experiments.

Coming now to the BC bilayer surface self-assembly, first experiments were performed with PS<sub>394</sub>-*b*-PAA<sub>58</sub> using water to trigger the hydrophobic effect. After rinsing and drying, solid-supported bilayers were characterized by ellipsometry in air (**Figure 2.9**). The position of the samples in the 'diffusion zone' in the trough did not appear to significantly affect the bilayer thickness of (14.7 ± 0.2) nm.

In comparison, PS<sub>394</sub>-*b*-PAA<sub>58</sub> bilayers prepared with aqueous NaOH solution (pH 11) have a slightly higher thickness, around (18.0 ± 0.1) nm as determined by ellipsometry (**Figure 2.10**, right). Since the carboxylic acids are fully deprotonated at this pH value, the PAA blocks on the top of the bilayer are certainly stretched due to intra- and intermolecular electrostatic repulsion between charged moieties.<sup>8</sup> When the substrate is removed from the solution and dried, the configuration remains frozen due to the glassiness of the inner PS blocks.

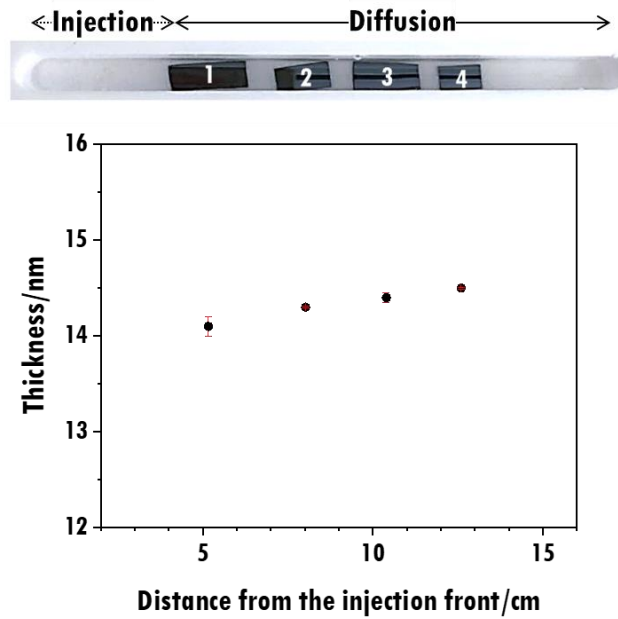
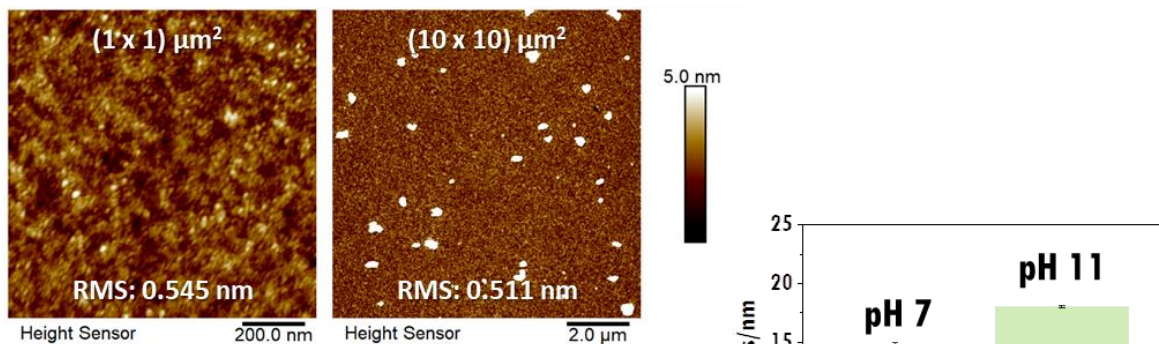


**Figure 2.9.** Illustration of the disposition of the samples in the trough (up) and respective thickness of the dried BC bilayers determined by ellipsometry (down) (error bars in red).

### Water

(pH 7)



### NaOH

(pH 11)

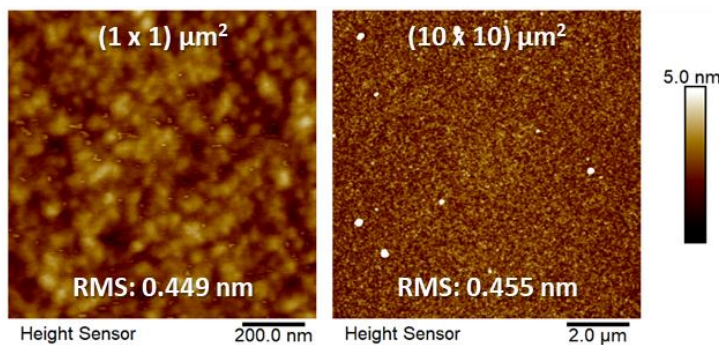


**Figure 2.10.** AFM images of the PS<sub>394</sub>-b-PAA<sub>58</sub> bilayers in air prepared using water (pH 7) (left, top) and NaOH solution (pH 11) to trigger the self-assembly (left, bottom) and respective thickness determined by ellipsometry (right).

Whenever water or NaOH solution was used to trigger the self-assembly, the thickness of the bilayer is systematically much higher than the corresponding monolayer. In fact, the collapsed structure that was obtained for the monolayer has never been observed with the bilayer as the higher polymer density in the bilayer prevents the dewetting of the grafted BCs. As seen by AFM, the bilayers prepared at pH 7 or 11 showed similar and rather smooth and homogeneous surface topography at  $1 \mu\text{m}^2$  scale (**Figure 2.10**, left). However, at larger magnifications ( $100 \mu\text{m}^2$ ), the bilayers prepared with water at pH 7 showed significantly more aggregates than those with aqueous NaOH solution. This evidence confirms that the aqueous NaOH solution promotes electrosteric repulsions between carboxylate groups thus giving more flexibility to BC chains and avoiding their premature aggregation. Following this result, all bilayers were prepared using aqueous NaOH solution at pH 11 in order to minimize the aggregate formation. The bilayers were also analysed by AFM using PeakForce in air and in water. As shown in **Figure 2.11**, the roughness of the bilayer is slightly higher in the aqueous environment. In water, PAA chains on the top of the bilayer are hydrated and swollen, protruding from the surface. Conversely, in air the PAA chains face a “bad solvent” situation and are likely more collapsed on the surface, resulting in a more homogeneous surface.

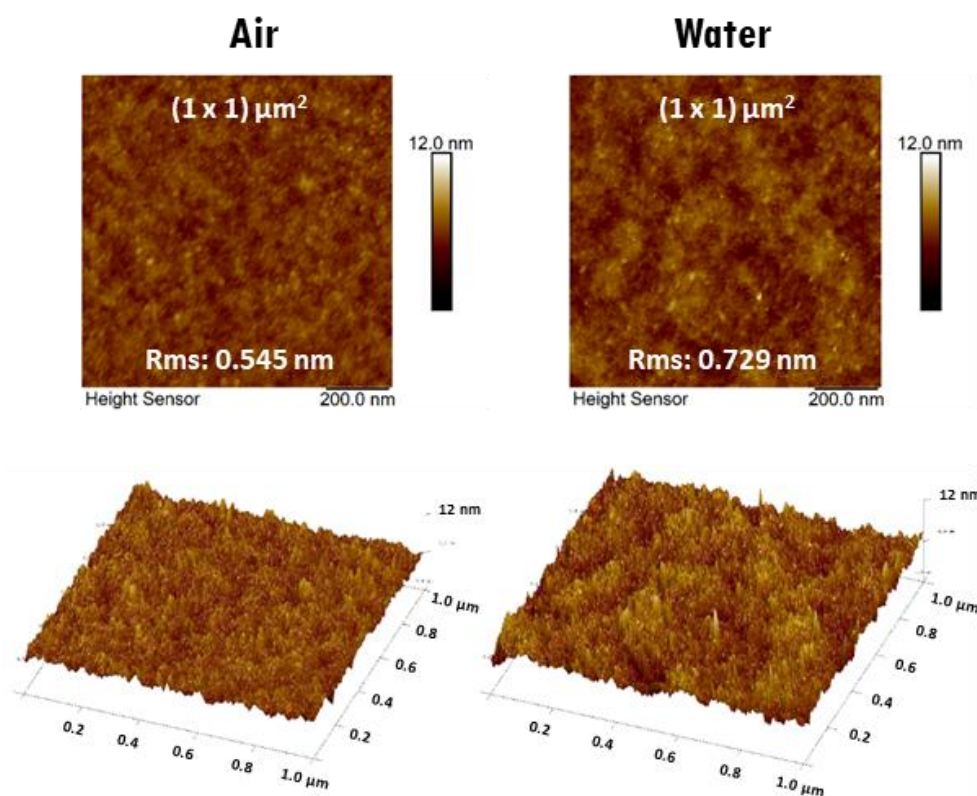


**Figure 2.11.** AFM images (PeakForce) of the PS<sub>394</sub>-b-PAA<sub>58</sub> bilayer in the dry and wet state. NaOH solution at pH11 was used for the self-assembly step.

## 1.2. Bilayer characterization

The monolayers, extensively described in **Chapter 1**, show a relatively low contact angle value due to a low grafting density of the BC which lead to a collapsed heterogeneous islet structure as shown in **Chapter 1 (Figure 1.14)**. Conversely, the density of the bilayers is much higher and the surface topography much more homogeneous as it can be observed by AFM (**Figure 2.10, Figure 2.11**). The water contact angle found for the bilayers is low, which is likely due to the hydrophilic nature of the PAA blocks localized on the structure (**Table 2.1**), especially when NaOH is used to self-assemble BCs since then PAA blocks are under their salt form (PAANa). Lower hysteresis, compared to the monolayer, is consistent with a more homogeneous polymer surface.

**Table 2.1.** Characteristics of the monolayer and the bilayer (in air) for two BC compositions: height measurements by AFM and surface contact angles (advancing, receding water contact angles and calculated hysteresis). NaOH solution at pH11 was used for the self-assembly step.

	Height/nm	$\theta_A$ /degree	$\theta_R$ /degree	$\Delta\theta$ /degree
ML PS <sub>182</sub> - <i>b</i> -PAA <sub>19</sub>	4.1 ± 1 *	67 ± 1	43 ± 3	25 ± 2
BL PS <sub>182</sub> - <i>b</i> -PAA <sub>19</sub>	16.2 ± 0.2**	63.8 ± 0.6	49 ± 2	15 ± 1
ML PS <sub>394</sub> - <i>b</i> -PAA <sub>58</sub>	8 ± 1*	66.05 ± 0.07	33 ± 1	33 ± 1
BL PS <sub>394</sub> - <i>b</i> -PAA <sub>58</sub>	18.0 ± 0.1 **	63 ± 1	40 ± 5	23 ± 3

\*Mean islet height determined by AFM using the 'section' tool in Nanoscope Analysis software. \*\* Height (thickness) of the bilayer determined by ellipsometry and confirmed by AFM scratch.

Bilayers made from a different BC composition, PS<sub>182</sub>-*b*-PAA<sub>19</sub>, were also successfully prepared, even though the size of the PS block ( $M_{PS} = 1.9 \cdot 10^4$  g/mol) was below the critical molecular weight for entanglements in the bulk ( $M_c = 3.2 \cdot 10^4$  g/mol) (**Figure 2.12**).<sup>9</sup> It demonstrates that the hydrophobicity of PS chains rather than their entanglement ensures the cohesion between the upper and lower BC layer. PS<sub>182</sub>-*b*-PAA<sub>19</sub> bilayers showed a decreased thicknesses of (16.2 ± 0.2) nm, to that found for PS<sub>394</sub>-*b*-PAA<sub>58</sub> (**Table 2.1**). In addition, the PS<sub>182</sub>-*b*-PAA<sub>19</sub> bilayers have a slightly lower hysteresis value than PS<sub>394</sub>-*b*-PAA<sub>58</sub> bilayers due to shorter PAA blocks.

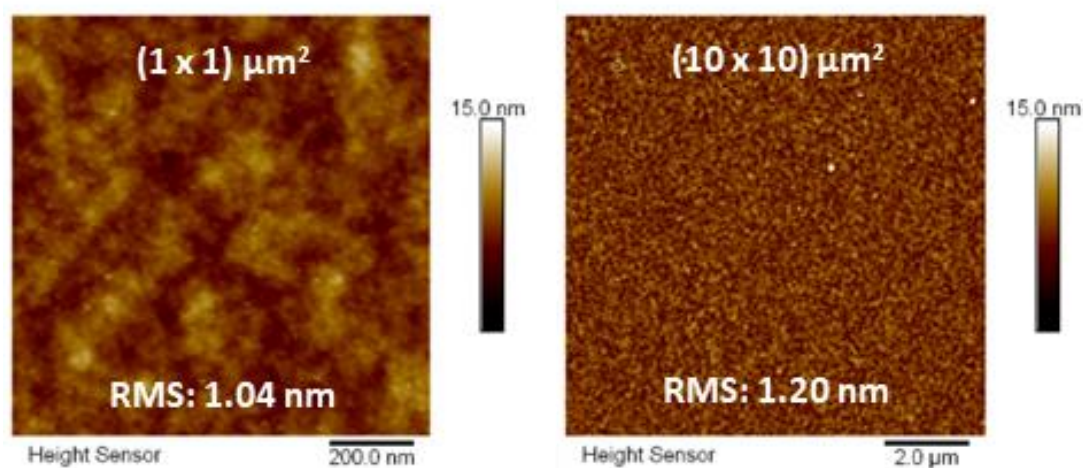


**Figure 2.12.** AFM images of  $PS_{182}$ - $b$ - $PAA_{19}$  bilayers. NaOH solution at pH11 was used for the self-assembly step.

Further evidence that PAA groups form the top of the bilayer was observed by AFM after incubation of  $PS_{394}$ - $b$ - $PAA_{58}$  bilayers with amino-modified PS latex particles, as shown in **Figure 2.13**.

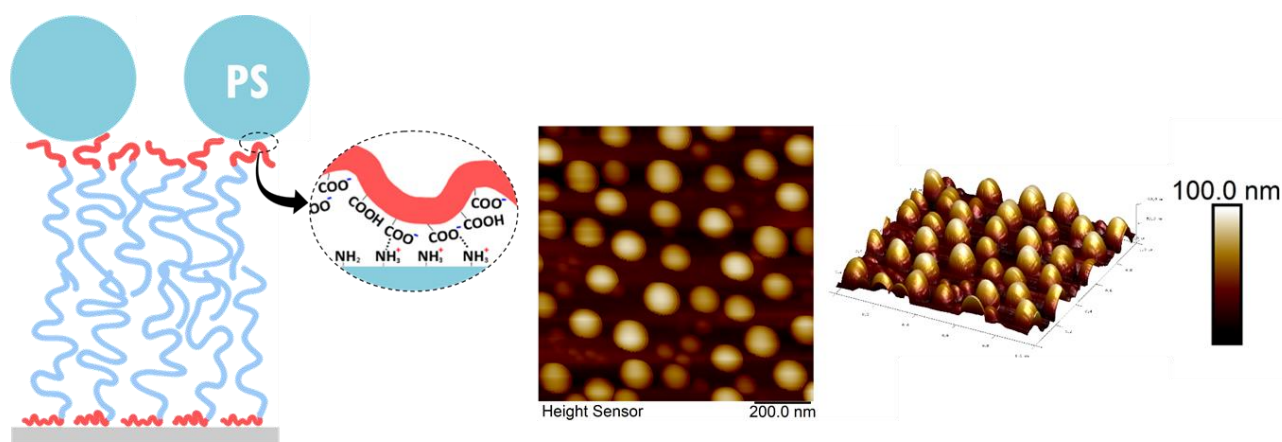


**Figure 2.13.** AFM image a  $PS_{394}$ - $b$ - $PAA_{58}$  bilayer after adsorption of the amino-modified PS latex particles with schematic illustrations demonstrating the PS latex adsorption in aqueous media.

Adsorption only occurs in the bilayer case where electrostatic interactions can develop between the protonated amino groups of latex particles with the carboxylate groups of the PAA blocks. For comparison,  $PS_{394}$ - $b$ - $PAA_{58}$  monolayers after incubation with the latex

particles retain its typical islet structure, showing no adsorption in agreement with the lack of interaction between the PS chains and the latex particles (**Appendix, Figure A3**).

Finally, a comparison between PS<sub>394</sub>-*b*-PAA<sub>58</sub> mono- and bilayers was done by PM-IRRAS (**Figure 2.14**).

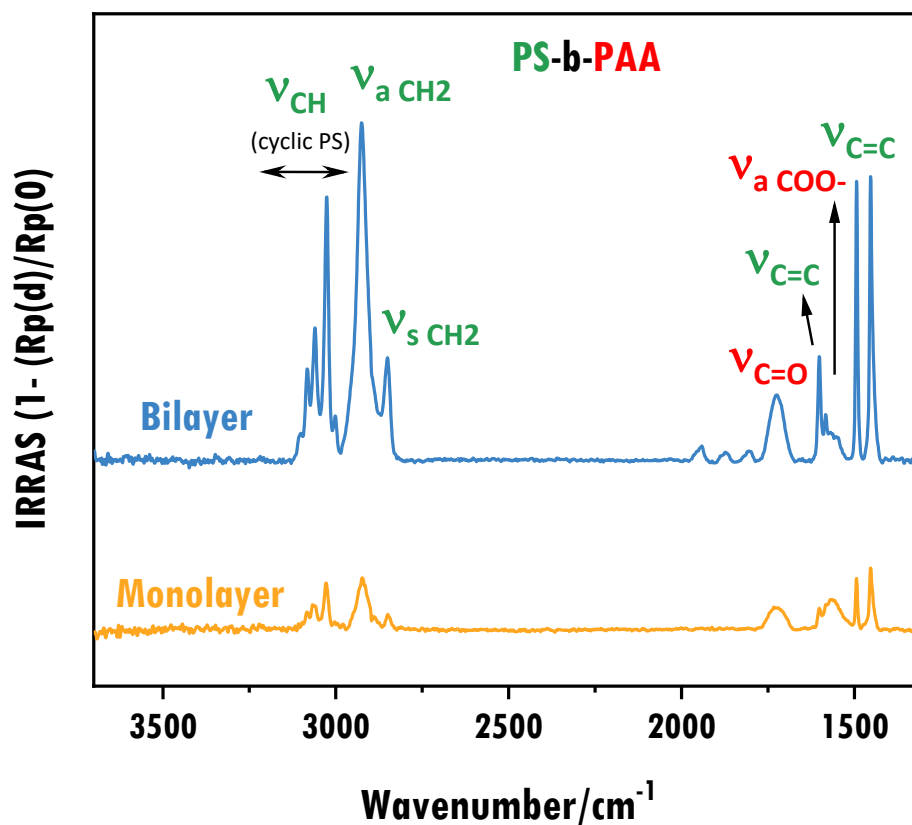


**Figure 2.14.** IRRAS spectra of a PS<sub>394</sub>-*b*-PAA<sub>58</sub> mono- and bilayer. Assignments in green are related to PS, while assignments in red are related to PAA groups.

Taking into account the PS-related bands, the average peak area values of monolayers (or bilayers) were obtained by measuring peak areas of two different samples. Specifically, three wavenumber ranges were considered for the analysis: 3130 – 2800 cm<sup>-1</sup> (related to CH stretching of PS aromatic rings and to the CH<sub>2</sub> asymmetric and symmetric stretching), 3130-2985 cm<sup>-1</sup> (related only to CH stretching of PS aromatic rings) and 1502-1480 cm<sup>-1</sup> (related to one peak of the C=C stretching). A detailed assignment of the spectra is shown in **Table 2.2**.

Table 2.2. IRRAS assignment.

Wavenumber range	Peak assignment
3130 – 2800 cm <sup>-1</sup>	3130 – 2985 cm <sup>-1</sup> : C-H (aromatic ring), $\nu_{\text{CH}}$
	CH <sub>2</sub> asymmetric ( $\nu_{\text{a,CH}_2}$ : 2925 cm <sup>-1</sup> ) and symmetric ( $\nu_{\text{s,CH}_2}$ : 2850 cm <sup>-1</sup> )
1786 – 1672 cm <sup>-1</sup>	C=O ( $\nu_{\text{CO}}$ : 1726 cm <sup>-1</sup> )
1624 – 1519 cm <sup>-1</sup>	C=C ( $\nu_{\text{C=C}}$ : 1601 cm <sup>-1</sup> )
	Asymmetric COO <sup>-</sup> ( $\nu_{\text{COO}^-}$ : 1563 cm <sup>-1</sup> )
1502 – 1421 cm <sup>-1</sup>	C=C ( $\nu_{\text{C=C}}$ : 1493 and 1453 cm <sup>-1</sup> )

Next, the ratio of monolayer peak area to bilayer peak area for each specific wavenumber range was obtained. An overall average, considering the individual averages for each range of wavenumbers, was then calculated. The values are summarized in Table 2.3.

Table 2.3. Calculated peak areas of PS<sub>394</sub>-b-PAA<sub>58</sub> mono- and bilayers and averaged values. # represent different samples (duplicate).

	3150 – 2800 cm <sup>-1</sup>	3130-2985 cm <sup>-1</sup>	1502-1480 cm <sup>-1</sup>
Monolayer (#1)	0.1329	0.0458	0.0098
Monolayer (#2)	0.1311	0.0479	0.0109
<b>Monolayer (average peak area)</b>	<b>0.1320</b>	<b>0.0469</b>	<b>0.0103</b>
Bilayer (#1)	0.7495	0.2458	0.0583
Bilayer (#2)	0.8129	0.2684	0.0618
<b>Bilayer (average peak area)</b>	<b>0.7812</b>	<b>0.2571</b>	<b>0.0601</b>
<b>Monolayer : Bilayer</b>	<b>5.92</b>	<b>5.49</b>	<b>5.83</b>
	<b>Bilayer = 5.75x Monolayer</b>		

It is observed that the bilayers have a peak area 5 times larger than that of the monolayers. As well known, the orientation of the chemical groups at the substrate strongly influences the intensity of the absorption bands in PM-IRRAS measurements: maximum absorption occurs when the groups are oriented perpendicularly to the substrate, whereas negligible absorption is measured when the chemical groups considered are oriented parallel to the surface. Figure 2.15 illustrates this surface selection rule.

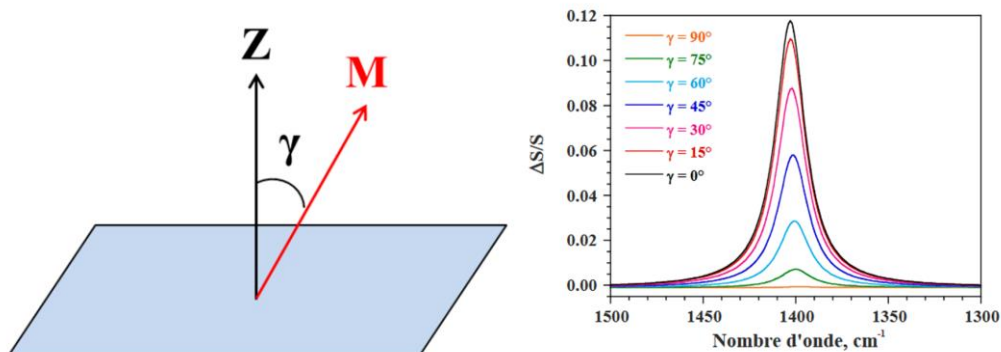


**Figure 2.15.** Exemplification of the surface selection rule. The image is reproduced from ref. 10.

The strong increase in intensity observed for the bilayer could then be related to either a greater amount of PS groups and/or a change in orientation of the PS chains (same for PAA blocks). Indeed, as observed by AFM, a much higher grafting density is observed for the bilayers, as no dewetting takes place. One can imagine that the PS chains in the hydrophobic reservoir are much more stretched, and, thus, an increase in the intensity due to a change in orientation is reasonable. Additionally, the bilayer obviously has another layer of BC, which explains the increase in band intensity.

However, the increase in intensity is much more than double (which would be expected, for instance, if we considered a dense BC monolayer and a similar layer being deposited at the top – which is not exactly our case but not too far from it), and thus additional phenomena must be related to this intensity increase. At this stage, no other potential explanation has been put forward and that is why additional NR analyses were performed. Note that the hypothesis of a multilayer system is completely ruled out there, since there is no physical/chemical reason for another BC layer to form on the top of the bilayer.

## 1.3. Advanced bilayer characterization with NR

### 1.3.1. Bilayer thickness

Taking advantage of the isotopic contrast experiments available on neutron-based techniques, NR was performed with  $\text{PS}_{394}\text{-}b\text{-PAA}_{58}$  bilayers prepared with BC containing either a hydrogenated or deuterated PS block. As the variation of the scattering length density (SLD) can be monitored through the bilayer (in the z-direction), 2 different configurations were studied, in which alternatively a deuterated (or hydrogenated) BC was used in the first step

(monolayer formation) and a hydrogenated (or deuterated) BC was used at the second step (bilayer formation), allowing the generation of mixed hydrogenated/deuterated bilayers as schematically presented in **Figure 2.16**.

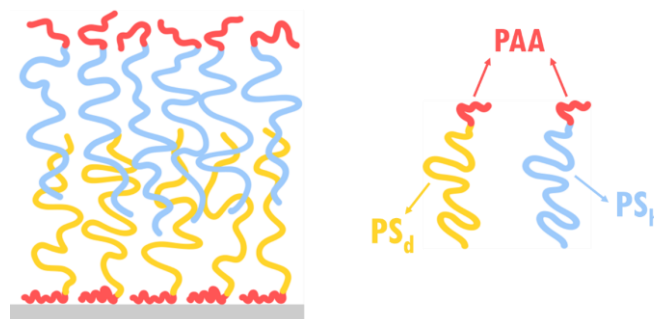


**Figure 2.16.** Schematic representation of a type of hydrogenated/deuterated  $PS_{394}\text{-}b\text{-}PAA_{58}$  mixed bilayer, with a bottom layer consisting of a BC containing a d-PS block and a top layer of a BC containing a h-PS block. The PAA block is hydrogenated in both situations.

NR curves of symmetric ( $PS_d\text{-}b\text{-}PAA$  and  $PS_h\text{-}b\text{-}PAA$ ) and asymmetric ( $PS_d\text{-}b\text{-}PAA/PS_h\text{-}b\text{-}PAA$  or  $PS_h\text{-}b\text{-}PAA/PS_d\text{-}b\text{-}PAA$ ) bilayers are shown in **Figure 2.17**.

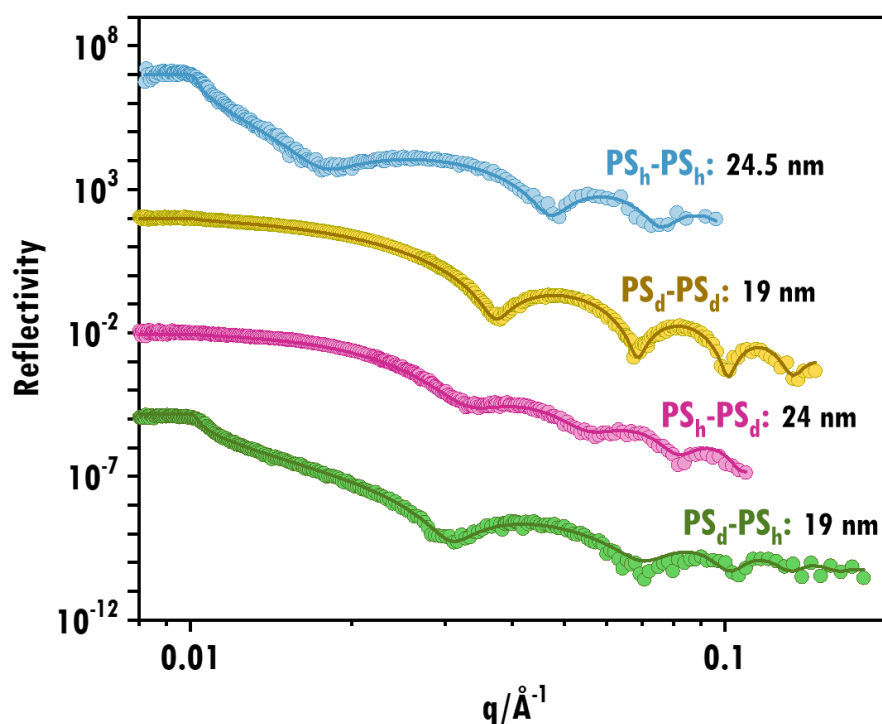


**Figure 2.17.** NR curves of  $PS_{394}\text{-}b\text{-}PAA_{58}$  bilayers in air prepared using only hydrogenated BC ( $PS_h\text{-}PS_h$ ) and deuterated ( $PS_d\text{-}PS_d$ ) and d/h or h/d mixed bilayers ( $PS_d\text{-}PS_h$ , for the bilayers prepared using deuterated PS for the first and hydrogenated PS for the second layer; and  $PS_h\text{-}PS_d$  for the inverse). The curves were shifted in the reflectivity axis for clarification.

From a fit of the NR curves, the overall layer thickness obtained (shown in the graph) appears to be in agreement with the previous findings using ellipsometry or AFM cutting.

It can be noticed, however, that fully hydrogenated ( $PS_h$ - $b$ -PAA) bilayers or the asymmetric ones prepared using a hydrogenated BC for the first monolayer ( $PS_h$ - $b$ -PAA/ $PS_d$ - $b$ -PAA) are thicker ( $\ell \sim 24$  nm) than the fully deuterated ( $PS_d$ - $b$ -PAA) bilayers or the asymmetric ones prepared using deuterated BC for the first monolayer ( $PS_d$ - $b$ -PAA/ $PS_h$ - $b$ -PAA) ( $\ell \sim 19$  nm). The thinner bilayers prepared using deuterated BC may be a result of a low BC grafting density, as it was observed that the AFM image of the deuterated BC monolayers does not show the islet pattern (**Appendix, Figure A4**).

One can also observe that the bilayer morphology seems to be independent on the deuterated/hydrogenated nature of the BCs (similar thickness were observed between  $PS_h$ - $b$ -PAA and  $PS_d$ - $b$ -PAA/ $PS_h$ - $b$ -PAA bilayers, or between  $PS_d$ - $b$ -PAA and  $PS_d$ - $b$ -PAA/ $PS_h$ - $b$ -PAA bilayers), meaning that the interactions taking place between the BC and the substrate and between the BC layers are not dependent on the PS isotope. Apart from being analysed in air, the bilayers were also analysed in deuterated water ( $D_2O$ ), as shown as example a mixed  $PS_d$ - $b$ -PAA/ $PS_h$ - $b$ -PAA bilayer in **Figure 2.18**.

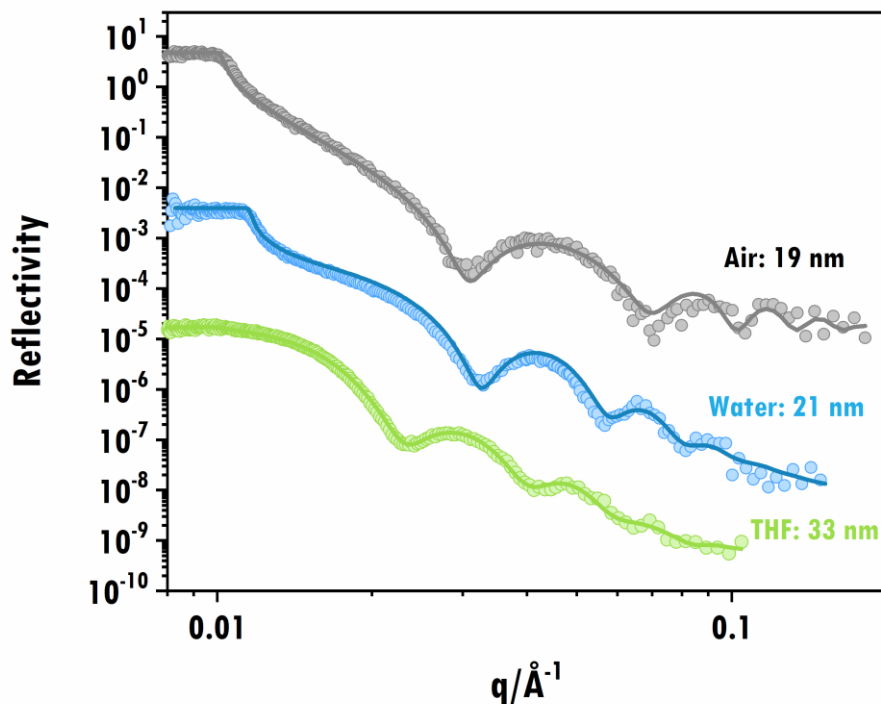


**Figure 2.18.** NR curves of  $PS_{394}$ - $b$ - $PAA_{58}$  bilayers in air, water and vapour of THF. The example shown is referred to the asymmetric bilayer  $PS_d$ - $b$ -PAA/ $PS_h$ - $b$ -PAA.

No significant thickness difference is observed when the bilayer is in water or in air meaning that both situations are considered as bad solvent conditions for the bilayer. On the other hand, the thickness of the BC bilayer increased when the sample was exposed to THF vapour, which is expected as THF is a good solvent for the BC, with a swelling ratio of 1.7. At this point, the different thicknesses obtained for PS<sub>394</sub>-*b*-PAA<sub>58</sub> mono- and bilayers due to different BC conformations can be discussed. **Figure 2.19** shows schematic illustrations of the BC mono- and bilayers conformations in air (“bad solvent”) and in THF with the overall layer thickness determined by NR, apart from the ML in air, which was determined by AFM (**Chapter 1**). Importantly to note, in order to keep the integrity of the BC bilayer, the analysis was performed in vapour of THF instead of immersion in the solvent.

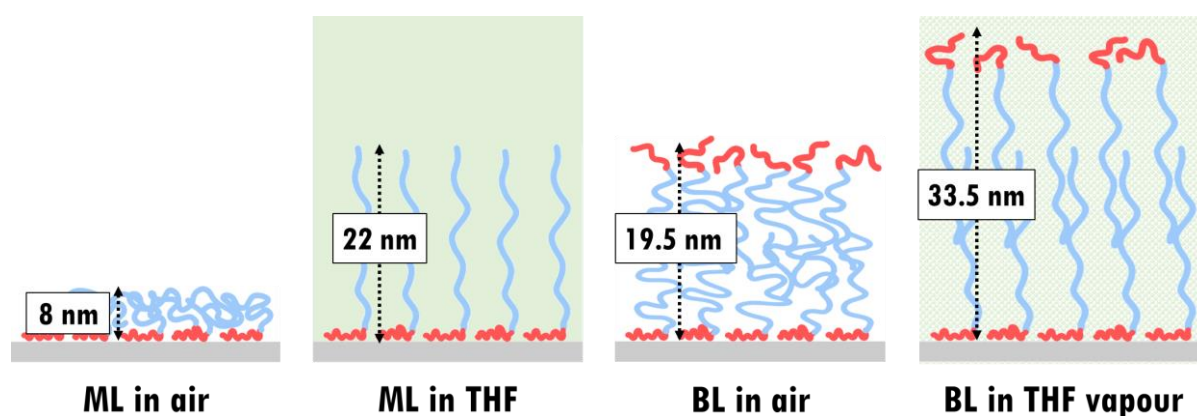


**Figure 2.19.** Schematic illustrations of a PS<sub>394</sub>-*b*-PAA<sub>58</sub> monolayers in air and in THF, and PS<sub>394</sub>-*b*-PAA<sub>58</sub> bilayers in air and in THF vapour, with its respective thickness values obtained by NR (in the case of the monolayer in air, the value shown was obtained by AFM as the height of the islet).

In the case of the BC monolayers, it has already been discussed in **Chapter 1** that, in air, an islet pattern with height of  $\sim 8$  nm is observed due to the dewetting of PS chains, a direct result of the relatively low BC grafting density. When the BC monolayer is immersed in THF, the PS chains adopt the most stretched conformation in order to maximize the contact with the good solvent: the BC monolayer thickness increases up to 22 nm, indicating a swelling ratio of 2.75. The swelling ratio observed for the monolayer is much larger than the one observed for the bilayer (1.76) mainly because of the difference in density: the monolayers are less dense, and thus, have less constraints to swell.

One can observe, however, that the thickness observed for the BC monolayer in THF ( $\sim 22$  nm) is quite comparable to the thickness of the BC bilayer in air ( $\sim 19.5$  nm). This result

could suggest a very strong interpenetration of the BC chains in the bilayer: hypothetically, the top layer of BC, being completely stretched, practically penetrates the bottom layer (also completely stretched) up to reach the substrate. At first, since the grafting density of the BC monolayer (bottom layer) is not very high, one could state that the second layer (top layer) could have plenty of room to penetrate; however, this highly pronounced interpenetration of stretched BC chains is very unlikely to take place. In fact, the thickness value observed for the BC bilayer in air is thought to be a sum of partial contributions of: **1) the interpenetration of BC chains** and **2) the collapse of the BCs when exposed to a “bad solvent” condition (air)**. As certainly a partial entanglement of the BC chains take place (otherwise the BC bilayers would not be kept together when passing from the air-water interface, for instance), the density of the BC bilayer, even if much higher than the one of the BC monolayer, still allows a partial collapse of the bilayer structure to air in order to minimize the contact with air. Indeed, when the BC bilayer is exposed to THF vapour, one can observe that the thickness increases up to  $\sim 33.5 \text{ nm}$ , which supports the previous statements. For instance, if a hypothetical thickness value of  $\sim 44 \text{ nm}$  was observed for the BC bilayer exposed to THF vapour (that is, exactly twice the thickness of the ML in THF), one could state that no interpenetration takes place in the BC bilayer: simply, the BC top layer would be built at the very end of the BC bottom layer. The measured value of the BC bilayer exposed to THF vapour, with a thickness value  $\sim 10.5 \text{ nm}$  less than this “hypothetical” situation confirms the fact that a partial interpenetration of PS chains take place. The overall increase on the BC bilayer when exposed to THF is then due to the swelling of the PS chains in both bottom and top layer.

### 1.3.2. Variation of the monomer volume fraction

Even more important than discussing only about the BL thickness values, with NR one can extract much more valuable information (by fitting) in the case of the mixed h/d bilayers, that is the variation of the scattering length density (SLD) perpendicular to the substrate and along the bilayer thickness. Since the experimental SLD of such system is a sum of the partial contributions of each of the deuterated and hydrogenated layers:

$$SLD_{total} = SLD_{d-PS} \phi(z)_{d-PS} + SLD_{h-PS} \phi(z)_{h-PS} \quad \text{Eq. 2}$$

where  $\phi(z)$  is the volume fraction at the  $z$  direction of deuterated and hydrogenated styrene monomers ( $\phi(z)_{d-PS} + \phi(z)_{h-PS} = 1$ ), one can obtain the  $z$ -variation of the volume fraction of both hydrogenated and deuterated monomers from the NR curves (**Figure 2.17**) as shown in **Figure 2.20**.

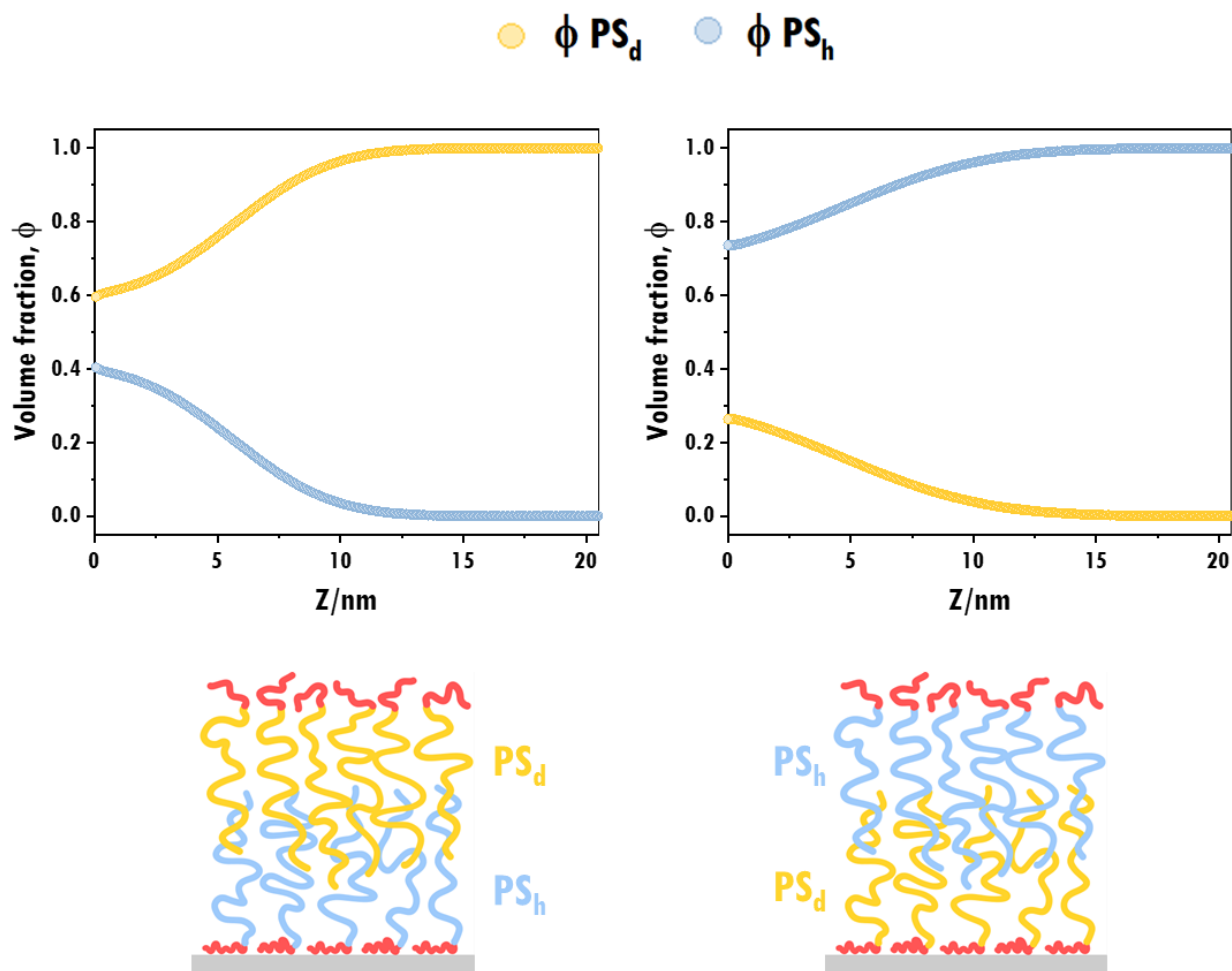


**Figure 2.20.** Variation of the volume fraction  $\phi(z)$  of both deuterated and hydrogenated styrene monomers in the mixed h/d bilayers.

Strikingly, it can be observed that for values very close to the substrate ( $z \approx 0$ ), the volume fraction of monomers from the top layer is far from zero for both bilayers. This suggests, at first, a very pronounced interdigitation of the BC chains. It can also be noticed that volume fractions of  $PS_h$ -*b*-PAA/ $PS_d$ -*b*-PAA and  $PS_d$ -*b*-PAA/ $PS_h$ -*b*-PAA bilayers are not symmetrical: for the bilayer prepared using h-PS for the monolayer, a  $\phi$  h-PS  $\sim 0.4$  is observed at  $z \approx 0$  (**Figure 2.20**, left), while for the bilayer prepared using d-PS for the monolayer, a  $\phi$  d-PS  $\sim 0.25$  is observed at  $z \approx 0$  (**Figure 2.20**, right). This finding, together with the lower BL

thickness of fully deuterated bilayers or those prepared using d-PS for the bottom layer (monolayer), confirms the lower grafting density of PS<sub>d</sub>-*b*-PAA.

Considering the PS<sub>h</sub>-*b*-PAA/PS<sub>d</sub>-*b*-PAA bilayer, one can observe a neat contribution of d-PS at values very close to zero ( $\phi_{d-PS} \sim 0.6$ ), even higher than the contribution of h-PS that is the BC forming the monolayer (bottom layer). As previously mentioned, this suggests a highly interpenetrated bilayer, with d-PS chains from the top layer reaching the substrate, even though this hypothesis is very unlikely to take place. A possibility that could explain both the lack of a pure contribution of hydrogenated (or deuterated) BC in the bottom layer and the fact that the composition of the "second layer" (top layer) is always greater at  $z \approx 0$  would be that the monolayer was modified before that the bilayer was formed. Specifically, the proposed hypothesis is that the BC bottom layer contains a mixture of deuterated and hydrogenated BCs. This mixed d/h BC bottom layer would be a result of the densification of the first hydrogenated monolayer with deuterated BCs (or vice versa). The densification process would not take place through interactions between the free BCs in solution and the amino-modified substrate since, as shown by the QCM experiments in **Chapter 1**, the BC adsorption is maximal for monolayer formation. Rather, it may show that free acid groups of BC in solution could interact through hydrogen bonding with the PAA blocks belonging to the first adsorbed monolayer (bottom layer). As previously shown by PM-IRRAS in **Chapter 1**, 42.5% of the acrylic acid groups were still under their protonated form in the monolayer. A schematic illustration of the composition of the asymmetric bilayer considering the densification hypothesis is shown in **Figure 2.21**.

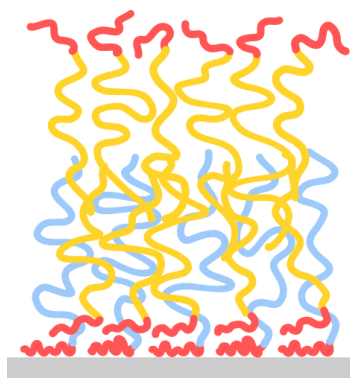


**Figure 2.21.** Schematic illustration of a PS<sub>394</sub>-*b*-PAA<sub>58</sub> asymmetric (PS<sub>h</sub>-*b*-PAA/PS<sub>d</sub>-*b*-PAA) bilayer: the adsorbed BC monolayer is composed of h-PS, shown in blue; BC containing d-PS (shown in yellow) was used to generate the bilayer, which first includes densification of the adsorbed monolayer likely by hydrogen bonding between PAA groups, followed by formation of the top layer as a result of the hydrophobic effect.

This assumption satisfies both NR and PM-IRRAS results. If a monolayer densification step takes place followed by bilayer formation, one would expect that more than twice the amount of BC would be required to form the final system. This would be in perfect agreement with PM-IRRAS results, which indicate a more than 5-fold increase in PS band intensity from the monolayer to the final bilayer structure. Importantly to note, the previous statements of PM-IRRAS data analysis of increased intensities due to the change in PS group configuration still hold true.

Unfortunately, this hypothesis of densification was not directly explored using NR, but strong evidences were obtained from the behavior of the  $\text{PS}_d\text{-}b\text{-PAA}/\text{PS}_h\text{-}b\text{-PAA}$  bilayer immersed in d-THF. As the second hydrogenated BC layer (top layer) is held together with the first deuterated layer by hydrophobic interactions, when the bilayer is immersed in non-selective solvent (d-THF), the top layer should be completely dissolved resulting in a deuterated BC monolayer. Such resulting layer would typically show no reflectivity signal, as the SLD values of d-PS and d-THF are quite similar ( $\text{SLD}_{\text{d-THF}} \approx \text{SLD}_{\text{d-PS}} \approx 6.35$ ). Surprisingly, an NR curve is obtained as shown in **Figure 2.22**, which necessarily implies that hydrogenated BC is present in the resulting layer to give rise to an SLD contrast.

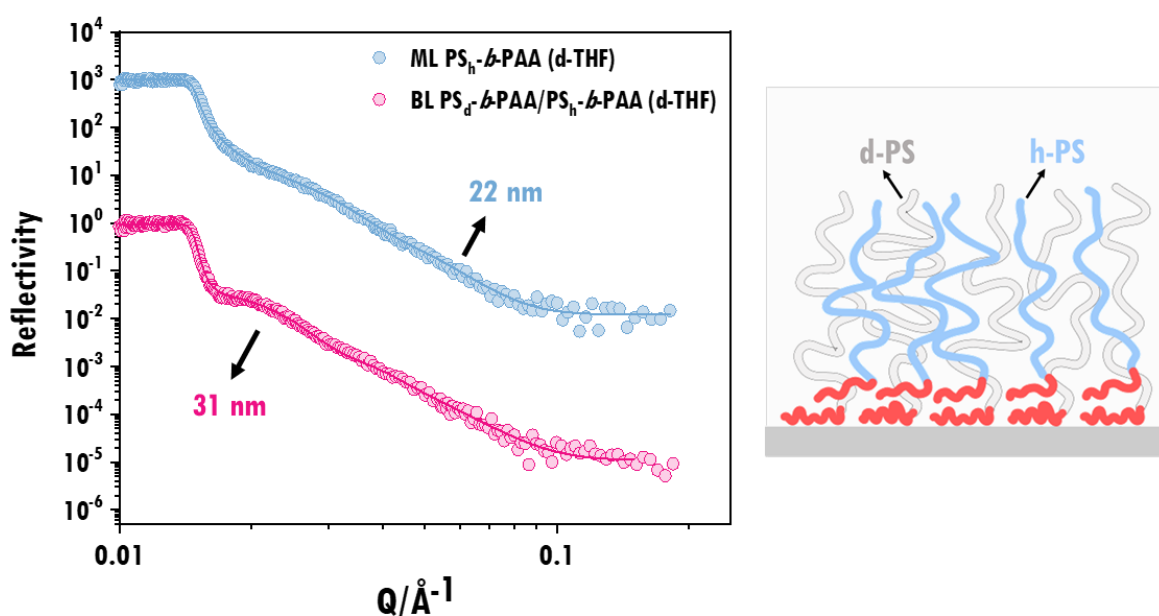


**Figure 2.22.** NR curves of  $\text{PS}_{394}\text{-}b\text{-PAA}_{58}$  monolayer (hydrogenated BC) and  $\text{PS}_{394}\text{-}b\text{-PAA}_{58}$  bilayer (deuterated/hydrogenated) immersed in d-THF (left). The curves have been translated for clarity. On the right, a schematic representation of the mixed h/d monolayer is proposed, where only h-PS chains are visible due to the contrast matching of d-THF and d-PS.

Curve fitting results in a thickness of  $\sim 31$  nm for the densified monolayer, in contrast to the monolayer thickness of  $\sim 22$  nm under the same conditions (immersed in THF) (**Chapter 1**). This layer, which is neither a monolayer nor a bilayer, is a mixture of deuterated and hydrogenated BC. Together with results from various other techniques (AFM, water contact angle measurements, QCM and PM-IRRAS), the NR findings supported the hypothesis that the densification of the monolayer occurs in the early stages before to the bilayer formation. All these results are summarized and analyzed in **Chapter 3**, dedicated to this “densification” phenomenon observed with PS-*b*-PAA copolymers.

## 2. Optimization of the BC self-assembly process

Some preliminary tests on the process optimization of PS<sub>394</sub>-*b*-PAA<sub>58</sub> bilayers, notably in terms of rinsing, *i.e.* the amount of water needed and the total rinsing time, were performed. The rinsing step is required to completely change the solvent nature (from non-selective to water) and to remove the BC aggregates formed in solution. The process involves the simultaneous injection and removal of pure water or NaOH solution, depending on the solution used to trigger the bilayer self-assembly. **Figure 2.23** illustrates the substrate at different stages of the rinsing step using optical microscopy and AFM.

It can be observed that the samples just after overnight and before the start of rinsing are quite clean (**Figure 2.23**, I). Indeed, the amount of water added to trigger self-assembly is very close to the critical water content, *i.e.*, self-assembly has probably taken place in the solution and on the surface of the substrate, but the formation of frozen structures has not yet been reached as the water content is still low. Looking at the respective AFM image of the sample, it can be observed that the substrate’s surface is still quite irregular, with some areas indicating the presence of a bilayer by a continuous surface, while others areas do not. Therefore, it can be concluded that the BC surface self-assembly was not completed at this stage.

In step II, where 12 mL of aqueous NaOH solution were added and removed from the 8 mL of BC solution filling the trough, the BC structures can be considered frozen, as the water content was quite high ( $> 60\%$ ); indeed, a continuous surface topography (with some aggregates) can be observed by AFM. However, optical images reveal that the substrate has a

dirty aspect, with irregularly attached BC films (for information, the AFM images were intentionally taken in the bright/clean areas).

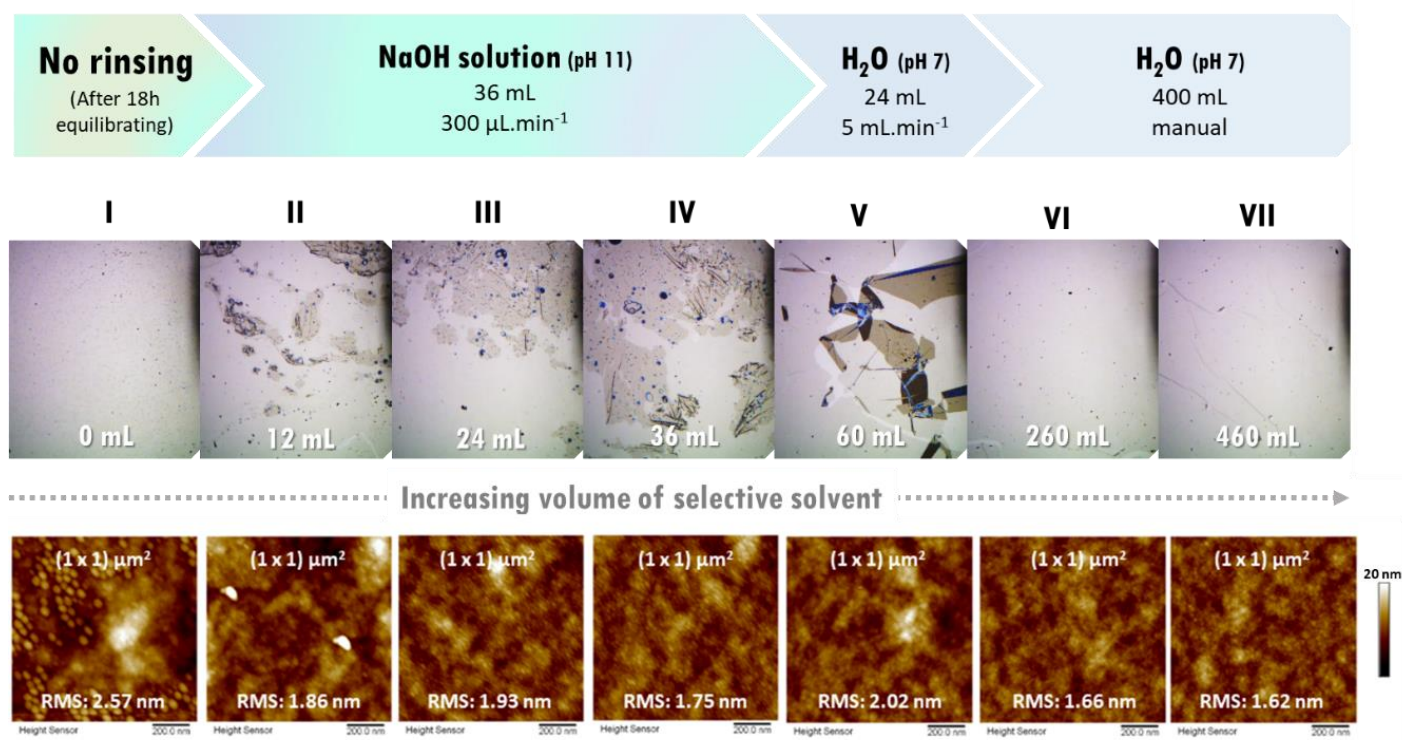


**Figure 2.23.** Optical images illustrating the substrate surface before and during the rinsing steps. The first image (I) represents the substrate removed from the trough after injection of 5% of water and equilibrium for 18h (overnight), i.e. without any rinsing with NaOH solution/water. The images from II to VII are related to different stages of the rinsing step, showing in the bottom of each optical image the total amount of NaOH/water that was used for the rinsing. The stage VII represents the sample after the complete rinsing step, where a total of 460 mL of aqueous NaOH/water was injected and removed. Each of the steps from I to VII is described by an optical image of the substrate and a respective AFM image, showed at the bottom.

As rinsing continues, the sample retains the continuous and homogeneous topography seen by AFM (**Figure 2.23**, III to V); however, the substrate is still visibly dirty until the step V meaning that: **1)** excess BC has self-assembled in solution leading to large and frozen aggregates; and **2)** the volume of water for rinsing is not enough to remove them from the trough. After that, the images shown in steps VI and VII, are quite homogeneous (as seen by AFM) and clean (as seen by optical images). No significant difference is observed between steps VI and VII, leading to the conclusion that the rinsing step might be terminated at step VI, *i.e.*, using 200 mL less water. Step VI is achieved when a total of 260 mL of selective solvent (NaOH aqueous solution + water) is added. As specified in **Figure 2.23**, a total of 260 mL of solvent added includes steps of injection and withdrawn with increasing rates (300 μL.min<sup>-1</sup> (36 mL), 5 mL.min<sup>-1</sup> (24 mL) and manual (200 mL)).

After this finding, a successful attempt to speed up the rinsing process was made by introducing the first rinsing step at a rate of 5 mL.min<sup>-1</sup> using only 12 mL, followed by a manual rinsing. **Figure 2.24** shows the result of this brief process optimization.

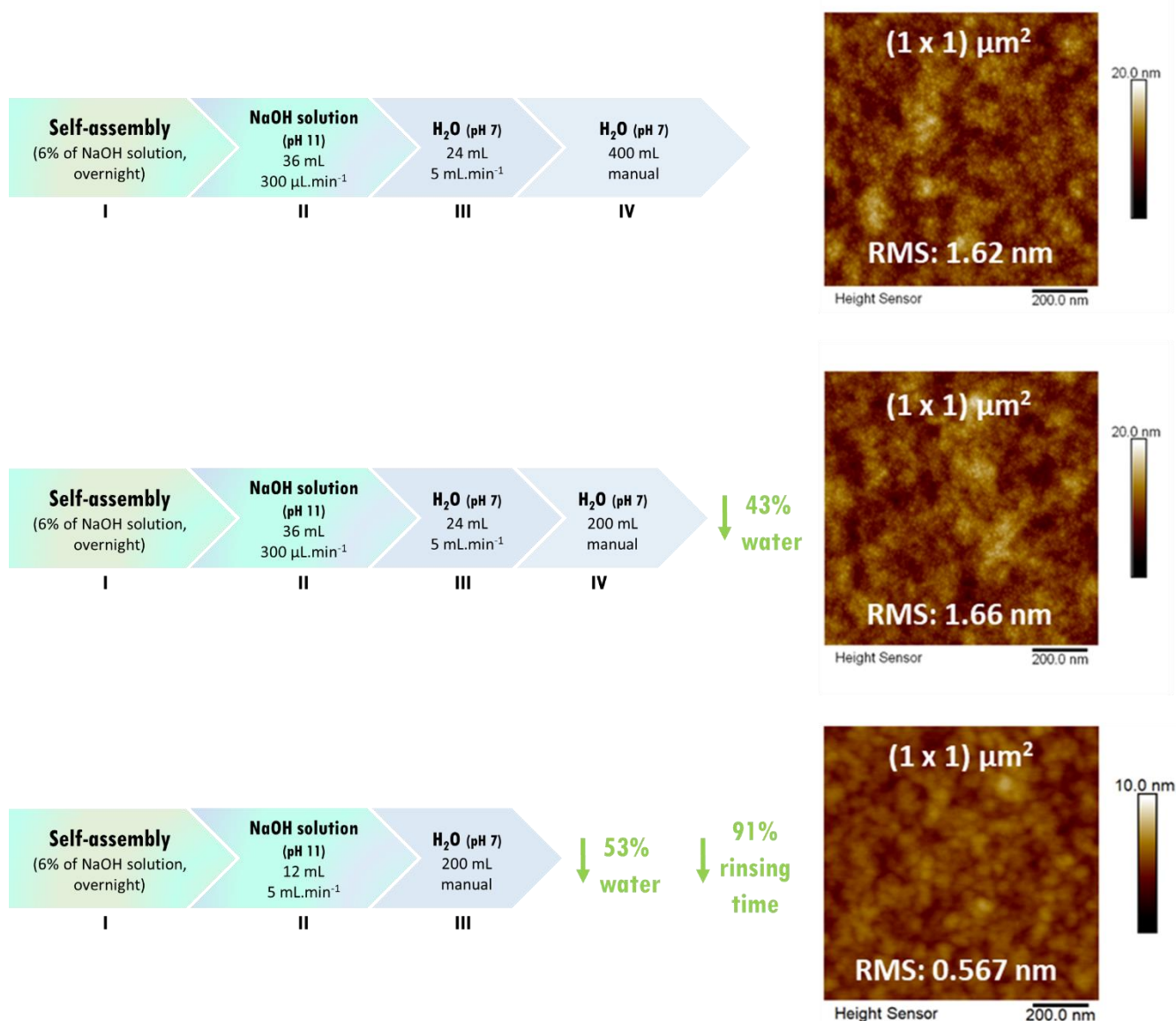


**Figure 2.24.** Protocols for improving the rinsing step. Top, the standard process; middle, an improved process reducing the amount of water during manual rinsing; and, bottom, the most successful process minimizing not only the amount of water but also the time spent rinsing. The AFM images shown on the right side of the image illustrate the bilayers obtained after each process.

To conclude, parameters such as the amount and ratio of water used to trigger the BL self-assembly, the waiting time and the rinsing were crucial for the generation of smooth and homogeneous BC bilayers. The rate of water addition must be slow, as described in **Figure 2.8**, in order to obtain a large diffusion zone, that is, to maximize the area for sample placing. The amount of water to trigger the BL self-assembly must be higher than the *cwc* value but still

close to this value in order to avoid the formation of BC aggregates in solution. After the addition of water, an equilibration time is required for the selective solvent to be evenly distributed (diffused) through all of the trough, triggering the self-assembly – if the rinsing step starts just after the addition of the selective solvent, heterogeneous bilayers are obtained. Even if 18 h (overnight) was fixed in this thesis for the generation of the BC bilayers, it has been demonstrated that the bilayers can be formed from 1 h of equilibration (**Appendix, Figure A5, Figure A6**). In any case, after the equilibration the BC bilayers are not completely formed because the amount of water in the system is still low (close to *cwc*): higher amounts of water are required to freeze the system, which will likely take place during the rinsing step. As long as the equilibration time is respected, the rinsing step can be performed with increase ratios of water injection/removal, resulting in homogeneous BC bilayers, as shown in **Figure 2.24** (bottom).

## Conclusions

---

The proposed fabrication method of solid-supported amphiphilic BC bilayers involves two steps: first, the adsorption of a BC monolayer in a non-selective solvent through specific interactions between the hydrophilic block and the substrate (deeply described in **Chapter 1**); and second, the self-assembly of BC in solution with those forming the adsorbed monolayer, taking place after the introduction of a selective solvent (water) which will change the polarity of the medium and trigger interactions between the BC hydrophobic blocks (explored in this chapter).

The self-assembly of BCs, known to be an out of equilibrium process, is highly dependent on many processing parameters, being the amount of water used to trigger the self-assembly the most critical one: it has to be enough to change the polarity of the system and thus trigger the BC formation (higher than *cwc*) at the interface, while it cannot be too large otherwise a pronounced formation of BC aggregates in solution takes place. A systematic injection and removal of water (named rinsing step) after the injection of water (and equilibration time) allows not only the removal of such aggregates formed in solution but also to “freeze” the structure of the BC bilayer formed at the interface, resulting in smooth and homogeneous bilayers.

The solid-supported PS-*b*-PAA bilayers could be prepared using BCs containing PS blocks above or below its critical entanglement mass, suggesting that hydrophobic interactions participate greatly to the bilayer integrity through a good cohesion between the layers. Additionally, the thickness of the BC bilayer can be tuned by using different  $M_w$  BCs.

It has been observed a certain level of entanglement (interdigitation) between the BCs when comparing the thickness of the BC bilayers (swollen in d-THF vapour) with the BC monolayers (swollen in THF): the thickness of a swollen bilayer is lower than the thickness of a swollen ML multiplied by two. Additionally, the conformation of the BC bilayer highly changes when the bilayer is exposed to air or d-THF vapour, indicating that a collapse of the structure takes place in contact to a bad solvent situation (or, in other words, that the bilayer is able to swell in the presence of d-THF vapour).

Last but not least, findings obtained by PM-IRRAS and NR experiments suggested that the presence of an additional intermediate step between the mono- and bilayer formation, named “the densification of the monolayer” step, which takes place at early steps of water addition (below reaching the cwc). Further evidences and discussion about this topic will be done in **Chapter 3**.

## References

- (1) Bourgès, C.; Shanahan, M. E. R. Influence of Evaporation on Contact Angle. *Langmuir* **1995**, *11*, 2820–2829. <https://doi.org/10.1021/j100218a018>.
- (2) Shanahan, M. E. R.; Bourgès, C. Effects of Evaporation on Contact Angles on Polymer Surfaces. *Int. J. Adhes. Adhes.* **1994**, *14* (3), 201–205. [https://doi.org/10.1016/0143-7496\(94\)90031-0](https://doi.org/10.1016/0143-7496(94)90031-0).
- (3) Buffeteau, T.; Desbat, B.; Turlet, J. M. Polarization Modulation FT-IR Spectroscopy of Surfaces and Ultra-Thin Films: Experimental Procedure and Quantitative Analysis. *Appl. Spectrosc.* **1991**, *45* (3), 380–389. <https://doi.org/10.1366/0003702914337308>.
- (4) Buffeteau, T.; Desbat, B.; Blaudez, D.; Turlet, J. M. Calibration Procedure to Derive IRRAS Spectra from PM-IRRAS Spectra. *Appl. Spectrosc.* **2000**, *54* (11), 1646–1650. <https://doi.org/10.1366/0003702001948673>.
- (5) Ramin, M. A.; Le Bourdon, G.; Daugey, N.; Bennetau, B.; Vellutini, L.; Buffeteau, T. PM-IRRAS Investigation of Self-Assembled Monolayers Grafted onto SiO<sub>2</sub>/Au Substrates. *Langmuir* **2011**, *27* (10), 6076–6084. <https://doi.org/10.1021/la2006293>.
- (6) Shen, H.; Eisenberg, A. Block Length Dependence of Morphological Phase Diagrams of the Ternary System of PS-*b*-PAA/Dioxane/H<sub>2</sub>O. *Macromolecules* **2000**, *33* (7), 2561–2572. <https://doi.org/10.1021/ma991161u>.
- (7) Johnson, B. K.; Prud'homme, R. K. Mechanism for Rapid Self-Assembly of Block Copolymer

- Nanoparticles. *Phys. Rev. Lett.* **2003**, *91* (11), 1–4.  
<https://doi.org/10.1103/PhysRevLett.91.118302>.
- (8) Lee, A. S.; Bütün, V.; Vamvakaki, M.; Armes, S. P.; Pople, J. A.; Gast, A. P. Structure of PH-Dependent Block Copolymer Micelles: Charge and Ionic Strength Dependence. *Macromolecules* **2002**, *35* (22), 8540–8551. <https://doi.org/10.1021/ma0114842>.
- (9) Fox, T. G.; Paul J. Flory. The Glass Temperature and Related Properties of Poly- Styrene. Influence of Molecular Weight. *J. Polym. Sci.* **1954**, 315–319.  
<https://doi.org/https://doi.org/10.1002/pol.1954.120147514>.
- (10) Siurdyban, E. Immobilisation de Dérivés Du Cryptophane-A Sur Des Surfaces Planes SiO<sub>2</sub>/or et or Ainsi Que Sur Des Nanoparticules Magnétiques, Université de Bordeaux, 2015.



# **Densification of the monolayer**

3



This chapter comprises a detailed study of the intermediate step between the first and second stages of the proposed fabrication method. As previously suggested, an additional step supposedly takes place in the early stages of the water addition for the bilayer formation, prior to the actual self-assembly. This step was first suggested after noticing that upon immersion of the solid-supported BC bilayer membrane in a non-selective solvent, the resulting BC layer was not similar to the initial BC monolayer as it will be shown later in the chapter (**Figure 3.1**).

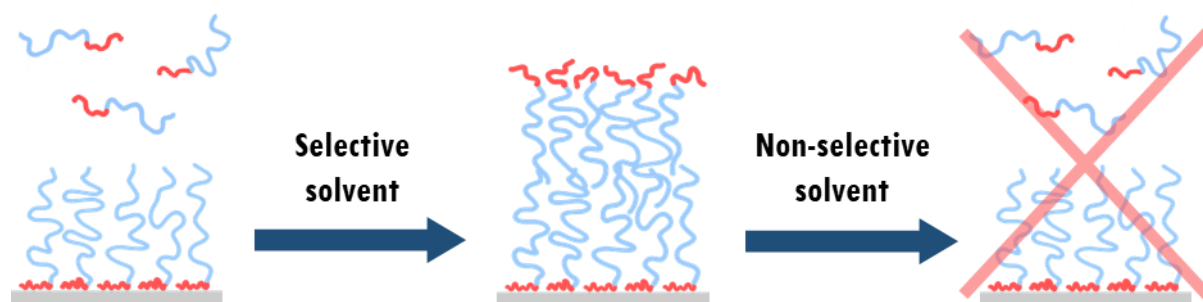


**Figure 3.1.** Schematic illustration of the bilayer “rinsing” process (immersion in a non-selective solvent). Ideally, the resulting layer should be identical to the initial monolayer, but this does not happen in the case of PS-b-PAA bilayers.

Initially, there is no clear explanation for the formation of this new layer, which appears different. Indeed, the BC bilayer is held together by hydrophobic interactions in the presence of a selective solvent; thus, if the solvent is replaced by a non-selective solvent, the bilayer must then be completely disassembled with a resulting layer similar to the initial BC monolayer. However, different complementary techniques clearly showed that this “rinsed bilayer” presented a similar thickness value to the BC monolayers but a smoother topography (similarly to the bilayer) and a higher hydrophobicity, different than the mono- and bilayer. Combining these results with those of NR and PM-IRRAS presented in **Chapter 2**, it was proposed that the “bilayer after rinsing in a non-selective solvent” is indeed a “densified monolayer”. Further PM-IRRAS measurements, presented in this chapter, qualitatively and quantitatively demonstrated that the compositions of the monolayer, densified monolayer and bilayer were different but in agreement with the increase of BC in each layer; more importantly, using deuterated and hydrogenated PS chains to obtain asymmetric bilayers (similarly to the NR experiments shown in **Chapter 2**), it was observed that in the “rinsed” bilayer, contributions of both hydrogenated and deuterated BCs were found. In order to understand and propose a mechanism for the “densification” process, QCM-d experiments

were made using PS-*b*-PAA monolayers and PAA homopolymer, where indeed it could be observed that adsorption of PAA chains onto the BC monolayer occurred in aqueous conditions at low pH but not in a non-selective solvent. Hydrogen interactions between PAA in solution and the adsorbed PAA blocks were hypothesized to be the cause of densification of the BC monolayer in the early stages of water addition. After drying with nitrogen and characterization by the above-mentioned techniques, these densified monolayers were used to prepare new BC bilayers with results similar to the previous ones shown in **Chapter 2**. A schematic representation of the fabrication of solid-supported PS-*b*-PAA bilayers including the densification step is shown in **Figure 3.2**.

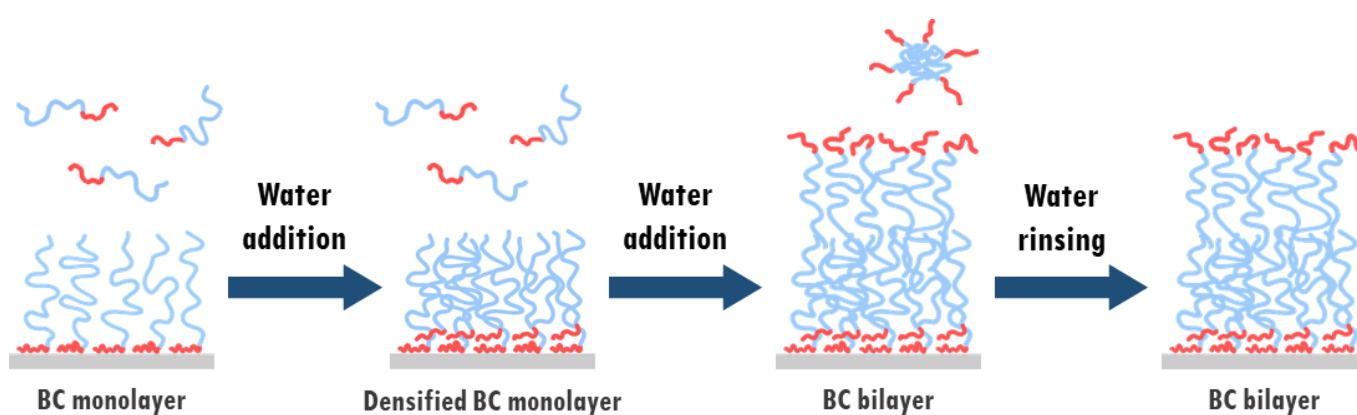


**Figure 3.2.** Schematic illustration of the proposed fabrication method for solid-supported PS-*b*-PAA bilayers membranes, including the densification step.

---

# Experimental

---

## Materials

PS<sub>182</sub>-*b*-PAA<sub>19</sub> and PS<sub>394</sub>-*b*-PAA<sub>58</sub> were purchased from Polymer Source (Canada) and used as received – it should be noted that the subscript numbers indicate the degree of polymerization (DP) of each polymer. N,N-dimethylformamide (DMF, 99.8%) was purchased from Acros Organics and tetrahydrofuran (THF, 99%) was purchased from Sigma-Aldrich and used in a solvent purification system (PureSolv MD) (that is, anhydrous THF with no stabilizers). Deionised water with a resistivity of 18.2 MΩ.cm at 25°C was obtained from a Milli-Q system (Millipore).

## Methodology

### 1.1. PS-*b*-PAA bilayer rinsing process in a non-selective solvent

The solid-supported BC bilayers, after rinsing with water and air drying, were immersed in DMF:THF (80:20) for 2h and then dried under nitrogen.

Thickness: The rinsed bilayer thickness deposited silicon wafers was measured using an UVISEL spectroscopic ellipsometer (Horiba Jobin Yvon, France). The data were acquired at three angles of incidence: 65°, 70° and 75° and wavelengths ranging from 260 to 860 nm. Data were fitted to a multi-layer model using the DeltaPsi Horiba built-in program. The thicknesses obtained through spectroscopic ellipsometry were systematically confirmed by AFM measurements. Several scratches were made on the polymer layer deposited on silicon wafers by pulling (and not cutting) sideways a sharp surgical scalpel blade and then imaging the generated scratches to estimate the film thickness (step height).

Surface topography: AFM images of the bilayers after rinsing were recorded in the dry state by using Tapping Mode in Air at a resolution of 512 x 512 pixels with a scan rate of 1 Hz with a Dimension ICON (Veeco, Bruker). The data was analysed with Nanoscope Analysis software.

Adsorption of PAA<sub>69</sub> on substrates functionalized with a PS<sub>394</sub>-*b*-PAA<sub>58</sub> monolayer: A Quartz Crystal Microbalance with dissipation (QCM-D) set-up (Q-Sense E4 instrument, Biolin Scientific, Sweden) with modified quartz crystal sensors coated with a PS<sub>394</sub>-*b*-PAA<sub>58</sub> monolayer was used to build the adsorption isotherm of a PAA<sub>69</sub> in various solvent conditions. As previously described, the adsorption of polymer chains on the PS<sub>394</sub>-*b*-PAA<sub>58</sub>-functionalised sensor could be precisely monitored by measuring the decrease in the resonance frequency  $F_n$  for each odd overtone. If the adsorbed mass forms a homogeneous rigid film without any loss, the relationship between frequency change  $\Delta F_n$  and the areal mass increment  $\Delta m$  is linear, as found by Sauerbrey<sup>1</sup>:

$$\frac{\Delta F_n}{n} = -\frac{2F_0^2}{\sqrt{\rho_q \mu_q}} \Delta m \quad \text{Eq.1}$$

where  $F_0$  is the resonant frequency of the crystal (5 MHz),  $\rho_q$  (2.648 g.cm<sup>-3</sup>) the quartz density and  $\mu_q$  (2.947 x 10<sup>11</sup> g.cm<sup>-1</sup> s<sup>-2</sup>) the shear modulus. The experiment consisted of injection of water adjusted at a specific pH into the chamber containing the sensor modified with a PS<sub>394</sub>-*b*-PAA<sub>58</sub> monolayer, followed by the injection at the same pH of PAA<sub>69</sub> and re-injection of an aqueous solution to remove unbound chains. A flow rate of 150 μL.min<sup>-1</sup> was used for each step. As a control, the same experiment was performed with PAA<sub>2k</sub> chains dissolved in non-selective DMF. No frequency shift or dissipation was observed (**Appendix, Figure A7**).

Contact angle measurements: Advancing and receding water contact angles ( $\theta_{adv}$ ,  $\theta_{rec}$ ) were measured with a Tracker tensiometer from Teclis (France) at room temperature. The static contact angle was recorded using the sessile drop method. With the help of a dosing syringe, a droplet of 3 μL of water (pH 7) was deposited on the substrate and the value of advancing contact angle was recorded 30 s after droplet deposition (importantly to note, no significant change was observed on the contact angle during this period). The average value was obtained by measuring two samples in two different positions each. The natural receding contact angles were determined by monitoring the evaporation of the sessile drop with time: a contact angle initially imposed in the advancing mode ( $\theta_A$ ) diminishes linearly with time when the liquid constituting the meniscus start to evaporate. When the water droplet is not pinned anymore, it will then recede at a constant angle ( $\theta_R$ ) marked by the presence of a visible plateau.

Polarization Modulation Infrared Reflection Absorption Spectroscopy (PM-IRRAS): The PM-IRRAS measurements were performed by Thierry Buffeteau at the Institute of Molecular Sciences (L'Institut des Sciences Moléculaires – ISM). Fully hydrogenated PS<sub>394</sub>-*b*-PAA<sub>58</sub> bilayers and mixed hydrogenated/deuterated PS<sub>394</sub>-*b*-PAA<sub>58</sub> bilayers were prepared onto SiO<sub>2</sub>/Au substrates (2.5 x 2.5 cm<sup>2</sup>), as described in **Chapter 2**. The substrates, after PM-IRRAS analysis, were rinsed in DMF:THF as described above and re-analysed.

## Results and discussion

### 1.1. Evidences of the densification of the monolayer

The adsorbed amount of BC in the second layer can be hardly determined by QCM as the BL self-assembly process cannot be reproduced in satisfactory conditions in the QCM set-up. Therefore, it was preferred to remove the second layer for its quantification by immersing the bilayer in a non-selective solvent. Ideally, as illustrated in **Figure 3.1**, after rinsing the BC bilayer in a non-selective solvent (and drying with nitrogen) one should obtain a regular BC monolayer with a 2-D islet pattern as seen by AFM imaging in **Chapter 1**. Conversely, the topography observed for this “rinsed bilayer” is different from the original monolayer but still quite close to the bilayer (**Figure 3.3**).

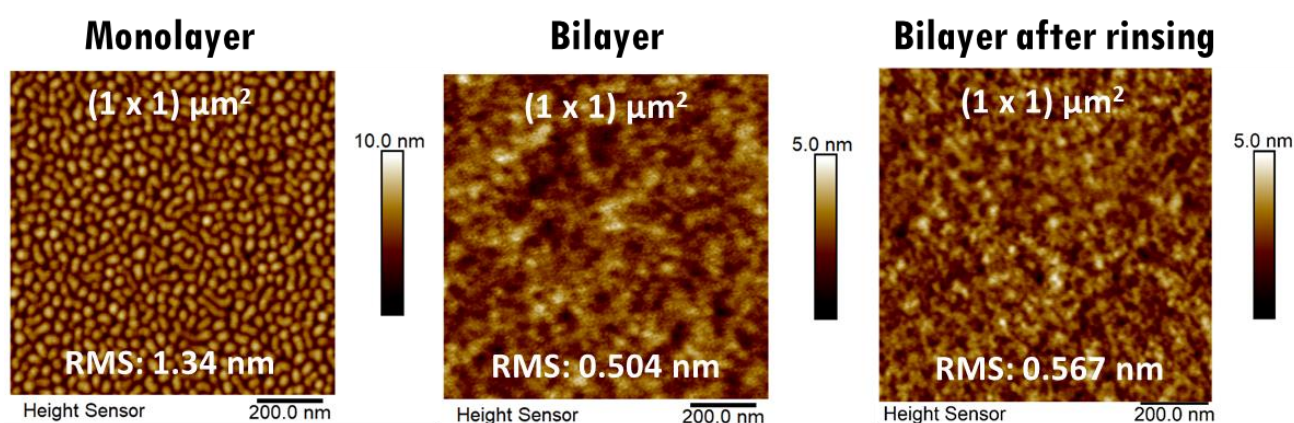


**Figure 3.3.** AFM images of a PS<sub>394</sub>-b-PAA<sub>58</sub> monolayer, bilayer and rinsed bilayer after 2 h in DMF:THF (80:20).

Although the topography of the rinsed bilayer seems relatively similar to the original bilayer, it would be erroneous to claim that the bilayer retained its physical integrity after immersion in a non-selective solvent where hydrophobic forces are absent. More specifically, the rinsed bilayer is much denser than the monolayer, which means that the dewetting of PS blocks could not take place conversely to what has been observed for the initial monolayer (**Chapter 1**). The resulting new layer is therefore different from the monolayer and the bilayer, even if the thickness of the layer of 7~8 nm is similar to the thickness of the BC monolayers of (**Figure 3.4**).

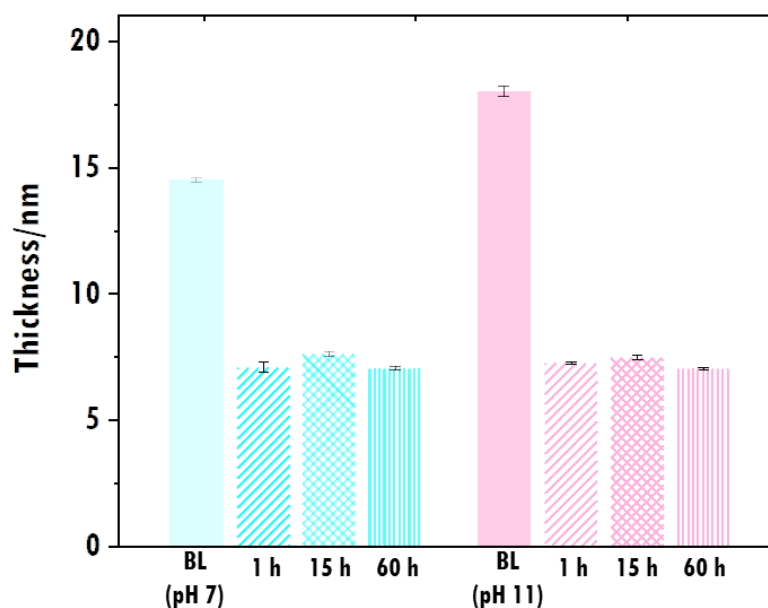


**Figure 3.4.** Thickness of the PS<sub>394</sub>-b-PAA<sub>58</sub> bilayer prepared with water (pH 7, left, blue) and the rinsed bilayer for 1, 15 and 60 h in DMF:THF (blue patterns). Thickness of the PS<sub>394</sub>-b-PAA<sub>58</sub> bilayer prepared in NaOH (pH 11, right, pink) and the bilayer after rinsing for 1, 15 and 60 h in DMF:THF (pink patterns).

It is important to note that regardless of the bilayer fabrication route (*i.e.* using water or aqueous NaOH solution) that could generate bilayers with different thicknesses, the rinsed bilayers exhibited similar thickness. Furthermore, immersion times from 1 to 60 h in the non-selective solvent does not seem to change the thickness of the rinsed layer, which means that after 1h, the BC forming the second layer are already dissolved in the solution again.

Finally, water contact angle measurements confirmed the hypothesis that the rinsed bilayer is indeed a much denser layer (**Figure 3.5**).

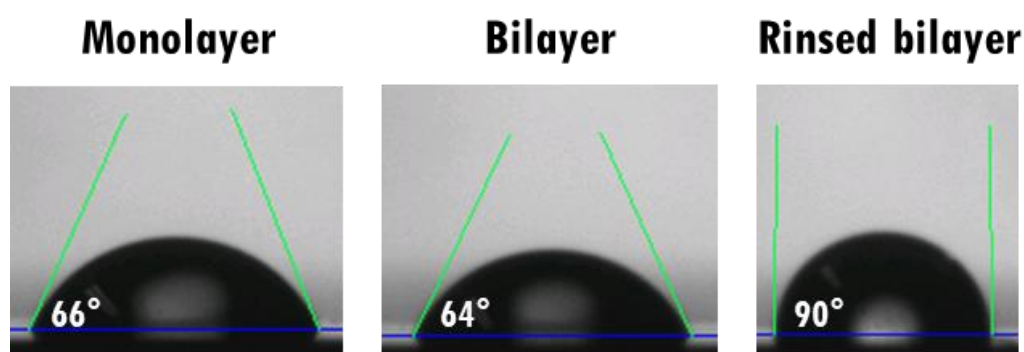


**Figure 3.5.** Water contact angle measurements of PS<sub>394</sub>-b-PAA<sub>58</sub> mono, bilayer and rinsed bilayer.

While the contact angle values of the mono- and bilayers are around 65–70°, the rinsed bilayer exhibits a much higher hydrophobicity ( $90 \pm 1^\circ$ ) comparable to that of a pure PS film.<sup>2</sup>

This increased hydrophobicity suggests that the BC molecules that participate in the densification of the monolayer are oriented in the same way as the first BC molecules in the monolayer, *i.e.*, hydrophilic blocks are located close to the substrate and PS blocks form a brush. However, the interactions leading to such a densification cannot be similar to acid-base interactions initially observed between the acid groups of the copolymer and the surface amine functions. Indeed, the presence of an adsorption maximum evidenced by QCM (**Chapter 1**) clearly demonstrated a saturation state of the monolayer in the DMF:THF mixture. Under these conditions, how would it be possible to adsorb even more copolymer at the monolayer? As also observed by PM-IRRAS in **Chapter 1**, after monolayer formation slightly less than half of the COOH groups are still present. Then, the proposed mechanism for this densification is the formation of hydrogen bonding between the free PAA groups of BCs in solution and the surface-anchored PAA groups. This interaction can only occur when the hydrophobic effect is triggered, that is, when water is added in the non-selective solvent.

In order to have more quantitative data, the rinsed PS<sub>394</sub>-*b*-PAA<sub>58</sub> bilayer was further characterized by PM-IRRAS and compared to the PS<sub>394</sub>-*b*-PAA<sub>58</sub> mono- and bilayer previously analysed in **Chapter 2 (Figure 3.6)**. By quickly comparing the peak intensities of the 3 layers plotted in **Figure 3.6**, one can observe an increase in intensity from the monolayer to the rinsed bilayer and then to the complete bilayer. For a better comparison of the data, the areas of the peaks rather than the intensity were calculated and compared to data described in **Chapter 2 (Table 3.1)**.

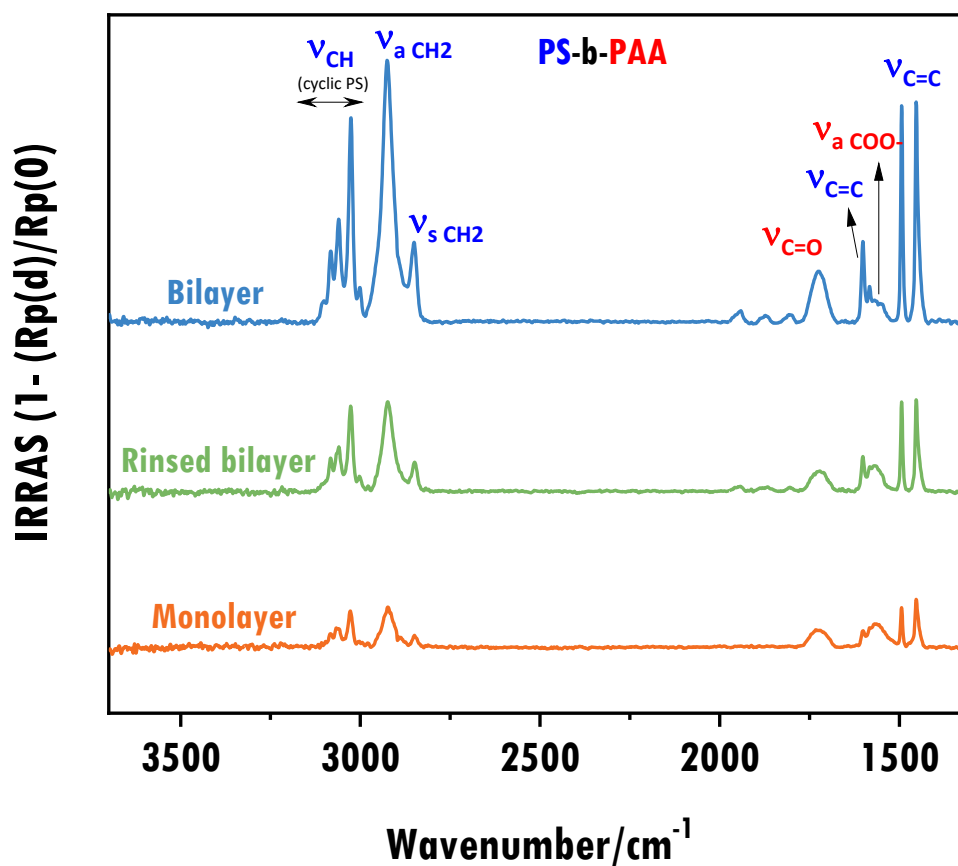


Figure 3.6. PM-IRRAS spectra of a PS<sub>394</sub>-b-PAA<sub>58</sub> monolayer, bilayer and rinsed bilayer in DMF:THF (80:20).

Table 3.1. Calculated peak areas of PS<sub>394</sub>-b-PAA<sub>58</sub> monolayer, bilayer and rinsed bilayer, and averaged values. # represent different samples (duplicate).

	3150 – 2800 cm <sup>-1</sup>	3130-2985 cm <sup>-1</sup>	1502-1480 cm <sup>-1</sup>
Monolayer (#1)	0.1329	0.0458	0.0098
Monolayer (#2)	0.1311	0.0479	0.0109
<b>Monolayer (average peak area)</b>	<b>0.1320</b>	<b>0.0469</b>	<b>0.0103</b>
Bilayer (#1)	0.7495	0.2458	0.0583
Bilayer (#2)	0.8129	0.2684	0.0618
<b>Bilayer (average peak area)</b>	<b>0.7812</b>	<b>0.2571</b>	<b>0.0601</b>
Rinsed bilayer (#1)	0.2939	0.1056	0.0223
Rinsed bilayer (#2)	0.3055	0.1177	0.0249
<b>Rinsed bilayer (average peak area)</b>	<b>0.2997</b>	<b>0.1117</b>	<b>0.0236</b>
<b>Rinsed bilayer : Monolayer</b>	<b>2.27</b>	<b>2.38</b>	<b>2.29</b>
	<b>Rinsed bilayer = 2.3-fold Monolayer</b>		
<b>Bilayer : Rinsed bilayer</b>	<b>2.61</b>	<b>2.30</b>	<b>2.55</b>
	<b>Bilayer = 2.5-fold Rinsed bilayer</b>		

For the PS-related bands, there is a 2.3-fold increase in the rinsed bilayer compared to the monolayer. Although the increase in peak areas may depend on the orientation of the groups, it seems reasonable as a first approximation to consider that this increase comes from a larger amount of adsorbed copolymer. Specifically, the double amount could mean that another identical layer of BC is added to densify the adsorbed BC monolayer, that is, for each adsorbed BC chain, another BC chain is added during densification.

As previously suggested, the densification of the first layer with the BC unimers in the early stages of water addition was assumed to be due to hydrogen-bonding between the free PAA blocks with surface-tethered PAA blocks of the monolayer. Considering the PAA bound-peak (C=O stretching at  $1726\text{ cm}^{-1}$ ), however, no difference is observed between the monolayer and rinsed bilayer (intensities are  $6.3 \cdot 10^{-4}$  and  $6.9 \cdot 10^{-4}$ , respectively). Knowing that indeed PS is present in the more quantity in the rinsed bilayer, as previously observed by the increased intensity, the only possible explanation for the PAA-related band similar intensity must be related to the orientation of the groups.

Interestingly, regarding PS-related bands, we find a 2.5-fold increase for the bilayer compared to the rinsed bilayer. If one considers the “densified monolayer” to be the actual bottom layer deposited on the substrate, this result suggests that the second layer is virtually almost an identical layer to the bottom layer being placed on the top. Again, we cannot discriminate the effects of group orientation, so the 2.5-fold increase must surely involve not only the amount of groups but also their conformation.

Making a very simplistic illustration, not considering contributions of the conformation on the absorbance values: if one considers a first adsorbed BC monolayer containing 10 BC chains, the densification (rinsed bilayer = 2.3-fold the monolayer) would add another 13 BC chains in the monolayer: the bottom layer consists thus on a total of 23 BC chains. After that, the bilayer is formed by adding a top layer of 34.5 BC chains (bilayer = 2.5-fold the rinsed bilayer, which is the bottom layer of the system), which would result in a final bilayer structure containing 57.5 BC chains. This means that the ratio of BC chains in the bilayer:BC chains in the monolayer is 5.75, exactly the ratio found through PM-IRRAS by the direct ratio of peak areas of mono- and bilayers. As mentioned, this very simplistic illustration does not take into account changes in the absorbance due to changes in chain conformation.

Similar to NR analysis, asymmetric hydrogenated/deuterated PS<sub>394</sub>-*b*-PAA<sub>58</sub> bilayers were prepared, this time, for analysis by PM-IRRAS. Since the deuterated-PS bands are shifted

in the spectrum, one can discriminate between hydrogenated and deuterated contributions in the bilayer and rinsed bilayer. It is important to explain the fabrication route of such asymmetric bilayer: the amino-modified substrates were immersed in a BC solution containing a hydrogenated BC for the formation of a first monolayer; then, the substrates were rinsed in DMF:THF and re-immersed in a BC solution, this time containing a deuterated BC. This means that deuterated BC is used to both densify the first hydrogenated layer and the second layer (bilayer). The results are shown in **Figure 3.7**.

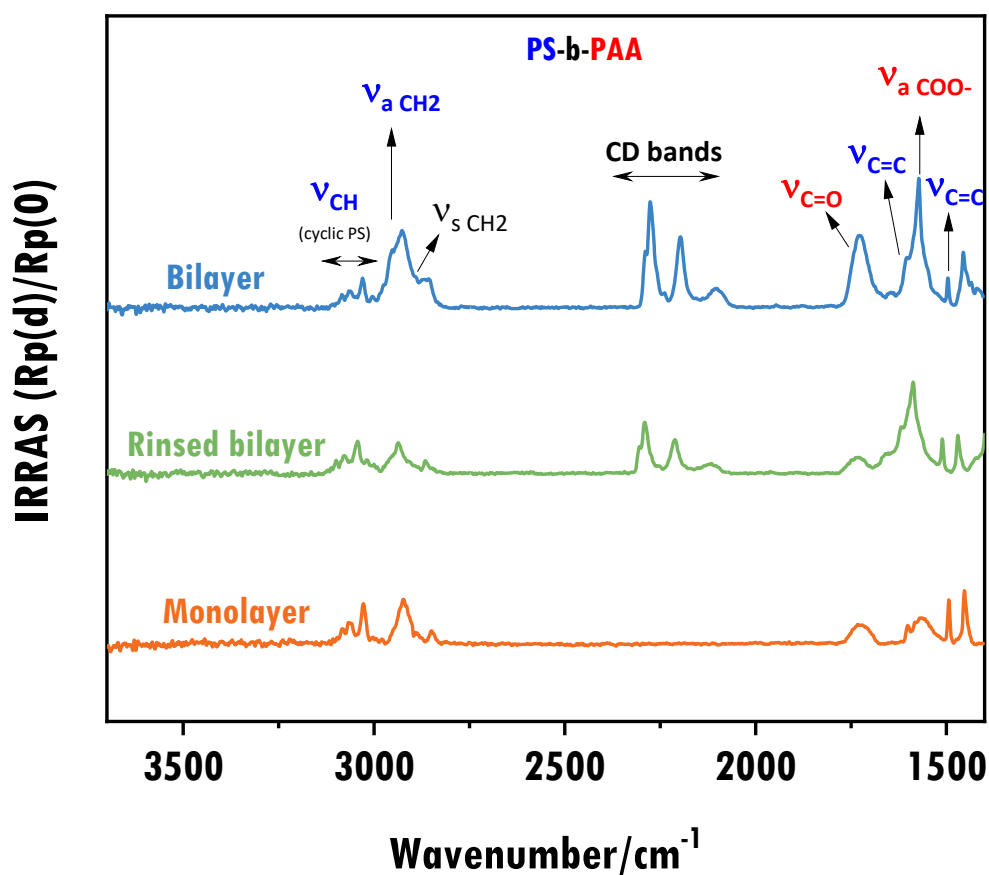


**Figure 3.7.** PM-IRRAS spectra of a PS<sub>394</sub>-b-PAA<sub>58</sub> monolayer and mixed h/d bilayer and rinsed bilayer. For the bilayer, hydrogenated BC was used for the generation of the monolayer, and deuterated BC was used for the generation of the top layer (and, thus, densification). The rinsed bilayer is then consisted of a hydrogenated BC monolayer densified with deuterated BC.

The densification of the hydrogenated BC monolayer with deuterated BC is clearly observed by the PM-IRRAS results: while the hydrogenated monolayer only shows PS<sub>h</sub> bands, the rinsed bilayer shows contributions from both PS<sub>d</sub> and PS<sub>h</sub> bands. In addition, a direct increase in PS<sub>d</sub>-related bands can be observed in the bilayer in comparison to the rinsed bilayer, as, indeed, another layer of deuterated BC is added through the self-assembly for the

formation of the bilayer structure. For a better comparison of the data, the areas of the peaks rather than the intensity were again calculated and summarized in **Table 3.2**.

**Table 3.2.** Calculated peak areas of PS<sub>394</sub>-b-PAA<sub>58</sub> monolayer, h/d bilayer and h/d rinsed bilayer, and averaged values. # represent different samples (duplicate).

	3150 – 2800 cm <sup>-1</sup>	3130-2985 cm <sup>-1</sup>	2320-2030 cm <sup>-1</sup>
<b>Monolayer (#1)</b>	0.1329	0.0458	-
<b>Monolayer (#2)</b>	0.1311	0.0479	-
<b>Monolayer (average peak area)</b>	<b>0.1320</b>	<b>0.0469</b>	-
<b>h/d Bilayer (#1)</b>	0.1041	0.0391	0.1872
<b>h/d Bilayer (#2)</b>	0.1209	0.0349	0.2466
<b>h/d Bilayer (average peak area)</b>	<b>0.1125</b>	<b>0.0370</b>	<b>0.2169</b>
<b>h/d Rinsed bilayer (#1)</b>	0.1183	0.0390	0.1090
<b>h/d Rinsed bilayer (#2)</b>	0.1113	0.0358	0.1165
<b>h/d Rinsed bilayer (average peak area)</b>	<b>0.1148</b>	<b>0.0374</b>	<b>0.1128</b>
<b>Rinsed bilayer : Monolayer</b> (h-PS bands)	<b>0.87</b>	<b>0.80</b>	-
	<b>Rinsed bilayer = 0.83-fold Monolayer</b>		
<b>Bilayer : Rinsed bilayer</b> (h-PS bands)	<b>0.98</b>	<b>0.99</b>	-
	<b>Bilayer = 0.98-fold Rinsed bilayer</b>		
<b>Bilayer : Rinsed bilayer</b> (d-PS bands)	-	-	<b>1.92</b>
	<b>Bilayer = 1.92-fold Rinsed bilayer</b>		

Regarding PS<sub>h</sub>-related bands of the monolayer and rinsed bilayer, as expected, a ratio close to 1:1 is obtained (more precisely, a ratio 1:0.83 was obtained, which may be related to small orientation effects), since the hydrogenated BC layer is the same in the monolayer and in the densified monolayer. The same 1:1 ratio is observed between the bilayer and rinsed bilayer, since the hydrogenated layer remains intact: the densification and the further formation of the second layer is made by deuterated BC.

Indeed, regarding PS<sub>d</sub>-related bands, one can observe a 1.92-fold increase of the bilayer compared to the rinsed bilayer. This suggests that the top layer (fully deuterated) is practically a double amount of the deuterated layer present in the densified monolayer. One can draw again a very simplistic illustration: considering a first adsorbed monolayer containing 10 BC hydrogenated BC chains, while the number of hydrogenated BC chains remains stable while, it was previously determined that the densification adds 13 BC chains to densify the monolayer. Thus, the final system is consisting on 23 BC molecules, among which 10 are hydrogenated and 13 deuterated. After that, the bilayer is formed by adding a top layer of

deuterated BC containing 25 BC chains (bilayer = 1.92-fold the rinsed bilayer, considering only the deuterated BC), which would result in a final bilayer structure containing 48 BC chains, among which 38 are deuterated and 10 are hydrogenated BC chains. This means that the ratio of BC chains (considering both hydrogenated and deuterated) in the bilayer:BC chains in the monolayer is 4.8, not far from what was previously obtained. Again, the differences might certainly be related to absorbance variations due to different chain conformations, which might result on increase or decrease on the IRRAS intensity.

In conclusion, similar to NR results shown in **Chapter 2**, the analysis of PM-IRRAS using different isotopes allowed to confirm the formation of a mixed h/d bottom layer (densified monolayer) prior to the formation of the BC bilayer. Although an exact quantitative analysis of the BC chains in the system could not be obtained, a rough idea on the structure of the BC bilayer could be drawn: the bilayer might be around 4.8 ~ 5.8-fold the monolayer. As extensively said, this increase takes into account not only a larger number of BC chains but also the conformation effects, so any concrete conclusion regarding the quantification is avoided.

## 1.2. Quantifying the BC mass on the densified monolayer

As previously explained, the bilayer formation cannot be followed using QCM-d. Specifically, that is due to the inability to mimic and control self-assembly on a 40  $\mu$ L QCM-d chamber, as well as some inherent limitations of QCM-d where the frequency change is the result of both BC adsorption and solvent density change (DMF:THF to water) and thus cannot be separated. However, with QCM-d the rinsed bilayer can be obtained and one can characterise the amount of BC adsorbed related to the densification process. As shown in **Figure 3.8**, an adapted mimetic version of the self-assembly process was performed inside the QCM-d with real time monitoring. Initially, the BC monolayer was formed in the QCM-d chamber, where excess BC solution is still present; injection of an aqueous solution of NaOH triggers self-assembly (here, control of the amount of water added was not possible - water was added slowly until the first point of decrease in frequency and then stopped), the system was left for 18 h for equilibrium and further rinsed with the same aqueous NaOH followed by DI water.

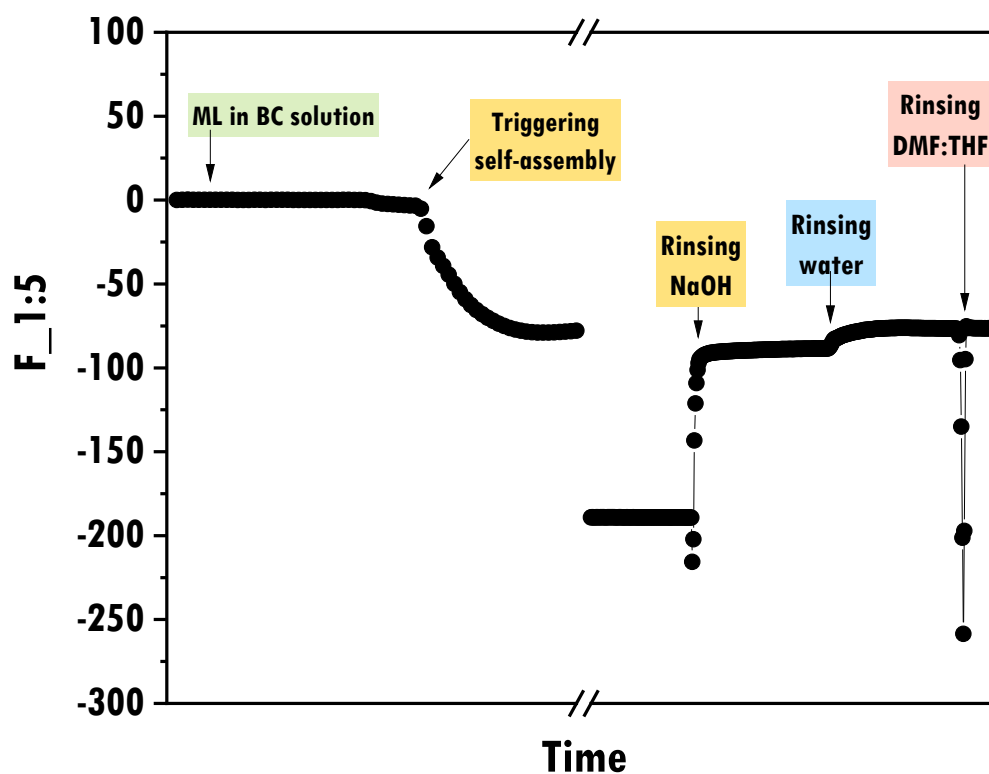


**Figure 3.8.** Real-time QCM monitoring of a “mimic” of the bilayer formation process.

Since the QCM chamber volume is very small, the amount of water added, although not quantified, is surely much larger than the measured *cwc*. After the water rinse, DMF:THF was added into the chamber to remove the second BC (bilayer), in case it may have formed, mimicking the rinsing of the bilayer described previously for solid-supported BC bilayers in silicon wafers. One can observe no significant shift in frequency, meaning that the bilayer was likely not formed. However, the frequency difference between the monolayer in DMF:THF and the final BC layer (after rinsing in DMF:THF) was -75.4 Hz, which is equivalent to a BC grafting density of  $13.5 \text{ mg}\cdot\text{m}^{-2}$ . As the BC grafting density observed for  $\text{PS}_{394}\text{-}b\text{-PAA}_{58}$  (determined in **Chapter 1**, averaged  $11 \text{ mg}\cdot\text{m}^{-2}$ ) it can be concluded that, in agreement with the PM-IRRAS results, after the densification of the monolayer the amount of BC adsorbed doubles. To confirm that the sample obtained after this QCM-d experiment was indeed a densified monolayer, ellipsometry measurements were performed in air and a thickness of 8 nm was obtained for the deposited layer (densified monolayer), in full agreement with the previous thickness values obtained for densified monolayers prepared onto silicon wafers. Moreover, as can be observed by AFM (**Figure 3.9**), the (multilayer) QCM-d sensor (intrinsically rougher

than the wafer), shows the same continuous and homogeneous surface topography of the densified monolayer.

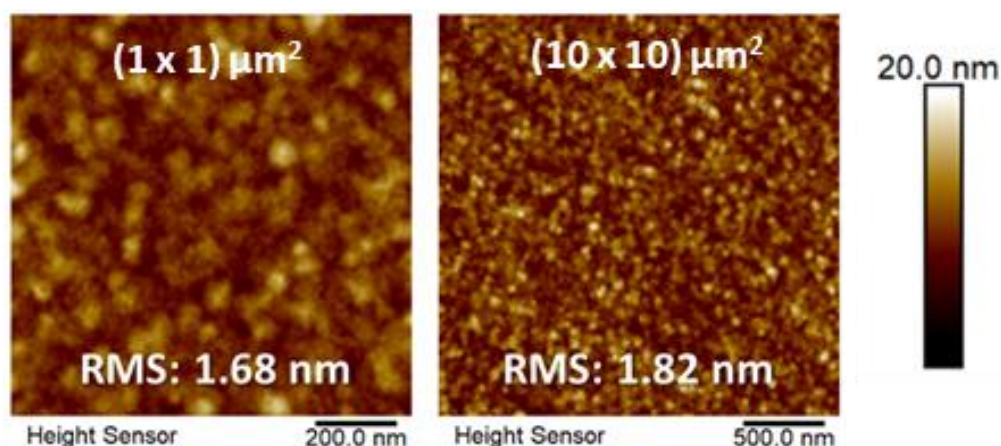


**Figure 3.9.** AFM image of the PS<sub>394</sub>-*b*-PAA<sub>58</sub> densified monolayer prepared onto QCM-d sensors after the QCM-d experiment.

In summary, the densification of the monolayer prior to bilayer formation was confirmed by various complementary techniques including AFM, ellipsometry, water contact angles and PM-IRRAS, with results in line with those of NR presented in **Chapter 2**. It was also possible to show by QCM-d that the grafting density of the densified monolayer is twice that of the original monolayer in perfect agreement with the PM-IRRAS results.

### 1.3. Investigating the possible interactions generating the densification

In order to better understand the nature of the interactions responsible for the densification, additional QCM-d experiments were performed. The adsorption of PAA<sub>69</sub> homopolymer onto QCM-sensors modified with a PS<sub>394</sub>-*b*-PAA<sub>58</sub> monolayer was monitored using aqueous solutions at pH values of 3.5, 7 and 11 (**Figure 3.10**).

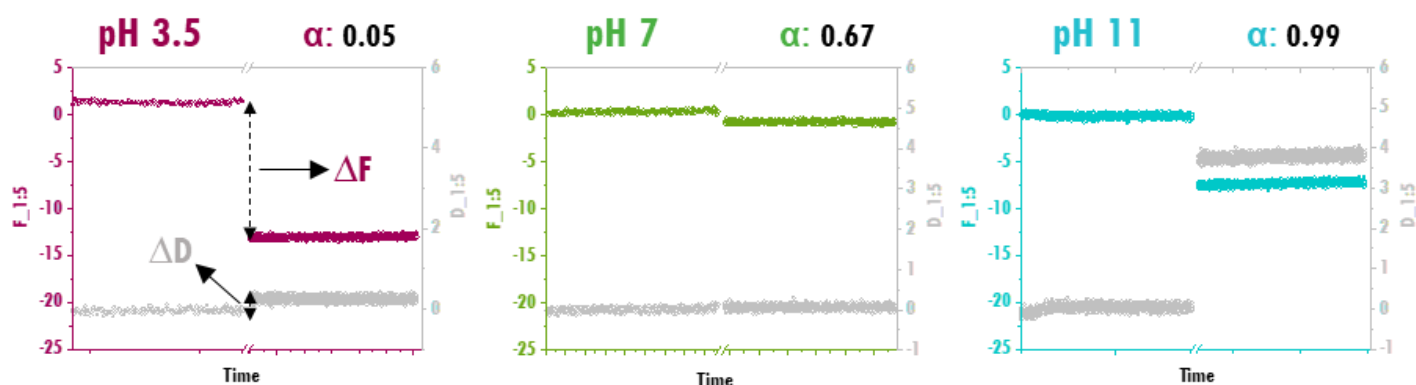


**Figure 3.10.** Real-time QCM measurements of PAA<sub>27</sub> adsorption at different pH values on QCM sensors previously coated with a PS<sub>394</sub>-b-PAA<sub>58</sub> monolayer. For each pH value, the respective degree of dissociation,  $\alpha$ , is shown.

In addition, the thickness of the monolayer adsorbed on the QCM sensor was analysed in air before and after PAA adsorption by ellipsometry. All results are summarized in **Table 3.3**.

**Table 3.3.** Values of frequency, dissipation and thickness variation before and after the experiment. The thickness values were determined by ellipsometry.

	pH 3.5	pH 7	pH 11
$\Delta F/\text{Hz}$	- 13	- 1	- 8
$\Delta D$	$0.3 \cdot 10^{-6}$	0	$3.7 \cdot 10^{-6}$
$\Delta \ell_{\text{ellipso}}/\text{nm}$	1.7	0.4	- 0.3

When PAA<sub>69</sub> solution at a pH 3.5 was injected, a  $\Delta F$  of -13 Hz (equivalent to an increase of  $2.3 \text{ mg}\cdot\text{m}^{-2}$ ) was observed, accompanied by a negligible shift of  $\Delta D$  ( $0.3 \cdot 10^{-6}$ ). In addition, a change in thickness  $\Delta \ell = 1.7 \text{ nm}$  was observed by ellipsometry. At pH 7 and 11 on the other hand, no significant  $\Delta \ell$  was observed, although a slight decrease in frequency was observed at pH 11.

At low pH values (pH 3.5,  $\alpha = 0.05$ ), COOH groups are fully protonated and the PAA chains adopt a more globular structure. In this case, the free PAA unimer molecules in the bulk can interact with the carboxylic groups present on the PAA blocks adsorbed on the surface through hydrogen bonds, as illustrated in **Figure 3.11**. This is consistent with the  $\Delta \ell$  and  $\Delta F$  values found, as well as with constant  $D$  since the film stiffness should remain unchanged after adsorption of short (and mostly collapsed) PAA molecules. Nevertheless, at higher pH values,

this is unlikely to happen due to the increase in ionization degrees. Indeed, negligible  $\Delta\ell$  were found for pH 7 and 11, discarding the possibility of PAA adsorption onto the monolayer. Although at pH 7, no events appeared to take place (negligible  $\Delta F$  and  $\Delta D$ ), at pH 11, a decrease in frequency  $\Delta F = -8$  Hz was observed, accompanied by an increase in dissipation,  $\Delta D = 3.7 \cdot 10^{-6}$ . In contrast to low pH values, PAA is fully ionized at pH 11 ( $\alpha = 0.99$ ) and these results reflect the highly solvated nature of PAA chains generating an extra contribution from the bound water molecules to the frequency and dissipation shifts within the adsorbed BC.

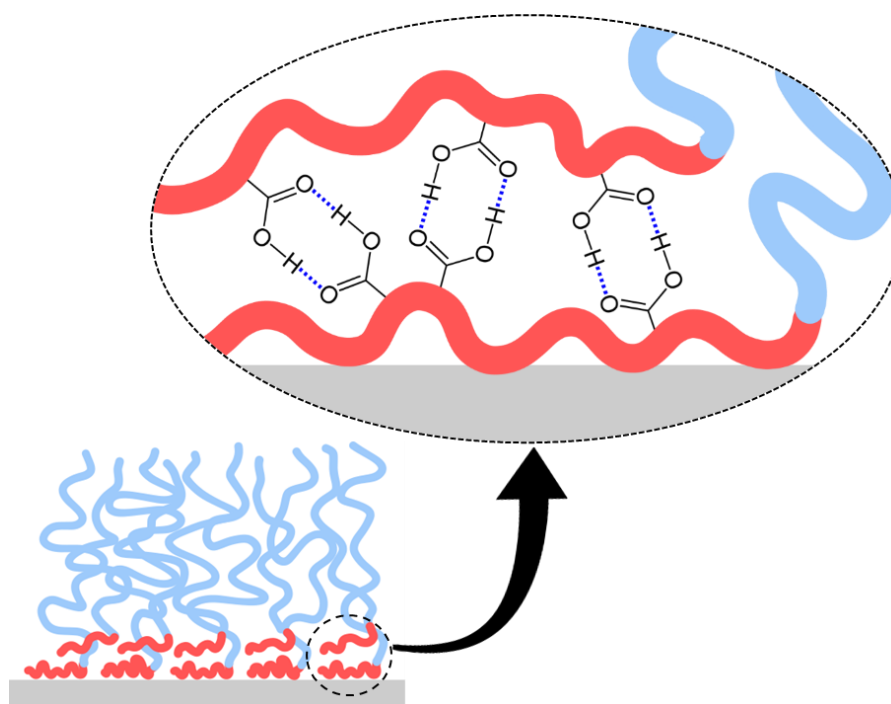


**Figure 3.11.** Schematic illustration of the proposed densification mechanism by hydrogen bonding of protonated carboxylic moieties from PAA chains prior to the formation of the second layer.

In summary, our results suggest that injection of water to trigger BC self-assembly can, at concentrations below CWC, induce a local environment that allows protonation of free PAA blocks. As the water concentration is not high (less than 5% before the initiation of self-assembly), the local pH can be significantly low generating hydrogen interactions between the free PAA chains and those already adsorbed on the surface, mainly due to the low grafting density of the adsorbed BC monolayer.

Importantly to note, the rinsed bilayers (*i.e.* densified monolayers) were used to make new bilayers, as shown in **Figure 3.12**. Apart from the few aggregates observed at high

magnification, bilayers prepared using the "rinsed bilayers" as monolayers exhibit similar topography and roughness to the original bilayers.

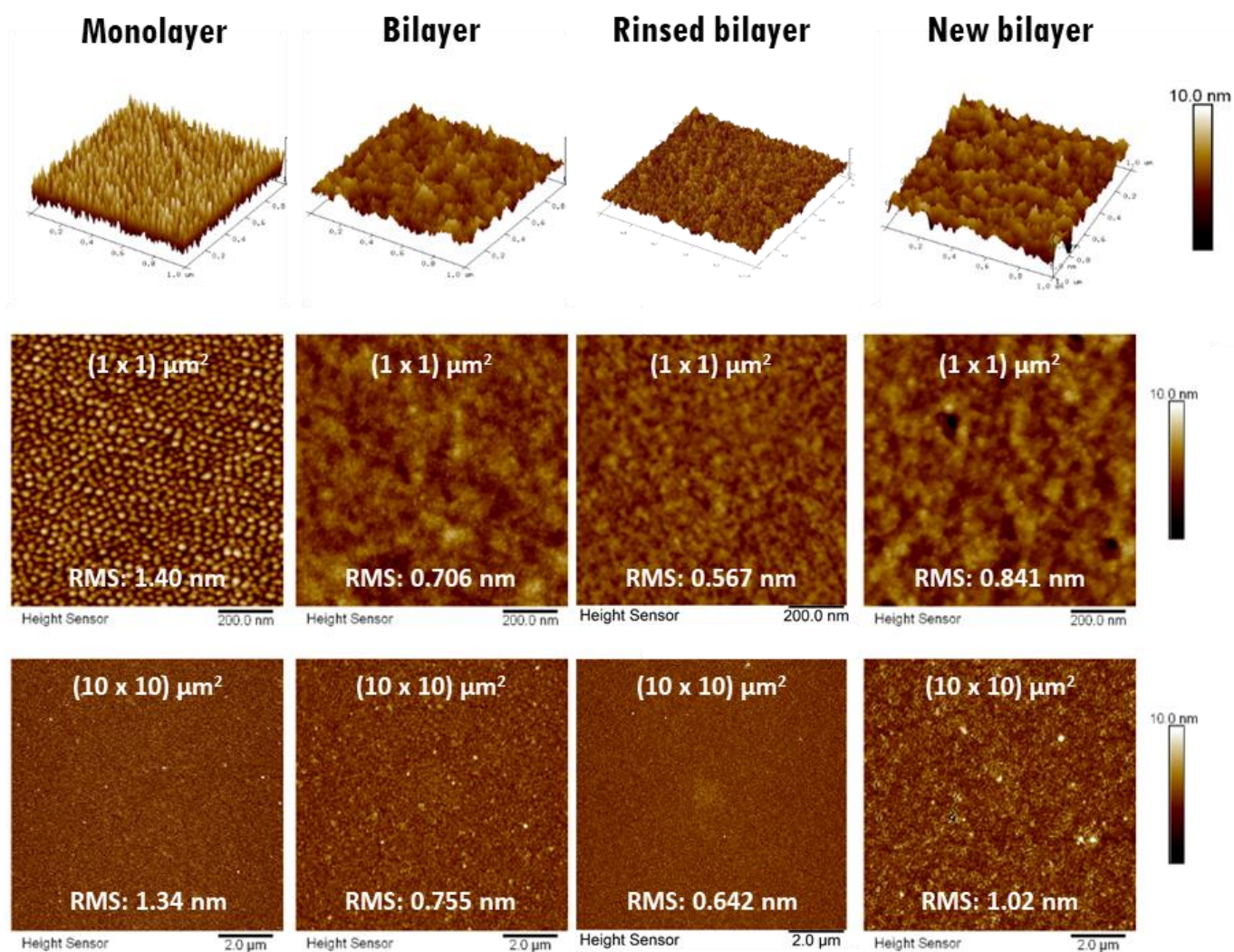


**Figure 3.12.** AFM images of a PS<sub>394</sub>-*b*-PAA<sub>58</sub> monolayer, bilayer, rinsed bilayer and new bilayer formed from a rinsed bilayer (i.e. from a densified monolayer).

### 1.3. Densification of the monolayer in other BC bilayer systems

The densification of the monolayer was also observed for bilayers prepared using BCs with shorter PAA blocks as shown in **Figure 3.13**, and for asymmetric BC bilayers, prepared using PS<sub>394</sub>-*b*-PAA<sub>58</sub> for the monolayer and PS<sub>182</sub>-*b*-PAA<sub>19</sub> for the bilayer (**Figure 3.14**, top),

which reinforces the hypothesis of hydrogen bonds between PAA chains as the mechanism responsible for the densification of the layer.

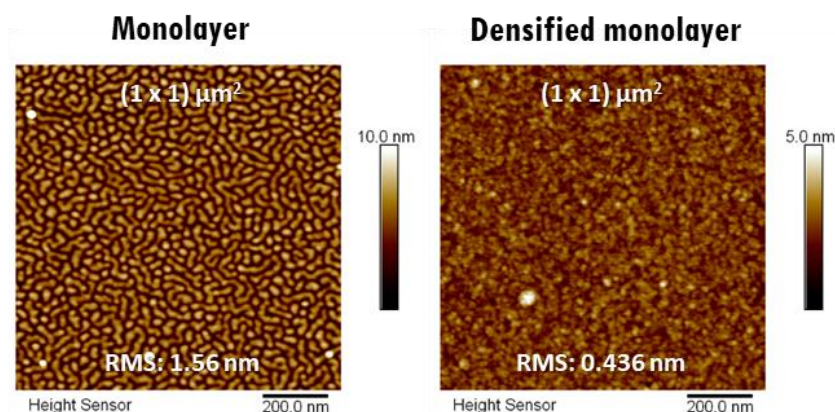


**Figure 3.13.** AFM images of the PS<sub>182</sub>-*b*-PAA<sub>19</sub> monolayer (left) and densified monolayer (i.e. rinsed bilayer, right).

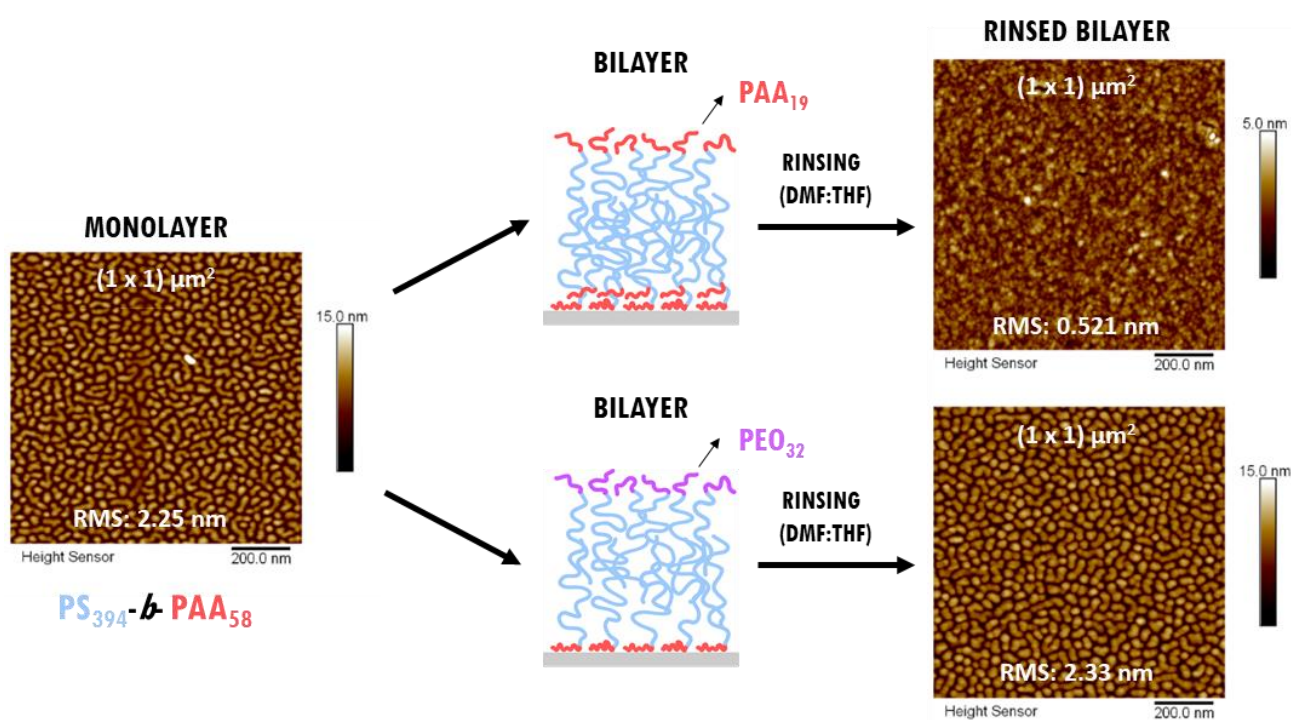


**Figure 3.14.** AFM images showing evidence of densification of the PS<sub>394</sub>-*b*-PAA<sub>58</sub> monolayer prepared from a PS<sub>182</sub>-*b*-PAA<sub>19</sub> top layer. Conversely, no densification is observed when the PS<sub>346</sub>-*b*-PEO<sub>32</sub> top layer was used.

Conversely, no densification was observed when the bilayer was assembled from a PS<sub>394</sub>-*b*-PAA<sub>58</sub> monolayer and a PS<sub>346</sub>-*b*-PEO<sub>32</sub> bilayer (Figure 3.14, down). The absence of densification may result from weaker hydrogen bonding interactions between PAA and PEO

chains. A further detailed study using BCs with different hydrophilic blocks could help to clarify to which extent the densification of the monolayer takes place.

## Conclusions

---

The densification of the solid-supported PS-*b*-PAA monolayers supposedly taking place in the early stages of the water addition for the bilayer formation, prior to the actual self-assembly, was confirmed with various characterization techniques.

The PS-*b*-PAA bilayers, once immersed in a non-selective solvent, give rise to a different layer, named “rinsed bilayer”, which was found to be much denser than the starting monolayer. Although no difference was observed on the thickness of the monolayer and the rinsed bilayer, the smoother AFM topography and highly increased hydrophobicity confirmed the higher BC grafting density. PM-IRRAS analysis allowed to characterize the rinsed bilayer as an intermediate layer between the mono- and bilayer. More importantly, by using the same strategy of preparing BC bilayers with different isotopes described in **Chapter 2** (NR experiments), PM-IRRAS allowed to prove that the first layer is indeed a mixture of hydrogenated and deuterated BCs, in fully agreement with the previous NR results.

With QCM-d, one could not only quantify the amount of BC involved on this densification step, but also demonstrate, using PAA solutions, that the densification only takes place at low pH values. This supports the proposed hypothesis that the densification of PS-*b*-PAA monolayers, taking place at early stages of water addition, is due to hydrogen interactions between PAA blocks of BC unimers in solution with adsorbed PAA blocks at the substrate.

## References

---

- (1) Sauerbrey, G. Use of Quartz Vibration for Weighing Films on a Microbalance. *Zeitschrift für Phys.* **1959**, *155* (2), 206–222. <https://doi.org/10.1007/BF01337937>.
- (2) Li, Y.; Pham, J. Q.; Johnston, K. P.; Green, P. F. Contact Angle of Water on Polystyrene Thin Films: Effects of CO<sub>2</sub> Environment and Film Thickness. *Langmuir* **2007**, *23* (19), 9785–9793. <https://doi.org/10.1021/la0636311>.

# **Generalizations, openings and perspectives**

# 4



The idea of this last chapter is to try to generalize and extend the Surface-Induced Self-Assembly of Amphiphilic BC Bilayers (SISAL) method to the fabrication of asymmetric bilayers, to the functionalization of colloidal substrates, to the encapsulation of active principles and to the study of particular properties of polymeric thin films (**Figure 4.1**).

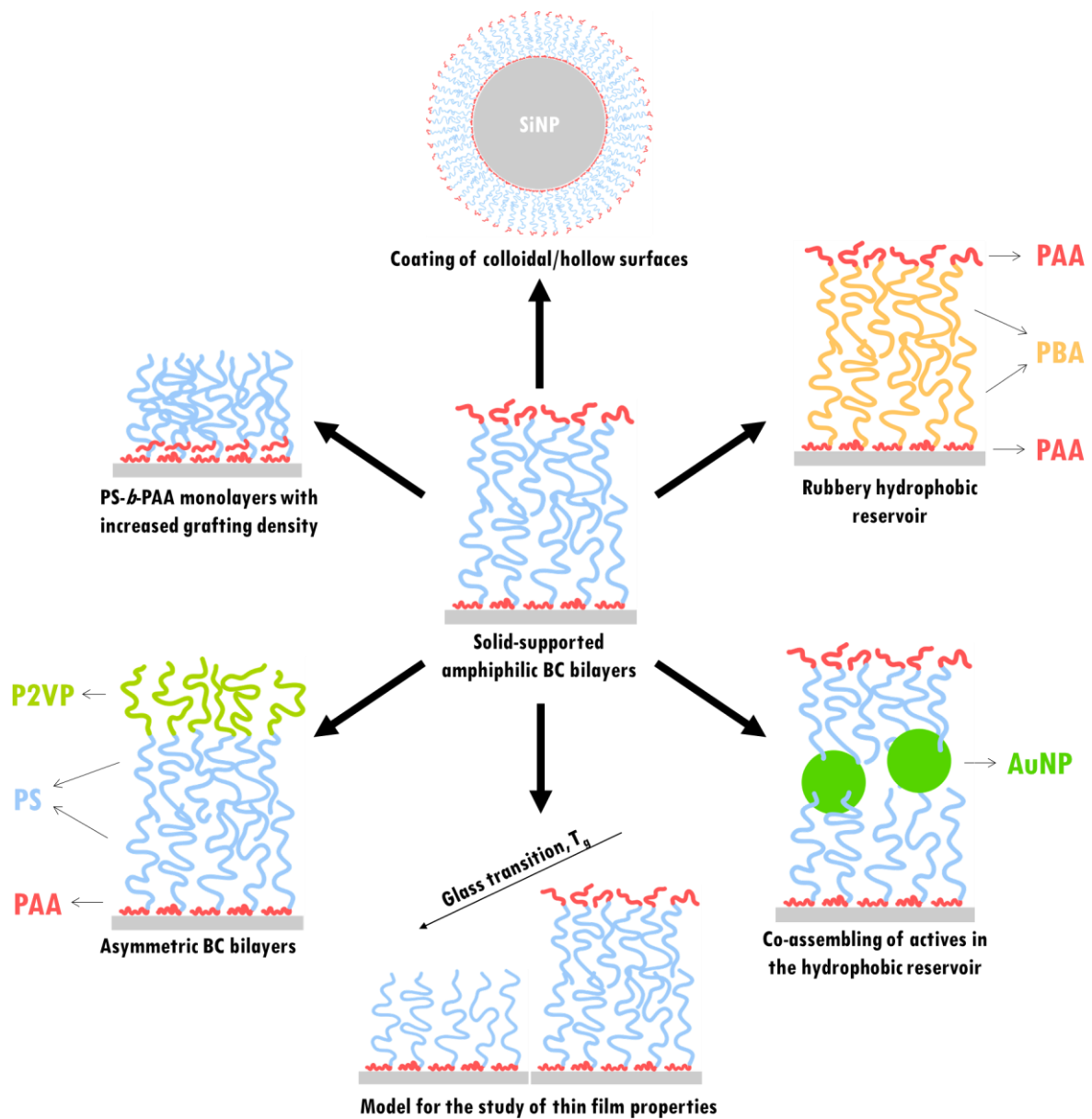


**Figure 4.1.** Generalisation, extension and possible applications of the solid-supported BC bilayers prepared using the SISAL method.

As demonstrated in **Chapter 3**, in the case of PS-*b*-PAA, monolayers with increased grafting density can be obtained after the rinsing of the solid-supported BC bilayers with a non-selective solvent.

It has also been shown that the SISAL method can generate asymmetric BC bilayers, composed of either the same BC with different size blocks or BCs containing different hydrophilic blocks, which is currently only possible using Langmuir-Blodgett (LB) deposition technique.

The encapsulation of hydrophobic actives within the hydrophobic reservoir of the BC bilayer by a co-assembly process has been demonstrated with gold nanoparticles (AuNPs), showing the possibility of encapsulating not only colloidal actives but also paving the way for the encapsulation of hydrophobic molecules of interest (drugs or fragrances, for instance).

The extension of the process to colloidal substrates has been recently established by Dr. Martin Fauquignon (LCPO, Bordeaux) in the framework of the ANR SISAL project illustrating the versatility of this fabrication method. The process, developed in this thesis on macroscopic planar substrates (silicon wafers), has been transferred to silica nanoparticles (SiO<sub>2</sub> NPs) allowing the generation of mono- and bilayer BC coatings.

Solid-supported BC bilayers, whose thickness and functionality are controlled, could be advantageously used as models for the study of singular properties of thin films. As an example, the first measurements of glass transition temperatures ( $T_g$ ) on PS-*b*-PAA monolayers and bilayers prepared in this work have been analysed by ellipsometry by Guillaume Vignaud (Université Bretagne Sud at Lorient). A work that certainly deserves to be continued.

Finally, the generation of solid-supported bilayers containing a rubbery hydrophobic block (*e.g.*, a poly(butyl acrylate)-*block*-poly(acrylic acid) – PBA-*b*-PAA) could help answer a central question: Does the glassy character of the hydrophobic blocks play an important role in the stability of BC bilayers on a solid support? Can we generate rubbery bilayers that retain their mechanical integrity upon passage through the water/air interface? Can only hydrophobic interactions between chains (with possible entanglements) be sufficient to generate bilayers that can be used in applications? In this work, the macromolecular synthesis of these BC PBA-*b*-PAA has been achieved but not yet the elaboration of BC rubbery bilayers.

Each of the proposed/envisaged applications are described in separated sections, while all the detailed experimental procedures are summarized in one (last) section of this chapter (Methods).

## 1. Generation of asymmetric BC bilayers

The notion of asymmetric BC bilayers in this work is viewed through either: **1)** bilayers obtained from BCs of same composition but with different block lengths for the mono- and bilayer; or **2)** bilayers containing BCs with a different chemical nature. So far, the only fabrication method to generate asymmetric BC bilayers supported on solid substrates is the LB technique, whose advantages and limitations were summarized earlier in the “State-of-the-art” chapter. With SISAL, the fabrication of asymmetric BC bilayers on solid supports has been demonstrated for the first time with PS-*b*-PAA copolymers of different molecular weights. As illustrated in **Figure 4.2**, the process consists on the formation of a PS<sub>394</sub>-*b*-PAA<sub>58</sub> monolayer, as described in **Chapter 2**; then the monolayer is rinsed in DMF:THF to remove extra BC unimers from the medium and the substrate is immersed in a PS<sub>182</sub>-*b*-PAA<sub>19</sub> solution in DMF:THF. Bilayer formation is then triggered after water addition through hydrophobic interactions between free PS<sub>182</sub>-*b*-PAA<sub>19</sub> and grafted hydrophobic PS blocks (PS<sub>394</sub>-*b*-PAA<sub>58</sub> monolayer). A final rinsing step then removes any BC micelles and other aggregates generated in the aqueous solution.

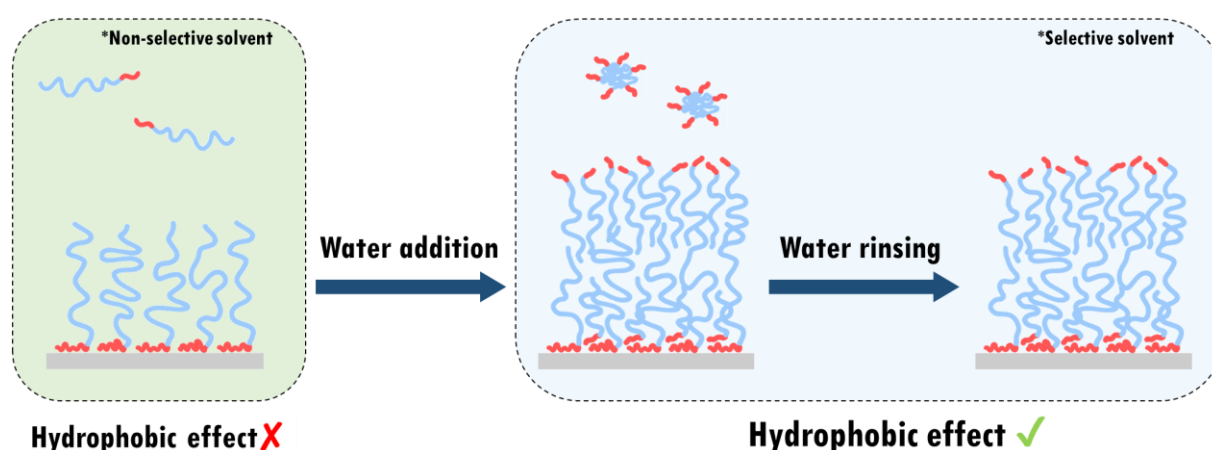


**Figure 4.2.** Illustrative scheme of the fabrication of asymmetric PS-*b*-PAA bilayers containing BCs of different molecular weights.

The formation of an asymmetric BC bilayer with thickness of  $(16.82 \pm 0.08)$  nm was observed by AFM, as illustrated in **Figure 4.3**. The bilayer thickness has an intermediate value between the symmetric bilayers of PS<sub>394</sub>-*b*-PAA<sub>58</sub> and PS<sub>182</sub>-*b*-PAA<sub>19</sub> ( $(18.0 \pm 0.1)$  and  $(16.2 \pm 0.2)$ nm, respectively), illustrating once again that the BL thickness can be tuned using different BC molecular weights. As shown in **Chapter 3**, the densification of this asymmetric bilayer also occurred, meaning that the bilayer structure is, in fact, a top layer of PS<sub>182</sub>-*b*-PAA<sub>19</sub> that interdiffuses into a mixed bottom layer consisting of grafted PS<sub>394</sub>-*b*-PAA<sub>58</sub> and hydrogen-bound PS<sub>182</sub>-*b*-PAA<sub>19</sub>, as illustrated in **Figure 4.2**.

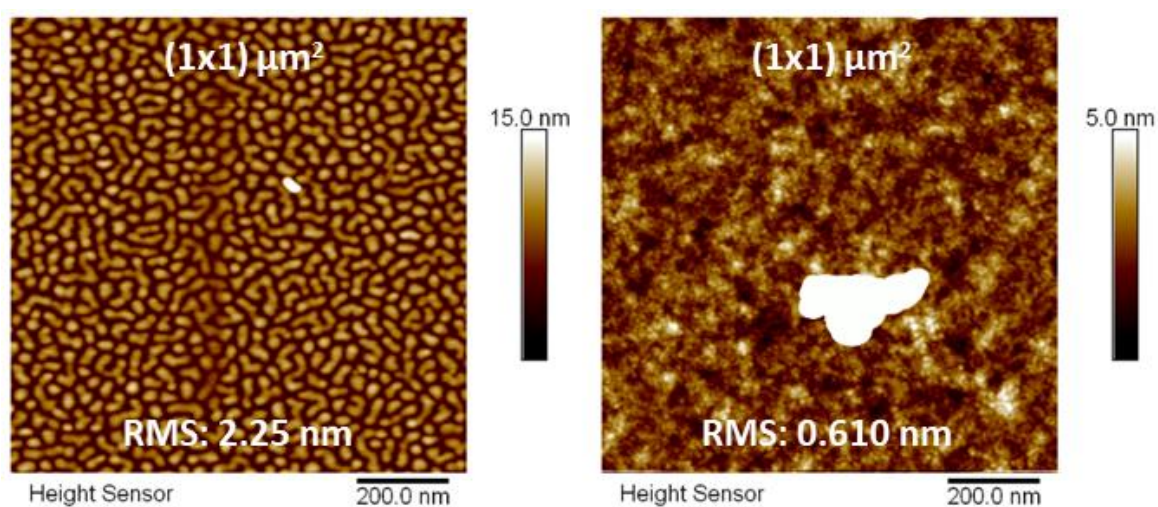


**Figure 4.3.** AFM images of the PS<sub>394</sub>-*b*-PAA<sub>58</sub> monolayer (left) and PS<sub>394</sub>-*b*-PAA<sub>58</sub> monolayer containing a second layer of PS<sub>182</sub>-*b*-PAA<sub>19</sub> (right).

The generation of asymmetric BC bilayers was also explored with different BCs, namely PS-*b*-PAA and PS-*b*-P2VP (polystyrene-*block*-poly(2-vinylpyridine)). Similar to the procedure described above, the fabrication method consists, first, of the formation of a PS<sub>394</sub>-*b*-PAA<sub>58</sub> monolayer which is rinsed in DMF:THF and immersed in a PS<sub>480</sub>-*b*-P2VP<sub>476</sub> solution, also prepared in DMF:THF. The formation of a bilayer is triggered after water addition through hydrophobic interactions between free PS<sub>480</sub>-*b*-P2VP<sub>476</sub> and grafted hydrophobic PS blocks (PS<sub>394</sub>-*b*-PAA<sub>58</sub> monolayer). A final rinsing step allows then to remove any BC micelles and/or other aggregates generated in the aqueous solution. The process is illustrated in **Figure 4.4**.

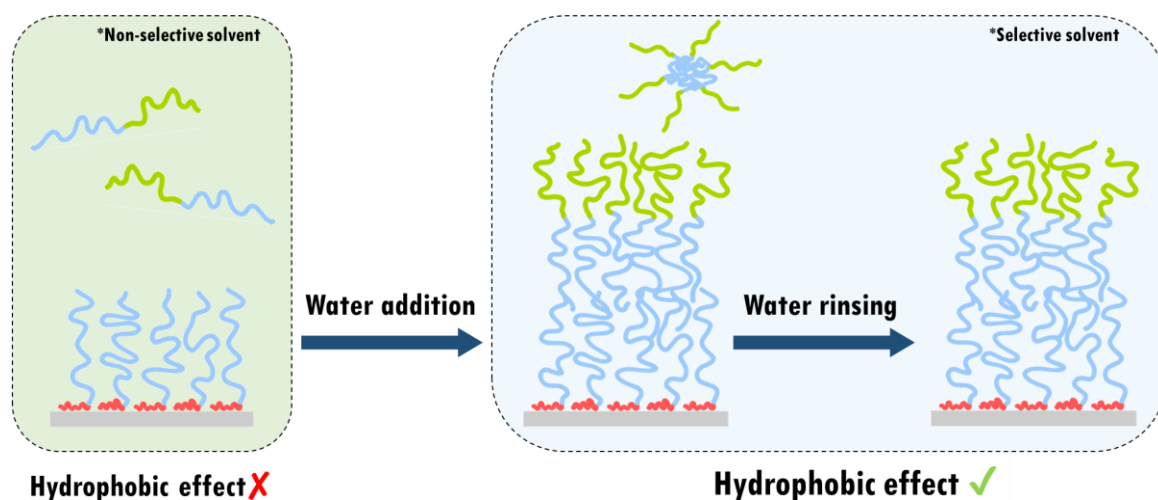


**Figure 4.4.** Illustrative scheme of the generation of asymmetric PS-*b*-PAA/PS-*b*-P2VP bilayers on solid support.

Smooth and homogeneous asymmetric BC bilayers of about 20 nm were obtained, although some aggregates were present at lower magnifications, as observed in **Figure 4.5**.

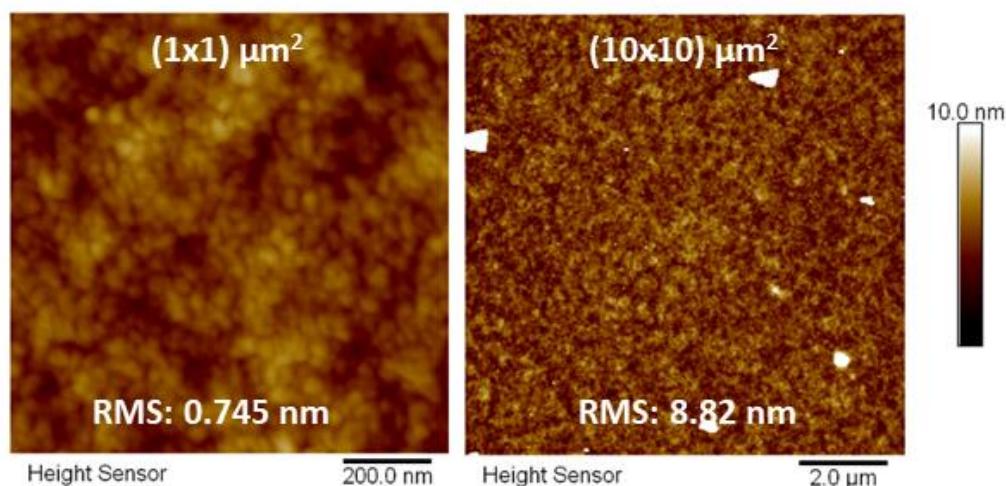


**Figure 4.5.** AFM images of asymmetric PS<sub>394</sub>-*b*-PAA<sub>58</sub>/PS<sub>480</sub>-*b*-P2VP<sub>476</sub> bilayers observed in air.

It is important to note that although a systematic densification study was not performed as for the symmetric PS-*b*-PAA bilayer, the slightly different patterns in the AFM images of the asymmetric bilayer after rinsing in DMF:THF could indicate that a densification step is also taking place (**Figure 4.6**).

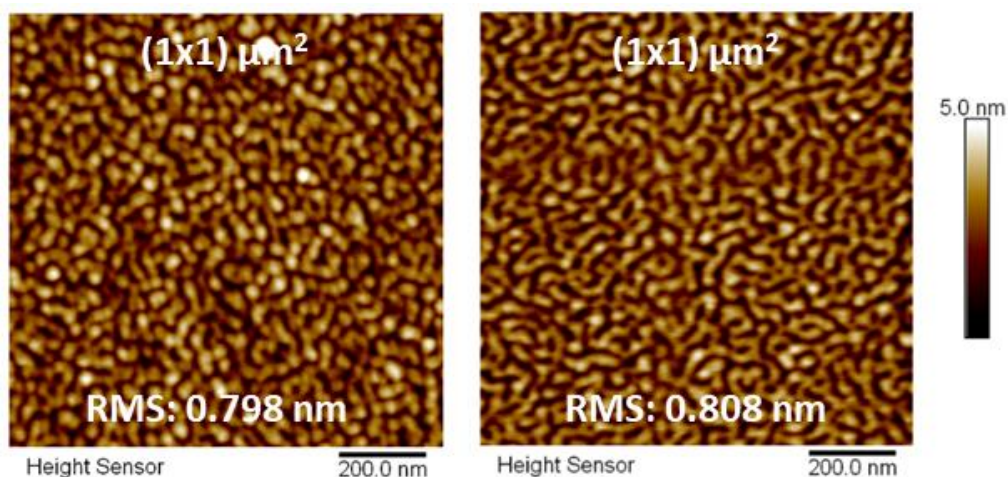


**Figure 4.6.** AFM images of the PS<sub>394</sub>-*b*-PAA<sub>58</sub> monolayer (left) and PS<sub>394</sub>-*b*-PAA<sub>58</sub>/PS<sub>480</sub>-*b*-P2VP<sub>476</sub> bilayer after rinsing in DMF:THF (right)

Indeed, there is the possibility of hydrogen bonding interactions between hydroxyl groups of PAA and pyridine groups of P2VP that could justify the densification of the monolayer, as illustrated in **Figure 4.7**.

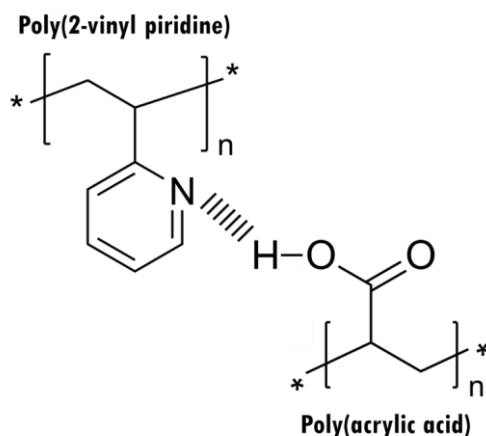


**Figure 4.7.** Schematic representation of possible hydrogen bonding between P2VP and PAA blocks.

Further studies are still needed to prove that densification step does occur here. If this is the case, the bilayer structure would be an upper layer of PS<sub>480</sub>-*b*-P2VP<sub>476</sub> interdiffusing with a mixed PS<sub>394</sub>-*b*-PAA<sub>58</sub>/PS<sub>480</sub>-*b*-P2VP<sub>476</sub> bottom layer. Otherwise, a bilayer would be observed consisting on a purely PS<sub>394</sub>-*b*-PAA<sub>58</sub> bottom layer and PS<sub>480</sub>-*b*-P2VP<sub>476</sub> top layer.

Whether densification occurs or not, the formation of such asymmetric BC bilayers contains a top layer of P2VP groups, which was accessed by AFM after incubation with citrate-capped gold nanoparticles (AuNPs) of  $(9 \pm 5)$  nm at pH 5 (**Figure 4.8**). The adsorption of AuNPs

onto the bilayer relies on acid-base interactions between citric acid and amine groups, proving the presence of P2VP groups at the top of the bilayer.

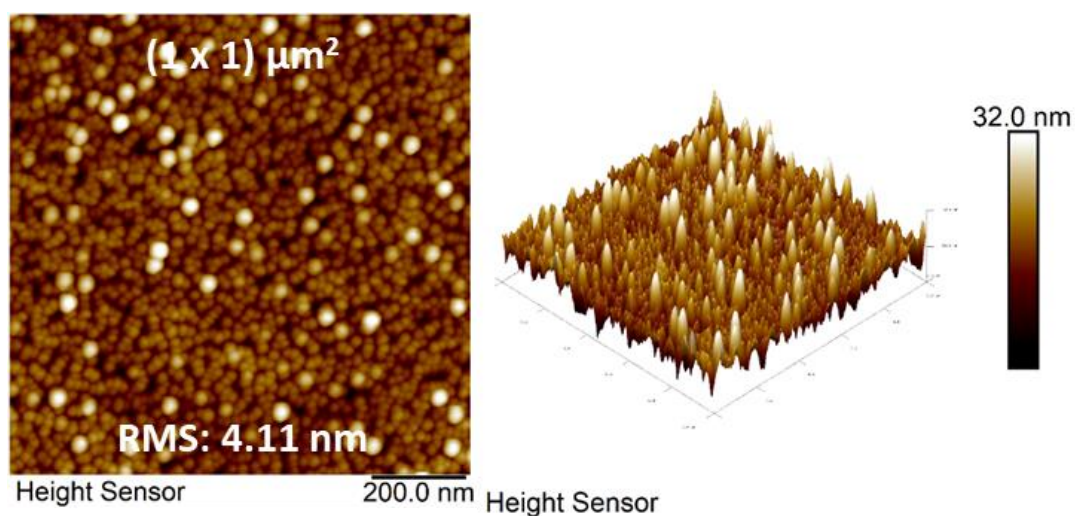


**Figure 4.8.** AFM image of the asymmetric  $PS_{394}\text{-}b\text{-}PAA_{58}/PS_{480}\text{-}b\text{-}P2VP_{476}$  bilayer in air after incubation with citrate-capped AuNPs and extensive rinsing with water.

## 2. Encapsulation of AuNP in the hydrophobic reservoir

In the SISAL fabrication method, the assembly of amphiphilic BCs with hydrophobic entities can be combined to generate actives encapsulated in the hydrophobic reservoir of the solid-supported bilayer. Here, we demonstrate the loading of colloidal hydrophobic structures (5-nm polystyrene-capped AuNPs, **Figure 4.9**) in the bilayer using, instead of a BC solution, a mixture of AuNPs and BCs prepared in a non-selective solvent.

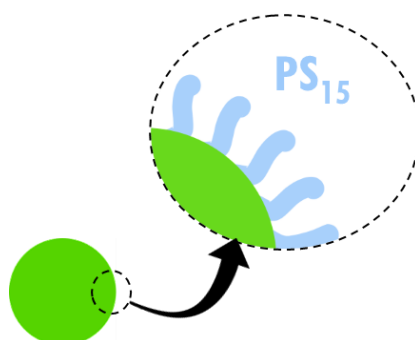


**Figure 4.9.** Illustration of PS-capped AuNPs: the nanoparticles, after synthesis, were functionalized with a thiol-terminated polystyrene of  $M_w$  1,600  $\text{g}\cdot\text{mol}^{-1}$  ( $PS_{15}$ , where the index refers to the degree of polymerization).

As the size of the AuNPs is appropriate to be encapsulated in the hydrophobic reservoir of the bilayer, the addition of water simultaneously triggers the formation of the second BC layer and the encapsulation of the AuNPs, as illustrated in **Figure 4.10**.

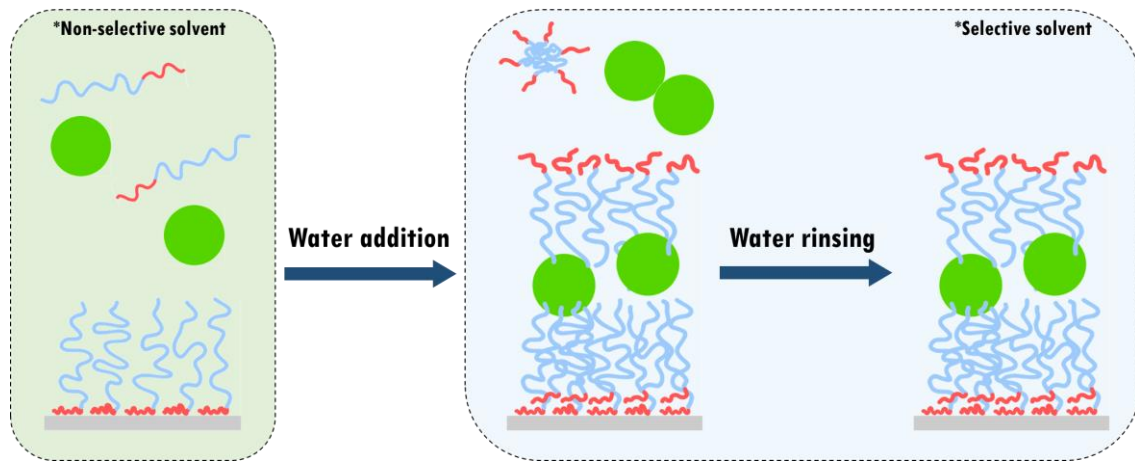


**Figure 4.10.** Immobilization of PS-coated AuNPs in the hydrophobic reservoir of PS-b-PAA bilayers by applying the SISAL approach.

An important point is that the critical water content remained unchanged within the presence of 50 wt.% AuNPs (AuNP:BC ratio = 1:17), as shown in **Figure 4.11**.

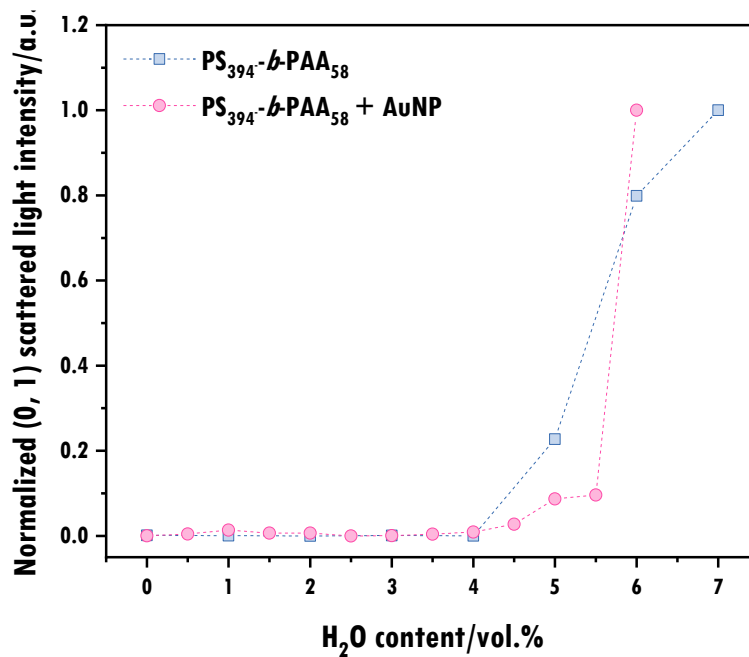


**Figure 4.11.** Critical water content of PS<sub>394</sub>-b-PAA<sub>58</sub> solutions prepared in DMF:THF (80:20) in the absence and presence of AuNPs 50wt.%.

At this ratio, the solid-supported BC bilayers encapsulated AuNPs without many aggregates on the surface, as shown below (**Figure 4.12**). If the AuNPs would have interacted together upon water addition, that is, if the cwc of AuNPs was lower than the cwc of the BC itself, one would observe the formation of large AuNP aggregates, possibly outside the bilayer, as the increased size would not match the overall thickness of the BC bilayer.

As it can be seen in the AFM images in **Figure 4.12**, when the ratio of AuNP is increased, more aggregate formation is observed at higher magnifications, which could indicate the disparity of AuNPs and BC with regards to the cwc.

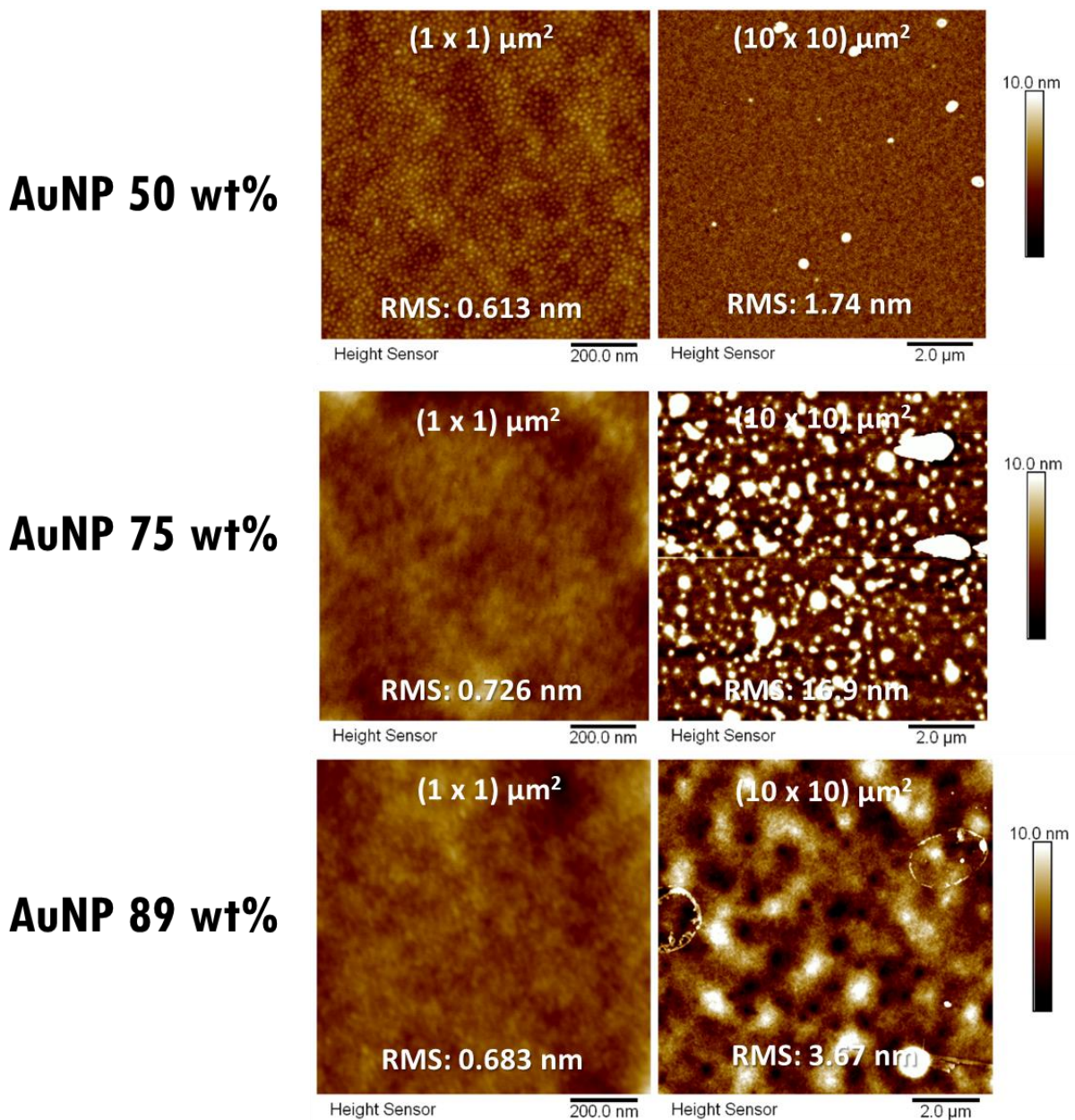


**Figure 4.12.** AFM images of bilayers prepared in the presence of AuNPs of different concentrations.

The bilayer thickness, obtained either by ellipsometry or AFM scratching (**Appendix, Figure A8**) showed no significant difference depending on the position of the sample in the trough (**Figure 4.13**), as for the bilayer formation in the absence of AuNPs shown in **Chapter 2**.

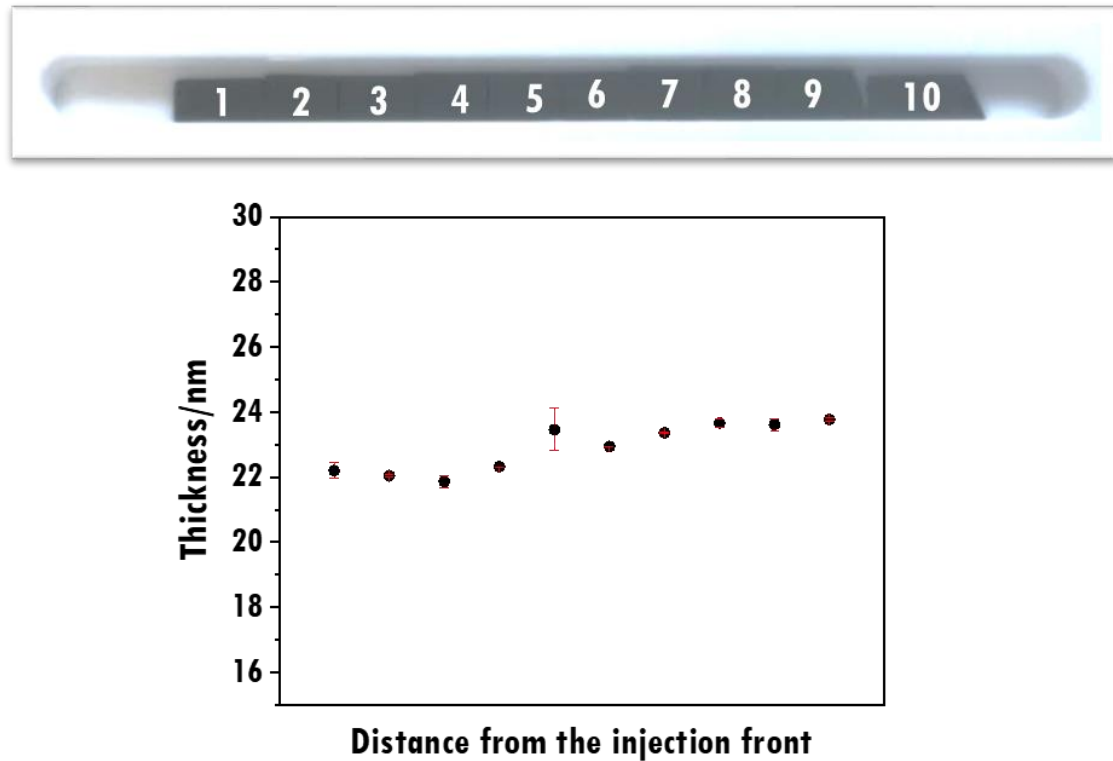


**Figure 4.13.** Thickness of the PS<sub>394</sub>-b-PAA<sub>58</sub> bilayers with encapsulated AuNPs.

The difference in bilayer thickness with and without encapsulated AuNPs is on average 5 nm, which is in agreement with the diameter of the AuNPs. One would expect the AuNPs to be dispersed in a "singular" manner in the BC matrix, meaning that no aggregates of AuNPs should be present. Indeed, when the bilayers are treated with oxygen plasma to remove organic constituents, the singular distribution of the nanoparticles is clearly evidenced by AFM, as shown in **Figure 4.14**.

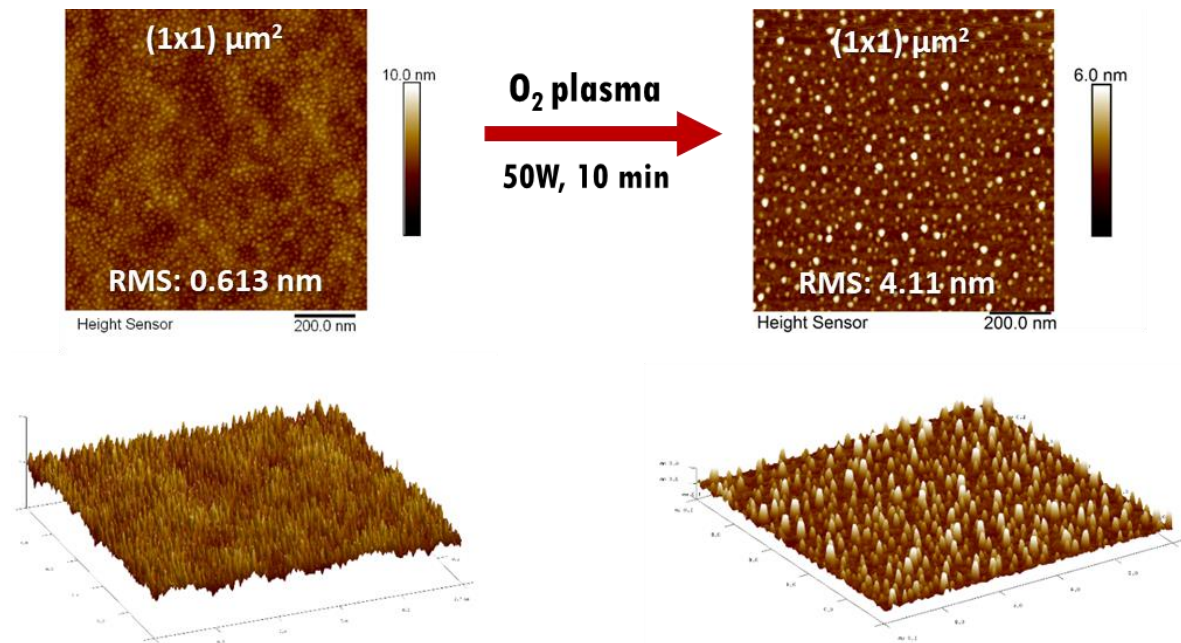


**Figure 4.14.** AFM images showing the surface organization of AuNP-loaded bilayer before (left) and after (right) oxygen plasma treatment.

Additionally, when comparing the bilayers from different locations in the trough (**Figure 4.13**) before and after the same treatment, the nanoparticles are nicely distributed all the way long (**Figure 4.15**).

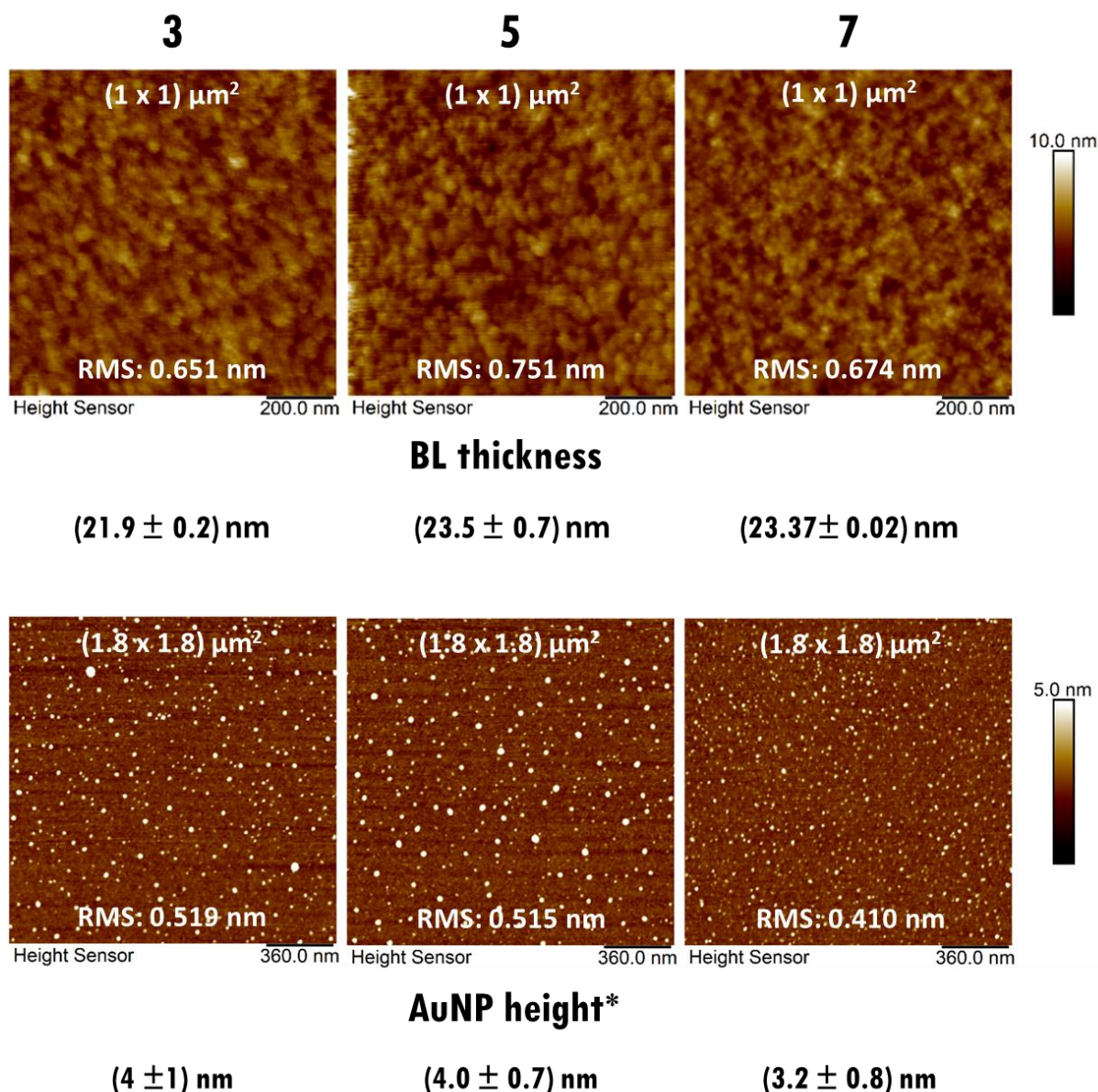


**Figure 4.15.** AFM images showing the surface organization of the AuNP-loaded BC bilayer before (top) and after (bottom) oxygen plasma treatment. Samples at different locations in the trough were analysed (the numbers refers to the positions indicated in **Figure 4.13**). Bilayers thickness values are also shown, as well as the average AuNPs height\* measured with the Nanoscope analysis software.

It is clear from these images that there is a characteristic distance between the AuNPs. At this stage we do not know the origin of this particular organization even if there are similarities with the morphology of BC islets found in PS-*b*-PAA monolayers in air (see **Figure 1.14**).

Knowing that AuNPs exhibit surface plasmon resonance (SPR), a non-destructive technique to characterize the encapsulated nanoparticles is UV-Vis spectroscopy. The 5-nm PS-capped AuNPs in this work were characterized in solution (Experimental section, **Figure**

4.24) and showed a typical strong absorption of the light related to the SPR at a wavelength  $\lambda \sim 520$  nm. The solid-supported BC bilayers, prepared on glass substrates (using cover slips for optical microscopy) in the presence or absence of AuNPs were also characterized, as shown in **Figure 4.16**. For this analysis, 4 samples were stacked and analyzed in air. For a better comparison, a droplet of AuNP dispersion was “sandwiched” between two glass cover slips, and BC bilayers without AuNPs were also analysed (4 samples stacked).

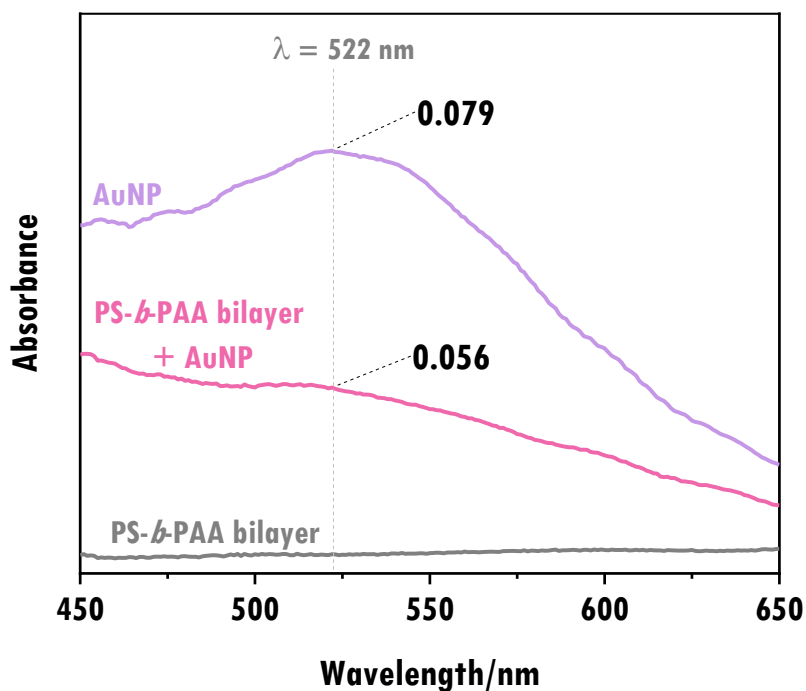


**Figure 4.16.** UV-Vis spectra of the AuNPs alone and PS<sub>394</sub>-*b*-PAA<sub>58</sub> bilayers in the presence and absence of AuNPs.

One can clearly observe a SPR on the solid-supported BC samples with encapsulated AuNPs, in contrast to a negligible absorption related to bare BC bilayers. However, the shape of the absorbance curve is not as defined as the AuNPs dispersion shown in **Figure 4.16** and **Figure 4.24**, since the encapsulated AuNPs are dispersed in a polymeric matrix and not in liquid. With this technique, indeed, one could state the presence of the AuNPs within the bilayer, however further characterization (quantification) should be done in order to obtain more details regarding the encapsulation loading.

Appart from being excellent candidates for the proof of concept of encapsulating actives within the solid-supported BC bilayers, AuNPs could also be used to trigger the opening of the BC bilayer under the effect of temperature and as a consequence use to release co-encapsulated molecules of interest.

### 3. Generation of PS-*b*-PAA bilayers onto colloids

The formation of amphiphilic BC bilayers has also been extended to non-planar surfaces, specifically, on the surface of colloidal substrates. Instead of amino-modified silicon wafers, amino-modified silicon dioxide nanoparticles (average diameter of 100 nm) synthesized by prof. Serge Ravaine (CRPP, Bordeaux) were used. The synthesized NPs were characterized by transmission electron microscopy (TEM), small angle neutron scattering (SANS) and dynamic light scattering (DLS) (**Figure 4.17**). The particles were found to be very well defined in size with a diameter of 100 nm but slightly aggregated due to the presence of amine functions on the surface.

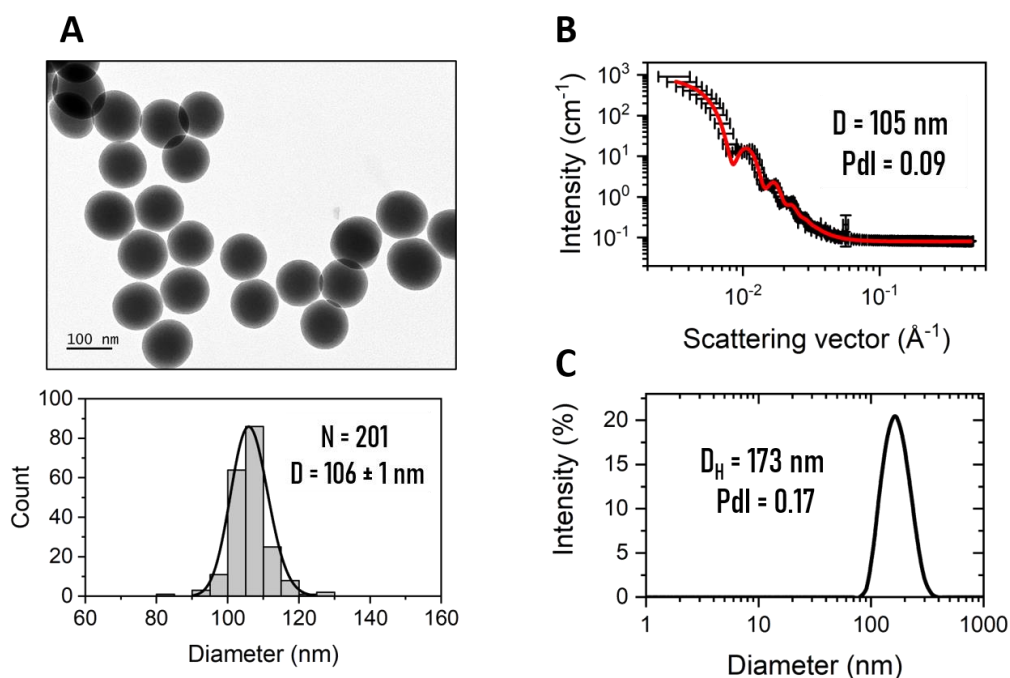


**Figure 4.17.** Characterization of the amino functionalized silica nanoparticles ( $\text{SiO}_2$ -NPs). **A.** Representative TEM picture of the amino-  $\text{SiO}_2$ -NPs (top) with their size distribution (bottom). **B.** Small angle neutron scattering spectrum of the amino-  $\text{SiO}_2$ -NPs in deuterated DMF. Data were fitted using sphere form factor with a hard sphere structure factor (red line). **C.** Size distribution of the amino-  $\text{SiO}_2$ -NPs by dynamic light scattering in DMF.

As on the planar surfaces, the assembly process was performed in two steps involving, first, the formation of a  $\text{PS}_{394}$ -*b*- $\text{PAA}_{58}$  monolayer in non-selective solvent conditions by using the same DMF:THF mixture as previously. Size distributions were determined by DLS for different weight ratios of  $\text{SiO}_2$ -NPs to BC (**Figure 4.18**).

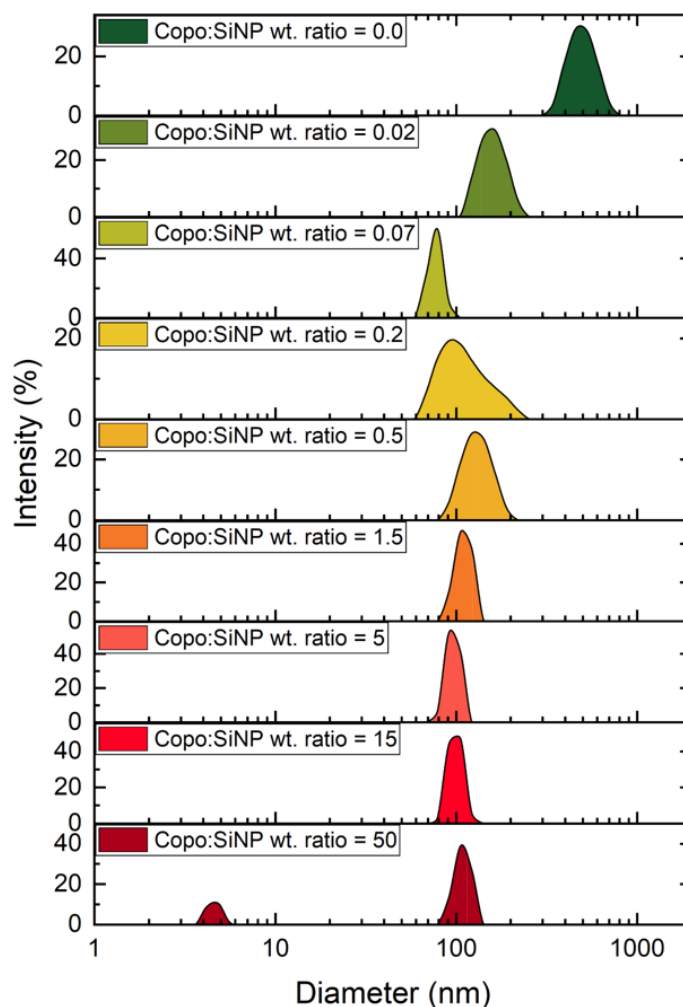


**Figure 4.18.** Intensity-weighted size distribution of mixtures of amino-functionalized silicon dioxide nanoparticles and PS<sub>394</sub>-b-PAA<sub>58</sub> BC prepared at different weight ratios (BC:SiO<sub>2</sub>-NPs) in DMF:THF (80:20) without purification.

It can be clearly seen in **Figure 4.18** that the presence of copolymer in solution allows to break the aggregates of nanoparticles. This is an indirect evidence of the interaction of surface amine groups with acid groups of the copolymer. When the BC monolayer is formed, a better stabilization due to the BC at the surface allows a better particle dispersion, with less aggregates, which is reflected on an apparent lower particle size. Additionally, it was possible to detect free polymer chains in solution at the highest mixing ratio (BC:SiO<sub>2</sub> NP = 50), showing a saturation of the nanoparticles surface. The BC monolayer formation at particle surface was also observed by TEM, as shown in **Figure 4.19**. However, DLS cannot be used to accurately determine the particle surface saturation because the scattering intensity of silica nanoparticles is much greater than that of excess free copolymer.

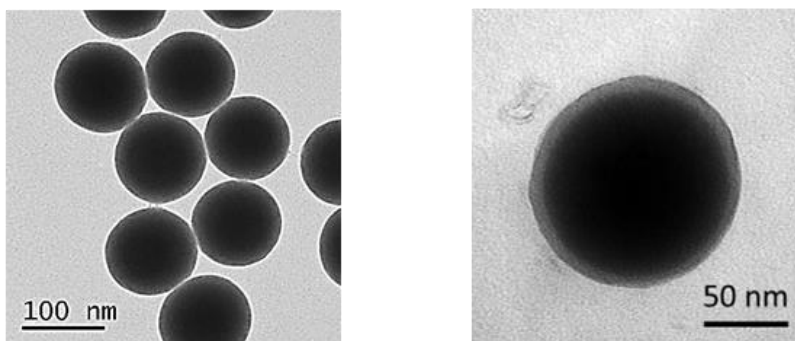


**Figure 4.19.** TEM images of the amine-modified SiO<sub>2</sub>-NPs before (left) and after (right) coating with a monolayer of PS<sub>394</sub>-*b*-PAA<sub>58</sub>.

After the BC monolayer formation, water was added to switch the solvent polarity and, thus, trigger the formation of the second BC layer. The particles were then washed and rinsed by successive centrifugations in order to disperse them in water or in a neutral pH buffer. The nanoparticles were characterized at the end of each assembly step, which allowed to determine the optimal experimental conditions leading to the formation of the layer.

As observed in **Figure 4.20**, size distributions determined by DLS seemed to remain practically constant for different BC:SiO<sub>2</sub>-NP mixing ratios. However, a slight increase in particle size at increasing mixing ratios is observed. This can be related to the increase of the hydrodynamic radius of particles in relation with the build-up of the BC bilayer at particle surface. This was also seen in TEM images (**Figure 4.21**) where a difference in surface coverage is clearly obtained depending on the mixing ratio. For a BC:SiO<sub>2</sub>-NP ratio of 15, a very homogeneous BC bilayer was formed.

An important aspect is that the BC bilayer coating stabilized particles against aggregation, resulting in particles completely dispersed in the medium. However, the present conditions need to be further optimized as the formation of some particle clusters resulting from bilayer fusion was observed in some cases (result not shown). This should be avoided by further studying the influence of the particle concentration on the overall BC self-assembly process. The rate of water addition, which also remains to be studied, could also play a role.

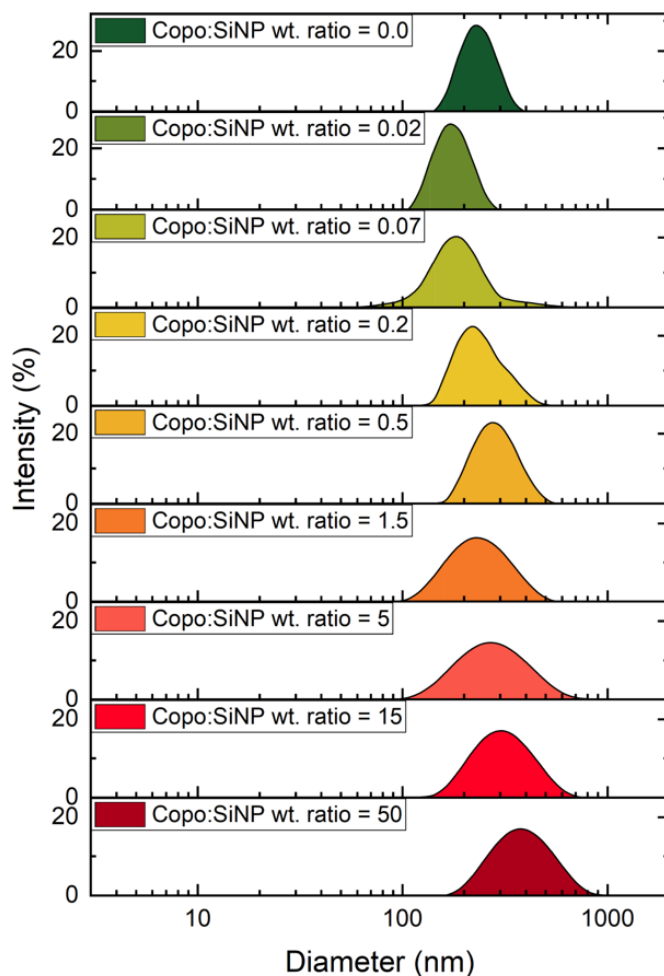


**Figure 4.20.** Intensity-weighted size distribution of mixtures of silica nanoparticles and PS-*b*-PAA at different weight ratios after water addition to trigger the BC self-assembly. DLS analysis were performed after several centrifugation/dispersion cycles in water.

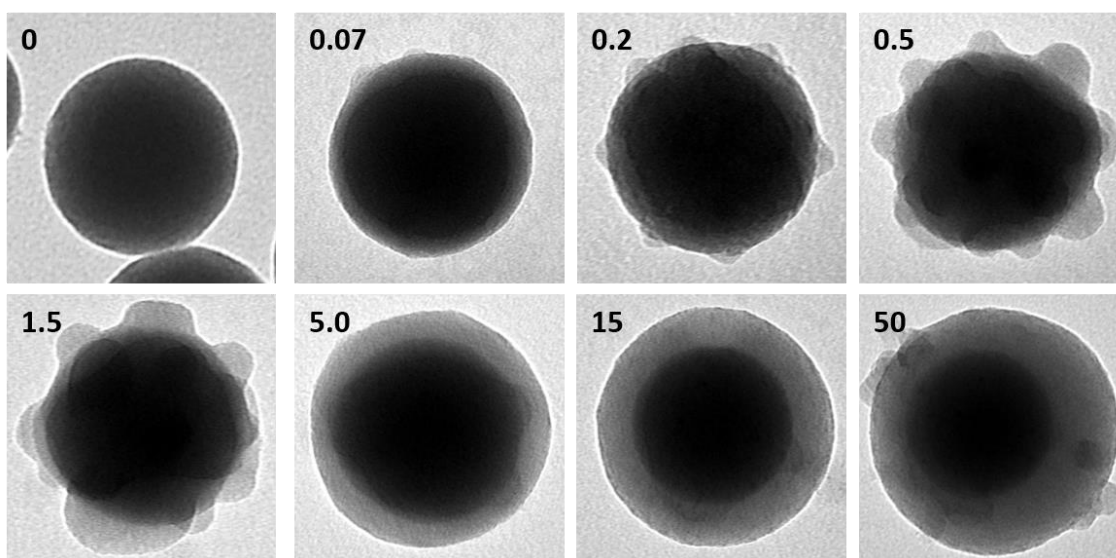


**Figure 4.21.** TEM pictures showing the formation of copolymer bilayer at the surface of silica nanoparticles for different BC:NP weight ratios, in water after purification of the excess copolymer by several centrifugation/resuspension cycles.

## 4. Solid-supported BC bilayers containing a rubbery hydrophobic block

In general, the self-assembly of amphiphilic BCs is known to be out of equilibrium, i.e., the micelles once formed are kinetically frozen and there is no exchange between unimers from different micelles.<sup>1</sup> In fact, whether a process is considered dynamic or frozen depends primarily on the height of the energy barrier ( $E_a$ ) for the extraction of an unimer from the core of a micelle, which scales with:

$$E_a \propto n^{2/3} \gamma \quad \text{Eq. 1}$$

where  $n$  is the degree of polymerization of the hydrophobic block and  $\gamma$  the interfacial tension of the micelle core with the solvent.<sup>2</sup> PS-*b*-PAA copolymers, used as model BCs for the generation of solid-supported bilayers through a surface-induced self-assembly process, contain polystyrene as the hydrophobic block, characterized by a strong hydrophobicity ( $\gamma_{\text{PS/water}} = 32 \text{ mN}\cdot\text{m}^{-1}$ ) and glassiness ( $T_{g,\text{bulk}} \approx 100 \text{ }^\circ\text{C}$ ).<sup>3</sup> Their self-assembly, widely described in the literature, is considered to form not only kinetically arrested aggregates but also physically frozen structures, the later feature being related to the very high  $T_g$  value.<sup>1,4-6</sup>

We have shown in **Chapter 2** that mechanically stable solid-supported BC bilayers containing PS blocks can be successfully prepared. Importantly, it was shown that the approach developed in this work can be applied with BCs containing vitreous hydrophobic PS blocks having molecular weight below the critical mass of entanglement ( $M_{c,\text{PS}} = 32,000 \text{ g}\cdot\text{mol}^{-1}$ ). The formation of entanglements and more specifically the interdigitation between the two layers is therefore not a prerequisite in the self-assembly mechanism. This interesting result can be attributed at first to the glassy character of the bilayers illustrated by a passage at the solution/air interface without delamination of the upper layer as it is generally the case for lipid bilayers for reasons of energy minimization.

If we want to generalize our approach, we need to show that it is possible to form bilayers with a rubbery core or, in other words, that only the hydrophobic interaction between the blocks is sufficient to maintain the integrity of the bilayer. It will then be very instructive to see if this works for hydrophobic blocks with molecular weight below the bulk-determined

$M_c$  critical mass. This should also provide a better understanding of the effects of confinement on chain entanglements and mobility (see paragraph 5).

The generation of solid-supported poly(butyl acrylate)-*b*-poly(acrylic acid) (PBA-*b*-PAA) bilayers could help to elucidate these different points. While the hydrophobicity does not change significantly compared to PS ( $\gamma_{\text{PBA/water}} = 20 \text{ mN.m}^{-1}$ ), PBA presents a rubbery character due to a much lower  $T_g$  value ( $T_g, \text{bulk} \approx -54 \text{ }^\circ\text{C}$ ).<sup>1</sup> Depending on whether solid-supported PBA-*b*-PAA bilayers can be generated with PBA blocks above and below the critical entanglement mass ( $M_{c, \text{PBA}} = 45,000 \text{ g.mol}^{-1}$ ), a better understanding and possibly an answer for the remaining questions can be drawn.

In this sense, during the last months of this PhD, the synthesis of PBA-*b*-PAA (with block sizes similar to the PS-*b*-PAA model used in this thesis work) has been undertaken. By sequential monomer addition using radical addition fragmentation transfer (RAFT) polymerization, a tert-butyl acrylate homopolymer (tBA) of desired DP size (similar to the PAA block used for PS-*b*-PAA) was first synthesized (PtBA). Then, the PBA-*b*-PtBA copolymers were prepared using the freshly prepared PtBA homopolymer as a macroinitiator. A final step, related to the acidolysis of the tert-butyl acrylate group for the generation of poly(acrylic acid) was undertaken using trifluoroacetic acid. Although the synthesis of PnBA-*b*-PtBA was successfully achieved, the deprotection (acidolysis) of the tBA group represented a significant issue that was not solved due to time constraints. Thus, the surface-induced self-assembly of PBA-*b*-PAA bilayers will be the focus of future research.

## 5. Solid-supported BC bilayers as models for the study of thin film properties

Polymer ultrathin films are widely studied because of their endless technological and industrial applications. When the thickness is reduced, the surface-to-volume ratio increases altering various physical properties like the glass transition temperature or the coefficient of thermal expansion. Instead of adopting a three-dimensional random coil conformation (as is typical in the bulk), the polymer chains adopt a conformational structure resembling a two-dimensional random coil. This reduction in dimensionality coupled with interfacial effects due to intermolecular forces changes the ways in which the polymer chains pack and entangle,

producing changes in the physical properties of the film. These initial observations inspired a community of researchers, over the past three decades, to investigate the influence interfacial confinement on the properties of thin polymeric films with a primary focus on the glass transition, although their findings might differ considerably, certainly due to differences in the processing conditions (annealing, nature of the substrate...) and the probing techniques (different physical grounds, model –dependency...)..<sup>7-10</sup>

There is therefore no clear consensus on the trend and origin of the observed deviations. Although very recently, a joint effort between CRPP and IRDL (Lorient, G. Vignaud) has conclusively demonstrated that the density of thin PS (and PMMA) films (< 100 nm) can vary with thickness due to confinement effects associated with surface interactions, suggesting a possible correlation between  $T_g$ , the coefficient of thermal expansion (CTE) and free volume of polymer thin films<sup>11,12</sup>. Much remains to be done and understood.

Therefore, we believe that our solid-supported BC bilayers prepared by the SISAL fabrication method can be useful to study the particular properties of thin polymer films more systematically since the thickness and interactions of the BL with the substrate and/or air interface can be easily tuned using BCs with different block size and nature. Indeed, the generation of ultra-thin homogeneous polymer films is a real challenge, especially below 30 nm where spinodal dewetting can occur.<sup>13,14</sup>

Very preliminary experiments were performed on our systems to measure  $T_g$  in confined geometry using an ellipsometer working at  $\lambda = 605$  nm equipped with a hot stage. In this type of measurement, the  $T_g$  is determined from the analysis of the raw ellipsometric angles  $\psi$  and  $\Delta$  related to the amplitude attenuation and the phase change during reflection, respectively. During heating of the film, these angles change linearly with temperature until reaching the glass transition temperature where a change in slope occurs. The  $T_g$  is taken at the bend of the curve.<sup>15</sup> The samples were annealed for 2 h at a temperature of 130 °C well above the  $T_g$  of the bulk PS to erase any thermal history prior to measurements. The experiments were performed under controlled relative humidity conditions, as it has recently been shown that this parameter can have an impact on the  $T_g$  of thin films that contain some high energy (hydrophilic) groups.<sup>16,17</sup>

As can be seen in **C**, a transition is present in the PS-*b*-PAA monolayer with a kink around 77 °C in agreement with the literature of the last three decades showing values decreasing well below the overall  $T_g$  with film thickness (PS).

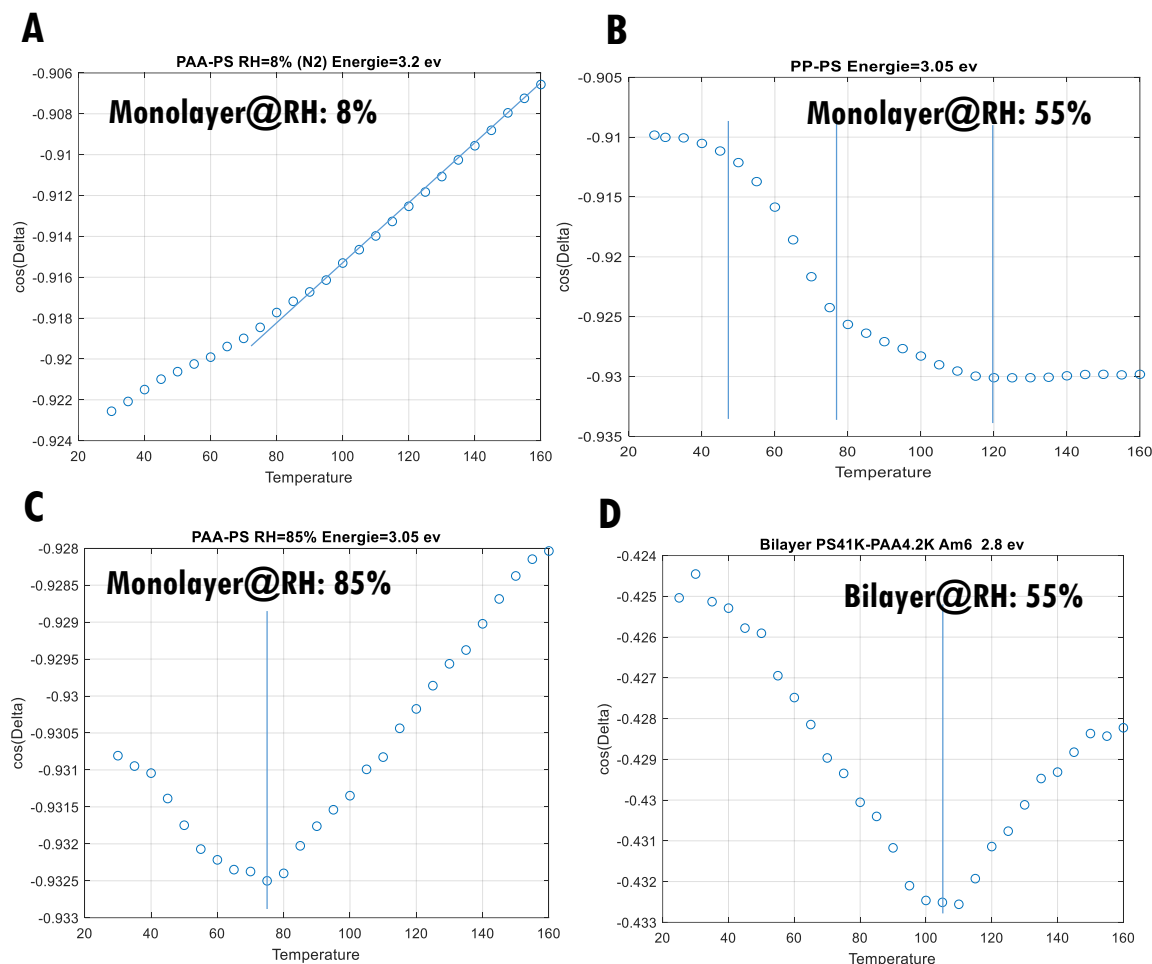


**Figure 4.22.** Variation of the  $\cos \Delta$  ellipsometric angle with temperature for a PS-*b*-PAA monolayer at **A** 8, **B** 55 and **C** 85% relative humidity (RH) and **D** bilayer at 55% RH. The different kinks observed in the curves are ascribed to different “glass” transition temperatures.

Surprisingly, when the RH is reduced to 55%, different kinks appear, suggesting contributions from various interfaces to the glass transition. By further reducing the RH to 8%, the transition is barely observable. These preliminary results indicate that while confinement effects are inherent in a thin-film geometry, the presence of moieties such as COOH groups at the substrate interface that naturally hydrate with relative humidity can also alter the interfacial forces and suppress or intricate these effects.<sup>17</sup>

In the case of the PS-*b*-PAA bilayer, a single transition is obtained slightly above 100 °C although 20 nm PS thin films have reduced  $T_g$  generally. In this case however, the PS/air

interface is not free, there is a layer of PAA chains probably responsible for the reduced mobility of the outermost surface. Indeed, it is known that the overlap of a PS film with a very thin layer of metal, for example, has a  $T_g$  identical to that of the bulk  $T_g$  for all measured film thicknesses. It is likely that the presence of an additional layer compensates for the effect of the liquid surface layer responsible for the drop in  $T_g$  in the case of PS films.<sup>18</sup>

These very preliminary experiments highlight the potential of our bilayer platform to systematically study the different parameters that can influence mobility,  $T_g$ , and density such as film thickness but also the interactions that take place at the free and substrate interfaces.

## 6. Methodologies

### 6.1. Generation of asymmetric BC bilayers

The generation of asymmetric  $PS_{394}\text{-}b\text{-}PAA_{58}/PS_{182}\text{-}b\text{-}PAA_{19}$  bilayers (where the first BC refers to the bottom layer and the second BC to the top layer) involved, first, the immersion of pre-functionalized wafers in the trough containing the  $PS_{394}\text{-}b\text{-}PAA_{58}$  (BC 1 g.L<sup>-1</sup> in DMF:THF 80:20, filtration with 0.1 μm PTFE filter, 2h incubation) for the adsorption of a BC monolayer. After that, the substrates were rinsed in another vial containing DMF:THF (80:20) to remove BC excess, and re-immersed in the trough containing, this time, the  $PS_{182}\text{-}b\text{-}PAA_{19}$  solution (BC 1 g.L<sup>-1</sup> in DMF:THF 80:20, filtration with 0.1 μm PTFE filter). An aqueous solution of NaOH (pH 11) was then slowly added with an infusion syringe pump (New Era, NE-300) at a rate of 50 μL.min<sup>-1</sup> until a water content of 6 vol.% was reached. The system was allowed to equilibrate for 18h (overnight). Afterward, a rinsing step including simultaneous injection of at one end and removal of the solution at the other were performed with two infusion syringe pumps at increasing flow rates (300 μL.min<sup>-1</sup> during 2 h using aqueous NaOH solution followed by 5 mL.min<sup>-1</sup> during 5 min using DI water). Finally, manual injection and removal of water was performed using a wash bottle and a peristaltic pump up to 400 mL to fully exchange the BC solution with water. The BC bilayers self-assembled on wafer substrates were then taken out carefully and dried under a nitrogen flow. Specifically, to minimize capillary forces at the air/water interface, the wafers were slowly removed vertically from the solution.

The idea is similar for the generation of BC bilayers with different BCs, for instance,  $PS_{394}\text{-}b\text{-}PAA_{58}/PS_{480}\text{-}b\text{-}P2VP_{476}$ : the bottom layer ( $PS_{394}\text{-}b\text{-}PAA_{58}$ ) is formed by adsorption of the

pre-functionalized wafers in a BC solution; the substrates are rinsed in solvent to remove BC excess and re-immersed in the other BC solution (PS<sub>480</sub>-*b*-P2VP<sub>476</sub>) prior to the water addition for the generation of the BC bilayer through self-assembly. The PS<sub>480</sub>-*b*-P2VP<sub>476</sub> copolymer used in this work was synthesized by Dr. Benjamin Cabannes-Boué (LCPO, Bordeaux). The cwc of the PS<sub>480</sub>-*b*-P2VP<sub>476</sub>

## 6.2. Encapsulation of AuNPs

### 6.2.1. Synthesis and characterization of PS-capped AuNP

\*The PS-capped AuNPs were synthesized by prof. Serge Ravaine (CRPP).

**Materials:** Hydrogen tetrachloroaurate (99,9%), tetraoctylammonium bromide, and sodium borohydride were purchased from Sigma-Aldrich and were used without further purification. Thiol-terminated polystyrene (PS-SH) ( $M_n = 1,600 \text{ g}\cdot\text{mol}^{-1}$ ) were purchased from Polymer Source, Inc. (Dorval, Canada). Deionised water with a resistivity of 18.2 M $\Omega$ .cm at 25°C was obtained from a Milli-Q system (Millipore).

**Experimental:** Gold nanoparticles with a spherical shape and diameter of  $5 \pm 1 \text{ nm}$  were synthesized using a procedure reported elsewhere.<sup>19</sup> Briefly, an aqueous solution of hydrogen tetrachloroaurate (30 ml, 30 mmol.L<sup>-1</sup>) was mixed with a solution of tetraoctylammonium bromide in toluene (80 ml, 50 mmol.L<sup>-1</sup>). The two-phase mixture was vigorously stirred until all the tetrachloroaurate was transferred into the organic layer. Then, PS-SH (0.84 mmol) was added to the organic phase. A freshly prepared aqueous solution of sodium borohydride (25 ml, 0.4 mol L<sup>-1</sup>) was slowly added under vigorous stirring. After further stirring for 1 h the organic phase was separated and mixed with 500 ml ethanol to remove excess PS-SH. The mixture was kept for 4 h at - 18 °C and the black precipitate was filtered off and washed with ethanol. The crude product was finally dissolved in 10 ml THF.

**Characterization:** The AuNPs, prepared were characterized using TEM (**Figure 4.23**), showing an average diameter of  $(5 \pm 1) \text{ nm}$ .

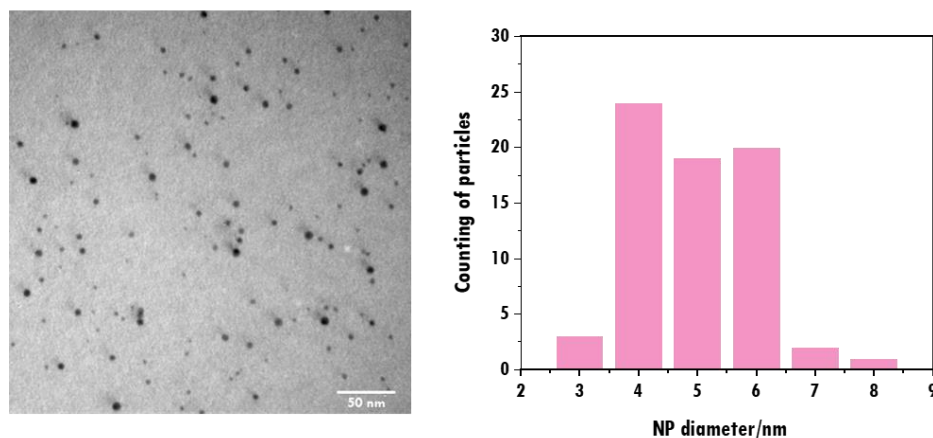


**Figure 4.23.** TEM image (left) and size distribution of the AuNPs (right).

The presence of a Plasmon Resonance band was observed at  $\lambda = 520$  nm using UV-Vis spectroscopy, and a diameter of  $\sim 11$  nm was obtained by DLS (2x the hydrodynamic radius), as shown in **Figure 4.24**.

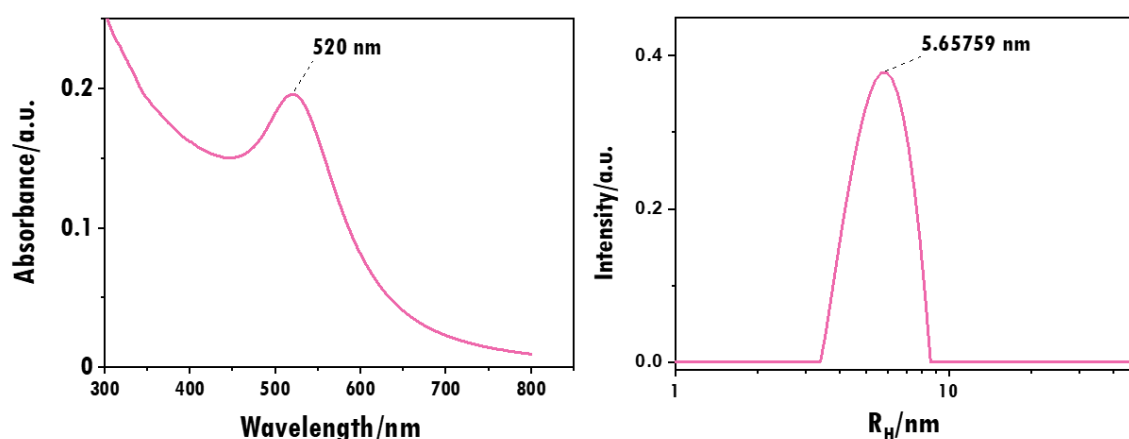


**Figure 4.24.** Absorbance UV-Vis spectrum (left) and DLS (right) of the AuNP dispersion in DMF:THF.

## 6.2.2. Self-assembly of PS-*b*-PAA bilayers in the presence of PS-capped AuNPs

For the BC monolayer formation, the pre-functionalized wafers were immersed in the trough containing a mixture of BC solution and AuNPs (8 mL of BC solution  $1 \text{ g.L}^{-1}$  mixed with  $196 \mu\text{L}$  of PS-capped AuNP dispersion (solid content:  $40.83 \text{ mg.mL}^{-1}$ ) - the mixture was filtered with  $0.1 \mu\text{m}$  pore size membrane). The following considerations were taken for the AuNP:BC ratio calculation: the volume of a single AuNP of  $6.5 \cdot 10^{-20} \text{ cm}^3$ , the mass of a single AuNP is

$1.26 \cdot 10^{-18}$  (density of gold =  $19.3 \text{ g.cm}^{-3}$ ) and the number of AuNPs comprised in  $196 \text{ }\mu\text{L}$  of dispersion of  $6.4 \cdot 10^{15}$ . Besides, the number of BC molecules comprised in  $8 \text{ mL}$  of  $1 \text{ g.L}^{-1}$  solution is  $1.1 \cdot 10^{17}$ . The calculated ratio AuNP to BC molecules is 17 ( $1.1 \cdot 10^{17}/6.4 \cdot 10^{15}$ ).

After 2 h of incubation, water was slowly added with an infusion syringe pump (New Era, NE-300) at a rate of  $50 \text{ }\mu\text{L.min}^{-1}$  until a water content of 6 vol.% was reached. The system was allowed to equilibrate for 18h (overnight). Afterward, a rinsing step including simultaneous injection of DI water at one end and removal of the solution at the other were performed with two infusion syringe pumps at increasing flow rates ( $300 \text{ }\mu\text{L.min}^{-1}$  during 2 h followed by  $5 \text{ mL.min}^{-1}$  during 5 min). Finally, manual injection and removal of water was performed using a wash bottle and a peristaltic pump up to 400 mL to fully exchange the BC solution with water. The BC bilayers self-assembled on wafer substrates were then taken out carefully and dried under a nitrogen flow. Specifically, to minimize capillary forces at the air/water interface, the wafers were slowly removed vertically from the solution.

## 6.3. Generation of PS-*b*-PAA bilayer onto colloids

### 6.3.1. PS-*b*-PAA monolayer formation

Amino-modified SiNP suspensions were prepared using dry DMF and THF (DMF:THF 80:20) at  $0.2 \text{ g.L}^{-1}$ . BC solutions at different concentrations were prepared in DMF:THF (80:20). For the BC monolayer formation, the SiNP suspension was first sonicated during 2 min (1 sec. on, 2 sec. off) at 80% power using a Vibra-Cell™ Ultrasonic Liquid Processors equipped with a CV18 sonication probe. The BC solution was added progressively during the sonication to reach a volume ratio of 1:1. The final suspension was vortexed, sonicated and kept under agitation for 24 h.

### 6.3.2. PS-*b*-PAA bilayer formation

For the BC bilayer formation, to the previous suspension containing the SiNP-supported BC monolayer, pure water was added drop by drop to be slightly above the CWC. After 1 h of incubation, a large volume of pure water was added to reach 50 vol.% in the system. In order to remove the BC aggregates in solution, the rinsing step consists on a centrifugation step, removal of the supernatant and addition of pure water, followed by

vortex and sonication. This rinsing process is repeated three times for complete removal of the BC aggregates.

## 6.4. Solid-supported BC bilayers containing a rubbery hydrophobic block

### 6.4.1. Synthesis of PBA-*b*-PAA

Materials: 1,4-dioxane and dichloromethane (DCM) were purchased from Sigma-Aldrich and Eurisotop, respectively, and used as received. Azobisisobutyronitrile (AIBN), n-butyl acrylate (nBA) and tert-butyl acrylate (tBA) were purchased from Sigma Aldrich. Monomers were purified by passing through a basic alumina column for inhibitor removal before use. Cyanomethyl dodecyl trithiocarbonate (RAFT agent) was purchased from ABCR (Karlsruhe, Germany) and used as received.

RAFT polymerization of PtBA: In a 15 mL schlenk tube, tBA (1.34 g, 1.5 mL, 10.45 mmol) was mixed with AIBN (0.0002 g, 1.2  $\mu$ mol) and RAFT agent (0.0563 g, 177  $\mu$ mol). The volume was adjusted with 1,4-dioxane to 5 mL and the flask was sealed with a rubber septum. The solution was stirred for a couple of minutes and an aliquot was removed for NMR. After that, the solution was degassed through freeze-pump-thaw degassing cycles until complete removal of dissolved oxygen and immersed into a thermostatic oil bath at 70 °C. Aliquots were removed from the reaction medium and analysed by NMR up to a monomer conversion of ~ 80%. Once the conversion was reached, the tube was removed from the oil bath to cool down and stop the reaction. 5 mL of 1,4-dioxane was added to the reaction tube, which was rotary-evaporated at 40 °C until no significant remained solvent was observed by NMR. No further purification was performed.

RAFT polymerization of PBA-*b*-PtBA: In a 15 mL schlenk tube, nBA (3.6 g, 4 mL, 28 mmol) was mixed with AIBN (0.0002 g, 1.2  $\mu$ mol) and the RAFT-PtBA (0.05321 g). The volume was adjusted with 1,4-dioxane to 12 mL and the flask was sealed with a rubber septum. The solution was stirred for a couple of minutes and an aliquot was removed for NMR. After that, the solution was degassed through freeze-pump-thaw degassing cycles until complete

removal of dissolved oxygen and immersed into a thermostatic oil bath at 70 °C. Aliquots were removed from the reaction medium and analysed by NMR up to a monomer conversion of ~ 80%. Once the conversion was reached, the tube was removed from the oil bath to cool down and stop the reaction. 5 mL of 1,4-dioxane was added to the reaction tube, which was rotary-evaporated at 40 °C until no significant remained solvent was observed by NMR. No further purification was performed.

Acidolysis of PBA-*b*-PtBA: PtBA-*b*-PBA was dissolved in DCM. Then, a 5 fold-excess of trifluoroacetic acid, TFA (mol % corresponding to the amount (in mol) of tBA units) was added. The mixture was stirred at room temperature for 72 h. After that, the reaction mixture is rotary evaporate, dissolved again in 1,4-dioxane, and rotary evaporate again. To check whether acidolysis was successful, NMR was performed.

## Conclusions

---

The proposed Surface-Induced Self-Assembly of Amphiphilic BC Bilayers (SISAL) fabrication method can be generalized and extended for several other applications. As explored in **Chapter 3**, with SISAL one can generate solid-supported PS-*b*-PAA bilayers that, once rinsed in a non-selective solvent, give rise to much denser PS brushes, in fair agreement with pure PS films. As high grafting density polymer brushes are usually obtained using “grafting from” techniques (described in the State-of-the-Art chapter), with our approach one could generate higher density PS brushes by using a PS-*b*-PAA copolymers and a simple “grafting to”-based approach.

It has been shown that by using the SISAL method one can generate not only symmetric but also asymmetric BC bilayers, either by using the same BC with different molecular weights for the first and second layer, or different BC chemical compositions, proved here by the fabrication of PS-*b*-PAA bilayers with different molecular weights or PS-*b*-PAA/PS-*b*-P2VP bilayers.

The assembly of amphiphilic BCs with hydrophobic entities can be combined to generate actives encapsulated in the hydrophobic reservoir of the solid-supported bilayer, as demonstrated here with polystyrene-capped gold nanoparticles.

The versatility of the SISAL method was also illustrated with the BC bilayer fabrication onto colloidal substrates with the work of Dr. Martin Fauquignon (LCPO, Bordeaux).

The solid-supported BC bilayers, generated using SISAL in planar substrates, could be advantageously used as models for the study of singular properties of thin films, as demonstrated with some preliminary measurements of glass transition temperatures ( $T_g$ ) on PS-*b*-PAA monolayers and bilayers by Guillaume Vignaud (Université Bretagne Sud at Lorient).

---

## References

---

- (1) Théodoly, O.; Jacquin, M.; Muller, P.; Chhun, S. Adsorption Kinetics of Amphiphilic Diblock Copolymers: From Kinetically Frozen Colloids to Macrosurfactants. *Langmuir* **2009**, *25* (2), 781–793. <https://doi.org/10.1021/la8030254>.
- (2) Lamprou, A.; Xie, D.; Storti, G.; Wu, H. Self-Association Dynamics and Morphology of Short Polymeric PBA-*b*/Co-PAA Surfactants. *Colloid Polym. Sci.* **2014**, *292* (3), 677–685. <https://doi.org/10.1007/s00396-013-3119-2>.
- (3) Jacquin, M.; Muller, P.; Cottet, H.; Théodoly, O. Self-Assembly of Charged Amphiphilic Diblock Copolymers with Insoluble Blocks of Decreasing Hydrophobicity: From Kinetically Frozen Colloids to Macrosurfactants. *Langmuir* **2010**, *26* (24), 18681–18693. <https://doi.org/10.1021/la103391p>.
- (4) Luo, L.; Eisenberg, A. Thermodynamic Size Control of Block Copolymer Vesicles in Solution. *Langmuir* **2001**, *17* (22), 6804–6811. <https://doi.org/10.1021/la0104370>.
- (5) Yu, Y.; Zhang, L.; Eisenberg, A. Morphogenic Effect of Solvent on Crew-Cut Aggregates of Amphiphilic Diblock Copolymers. *Macromolecules* **1998**, *31* (4), 1144–1154. <https://doi.org/10.1021/ma971254g>.
- (6) Zhang, L.; Shen, H.; Eisenberg, A. Phase Separation Behavior and Crew-Cut Micelle Formation of Polystyrene-*b*-Poly(Acrylic Acid) Copolymers in Solutions. *Macromolecules* **1997**, *30* (4), 1001–1011. <https://doi.org/10.1021/ma961413g>.
- (7) Priestley, R. D.; Ellison, C. J.; Broadbelt, L. J.; Torkelson, J. M. Materials Science: Structural Relaxation of Polymer Glasses at Surfaces, Interfaces, and in Between. *Science* (80-. ). **2005**, *309* (5733), 456–459. <https://doi.org/10.1126/science.1112217>.
- (8) De Gennes, P. G. Glass Transitions in Thin Polymer Films. *Eur. Phys. J. E* **2000**, *2* (3), 201–205. <https://doi.org/10.1007/PL00013665>.
- (9) Forrest, J. A.; Dalnoki-Veress, K.; Stevens, J. R.; Dutcher, J. R. Effect of Free Surfaces on the Glass Transition Temperature of Thin Polymer Films. *Phys. Rev. Lett.* **1996**, *77* (10), 2002–2005. <https://doi.org/10.1103/PhysRevLett.77.2002>.
- (10) Hsu, D. D.; Xia, W.; Song, J.; Keten, S. Glass-Transition and Side-Chain Dynamics in Thin Films: Explaining Dissimilar Free Surface Effects for Polystyrene vs Poly(Methyl Methacrylate). *ACS Macro Lett.* **2016**, *5* (4), 481–486. <https://doi.org/10.1021/acsmacrolett.6b00037>.
- (11) Unni, A. B.; Vignaud, G.; Chapel, J. P.; Giermanska, J.; Bal, J. K.; Delorme, N.; Beuvier, T.; Thomas, S.; Grohens, Y.; Gibaud, A. Probing the Density Variation of Confined Polymer Thin Films via Simple Model-Independent Nanoparticle Adsorption. *Macromolecules* **2017**, *50* (3), 1027–1036. <https://doi.org/10.1021/acs.macromol.6b02617>.

- (12) Giermanska, J.; Ben Jabrallah, S.; Delorme, N.; Vignaud, G.; Chapel, J. P. Direct Experimental Evidences of the Density Variation of Ultrathin Polymer Films with Thickness. *Polymer (Guildf)*. **2021**, 228 (June), 123934. <https://doi.org/10.1016/j.polymer.2021.123934>.
- (13) Xie, R.; Karim, A.; Douglas, J. F.; Han, C. C.; Weiss, R. A. Spinodal Dewetting of Thin Polymer Films. *Phys. Rev. Lett.* **1998**, 81 (6), 1251–1254. <https://doi.org/10.1103/PhysRevLett.81.1251>.
- (14) Bal, J. K.; Beuvier, T.; Unni, A. B.; Anabela, E.; Panduro, C. Stability of Polymer Ultrathin Films. **2015**, No. Xx, 8184–8193.
- (15) El Ouakili, A.; Vignaud, G.; Balnois, E.; Bardeau, J. F.; Grohens, Y. Multiple Glass Transition Temperatures of Polymer Thin Films as Probed by Multi-Wavelength Ellipsometry. *Thin Solid Films* **2011**, 519 (6), 2031–2036. <https://doi.org/10.1016/j.tsf.2010.10.015>.
- (16) Kim, S.; Mundra, M. K.; Roth, C. B.; Torkelson, J. M. Suppression of the t G-Nanoconfinement Effect in Thin Poly(Vinyl Acetate) Films by Sorbed Water. *Macromolecules* **2010**, 43 (11), 5158–5161. <https://doi.org/10.1021/ma1005606>.
- (17) Nguyen, H. K.; Labardi, M.; Lucchesi, M.; Rolla, P.; Prevosto, D. Plasticization in Ultrathin Polymer Films: The Role of Supporting Substrate and Annealing. *Macromolecules* **2013**, 46 (2), 555–561. <https://doi.org/10.1021/ma301980w>.
- (18) Sharp, J. S.; Teichroeb, J. H.; Forrest, J. A. The Properties of Free Polymer Surfaces and Their Influence on the Glass Transition Temperature of Thin Polystyrene Films. *Eur. Phys. J. E* **2004**, 15 (4), 473–487. <https://doi.org/10.1140/epje/i2004-10078-0>.
- (19) Brust, M.; Walker, M.; Bethell, D.; Schiffrin, D. J.; Whyman, R. Synthesis of Thiol-Derivatized Gold Nanoparticles in a Two-Phase Liquid-Liquid System. *J. Chem. Soc. Chem. Commun.* **1994**, 801–802. <https://doi.org/DOI> <https://doi.org/10.1039/C39940000801>.



# General conclusions

In this PhD work we have developed a new method for the fabrication of amphiphilic block copolymer films, structured as bilayers on solid substrates. The method is based on the general principle of self-assembly of amphiphilic molecules in aqueous medium governed by the hydrophobic effect as described for surfactants. The novelty consisted in reproducing the principle of micellization of amphiphilic block copolymers at a solid-liquid interface. Thus, the proposed SISAL approach (Surface-Induced Self-Assembly of Amphiphilic Block Copolymer Bilayers), involves the adsorption of a first BC monolayer in a non-selective solvent by physico-chemical interactions between the hydrophilic block and the substrate, followed by the formation of a second monolayer by self-assembly of BCs in solution with the BCs from the first monolayer, after the introduction of a selective solvent (water) which will change the polarity of the medium and thus trigger interactions between the hydrophobic blocks of BCs. Unlike lipid bilayer self-assembly, which is usually done by fusion of lipid vesicles (liposomes) to the surface of a solid substrate, the SISAL method involves the BC self-assembly in two distinct steps. This is the strength and versatility of this new process which can be used, in principle, on substrates of any shape and size (planar, colloidal, hollow), with a very large variety of block copolymers well beyond the only ones whose composition allows the formation of polymer vesicles (polymersomes) in solution, and last but not least, enable the formation of asymmetric bilayers. Each of the steps in the fabrication method has been carefully studied and well characterized, mainly with the PS-*b*-PAA model system carrying a glassy hydrophobic block whose self-assembly in solution has been extensively studied in the literature. The formation of the BC monolayer in a non-selective solvent, described in detail in **Chapter 1**, is the starting point of the fabrication process. The grafting density as well as the thickness of the monolayer depend on the composition and the molar mass of the copolymer, as described in the Marques-Joanny mean-field theory. Experimentally, the adsorbed monolayers showed an islet-like structure when observed in air (AFM) due to a partial dewetting of the PS blocks to minimize the free energy of the system, recalling the low density expected for this type of “grafting onto” polymer brushes. A priori, it seems important to have a high grafting density so that the adsorbed monolayer can develop sufficient interactions with the copolymers in solution during the formation of the second monolayer. However, the

densification process highlighted in **Chapter 3** tends to demonstrate that the initial formation of a densely grafted monolayer is not a critical condition, at least in the case of PS-*b*-PAA copolymers. The formation of the bilayer by water addition to the medium was observed and thoroughly characterized in **Chapter 2** by numerous techniques such as AFM, neutron reflectivity and PM-IRRAS for PS blocks below and above the “bulk” critical mass between entanglements. These experiments validated the general principle of the SISAL approach and the robustness of the generated bilayer, which maintained their mechanical integrity and did not delaminate when passing through the liquid/air interface.

On the other hand, the densification step of the monolayer remains partially misunderstood. In particular, it would be necessary in the future to understand how hydrogen bonds, assuming that they really exist, can be established between the PAA blocks of the adsorbed copolymers and those which are still in solution, especially in the case where a diluted sodium hydroxide solution (pH 11) is used to trigger the hydrophobic effect. Moreover, the question of the generalization of this densification phenomenon which was observed with PS- *b*-PAA copolymers but not with those of the PS-*b*-PEO type is also raised.

The formation of supported block copolymer bilayers has been little described to date. The main reason is that there are no universal methods for making such bilayers. Langmuir Blodgett or vesicle fusion techniques all have their limitations. With the SISAL method, we believe that it is now possible to fabricate such bilayers on different substrates and with different block copolymer compositions. Thus, we were able to demonstrate in **Chapter 4** that the self-assembly of copolymer bilayers can be performed on the surface of colloidal particles and that asymmetric bilayers (PS- *b*-PAA/PS- *b*-P2VP) could also be obtained. It will be important to study further the parameters governing the organization, conformation and thickness of the BC bilayer. In the case of polymer vesicles or free-standing membranes, these parameters are **i)** the stretching of the hydrophobic blocks in the membrane **ii)** the interfacial tension between the core and the shell **iii)** and the repulsive interaction between hydrophilic blocks. However, there is a main difference between a polymer membrane in a vesicle (or free-standing membrane) and a solid-supported polymer bilayer since in the latter situation, the first BC layer is physically attached to a surface (fluid membranes will not be prone to thermal undulations anymore for example). Thus, in a sense, the supported BC bilayers are not really symmetric compared to vesicle membrane. Therefore, in addition, to the BC molecular weight and composition, the BC grafting density and the conformation of

hydrophobic blocks in the monolayer are additional parameters to consider on the final structure of the bilayer. Furthermore, only hydrophobic PS blocks were studied in this work. It would be very important to fully generalize the SISAL approach to study a system with a rubbery block to better understand whether the robustness of the bilayers is a matter of mechanics due to a glassy reservoir or whether only hydrophobic interactions between the chains (entangled or not) can maintain the mechanical integrity of the generated bilayers.

This PhD work had no specific application in mind, as it was mainly a fundamental study of the self-assembly process from a surface. However, we were able to show that bilayers could be functionalized on the surface using copolymers of various compositions and that gold nanoparticles could be co-assembled within the hydrophobic reservoir (**Chapter 4**). This should open perspectives in terms of applications in the field of so-called functional surfaces such as for the development of sensors capable of detecting a physicochemical modification in the surrounding environment. Applications in opto-electronics can also be imagined, in particular by using conductive block copolymers. Finally, and importantly, obtaining BC bilayers calibrated in thickness and composition with a tunable interfacial interaction according to the nature of the hydrophilic block provides an efficient platform to perform fundamental studies on the peculiar physical properties of thin polymer films.



# Appendix

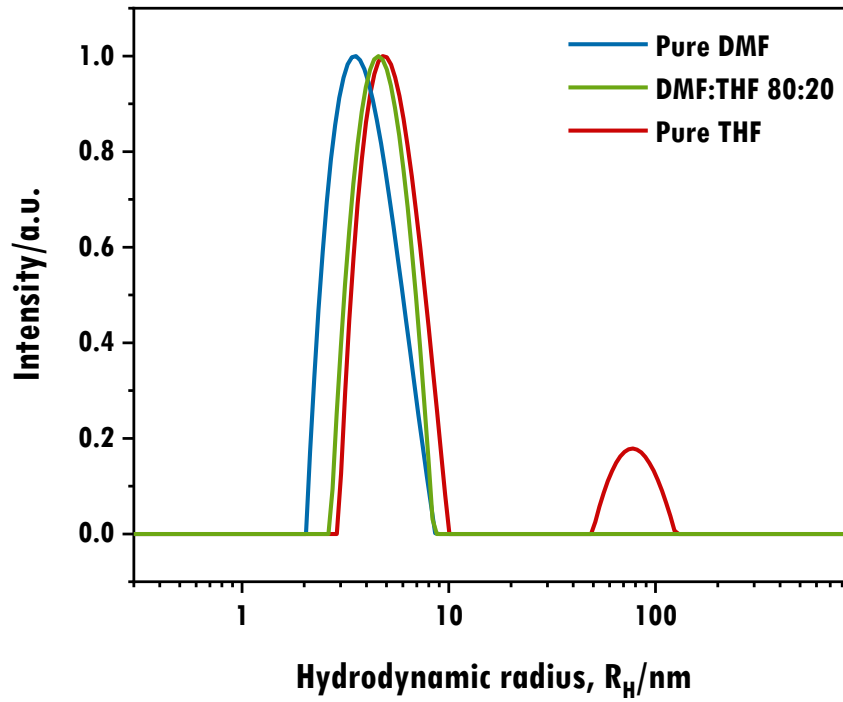


Figure A1. DLS of  $PS_{394}$ - $b$ - $PAA_{58}$  solutions in DMF, THF and DMF:THF (80:20 vol:vol).

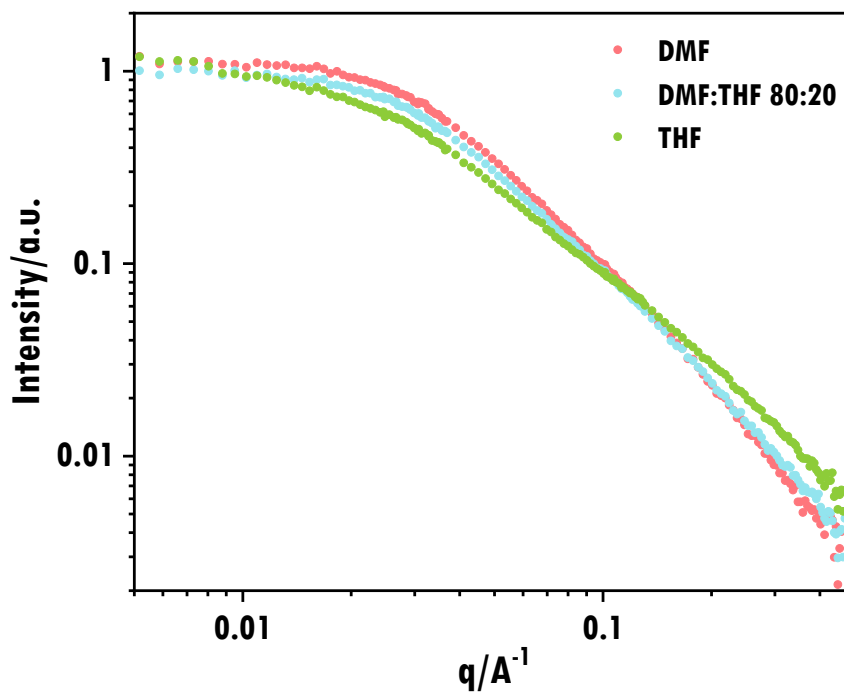
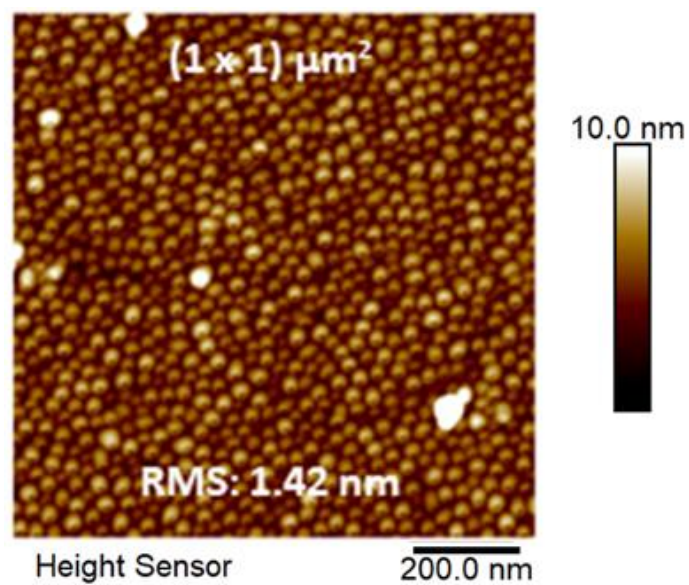
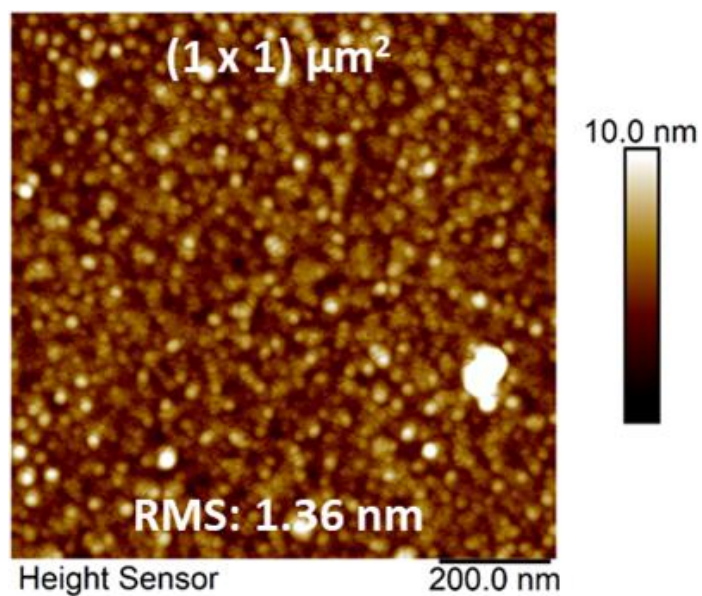


Figure A2. SANS of  $PS_{394}$ - $b$ - $PAA_{58}$  solutions in DMF, THF and DMF:THF (80:20 vol:vol).



**Figure A3.** AFM image of a  $\text{PS}_{394}\text{-}b\text{-PAA}_{58}$  monolayer after adsorption of the amino-modified PS latex particles and rinsing.



**Figure A4.** AFM image of a deuterated  $\text{PS}_{394}\text{-}b\text{-PAA}_{58}$  monolayer.

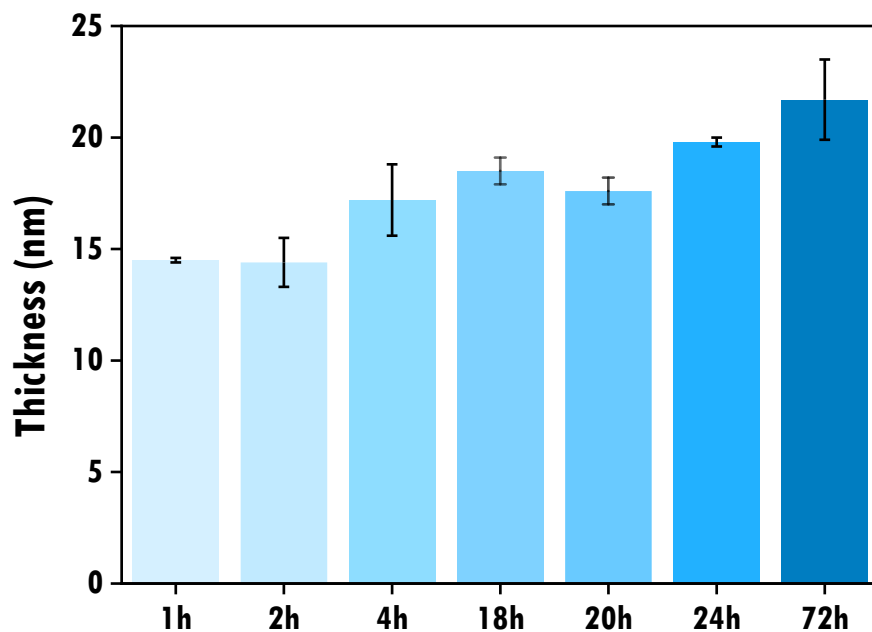


**Figure A5.** Thickness determined by ellipsometry for bilayer assembly kinetics using NaOH at pH 11 as the triggering solution.

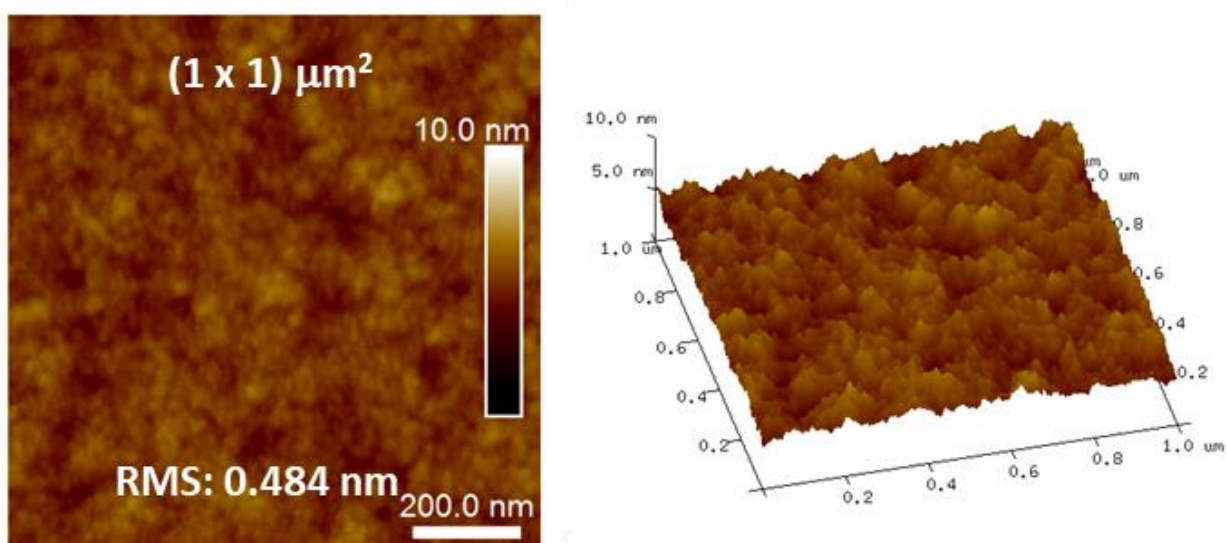


**Figure A6.** AFM image of a PS<sub>394</sub>-*b*-PAA<sub>58</sub> bilayer prepared with 1 h of equilibration after the triggering with an aqueous NaOH solution at pH 11

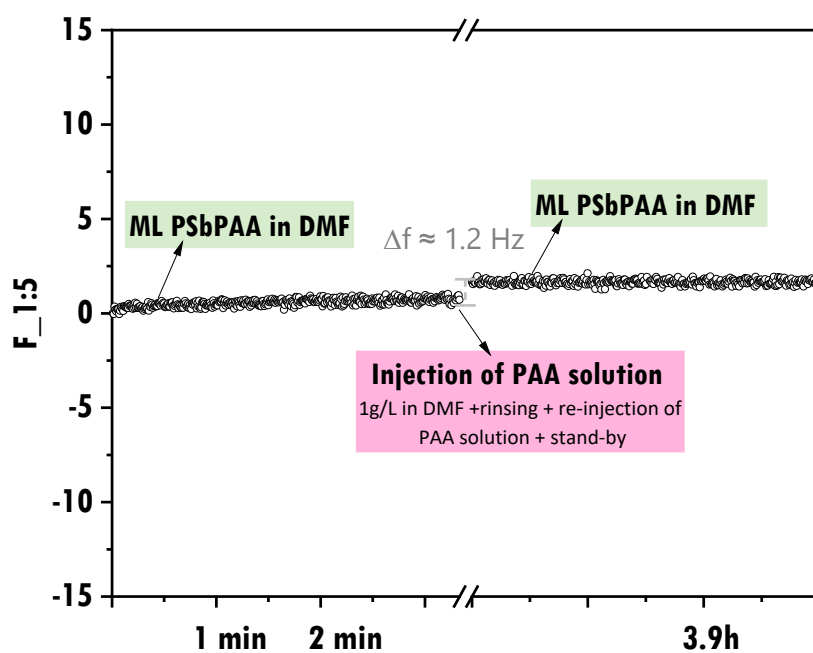


**Figure A7.** Real-time QCM measurements of PAA<sub>69</sub> adsorption in DMF on QCM sensors previously coated with a PS<sub>394</sub>-*b*-PAA<sub>58</sub> monolayer.

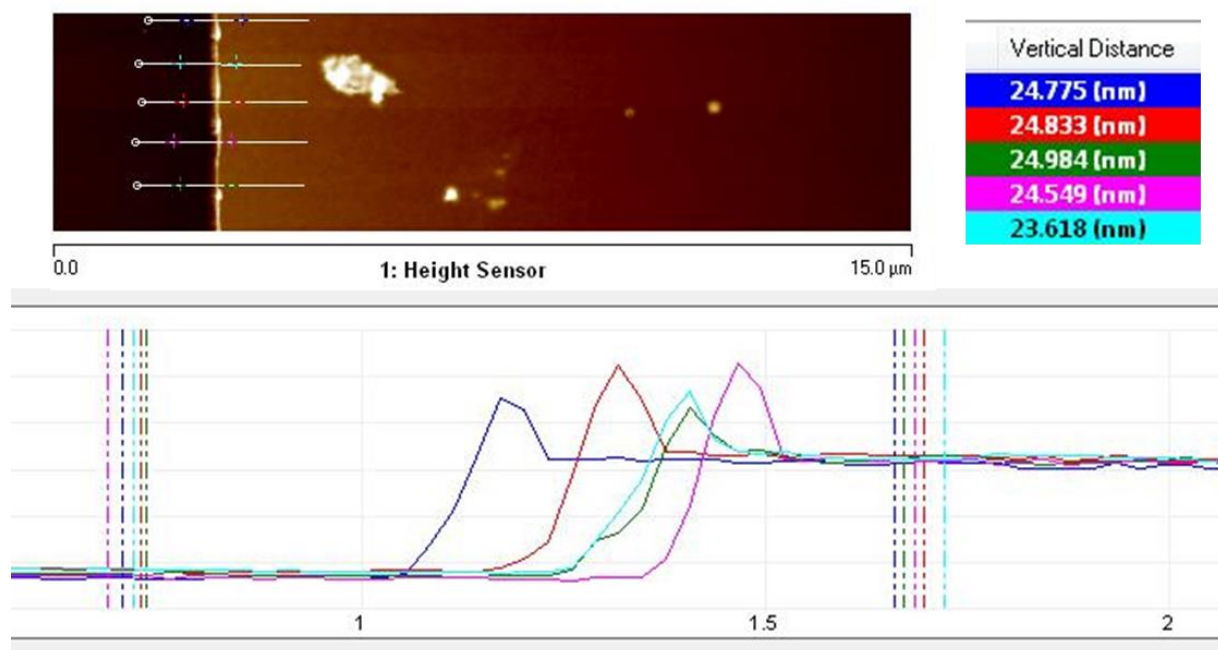


**Figure A8.** AFM image (top, left) of the scratching used to measure the thickness of AuNP-loaded PS<sub>394</sub>-*b*-PAA<sub>58</sub> bilayers. Vertical distances (top right) measured from the scratch of the AuNP-loaded bilayer (bottom), giving an average thickness value of  $(24.6 \pm 0.5)$  nm.